



**HAL**  
open science

# Studies of scattering and anisotropic media with Mueller polarimetry : towards digital histology and optical biopsy of tissue

Hee Ryung Lee

► **To cite this version:**

Hee Ryung Lee. Studies of scattering and anisotropic media with Mueller polarimetry : towards digital histology and optical biopsy of tissue. Physics [physics]. Institut Polytechnique de Paris, 2020. English. NNT : 2020IPPAX085 . tel-03144485

**HAL Id: tel-03144485**

**<https://theses.hal.science/tel-03144485>**

Submitted on 17 Feb 2021

**HAL** is a multi-disciplinary open access archive for the deposit and dissemination of scientific research documents, whether they are published or not. The documents may come from teaching and research institutions in France or abroad, or from public or private research centers.

L'archive ouverte pluridisciplinaire **HAL**, est destinée au dépôt et à la diffusion de documents scientifiques de niveau recherche, publiés ou non, émanant des établissements d'enseignement et de recherche français ou étrangers, des laboratoires publics ou privés.

# Studies of Scattering Anisotropic Media with Mueller Polarimetry: Towards Digital Histology and Optical Biopsy

Thèse de doctorat de l'Institut Polytechnique de Paris  
préparée à École Polytechnique

École doctorale n°626 Ecole Doctorale de l'Institut Polytechnique de Paris (ED IP Paris)  
Spécialité de doctorat: Physique

Thèse présentée et soutenue à Palaiseau, le 26 Novembre 2020, par

**HEE RYUNG LEE**

## Composition du Jury:

François Goudail Prof., IOGS (UMR 8501), France	Président
Walter Blondel Prof., University of Lorraine (UMR 7039), France	Rapporteur
Anabela Da Silva DR2 CNRS, Institut Fresnel (UMR 7249), France	Rapporteur
Elise Colin-Koeniguer Dr., ONERA, Palaiseau, France	Examineur
Tatiana Novikova Dr., Ecole polytechnique, IP Paris (UMR 7647), France	Directeur de thèse
Enrique Garcia-Caurel Dr., Ecole polytechnique, IP Paris (UMR 7647), France	Co-Directeur
Jessica Ramella-Roman Prof., Florida International University, USA	Invité
Igor Meglinski Prof., Aston University, Birmingham, UK	Invité
Philippe Schucht Prof., University Hospital Inselspital Bern, Switzerland	Invité



# Acknowledgment

I would like firstly to thank Prof. Walter Blondel, Dr. Anabela Da Silva, who reviewed this thesis manuscript, and Prof. François Goudail, Dr. Elise Colin-Koeniguer, Prof. Jessica Ramella-Roman, Prof. Igor Meglinski and Prof. Philippe Schucht for accepting to be part of the jury.

I am deeply grateful to Dr. Tatiana Novikova, my supervisor, for her guidance of my research work over three and a half years. Thanks to her thoughtful support and encouragement of my studies of biophotonics with Mueller polarimetry, I was able to quickly adapt to the new research field and maintain my passion for the research during my PhD course. During my thesis work her advices improved my grasp of Mueller polarimetry and related subjects. Monte Carlo modeling and data interpretation could not be complete without her help. I also would like to express my profound gratitude to Dr. Tatiana Novikova for providing me valuable opportunities for an overseas experience such as contribution to the international conferences and performing international research internship visits. I also wholeheartedly thank my co-supervisor Dr Enrique Garcia-Caurel and Dr Angelo Pierangelo for teaching me how to use polarimetric instruments. The discussions with Prof. Razvigor Ossikovski help me to understand the algebra of Mueller matrices. I am grateful to Dr Sofia Dembski, Dr Christian Lotz, Dr Florian Kai Groeber-Becker from the Fraunhofer Institute for Silicate Research, Wurzburg, Germany and to Prof Philippe Schucht from the University Hospital of Bern, Switzerland, for providing me an opportunity to work with the biological tissue specimens.

I would like to express my gratitude to Prof. Igor Meglinski for igniting my interest in biophotonics. His fascinating presentation on biomedical applications of light, which I attended during his research visit to LPICM, motivated me to apply for the PhD in this field. I thank Prof. Jessica Ramella-Roman for giving me a wonderful research experience in her laboratory at Florida International University. I felt comfortable during my research visit because of her warm-hearted care. I also thank Prof. Jessica Ramella-Roman for giving me an opportunity to learn more about non-linear optics. I also want to thank Dr. Alexander Doronin for his assistance and explanations while doing my computational work in the Victoria University of New Zealand.

I also sincerely thank Prof. Yvan Bonnassieux and Prof. Jin Jang, who were my supervisors of the KHU-X dual master course, for their support. They provided me a chance to complete my master course in both countries (South Korea and France). Their support enabled me to start and adapt well to work in Ecole Polytechnique.

I thank Dr. Pengcheng Li, who was an exchange PhD student at LPICM for helping in benchmarking of our polarized Monte Carlo software. I also thank Junha Park as his knowledge of computer sciences helped me to start with the image processing during my PhD work.

I sincerely want to thank all my past and present co-workers for their assistance and friendship: Dr. Ilyas Saytashev, Dr. Shubham Chandel, Heechul Woo, Seonyong Park, Yongjeong Lee, Minjin Kim, Hindia Nahdi, Akiki Ghewa, Gookbin Cho, Seong Gil Kang, Haeyeon Jun, Yun Ho Ahn, Junbum Park, Youngro Lee, Jinhyeok Im, Jihye Baik, Yeonsoo Cho, Jisoo Oh, and Myeongseop Kim.

Finally, I thank my brother Hee Jae Lee and my parents, who have always believed in me and cheered me up. Their constant support has become a source of great energy for me.



# Table of Contents

<b>Abstract .....</b>	<b>1</b>
<b>General introduction .....</b>	<b>3</b>
<b>Chapter 1. Basic Concepts of Polarimetry .....</b>	<b>6</b>
1.1. Polarization Ellipse.....	7
1.2. Stokes polarization parameters and Stokes vector.....	10
1.2.1. Derivation of Stokes parameters.....	10
1.2.2. The Stokes vector .....	13
1.2.3. Poincaré Sphere .....	14
1.3. Mueller matrices of basic optical components .....	15
1.3.1. Mueller matrix of a polarizer .....	17
1.3.2. Mueller matrix of a retarder.....	19
1.3.3. Mueller matrix of a rotator .....	20
1.3.4. Mueller matrix of rotated optical element .....	21
1.3.5. Mueller matrix of a depolarizer .....	23
1.4. Decompositions of the Mueller matrix .....	24
1.4.1. Noise in the experimental Mueller matrix data .....	25
1.4.2. Lu-Chipman decomposition of the Mueller matrix .....	26
1.4.3. Logarithmic decomposition of the Mueller Matrix .....	30
1.5. Conclusions .....	32
References .....	33
<b>Chapter 2. Mueller Polarimetry: instrumental aspects .....</b>	<b>35</b>
2.1. General principles of Mueller polarimetry .....	36
2.1.1. Design optimization of the complete Mueller polarimeter .....	37
2.1.2. Calibration of The complete Mueller polarimeter .....	40
2.2. Imaging Mueller polarimeter based on ferroelectric liquid crystals .....	44
2.2.1. Mueller microscope in transmission configuration .....	45
2.2.2. Wide-field imaging Mueller polarimeter in reflection configuration.....	47
2.3 Conclusions .....	48
References .....	49

<b>Chapter 3. Polarimetric Data Post-processing and Modeling</b> .....	<b>52</b>
3.1. Image segmentation with statistical DBSCAN algorithm .....	53
3.2. Classification of clustering algorithms .....	54
3.3. DBSCAN clustering algorithm.....	57
3.3.1. Definitions of DBSCAN algorithm .....	57
3.3.2. Original version of DBSCAN algorithm .....	58
3.3.3. Upgraded version of DBSCAN algorithm.....	59
3.3.4. Optimization of the DBSCAN algorithm .....	60
3.3.4.1. <i>Determination of the optimal epsilon value</i> .....	60
3.3.4.2. <i>Comparison between the original and updated versions of the DBSCAN algorithm</i> .....	62
3.4. Modeling of polarized light propagation through biological tissue .....	66
3.4.1. Multiple scattering by spherical particles .....	66
3.4.1.1 <i>Parameters of scattering media</i> .....	67
3.4.1.2. <i>Vector radiative transfer equation</i> .....	71
3.4.2. Monte Carlo algorithm for solution of VRTE in scattering media .....	72
3.4.2.1. <i>Generation of random numbers with given probability distributions.</i> .....	73
3.4.2.2. <i>Photon coordinates and trajectories.</i> .....	75
3.4.3. Monte Carlo algorithm for anisotropic scattering media.....	80
3.4.3.1. <i>Optical anisotropy of tissue</i> .....	80
3.4.3.2. <i>Validation of the updated Monte Carlo algorithm</i> .....	82
3.5. Conclusions .....	84
References .....	85
<b>Chapter 4. Digital histology of thin sections of human skin tissue models with Mueller microscopy</b> .....	<b>87</b>
4.1. Human Skin Equivalent (HSE) .....	88
4.2. Dependence of polarization and depolarization parameters on sample thickness .....	90
4.2.1. Measurements of skin sample thickness.....	91
4.2.2. Thickness dependence of polarization and depolarization parameters.....	94
4.3. Image segmentation (DBSCAN) for advanced analysis of tissue polarimetric properties .....	98
4.4. Mitigating the impact of the spatial fluctuations of tissue section thickness. ....	103
4.5. Monte Carlo modeling of experimental polarimetric data for dermal layer of HSE.....	106
4.5.1. Optical models of HSE dermal layer .....	107
4.5.2. Rotation invariants of logarithmic decomposition.....	108
4.5.3. Choice of an appropriate optical model of the dermis.....	111
4.5.3.1. <i>Ruled out optical models</i> .....	111
4.5.3.2. <i>SCB optical model</i> .....	113
4.6. Conclusions .....	115
References .....	116

<b>Chapter 5. Wide-field imaging Mueller polarimetry for the visualization of brain white matter fiber tracts .....</b>	<b>119</b>
5.1. Introduction .....	119
5.2. Materials and Methods .....	122
5.2.1. Sample preparation .....	122
5.2.2. Measurement Protocol .....	123
5.3. Results and discussion .....	123
5.3.1. Fixed human brain tissue .....	123
5.3.2. Fresh animal brain tissue .....	129
5.4. Conclusions .....	132
References .....	133
<b>General conclusions and Perspectives .....</b>	<b>136</b>
<b>List of Figures .....</b>	<b>138</b>
<b>List of Tables .....</b>	<b>143</b>
<b>Appendix A – List of Publications .....</b>	<b>144</b>
<b>Appendix B – Conferences, Workshops, Exchange research visits, and Scholarships.....</b>	<b>146</b>
<b>Appendix C – Résumé de la thèse en français .....</b>	<b>149</b>

# Abstract

Imaging Mueller polarimetry represents an emerging optical technique for a non-invasive diagnostics of tissue. This optical modality explores the extreme sensitivity of polarized light to the microstructure of a sample under study and provides the most complete information on sample polarimetric properties.

First, the potential of the transmission Mueller microscope operating in the visible wavelength range for digital histology analysis was studied on the unstained histological sections of human skin equivalents. Logarithmic decomposition of the experimental Mueller matrices was combined with the statistical density-based clustering algorithm for the applications with noise (DBSCAN) for diagnostic segmentation of the microscope images of human skin models. The validity of the differential Mueller matrix formalism for fluctuating homogenous depolarizing media was confirmed experimentally for biological tissue. An original method was suggested to mitigate the impact of thickness variation that could affect the accuracy of polarimetric diagnostics of thin tissue sections. A new version of the DBSCAN algorithm was developed to reduce the calculation time and, thus, to allow clustering of large size datasets. When dataset outliers (noise) were effectively filtered out, the contrast between the dermal and epidermal zones of human skin equivalents was significantly increased. Polarized Monte Carlo modeling of the experimental Mueller matrices of thin sections of human skin equivalents confirmed that both linear dichroism and anisotropy of depolarization detected within the dermal zone are due to the presence of well-aligned collagen fibers.

The ex-vivo proof-of-principle studies of the sensitivity of backscattered polarized light to the highly ordered structure of healthy brain white matter are presented in the second part. The thick sections of the formalin-fixed human brain and fresh calf brain were imaged in reflection configuration using wide-field imaging Mueller polarimeter operating in the visible wavelength range. It is known that brain tumors break the highly ordered structure of brain white matter because tumor cells grow in a chaotic way. However, this difference in structural complexity is hardly detectable with a state-of-the-art operative microscope during neurosurgery because of low visual contrast between tumor and healthy brain tissue. We studied the capability of the wide-field imaging Mueller polarimetry to visualize the fiber tracts of healthy brain white matter by detecting the anisotropy of its refractive index (i.e., the birefringence of brain white matter that will be erased by the tumor). The experimental Mueller matrices of brain specimens were processed using the algorithm of Lu-Chipman polar decomposition. The maps of the azimuth of the optical axis of uniaxial linear birefringent medium demonstrated the compelling correlation with the microscopy images of

silver-stained histological sections of brain tissue, a gold standard technique for the visualization of brain white matter fiber tracts *ex-vivo*. These results show the potential of wide-field imaging Mueller polarimetry to provide information on the relative spatial orientation of brain fiber tracts, which can help to detect the exact border between the tumor and surrounding brain tissue, guide neurosurgeon during tumor resection, and improve patient outcomes.

# General Introduction

The global healthcare industry has been growing at an impressive rate in recent years (e.g., 7.3% annual growth rate from 2014 to 2018). It is already one of the biggest overall and its growth is expected to continue [1], [2]. Looking at the trends in healthcare we may note that the estimated number of cancer occurrences (based on estimated population increase) also will grow from 18.1 million in 2018 to 29.5 million in 2040 [3]. As cancer becomes the second leading cause of death [3] (e.g., around 9.6 million deaths in 2018), the importance of cure for cancer patients has also increased. Early detection of cancer could significantly reduce cancer burden because of a higher patient survival rate, decrease in morbidity and cost of treatment.

Therefore, in order to improve the healthcare, new medical imaging devices / technologies (e.g., computed tomography (CT) scanners, real-time ultrasonography, etc.) have been developed and implemented in clinical practice for accurate diagnostics. The histopathology, which is a clinical gold-standard technique for the diagnosis of tissue specimens [4], has also been exploring a variety of optical techniques (e.g. optical coherence tomography (OCT), second harmonic generation (SHG), two-photon excitation fluorescence (TPEF), fluorescence, and polarized light microscopy).

In general, biological tissue is a strongly scattering medium. In addition, the presence of ordered microstructures within tissue induces an optical anisotropy (i. e. anisotropy of tissue refractive index). Pathological alterations modify both scattering and anisotropic properties of healthy tissue. It is known that polarized light is very sensitive to these alterations, because they affect both depolarization and phase shift of the polarized light beam after its interaction with biological tissue. We used a complete Muller polarimetry approach for tissue imaging both in transmission (microscopic scale) and reflection (macroscopic scale) configurations. Applying the appropriate algorithms of non-linear compression (or decomposition) of Mueller matrices we obtained the depolarization and polarization (retardance, dichroism) parameters of measured biological tissues and explored their capabilities to serve as the optical markers of diseased zones in the polarimetric images of tissue. The results of the studies are summarized in this thesis consisting of five chapters.

The Chapter 1 describes the fundamentals of optical polarization and introduces the framework of Stokes-Mueller formalism for the description of polarized light that we will use throughout this thesis. Two Mueller matrix decomposition algorithms (Lu-Chipman and logarithmic) used in our studies for the calculation of polarimetric properties of tissue samples are presented and discussed in details.

The concepts of optimal design and calibration of a complete Mueller polarimeter are presented and discussed in the Chapter 2. Two multi-spectral ferroelectric-liquid crystal-based imaging Mueller matrix polarimeters, namely transmission Mueller microscope and wide-field Mueller imaging system operating in reflection configuration are also described therein. The former and latter instruments were used for the measurements of thin and thick tissue sections, respectively.

The data processing and interpretation algorithms (image segmentation and Monte Carlo modeling) are introduced and discussed in the Chapter 3. A brief review of the data clustering techniques is presented with a special focus on the density-based spatial clustering for the applications with noise (DBSCAN) algorithm (both original and updated versions) that will be later used for the diagnostic segmentation of the polarimetric images of tissue. Monte Carlo algorithm for modeling of polarized light propagation in anisotropic scattering media is discussed. We briefly introduce the vector radiative transfer equation for description of the interaction of polarized light with multiple scattering media and describe the Monte Carlo algorithm for its solution. The updated version of the Monte Carlo algorithm that accounts for the anisotropy of scattering media was developed and validated by the simulations of both isotropic and anisotropic optical phantoms of biological tissue.

In the following chapters we present and discuss the results of our studies of different types of biological tissue with imaging Mueller polarimeters in transmission and reflection configurations.

The Chapter 4 is dedicated to the polarimetric studies anisotropic scattering medium, namely, dermal layer of thin sections of human skin tissue models. The validation of the differential Mueller matrix formalism for fluctuating anisotropic media is performed using the experimental Mueller matrices of dermal layer of human skin equivalents and their logarithmic decomposition. The segmentation of polarimetric images of thin sections of skin tissue is done by applying the DBSCAN algorithm and results are commented. The method to mitigate the impact of tissue thickness fluctuations on its measured polarimetric parameters is introduced. Different optical models of a dermal layer of skin were tested for the interpretation of measurement results for thin sections of human skin tissue models. Monte Carlo simulations demonstrate that the anisotropy of linear depolarization, linear retardance, and linear dichroism that were observed for dermal layer of skin in our experiments are related to the presence of well-aligned collagen fibers.

The polarimetric studies of thick sections of fixed and fresh brain tissue specimens are presented in the Chapter 5. Both types of specimens were measured with the wide-field imaging Mueller polarimeter in backscattering configuration. The maps of polarimetric parameters, such as scalar linear retardance and depolarization, show clear border between the zones of grey and white matter of the brain. The directions of brain white matter fiber tracts are well represented by the azimuth of the optical axis calculated pixel-wise with Lu-Chipman decomposition of experimental Mueller matrix images. This correlation was confirmed by the conventional histology analysis of corresponding silver-stained thin sections of fixed brain tissue. The simple image processing techniques (e.g. fusion and

cropping) were tested for a better visualization of white matter border and directions of the fiber tracts in the imaging plane.

The conclusion contains brief summary of my PhD results and their possible applications for both digital histology and optical biopsy of tissue. The perspectives of further research studies are also discussed.

## References

1. <https://www.bls.gov/ooh/healthcare/home.htm>
2. <https://policyadvice.net/health-insurance/insights/health-care-industry/>
3. <https://www.who.int/news-room/fact-sheets/detail/cancer>
4. Histopathology is ripe for automation. *Nat. Biomed. Eng.*, Vol. 1, p.p. 925, 2017.

# Chapter 1

## Basic concepts of polarimetry

1.1. Polarization Ellipse.....	7
1.2. Stokes polarization parameters and Stokes vector.....	10
1.2.1. Derivation of Stokes parameters.....	10
1.2.2. The Stokes vector .....	13
1.2.3. Poincaré Sphere .....	14
1.3. Mueller matrices of basic optical components .....	15
1.3.1. Mueller matrix of a polarizer.....	17
1.3.2. Mueller matrix of a retarder.....	19
1.3.3. Mueller matrix of a rotator .....	20
1.3.4. Mueller matrix of rotated optical element .....	21
1.3.5. Mueller matrix of a depolarizer .....	23
1.4. Decompositions of the Mueller matrix .....	24
1.4.1. Noise in the experimental Mueller matrix data .....	25
1.4.2. Lu-Chipman decomposition of the Mueller matrix .....	26
1.4.3. Logarithmic decomposition of the Mueller Matrix .....	30
1.5. Conclusions .....	32
References .....	33

Polarization is one of the fundamental properties of light, along with the intensity, frequency, and coherency. The study of optical polarization can lead to a deeper understanding of the nature of light itself as well as can help in the revealing of the optical properties of an object (biological tissue in our study) interacting with a polarized incident beam. Thus, understanding the fundamentals of light polarization is a prerequisite for exploring this property of light for a biomedical diagnostics. In this chapter, we briefly review the theoretical frameworks for the description of polarized light. First, we introduce the concept of the polarization ellipse (e.g., orientation, ellipticity, phase shift) for completely polarized light. Then, we define the Stokes parameters to characterize the completely polarized, partially polarized, or unpolarized light, introduce the Poincaré sphere as the generalization of

the concept of polarization ellipse and define the transfer matrix (or Mueller matrix) that describes the modifications of the Stokes parameters of the incident light by the interaction with a sample. The examples of the Mueller matrices of the basic optical elements (polarizer, retarder, and depolarizer) are provided. Next, we discuss the different algorithms of Mueller matrix decompositions. The criterion of the physically realizable Mueller matrix is introduced based on eigenvalues of the corresponding coherence matrix. Cloude sum decomposition of Mueller matrices is described and its application for noise filtering is discussed [1]. Polar Lu-Chipman decomposition [2] and logarithmic decomposition [3], [4] of Mueller matrices for the physical interpretation of Mueller matrix data in terms of polarimetric properties of the sample are also introduced and discussed.

## 1.1. Polarization Ellipse

Apart from the intensity of light that represents a scalar quantity, the vector nature of light is described by its polarization. Electromagnetic (EM) waves present synchronized oscillations of the electric and magnetic fields. When EM wave propagates in homogenous isotropic media both electric and magnetic field components oscillate within a plane orthogonal to the direction of EM wave propagation (so-called transverse wave). Being a solution of Maxwell equations [5], the electric field of a plane polarized monochromatic EM wave that propagates in z-direction in free space, can be described at time  $t$  and any point  $(x, y)$  as

$$\begin{aligned} E_x(z, t) &= E_{0x} \cos(\omega t - kz + \delta_x) \\ E_y(z, t) &= E_{0y} \cos(\omega t - kz + \delta_y) \end{aligned} \quad (1.1)$$

where  $E_{0x}$  and  $E_{0y}$  are constant maximum amplitudes,  $\delta_x$  and  $\delta_y$  are arbitrary constant phases,  $\omega$  is the angular frequency,  $k$  is the wavenumber, and the subscripts  $x$  and  $y$  refer to the components in the  $x$ - and  $y$ -directions, respectively [6], [7].

The time duration for one cycle of the plane EM wave is only  $10^{-15}$  seconds at optical frequencies. Thus, the EM wave can be considered as “instantaneous,” and the equations for the transverse components of electric field can be re-written as:

$$\begin{aligned} E_x &= E_{0x} \cos(\tau + \delta_x) \\ E_y &= E_{0y} \cos(\tau + \delta_y) \end{aligned} \quad (1.2)$$

where  $\tau = \omega t - kz$  denotes the propagator. The Eq. (1.2) can be modified as follows:

$$\begin{aligned} \frac{E_x}{E_{0x}} &= \cos\tau \cos\delta_x - \sin\tau \sin\delta_x \\ \frac{E_y}{E_{0y}} &= \cos\tau \cos\delta_y - \sin\tau \sin\delta_y \end{aligned} \quad (1.3)$$

Hence,

$$\begin{aligned}\frac{E_x}{E_{0x}} \sin \delta_y - \frac{E_y}{E_{0y}} \sin \delta_x &= \cos \tau \sin(\delta_y - \delta_x) \\ \frac{E_x}{E_{0x}} \cos \delta_y - \frac{E_y}{E_{0y}} \cos \delta_x &= \sin \tau \sin(\delta_y - \delta_x)\end{aligned}\quad (1.4)$$

Squaring and adding two equations in Eq. (1.4) gives

$$\frac{E_x^2}{E_{0x}^2} + \frac{E_y^2}{E_{0y}^2} - 2 \frac{E_x}{E_{0x}} \frac{E_y}{E_{0y}} \cos \delta = \sin^2 \delta \quad (1.5)$$

where  $\delta = \delta_y - \delta_x$  is the phase shift between the orthogonal transverse components of the electric field of the plane EM wave. Eq. (1.5) is the equation of an ellipse for  $E_x$  and  $E_y$  in the  $(x, y)$  coordinate system. The center of ellipse is located at the point  $(0, 0)$ , the presence of a product term  $E_x E_y$  indicates that this ellipse can be rotated, i.e., its axes are not necessarily parallel to  $x$  and  $y$  axes [6], [8], [9].

As we eliminated the propagator term (see Eq. (1.5)), the locus of points, describing the electric field vector of a propagating EM wave, forms an ellipse at any instant of time at any point  $z$ . This ellipse is called the polarization ellipse, and it can be parametrized in different ways. First, it can be inscribed within a rectangle with sides  $2E_{0x}$  and  $2E_{0y}$  (see Fig. 1.1). The polarization ellipse is generally rotated through the angle  $\psi$  which means that the axes of the ellipse do not coincide with the  $x$  and  $y$  axes of the coordinate system (see Fig. 1.1).

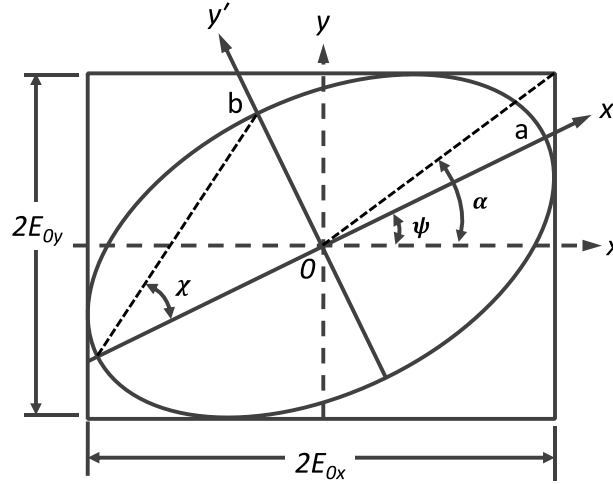


**Figure 1.1** Description of a polarization ellipse in the  $x$ - $y$  laboratory coordinate system.  $\psi$  is the orientation angle,  $\chi$  is the ellipticity angle,  $\alpha$  is the auxiliary angle.

We shall denote by  $x$  and  $y$  the axes of the laboratory coordinate system, and by  $x'$  and  $y'$  the axes of the rotated coordinate system, then the values of the components of the electric field  $E'_x$  and  $E'_y$  in the rotated coordinate system are given by

$$\begin{aligned}
E'_x &= E_x \cos \psi + E_y \sin \psi \\
E'_y &= -E_x \sin \psi + E_y \cos \psi
\end{aligned}
\tag{1.6}$$

where the orientation (or azimuth) angle  $\psi$  ( $0 \leq \psi \leq \pi$ ) is the angle between the  $x$  and  $x'$  axes. If we denote by  $2a$  and  $2b$  ( $a \geq b$ ) the lengths of the major and minor axes of the polarization ellipse respectively, then  $E'_x$  and  $E'_y$  can be expressed as:

$$\begin{aligned}
E'_x &= a \cos(\tau + \delta') \\
E'_y &= \pm b \sin(\tau + \delta')
\end{aligned}
\tag{1.7}$$

where  $\delta'$  is an arbitrary phase, and the  $\pm$  sign denotes the two possible directions of oscillation of the electric field vector (clockwise or counter-clockwise). Substituting Eqs (1.2) and (1.7) into (1.6), we find out that

$$\begin{aligned}
a^2 &= E_{0x}^2 \cos^2 \psi + E_{0y}^2 \sin^2 \psi + 2E_{0x}E_{0y} \cos \psi \sin \psi \cos \delta \\
b^2 &= E_{0x}^2 \sin^2 \psi + E_{0y}^2 \cos^2 \psi - 2E_{0x}E_{0y} \cos \psi \sin \psi \cos \delta \\
a^2 + b^2 &= E_{0x}^2 + E_{0y}^2 \\
\pm ab &= E_{0x}E_{0y} \sin \delta
\end{aligned}
\tag{1.8}$$

Furthermore,

$$\tan 2\psi = \frac{2E_{0x}E_{0y}}{E_{0x}^2 - E_{0y}^2} \cos \delta
\tag{1.9}$$

Eq. (1.8) and (1.9) represent the relation between the angle of rotation  $\psi$  and the parameters  $E_{0x}$ ,  $E_{0y}$ , and  $\delta$ . The auxiliary angle  $\alpha$  can be described as [6], [9]

$$\tan \alpha = \frac{E_{0y}}{E_{0x}} \quad (0 \leq \alpha \leq \frac{\pi}{2})
\tag{1.10}$$

Then, Eq. (1.9) can be rewritten as:

$$\tan 2\psi = \tan 2\alpha \cos \delta
\tag{1.11}$$

Introducing the angle of ellipticity  $\chi$ , defined as

$$\tan \chi = \frac{\pm b}{a} \quad (-\frac{\pi}{4} \leq \chi \leq \frac{\pi}{4})
\tag{1.12}$$

we can get the relation between  $\chi$  and the parameters  $E_{0x}$ ,  $E_{0y}$ , and  $\delta$  as:

$$\sin 2\chi = \frac{\pm 2ab}{a^2 + b^2} = \frac{2E_{0x}E_{0y}}{E_{0x}^2 + E_{0y}^2} \sin \delta = (\sin 2\alpha) \sin \delta \quad (1.13)$$

As shown in Eqs (1.8) - (1.13), the polarization ellipse can be described by angles of orientation  $\psi$  and ellipticity  $\chi$ , as well as by its major,  $E_{0x}$ , and minor,  $E_{0y}$ , axes and the relative phase shift  $\delta$ . In general, the completely polarized light that is described by the polarization ellipse is said to be elliptically polarized. However, the polarization ellipse can have particular degenerate forms (e.g., line or circle) depending on the values of the maximum amplitudes  $E_{0x}$ ,  $E_{0y}$ , and the phase shift  $\delta$ .

For example, when either  $E_{0x} = 0$  or  $E_{0y} = 0$  the light is said to be linear horizontally polarized or vertically polarized, as the electric field vector oscillates along the  $x$  and  $y$  axes, respectively. If  $\delta = 0$  or  $\pi$ , the light is linear  $-45^\circ$ - and  $+45^\circ$ -polarized. Finally, the light is called right or left circularly polarized when  $E_{0x} = E_{0y} = E_0$  and  $\delta = \pi/2$  or  $3\pi/2$ , respectively.

## 1.2. Stokes polarization parameters and Stokes vector

The concept of the polarization ellipse that excludes the propagator from the description of the transverse components of the optical field, is very useful for the description of the various states of completely polarized light (e.g., linearly or circularly polarized light) by a single equation. However, this concept has several limitations. The first one comes from the fact that the direct observation of the polarization ellipse in the experiments is not possible because of too short oscillation time of the electric field vector ( $\sim 10^{-15}$  s) at optical frequencies. Another serious limitation is the capability of the polarization ellipse to describe completely polarized light only. It means that this concept is applicable for the description of neither unpolarized light nor partially polarized light that represent the larger portion of natural light. Thus, the polarization ellipse represents an idealization of the behavior of light at any given moment of time.

To overcome these limitations an alternative description of polarized light in terms of the directly observable intensity, that is derived by time averaging of the squared amplitude of electric field, has been considered. By measuring the intensity, we can obtain four parameters (so-called Stokes parameters) that describe completely or partially polarized, as well as totally depolarized (unpolarized) light. These four Stokes parameters can be arranged in a 4x1 column matrix that is called the Stokes vector. The derivation of the Stokes parameters and some special forms of the Stokes vector for the particular states of the polarization, as well as the concept of the Poincaré sphere are discussed in the following subsections.

### 1.2.1. Derivation of Stokes parameters

We consider a pair of orthogonal plane waves with the electric field vector oscillating along the  $x$ - and  $y$ -axes, respectively, at a space point  $z = 0$ :

$$\begin{aligned}
E_x(t) &= E_{0x}(t) \cos(\omega t + \delta_x(t)) \\
E_y(t) &= E_{0y}(t) \cos(\omega t + \delta_y(t))
\end{aligned}
\tag{1.14}$$

where  $E_{0x}(t)$  and  $E_{0y}(t)$  are the instantaneous amplitudes,  $\delta_x(t)$  and  $\delta_y(t)$  are the instantaneous phases, and  $\omega$  is the instantaneous angular frequency.

By excluding the term  $\omega t$  from Eq. (1.14), we obtain the expression for the polarization ellipse at a given instant of time [6],

$$\frac{E_x^2(t)}{E_{0x}^2(t)} + \frac{E_y^2(t)}{E_{0y}^2(t)} - 2 \frac{E_x(t) E_y(t)}{E_{0x}(t) E_{0y}(t)} \cos \delta(t) = \sin^2 \delta(t)
\tag{1.15}$$

where  $\delta(t) = \delta_y(t) - \delta_x(t)$  is the relative phase factor between the orthogonal transverse components.

For monochromatic EM waves, the phase factors and amplitudes are constant (i.e., do not depend on time). Then, the Eq. (1.15) can be written as

$$\frac{E_x^2(t)}{E_{0x}^2} + \frac{E_y^2(t)}{E_{0y}^2} - 2 \frac{E_x(t) E_y(t)}{E_{0x} E_{0y}} \cos \delta = \sin^2 \delta
\tag{1.16}$$

To remove the time dependence completely, one needs to average Eq. (1.16) only over a single period  $T$  of time oscillations because of the periodicity of  $E_x(t)$  and  $E_y(t)$ . The symbol  $\langle \dots \rangle$  describes the time average, and Eq. (1.16) is modified as [6], [9]

$$\begin{aligned}
\frac{\langle E_x^2(t) \rangle}{E_{0x}^2} + \frac{\langle E_y^2(t) \rangle}{E_{0y}^2} - 2 \frac{\langle E_x(t) E_y(t) \rangle}{E_{0x} E_{0y}} \cos \delta &= \sin^2 \delta \\
\langle E_i(t) E_j(t) \rangle &= \lim_{T \rightarrow \infty} \frac{1}{T} \int_0^T E_i(t) E_j(t) dt \quad i, j = x, y
\end{aligned}
\tag{1.17}$$

Multiplying Eq. (1.17) by  $4E_{0x}^2 E_{0y}^2$ , we find that

$$\begin{aligned}
4E_{0x}^2 \langle E_x^2(t) \rangle + 4E_{0y}^2 \langle E_y^2(t) \rangle - 8E_{0x} E_{0y} \langle E_x(t) E_y(t) \rangle \cos \delta \\
= (2E_{0x} E_{0y} \sin \delta)^2
\end{aligned}
\tag{1.18}$$

From Eq. (1.14), we obtain that

$$\begin{aligned}
\langle E_x^2(t) \rangle &= \frac{1}{2} E_{0x}^2 \\
\langle E_y^2(t) \rangle &= \frac{1}{2} E_{0y}^2 \\
\langle E_x(t) E_y(t) \rangle &= \frac{1}{2} E_{0x} E_{0y} \cos \delta
\end{aligned}
\tag{1.19}$$

Substituting Eqs (1.19) into Eq. (1.18), then adding and subtracting the sum  $E_{0x}^4 + E_{0y}^4$  to the left-hand side, allows Eq. (1.18) to be rewritten as:

$$(E_{0x}^2 + E_{0y}^2)^2 - (E_{0x}^2 - E_{0y}^2)^2 - (2E_{0x}E_{0y}\cos\delta)^2 = (2E_{0x}E_{0y}\sin\delta)^2 \quad (1.20)$$

We denote that the quantities inside the parentheses as [6], [9]

$$\begin{aligned} S_0 &= E_{0x}^2 + E_{0y}^2 = E_x E_x^* + E_y E_y^* \\ S_1 &= E_{0x}^2 - E_{0y}^2 = E_x E_x^* - E_y E_y^* \\ S_2 &= 2E_{0x}E_{0y}\cos\delta = E_x E_y^* + E_y E_x^* \\ S_3 &= 2E_{0x}E_{0y}\sin\delta = i(E_x E_y^* - E_y E_x^*) \end{aligned} \quad (1.21)$$

They further obey the relation

$$S_0^2 = S_1^2 + S_2^2 + S_3^2 \quad (1.22)$$

The four real quantities  $S_0$ ,  $S_1$ ,  $S_2$ , and  $S_3$ , are expressed in terms of the intensities. i.e., they are observables. They represent the Stokes polarization parameters of a plane EM wave. The parameter  $S_0$  is the total intensity of the light. The  $S_1$  parameter stands for the amount of linear horizontal or vertical polarization, the parameter  $S_2$  indicates the amount of linear  $\pm 45^\circ$  polarization, and the  $S_3$  one shows the amount of right- or left-handed circular polarization of the light beam. The Stokes parameters for any polarization state (general form) obey the relation (1.22) [6], [9].

Since the amplitudes and phases of partially polarized light fluctuate slowly, Eqs. (1.21) are valid for a short period of time only. It can be shown that the general relation between the four Stokes parameters for any state of light polarization is given by

$$S_0^2 \geq S_1^2 + S_2^2 + S_3^2 \quad (1.23)$$

where the equality corresponds to the case of completely polarized light, whereas the inequality holds for partially polarized (or for unpolarized) light. The orientation angle  $\psi$  of the polarization ellipse can be expressed in terms of the Stokes parameters as:

$$\tan 2\psi = \frac{2E_{0x}E_{0y}\cos\delta}{E_{0x}^2 - E_{0y}^2} = \frac{S_2}{S_1} \quad (1.24)$$

The ellipticity angle  $\chi$  can be expressed as:

$$\sin 2\chi = \frac{2E_{0x}E_{0y}\sin\delta}{E_{0x}^2 + E_{0y}^2} = \frac{S_3}{S_0} \quad (1.25)$$

The last three Stokes parameters describe the polarized part of the light beam, so we define the degree of polarization (*DOP*) parameter as

$$DOP = \frac{I_{\text{pol}}}{I_{\text{tot}}} = \frac{(S_1^2 + S_2^2 + S_3^2)^{1/2}}{S_0} \quad 0 \leq P \leq 1 \quad (1.26)$$

where the  $I_{\text{tot}}$  is the total intensity of the light beam and the  $I_{\text{pol}}$  indicates the intensity of the sum of the polarization components. When  $P = 1$ , the light beam is completely polarized;  $P = 0$  represents unpolarized light, and the values within the range  $0 < P < 1$  describe partially polarized light. [1], [6], [9], [10] Similarly, the degree of linear polarization (*DOLP*) and the degree of circular polarization (*DOCP*) are defined as

$$DOLP = \frac{(S_1^2 + S_2^2)^{1/2}}{S_0} \quad 0 \leq P_L \leq 1 \quad (1.27)$$

$$DOCP = \frac{S_3}{S_0} \quad 0 \leq P_C \leq 1 \quad (1.28)$$

where  $P_L = 1$  corresponds to complete linearly polarized light, and  $P_C = 1$  represents the complete circularly polarized light.

## 1.2.2. The Stokes vector

The four real-valued Stokes parameters  $S_0, S_1, S_2,$  and  $S_3$  can be arranged in a 4x1 column matrix that we called the Stokes vector of a plane EM wave. [6], [7], [9]

$$S = \begin{bmatrix} S_0 \\ S_1 \\ S_2 \\ S_3 \end{bmatrix} = \begin{bmatrix} E_{0x}^2 + E_{0y}^2 \\ E_{0x}^2 - E_{0y}^2 \\ 2E_{0x}E_{0y}\cos\delta \\ 2E_{0x}E_{0y}\sin\delta \end{bmatrix} \quad (1.29)$$

The amplitudes  $E_{0x}$  and  $E_{0y}$  can be expressed in terms of the auxiliary angle  $\alpha$  ( $0 \leq \alpha \leq \pi/2$ ) and  $E_0 = \sqrt{E_{0x}^2 + E_{0y}^2}$  as

$$\begin{aligned} E_{0x} &= E_0 \cos\alpha \\ E_{0y} &= E_0 \sin\alpha \end{aligned} \quad (1.30)$$

Substituting Eq. (1.30) into Eq. (1.29) leads to

$$S = S_0 \begin{bmatrix} 1 \\ \cos 2\alpha \\ \sin 2\alpha \cos \delta \\ \sin 2\alpha \sin \delta \end{bmatrix} \quad (1.31a)$$

If the light is fully polarized, Eq. (1.31a) can be expressed as

$$S = S_0 \begin{bmatrix} 1 \\ \cos 2\chi \cos 2\psi \\ \cos 2\chi \sin 2\psi \\ \sin 2\chi \end{bmatrix} \quad (1.31b)$$

As it was previously explained, the polarization ellipse degenerates to particular forms for particular values of  $E_{0x}$ ,  $E_{0y}$ , and  $\delta$ . The corresponding Stokes vectors describe these special forms of polarized light (e.g., linear - horizontal, vertical, and  $+45^\circ$ -, and  $-45^\circ$ - and circular - right and left); they are shown in Tab. 1.1.

**Table 1.1** Stokes vectors for linear horizontally, linear vertically, linear  $+45^\circ$ , linear  $-45^\circ$ , right circularly, and left circularly polarized light.

Linear Horizontally Polarized Light (LHP)	Linear Vertically Polarized Light (LVP)	Linear $+45^\circ$ Polarized Light (L+45)
$S = I_0 \begin{bmatrix} 1 \\ 1 \\ 0 \\ 0 \end{bmatrix}$ $E_{0y} = 0, I_0 = E_{0x}^2$	$S = I_0 \begin{bmatrix} 1 \\ -1 \\ 0 \\ 0 \end{bmatrix}$ $E_{0x} = 0, I_0 = E_{0y}^2$	$S = I_0 \begin{bmatrix} 1 \\ 0 \\ 1 \\ 0 \end{bmatrix}$ $E_{0x} = E_{0y} = E_0, \delta = 0$ $I_0 = 2E_0^2$
Linear $-45^\circ$ Polarized Light (L-45)	Right Circularly Polarized Light (RCP)	Left Circularly Polarized Light (LCP)
$S = I_0 \begin{bmatrix} 1 \\ 0 \\ -1 \\ 0 \end{bmatrix}$ $E_{0x} = E_{0y} = E_0, \delta = 180^\circ$ $I_0 = 2E_0^2$	$S = I_0 \begin{bmatrix} 1 \\ 0 \\ 0 \\ 1 \end{bmatrix}$ $E_{0x} = E_{0y} = E_0, \delta = 90^\circ$ $I_0 = 2E_0^2$	$S = I_0 \begin{bmatrix} 1 \\ 0 \\ 0 \\ -1 \end{bmatrix}$ $E_{0x} = E_{0y} = E_0, \delta = -90^\circ$ $I_0 = 2E_0^2$

### 1.2.3. Poincaré sphere

The polarization ellipse can be represented on the complex plane. On the other hand, Eqs (1.31) represent the relation between Cartesian coordinates and spherical coordinates. Hence, the polarization ellipse can be projected onto a sphere, called the Poincaré sphere. [16], [9]. Using the Poincaré sphere concept, we can simplify many calculations as well as provide simple and compelling illustration on how the polarized light interacts with both the polarizing elements (polarizer, retarder, and rotator) and the depolarizers. We set  $S_0 = 1$  for the first Stokes parameter. Any point on the unit radius Poincaré sphere (see Fig. 1.2) corresponds to the three Stokes parameters  $S_1$ ,  $S_2$ , and  $S_3$  of the elliptically polarized light. The properties of the Poincaré sphere are summarized below:

1. The blue lined-spherical triangle can be described by the ellipticity angle  $\chi$ , orientation (or azimuth) angle  $\psi$ , and auxiliary angle  $\alpha$ .
2. The point  $P(2\chi, 2\psi)$  on the Poincaré sphere surface is specified in terms of its latitude ( $2\chi$ ) and its longitude ( $2\psi$ ), where  $-\pi/2 \leq 2\chi \leq \pi/2$  and  $-\pi \leq 2\psi \leq \pi$ , respectively.
3. The equator on the Poincaré sphere ( $2\chi = 0^\circ$ ) corresponds to linearly polarized light. The longitude  $2\psi = 0^\circ, 90^\circ, 180^\circ$ , and  $270^\circ$  represent the linear horizontal, linear  $+45^\circ$ , linear vertical, and linear  $-45^\circ$  polarized light, respectively.
4. The prime meridian ( $2\psi = 0^\circ$ ) relates to non-rotated elliptically polarized light. Moving up along the prime meridian (longitude  $2\chi = 0^\circ$  to  $90^\circ$  - the north pole) leads to linear horizontally, right elliptically, and right circularly polarized light, in this order. Similarly, moving down from the equator to the south pole ( $2\chi = -90^\circ$ ) leads to changing left elliptically polarized light to left circularly polarized light.

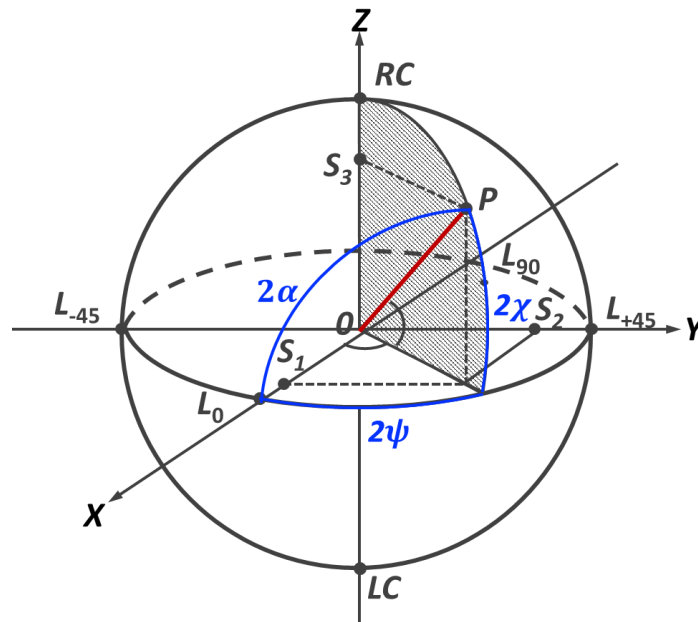


**Figure 1.2** The Poincaré sphere.  $L_0$ ,  $L_{90}$ ,  $L_{+45}$ ,  $L_{-45}$ ,  $RC$ , and  $LC$  represents the linear horizontal, linear vertical, linear  $+45^\circ$ , linear  $-45^\circ$ , right circular, left circular polarized light, respectively.

### 1.3. Mueller matrices of basic optical components

As mentioned above, the Stokes parameters enable us to describe the fundamental properties of polarized light. Thus, when the incident light interacts with the sample, the incident and the emerging beams can be described by the Stokes parameters  $S_i$  and  $S'_i$  ( $i = 0, 1, 2, 3$ ), respectively (see Fig. 1.3).

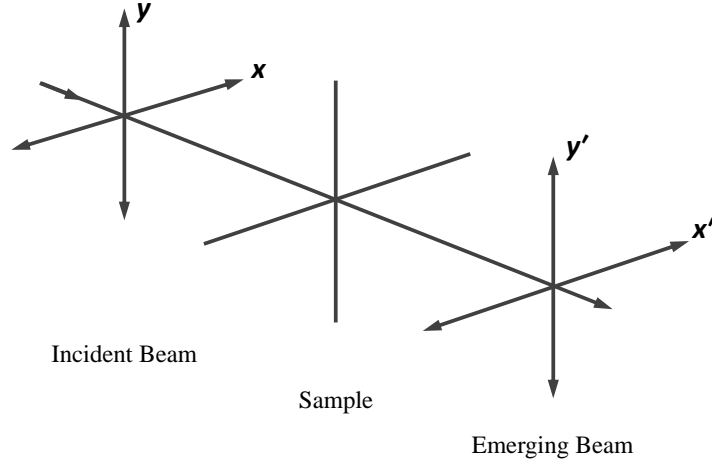


**Figure 1.3** The incident beam interacts with a sample, and the emerging beam comes out.

The relation between the incident and emerging beam can be expressed as a linear combination of the two sets of four Stokes parameters  $S_i$  and  $S'_i$  ( $i = 0, 1, 2,$  and  $3$ ):

$$\begin{aligned}
 S'_0 &= m_{00}S_0 + m_{01}S_1 + m_{02}S_2 + m_{03}S_3 \\
 S'_1 &= m_{10}S_0 + m_{11}S_1 + m_{12}S_2 + m_{13}S_3 \\
 S'_2 &= m_{20}S_0 + m_{21}S_1 + m_{22}S_2 + m_{23}S_3 \\
 S'_3 &= m_{30}S_0 + m_{31}S_1 + m_{32}S_2 + m_{33}S_3
 \end{aligned} \tag{1.32}$$

Eq. (1.32) can be written as a matrix form:

$$\begin{bmatrix} S'_0 \\ S'_1 \\ S'_2 \\ S'_3 \end{bmatrix} = \begin{bmatrix} m_{00} & m_{01} & m_{02} & m_{03} \\ m_{10} & m_{11} & m_{12} & m_{13} \\ m_{20} & m_{21} & m_{22} & m_{23} \\ m_{30} & m_{31} & m_{32} & m_{33} \end{bmatrix} \begin{bmatrix} S_0 \\ S_1 \\ S_2 \\ S_3 \end{bmatrix} \tag{1.33}$$

$$S' = M \cdot S$$

where  $S'$  and  $S$  are the Stokes vectors and  $M$  is the  $4 \times 4$  real matrix (called the Mueller matrix).

The polarization state of the incident beam is practically always changed during the interaction with matter. These changes of the polarization state could be due to changes in 1) the amplitudes of the electric field components, 2) the phase shift between the electric field components, 3) the oscillation direction of the orthogonal field components, or 4) energy can be transferred from the totally polarized states to the unpolarized one. We call an optical element that attenuates the amplitudes of the orthogonal field components unequally a **polarizer** (or **diattenuator**). An optical element that introduces a phase shift between the orthogonal components is called a **retarder** (or **compensator**, **phase shifter**). When the orthogonal components of the optical beam are rotated through an angle  $\theta$ , the polarizing element is called a **rotator**. All three polarizing elements (polarizer, retarder, and rotator) change the polarization state of the incident optical beam. Finally, if the energy in the

polarized state is transferred to the unpolarized state, the corresponding element is called a **depolarizer**. Now, we will introduce the Mueller matrices of each of the above mentioned basic optical elements.

### 1.3.1. Mueller matrix of a polarizer

The polarizer acts as an anisotropic attenuator. In an optical system, the polarizer can be considered either as a generator (i.e., the element that produces polarized light) or as an analyzer (i.e., the element that analyzes polarized light). When a polarized beam of light is incident on a polarizer, the components of the incident beam, denoted by  $E_x$  and  $E_y$ , along with the components of the emerging beam,  $E'_x$  and  $E'_y$ , are parallel to the polarizer transmission axes (see Fig. 1.4). The amplitude attenuation coefficients along the two orthogonal transmission axes of polarizer are denoted as  $p_x$  and  $p_y$ , respectively. The relation between the incident and emerging light field components can be written as [6]

$$\begin{aligned} E'_x &= p_x E_x \quad (0 \leq p_x \leq 1) \\ E'_y &= p_y E_y \quad (0 \leq p_y \leq 1) \end{aligned} \quad (1.34)$$

Depending on the factor  $p_x(p_y)$ , there can be either no attenuation ( $p = 1$ ) or complete attenuation ( $p = 0$ ) of the electric field component along the orthogonal transmission axes.

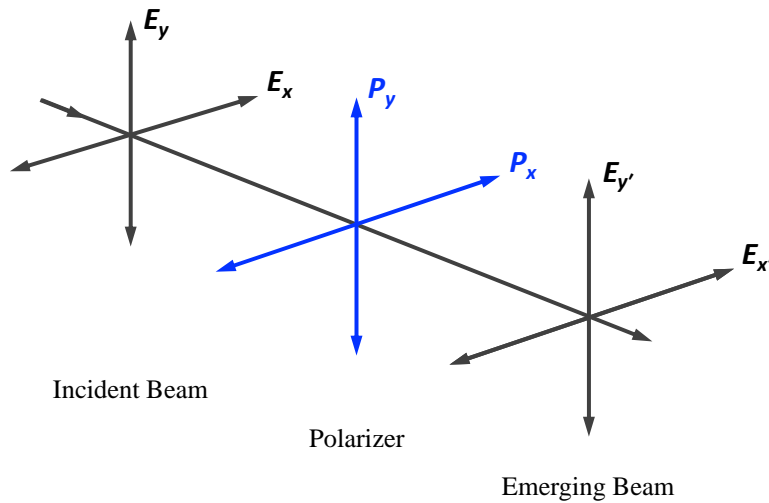


**Figure 1.4** The propagation of polarized light through a polarizer.  $p_x$  and  $p_y$  are the attenuation coefficients.

The Stokes vector of the incident beam that interacts with a polarizer can be related to the Stokes vector of the emerging beam as

$$\begin{bmatrix} S'_0 \\ S'_1 \\ S'_2 \\ S'_3 \end{bmatrix} = \frac{1}{2} \begin{bmatrix} p_x^2 + p_y^2 & p_x^2 - p_y^2 & 0 & 0 \\ p_x^2 - p_y^2 & p_x^2 + p_y^2 & 0 & 0 \\ 0 & 0 & 2p_x p_y & 0 \\ 0 & 0 & 0 & 2p_x p_y \end{bmatrix} \begin{bmatrix} S_0 \\ S_1 \\ S_2 \\ S_3 \end{bmatrix} \quad (1.35)$$

Thus, the Mueller matrix of a polarizer is written as

$$M = \frac{1}{2} \begin{bmatrix} p_x^2 + p_y^2 & p_x^2 - p_y^2 & 0 & 0 \\ p_x^2 - p_y^2 & p_x^2 + p_y^2 & 0 & 0 \\ 0 & 0 & 2p_x p_y & 0 \\ 0 & 0 & 0 & 2p_x p_y \end{bmatrix} \quad (0 \leq p_{x,y} \leq 1) \quad (1.36)$$

This matrix can be written in the general form:

$$M = \frac{p^2}{2} \begin{bmatrix} 1 & \cos 2\gamma & 0 & 0 \\ \cos 2\gamma & 1 & 0 & 0 \\ 0 & 0 & \sin 2\gamma & 0 \\ 0 & 0 & 0 & \sin 2\gamma \end{bmatrix} \quad (0^\circ \leq \gamma \leq 90^\circ) \quad (1.37)$$

where  $p_x^2 + p_y^2 = p^2$ ,  $p_x = p \cos 2\gamma$  and  $p_y = p \sin 2\gamma$ ,  $\gamma$  is the dichroism angle.

Using Eq. (1.36), the Mueller matrix of the *neutral density filter* ( $p_x = p_y = p'$ ) becomes

$$M = p'^2 \begin{bmatrix} 1 & 0 & 0 & 0 \\ 0 & 1 & 0 & 0 \\ 0 & 0 & 1 & 0 \\ 0 & 0 & 0 & 1 \end{bmatrix} \quad (1.38)$$

The neutral density filter does not affect the polarization state of an optical beam whereas it changes its intensity. The Mueller matrix of the *ideal linear polarizer* (transmission along one axis only) is given by [6], [9]

1)  $p_x = 0$ ,  $p_y = 1$  (*linear vertical polarizer*)

$$M = \frac{1}{2} \begin{bmatrix} 1 & -1 & 0 & 0 \\ -1 & 1 & 0 & 0 \\ 0 & 0 & 0 & 0 \\ 0 & 0 & 0 & 0 \end{bmatrix} \quad (1.39)$$

2)  $p_x = 1$ ,  $p_y = 0$  (*linear horizontal polarizer*)

$$M = \frac{1}{2} \begin{bmatrix} 1 & 1 & 0 & 0 \\ 1 & 1 & 0 & 0 \\ 0 & 0 & 0 & 0 \\ 0 & 0 & 0 & 0 \end{bmatrix} \quad (1.40)$$

Notice that if the incident beam is completely unpolarized then the maximum intensity of the emerging linear polarized beam cannot exceed 50% of the intensity of the incident beam.

### 1.3.2. Mueller matrix of a retarder

A retarder is a polarizing element that introduces a phase shift  $\phi$  between the orthogonal components of the field of the incident beam. For example, the phase shift  $\phi$  can be accomplished by a retarder producing a phase shifts of  $+\phi/2$  along the  $x$ -axis and a phase shift of  $-\phi/2$  along the  $y$ -axis (see Fig. 1.5). We refer the axes  $x$  and  $y$  as the fast and the slow axes of a retarder, respectively.

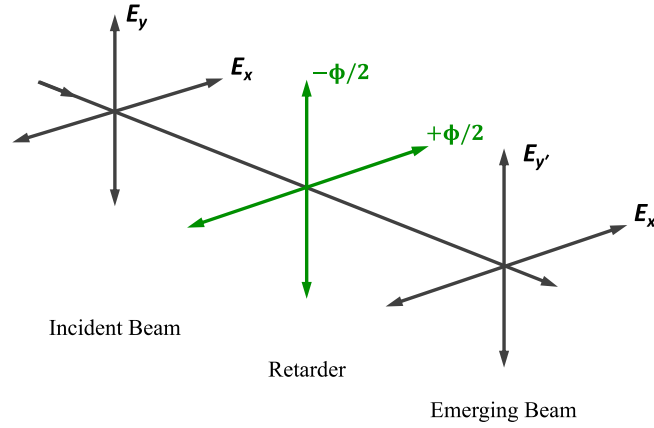


**Figure 1.5** The propagation of polarized light through a retarder. The two-phase shifts ( $+\phi/2$  and  $-\phi/2$ ) are along the  $x$ - and  $y$ -axis, respectively.

The Stokes vectors of the incident beam and the emerging beams are related as

$$\begin{bmatrix} S'_0 \\ S'_1 \\ S'_2 \\ S'_3 \end{bmatrix} = \begin{bmatrix} 1 & 0 & 0 & 0 \\ 0 & 1 & 0 & 0 \\ 0 & 0 & \cos \phi & \sin \phi \\ 0 & 0 & -\sin \phi & \cos \phi \end{bmatrix} \begin{bmatrix} S_0 \\ S_1 \\ S_2 \\ S_3 \end{bmatrix} \quad (1.41)$$

Therefore, the Mueller matrix of a retarder with a phase shift  $\phi$  is given by

$$M = \begin{bmatrix} 1 & 0 & 0 & 0 \\ 0 & 1 & 0 & 0 \\ 0 & 0 & \cos \phi & \sin \phi \\ 0 & 0 & -\sin \phi & \cos \phi \end{bmatrix} \quad (1.42)$$

It is worth noting that the emerging beam preserves the intensity of the incident beam (i.e., there is no loss in intensity) after interaction with an ideal retarder. In the special case of phase shift of  $\phi = 90^\circ$ , the phase of one component of the electric field is delayed with respect to the orthogonal field component by a quarter of a wave. We called this retarder a quarter-wave retarder; its Mueller matrix is given by

$$M = \begin{bmatrix} 1 & 0 & 0 & 0 \\ 0 & 1 & 0 & 0 \\ 0 & 0 & 0 & 1 \\ 0 & 0 & -1 & 0 \end{bmatrix} \quad (1.43)$$

When linearly polarized light beam is incident on a quarter-wave retarder (and the polarization plane of linearly polarized light is oriented at  $+45^\circ$  or  $-45^\circ$  with respect to the fast axis of a retarder), it is transformed into a right- or left-circularly polarized light, respectively. Conversely, a quarter-wave plate can transform the incident circularly polarized light into the linear polarized light.

When the phase shift is  $\phi = 180^\circ$ , the phase of one component of the electric field of the beam is delayed with respect to the orthogonal component by half a wave. We called this retarder as a half-wave retarder. Its Mueller matrix is given by

$$M = \begin{bmatrix} 1 & 0 & 0 & 0 \\ 0 & 1 & 0 & 0 \\ 0 & 0 & -1 & 0 \\ 0 & 0 & 0 & -1 \end{bmatrix} \quad (1.44)$$

The negative signs of the elements  $m_{22}$  and  $m_{33}$  indicate that a half-wave retarder reverses the ellipticity and orientation of the polarization state of the incident beam:

$$\begin{aligned} \psi' &= 90^\circ - \psi \\ \chi' &= 90^\circ + \chi \end{aligned} \quad (1.44a)$$

### 1.3.3. Mueller matrix of a rotator

A rotator is a polarizing element that rotates orthogonal components of the electric field of the incident beam through an angle  $\theta$  (see Fig. 1.6). The point  $P$  can be described in both the  $E_x, E_y$  coordinate system (Eq. 1.45) and the  $E'_x, E'_y$  coordinate system by Eq. (1.45) and Eq. (1.46), respectively.

$$\begin{aligned} E_x &= E \cos \beta \\ E_y &= E \sin \beta \end{aligned} \quad (1.45)$$

$$\begin{aligned} E'_x &= E \cos(\beta - \theta) \\ E'_y &= E \sin(\beta - \theta) \end{aligned} \quad (1.46)$$

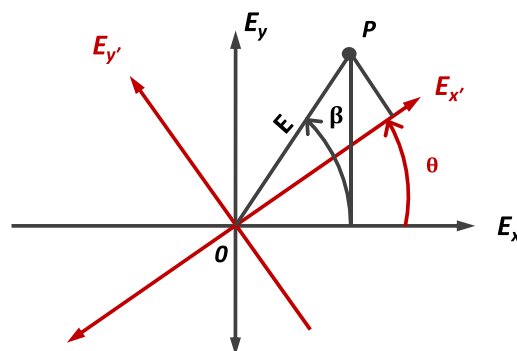


**Figure 1.6** The rotation of the optical field components by a rotator.

Expanding the trigonometric functions in Eqs (1.46) and substituting Eqs (1.45) into Eqs (1.46) leads to

$$\begin{aligned} E'_x &= E_x \cos \theta + E_y \sin \theta \\ E'_y &= -E_x \sin \theta + E_y \cos \theta \end{aligned} \quad (1.47)$$

The Mueller matrix of a rotator can be derived by formulating the relation between the Stokes parameters for the amplitudes of the electric field  $E$  and  $E'$

$$M(2\theta) = \begin{bmatrix} 1 & 0 & 0 & 0 \\ 0 & \cos 2\theta & \sin 2\theta & 0 \\ 0 & \sin 2\theta & \cos 2\theta & 0 \\ 0 & 0 & 0 & 1 \end{bmatrix} \quad (1.48)$$

It is worth noting that the physical rotation through the angle  $\theta$  results in the appearance of the angle  $2\theta$  in Eq. (1.48) because the Mueller matrix describes the transfer of the intensities that represent the squared amplitude of the electric field.

### 1.3.4. Mueller matrix of rotated optical element

We derived the Mueller matrix of basic polarizing elements (polarizer, retarder, and rotator) assuming that the axes of these elements are aligned along the  $x$ - and  $y$ -axes of the coordinate system. However, in reality, the polarizing elements are very often rotated. Then, we need to consider the derivation of the Mueller matrix of rotated polarizing elements [6], [9].

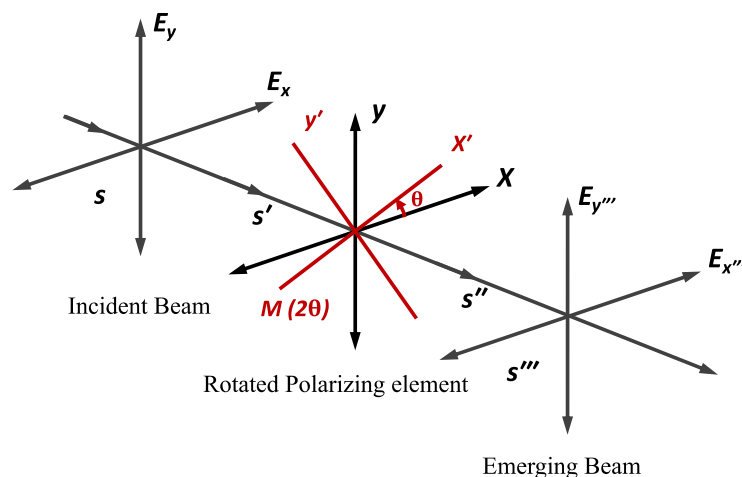


**Figure 1.7** Derivation of the Mueller matrix of rotated polarizing element.

1. The axes  $(x, y)$  of the polarizing component are rotated through the angle  $\theta$  to the  $(x', y')$  axes. We have to consider the Stokes vector of the incident beam in the  $(x', y')$  coordinate system. It is defined by the following relation:

$$S' = M_R(2\theta)S \quad (1.49)$$

where  $M_R(2\theta)$  is the Mueller matrix of a rotator.

2. The Stokes vector  $S'$  interacts with the optical components described by the Mueller matrix  $M$ . Then, the beam emerging from the rotated polarizing element is

$$S'' = MS' = MM_R(2\theta)S \quad (1.50)$$

3. Finally, the components of the emerging beam should be expressed in the original  $(x, y)$  coordinate system. It is done by a rotation by the same angle but in the opposite direction  $(-\theta)$ :

$$S''' = M_R(-2\theta)MS' = M_R(-2\theta)MM_R(2\theta)S \quad (1.51)$$

The Mueller matrix of the rotated polarizing component can be described as the product of the matrices  $M_R(-2\theta)MM_R(2\theta)$ . In particular, the Mueller matrices of the rotated polarizer and the rotated retarder are described by Eq. (1.51). The Mueller matrix of the rotated rotator does not change -  $M_R(2\theta)$ .

Substituting Eq. (1.37) and Eq. (1.48) into Eq. (1.51) gives the Mueller matrix of a rotated polarizer as: [6], [9], [11]

$$M = \frac{1}{2} \begin{bmatrix} 1 & \cos 2\gamma \cos 2\theta & \cos 2\gamma \sin 2\theta & 0 \\ \cos 2\gamma \cos 2\theta & \cos^2 2\theta + \sin 2\gamma \sin^2 2\theta & (1 - \sin 2\gamma) \sin 2\theta \cos 2\theta & 0 \\ \cos 2\gamma \sin 2\theta & (1 - \sin 2\gamma) \sin 2\theta \cos 2\theta & \sin^2 2\theta + \sin 2\gamma \cos^2 2\theta & 0 \\ 0 & 0 & 0 & 1 \end{bmatrix} \quad (1.52)$$

We have set  $p^2 = 1$  for simplicity. The angle  $\gamma = 0^\circ, 45^\circ$ , and  $90^\circ$  correspond to a linear horizontal polarizer, a neutral density filter, and a linear vertical polarizer, respectively. The Mueller matrix of an ideal linear horizontal polarizer reduces to

$$M = \frac{1}{2} \begin{bmatrix} 1 & \cos 2\theta & \sin 2\theta & 0 \\ \cos 2\theta & \cos^2 2\theta & \sin 2\theta \cos 2\theta & 0 \\ \sin 2\theta & \sin 2\theta \cos 2\theta & \sin^2 2\theta & 0 \\ 0 & 0 & 0 & 1 \end{bmatrix} \quad (1.53)$$

The Mueller matrix of a rotated retarder can be expressed by substituting Eqs (1.42) and (1.48) into Eq. (1.51), and it is written as [6], [9], [11]

$$M = \begin{bmatrix} 1 & 0 & 0 & 0 \\ 0 & \cos^2 2\theta + \cos \phi \sin^2 2\theta & (1 - \cos \phi) \sin 2\theta \cos 2\theta & -\sin \phi \sin 2\theta \\ 0 & (1 - \cos \phi) \sin 2\theta \cos 2\theta & \sin^2 2\theta + \cos \phi \cos^2 2\theta & \sin \phi \cos 2\theta \\ 0 & \sin \phi \sin 2\theta & -\sin \phi \cos 2\theta & \cos \phi \end{bmatrix} \quad (1.54)$$

Using Eq. (1.54), the Mueller matrix of a quarter-wave retarder ( $\phi = 90^\circ$ ) reduces to

$$M = \begin{bmatrix} 1 & 0 & 0 & 0 \\ 0 & \cos^2 2\theta & \sin 2\theta \cos 2\theta & -\sin 2\theta \\ 0 & \sin 2\theta \cos 2\theta & \sin^2 2\theta & \cos 2\theta \\ 0 & \sin 2\theta & -\cos 2\theta & 0 \end{bmatrix} \quad (1.55)$$

where  $\theta$  is the rotation angle. If the incident beam is circularly polarized (see Tab. 1.1), the emerging beam will be then linear polarized:

$$S = \begin{bmatrix} 1 \\ \mp \sin 2\theta \\ \pm \cos 2\theta \\ 0 \end{bmatrix} \quad (1.56)$$

The Mueller matrix of a half-wave retarder ( $\phi = 180^\circ$ ) can be expressed as

$$M = \begin{bmatrix} 1 & 0 & 0 & 0 \\ 0 & \cos 4\theta & \sin 4\theta & 0 \\ 0 & \sin 4\theta & -\cos 4\theta & 0 \\ 0 & 0 & 0 & -1 \end{bmatrix} \quad (1.57)$$

where  $\theta$  is the rotation angle.

The Mueller matrix described by Eq. (1.57) is similar to the Mueller matrix of a rotator (see Eq. (1.48)). However, there are some essential differences. We note that the ellipticity angle  $\chi$  is changed to  $\chi + 90^\circ$  after the interaction of the incident polarized light with a rotated half-wave retarder, whereas it is not affected by the interaction with a true rotator. The orientation angle  $\psi$  changes to  $\psi - \theta$  by a rotator. In case of polarized light incident to a rotated half-wave retarder the orientation angle  $\psi$  changes to  $2\theta - \psi$ . Half-wave plates are known as polarizing components that reverse the polarization state of the incident light. For example, if the incident light is a linear  $+45^\circ$  polarized light, the emerging beam shows linear  $-45^\circ$  polarized light after being transmitted through a half-wave retarder aligned with  $(x, y)$  axes ( $\theta = 0^\circ$ ).

### 1.3.5. Mueller matrix of a depolarizer

Contrary to the basic polarizing elements (polarizer, retarder, and rotator), the depolarizer is an optical element that converts the polarized state of the incident beam into unpolarized (or partially polarized) state of the emerging beam, as illustrated in Fig. 1.8 [6], [9].

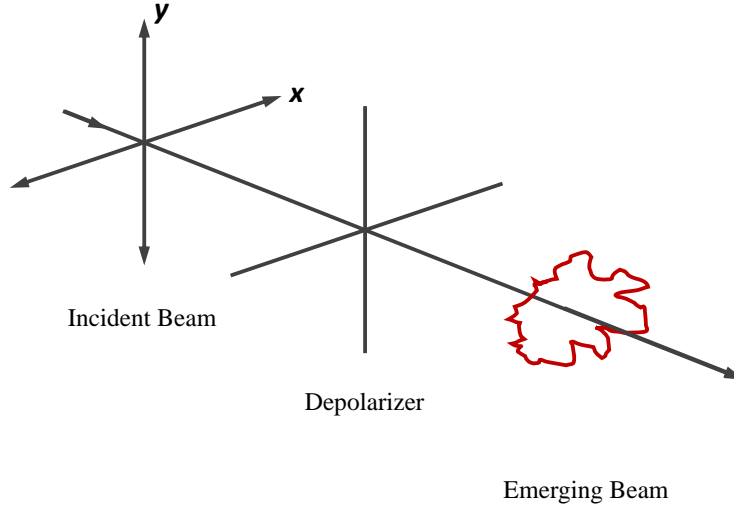


**Figure 1.8** Propagation of polarized light through a depolarizer.

The impact of a depolarizer on an incident totally polarized light beam can be illustrated using the Poincaré sphere by the migration of the point from the surface towards the center of the sphere along a radius. The Mueller matrix of an intrinsic depolarizer [8] can be diagonalized by the unitary transformation, and it can be written as [6], [9], [10]

$$M = \begin{bmatrix} 1 & 0 & 0 & 0 \\ 0 & a & 0 & 0 \\ 0 & 0 & b & 0 \\ 0 & 0 & 0 & c \end{bmatrix} \quad (|a|, |b|, |c| \leq 1) \quad (1.58)$$

The depolarizer reduces the degree of polarization. The partial polarization of the emerging beam, results from the incoherent superposition of the totally polarized states. Hence, in practice, the depolarization may arise when we measure a sample that has spatial or temporal inhomogeneity. For example, the multiple scattering of incident beam will generate various output polarization states and introduce the depolarization when these states are summed incoherently.

## 1.4. Decompositions of the Mueller matrix

For a real-valued  $4 \times 4$  matrix to be a physically realizable Mueller matrix, it should map a physical Stokes vector of the incident light beam into a physical Stokes vector of the emerging light beam, i.e., the degree of polarization must obey Eq. (1.26). The measured Mueller matrix (or transfer matrix of a sample) represents a mixture of pure (or non-depolarizing) contributions, depolarization, and noise. Therefore, before attributing the magnitude of a particular element of Mueller matrix to retardance, diattenuation or depolarization of a sample under study we have to check the physical realizability of the Mueller matrix, and, in case the above-mentioned check failed, find the closest possible physically realizable Mueller matrix by performing noise filtering of experimental data. Then,

we decompose Mueller matrix to obtain the optical properties of the sample. For example, birefringence, dichroism, and depolarization of the sample can be extracted from Mueller matrix by applying the particular decomposition algorithms (e.g., Lu-Chipman polar decomposition, logarithmic decomposition, Cloude sum decomposition, etc.). [6], [8], [9]

### 1.4.1. Noise in the experimental Mueller matrix data

Within the framework of the Stokes-Mueller formalism, the Stokes vector of light having interacted with a linear optical system is represented by the linear combination of the Stokes vector elements of the incident beam. As a reminder, the degree of polarization of the emerging Stokes vector has to be less than or equal to one.

$$DOP = \frac{I_{\text{pol}}}{I_{\text{tot}}} = \frac{(S_1^2 + S_2^2 + S_3^2)^{1/2}}{S_0} \quad 0 \leq p \leq 1 \quad (1.26)$$

Further, it has been shown that the Mueller matrix has to obey the constraint [6], [9], [12]

$$Tr(MM^T) = \sum_{i,j=0}^3 m_{ij}^2 \leq 4m_{00}^2 \quad (1.59)$$

where the sign of equality represents a non-depolarizing system.

S. Cloude [1] demonstrated that the necessary and sufficient condition for a Mueller matrix to be physically realizable is the non-negativity of the eigenvalues of the corresponding coherency matrix, namely, the  $4 \times 4$  Hermitian positive semi-definite matrix  $T_c$ , (i.e.,  $z^* T_c z \geq 0$  for any non-zero  $4 \times 1$  complex vector  $z$ , where  $z^*$  denotes the conjugate transpose of  $z$ ) with the elements defined as follows:

$$\begin{aligned} t_{00} &= \frac{m_{00} + m_{11} + m_{22} + m_{33}}{2} & t_{01} &= \frac{m_{01} + m_{10} - i(m_{23} - m_{32})}{2} \\ t_{02} &= \frac{m_{02} + m_{20} + i(m_{13} - m_{31})}{2} & t_{03} &= \frac{m_{03} + m_{30} - i(m_{12} - m_{21})}{2} \\ t_{10} &= \frac{m_{01} + m_{10} + i(m_{23} - m_{32})}{2} & t_{11} &= \frac{m_{00} + m_{11} - m_{22} - m_{33}}{2} \\ t_{12} &= \frac{m_{12} + m_{21} + i(m_{03} - m_{30})}{2} & t_{13} &= \frac{m_{13} + m_{31} - i(m_{02} - m_{20})}{2} \\ t_{20} &= \frac{m_{02} + m_{20} - i(m_{13} - m_{31})}{2} & t_{21} &= \frac{m_{12} + m_{21} - i(m_{03} - m_{30})}{2} \\ t_{22} &= \frac{m_{00} - m_{11} + m_{22} - m_{33}}{2} & t_{23} &= \frac{m_{23} + m_{32} + i(m_{01} - m_{10})}{2} \\ t_{30} &= \frac{m_{03} + m_{30} + i(m_{12} - m_{21})}{2} & t_{31} &= \frac{m_{13} + m_{31} + i(m_{02} - m_{20})}{2} \\ t_{32} &= \frac{m_{23} + m_{32} - i(m_{01} - m_{10})}{2} & t_{33} &= \frac{m_{00} - m_{11} - m_{22} + m_{33}}{2} \end{aligned} \quad (1.60a)$$

Then, the eigenvalues and eigenvectors of the coherency matrix  $T_c$  can be used to decompose matrix  $T_c$  into the sum:

$$T_c = \lambda_0 T_{c0} + \lambda_1 T_{c1} + \lambda_2 T_{c2} + \lambda_3 T_{c3} \quad (1.61)$$

where the  $\lambda_i$  ( $i = 0, 1, 2, 3$ ) are the eigenvalues of  $T_c$ , and  $T_{ci}$  are projector matrices constructed from the eigenvectors of  $T_c$  [1], [13], [14]. The eigenvalues are real because the coherency matrix is Hermitian positive semi-definite, and the eigenvectors are complex-valued [15], [16]. The eigenvalues  $\lambda_i$  ( $i = 0, 1, 2, 3$ ) verify  $\lambda_0 \gg \lambda_1 \gg \lambda_2 \gg \lambda_3$ . A small negative eigenvalue of the coherence matrix can be the result of system noise or measurement errors. Therefore, it is a prerequisite to check the eigenvalues of the coherency matrix before applying the decomposition algorithm for extracting the polarimetric properties. The eigenvalue ratio, which represents the ratio of the largest negative eigenvalue to the dominant eigenvalue in decibels, is used as a criterion of the closeness to realizability [6]. The experimental noise on the Mueller matrix can be filtered by subtraction of the eigenvector contribution corresponding to the negative eigenvalue. We construct a diagonal matrix  $\Lambda = \text{diag}(\lambda_0, \lambda_1, \lambda_2, \lambda_3)$  and set all negative eigenvalues to zero. Then, we define a matrix  $V$  composed of the eigenvectors of the coherency matrix  $T$  and perform similarity transform  $N = V\Lambda V^{-1}$ , where  $N$  is the coherence matrix corresponding to the closest physically realizable Mueller matrix [17] that we reconstruct by using the following set of the equations:

$$\begin{aligned} M_{00} &= 2N_{00} - M_{11} - M_{01} - M_{10} & M_{10} &= (N_{00} + N_{11} - N_{22} - N_{33})/2 \\ M_{01} &= M_{10} + N_{22} - N_{11} & M_{11} &= N_{00} - N_{11} - M_{01} \\ M_{02} &= \text{Re}(N_{10} + N_{32}) & M_{12} &= \text{Re}(2N_{10}) - M_{02} \\ M_{20} &= \text{Re}(N_{20} + N_{31}) & M_{21} &= \text{Re}(2N_{20}) - M_{20} \\ M_{22} &= \text{Re}(N_{30} + N_{21}) & M_{33} &= \text{Re}(2N_{30}) - M_{22} \\ M_{03} &= -\text{Im}(N_{10} + N_{32}) & M_{13} &= \text{Im}(2N_{32}) + M_{03} \\ M_{30} &= \text{Im}(N_{20} + N_{31}) & M_{31} &= \text{Im}(2N_{20}) - M_{30} \\ M_{32} &= \text{Im}(N_{30} + N_{21}) & M_{23} &= \text{Im}(2N_{21}) - M_{32} \end{aligned} \quad (1.60b)$$

### 1.4.2. Lu-Chipman decomposition of the Mueller matrix

If the measured Mueller matrix is physically realizable, usually its elements do not allow the direct interpretation in terms of the polarization (diattenuation, retardance) and depolarization parameters of the sample. To extract this information from the experimental Mueller matrix we use a phenomenological approach and decompose Mueller matrix into a set of Mueller matrices of basic optical elements (diattenuator, retarder, depolarizer). The Mueller algebra is well developed and provides a toolkit of different decomposition algorithms [8]. We describe below two algorithms of Mueller matrix decomposition that we used in our studies.

Lu-Chipman polar decomposition [2] is one of the non-linear polarimetric data compression algorithms that allows a depolarizing Mueller matrix to be decomposed into the product of three matrices, namely, the Mueller matrices of a diattenuator  $M_D$ , a retarder  $M_R$ , and a depolarizer  $M_\Delta$ .

$$M = M_\Delta M_R M_D \quad (1.62)$$

As the matrix product does not commute, the sequential order of the optical elements is fixed for this decomposition algorithm. As discussed, a diattenuator (polarizer) affects the intensity transmittance  $T$  of the incident polarization states without introducing a phase shift. Then, the diattenuation is defined in transmission (reflection) configuration as:

$$D \equiv \frac{T_{max} - T_{min}}{T_{max} + T_{min}} \quad (0 \leq D \leq 1) \quad (1.63)$$

The intensity transmittance can be written in terms of the ratio of the first elements of the emerging and incident Stokes vectors:

$$T = \frac{s'_0}{s_0} = \frac{m_{00}s_0 + m_{01}s_1 + m_{02}s_2 + m_{03}s_3}{s_0} \quad (1.64)$$

It can be shown that the maximum and minimum transmittances are given by

$$\begin{aligned} T_{max} &= m_{00} + \sqrt{m_{01}^2 + m_{02}^2 + m_{03}^2} \\ T_{min} &= m_{00} - \sqrt{m_{01}^2 + m_{02}^2 + m_{03}^2} \end{aligned} \quad (1.65)$$

Substituting Eq. (1.65) into Eq. (1.63) gives the scalar diattenuation of Mueller matrix:

$$D = \frac{T_{max} - T_{min}}{T_{max} + T_{min}} = \frac{1}{m_{00}} \sqrt{m_{01}^2 + m_{02}^2 + m_{03}^2} \quad (1.66)$$

The components of the diattenuation vector  $\mathbf{D} = (D_H, D_{45}, D_C)^T$  are given by

$$\begin{aligned} D_H &= \frac{T_H - T_V}{T_H + T_V} = \frac{m_{01}}{m_{00}} \\ D_{45} &= \frac{T_{45} - T_{135}}{T_{45} + T_{135}} = \frac{m_{02}}{m_{00}} \\ D_C &= \frac{T_R - T_L}{T_R + T_L} = \frac{m_{03}}{m_{00}} \end{aligned} \quad (1.67)$$

where  $T_H$ ,  $T_V$ ,  $T_{45}$ ,  $T_{135}$ ,  $T_R$ , and  $T_L$  are the transmittances for horizontally, vertically, linearly 45°, linearly 135°, right circularly, and left circularly polarized light, respectively.

The scalar value of the polarizance  $P$  represents the polarization of the incident, unpolarized light due to the interaction with the sample characterized by its Mueller matrix  $M$ :

$$P = \frac{1}{m_{00}} \sqrt{m_{10}^2 + m_{20}^2 + m_{30}^2} \quad (0 \leq P \leq 1) \quad (1.68)$$

The components of the polarizance vector are given by

$$\mathbf{P} = \begin{pmatrix} P_H \\ P_{45} \\ P_C \end{pmatrix} = \frac{1}{m_{00}} \begin{pmatrix} m_{10} \\ m_{20} \\ m_{30} \end{pmatrix} \quad (1.69)$$

Thus, the nondepolarizing Mueller matrix can be described as the product of the Mueller matrix of retarder,  $M_R$  and diattenuator,  $M_D$ .

$$M = M_R M_D \quad (1.70)$$

Using the diattenuation and polarizance vectors, the normalized Mueller matrix is written as

$$M = m_{00} \begin{bmatrix} 1 & m_{01} & m_{02} & m_{03} \\ m_{10} & m_{11} & m_{12} & m_{13} \\ m_{20} & m_{21} & m_{22} & m_{23} \\ m_{30} & m_{31} & m_{32} & m_{33} \end{bmatrix} = m_{00} \begin{bmatrix} 1 & \mathbf{D}^T \\ \mathbf{P} & m \end{bmatrix}, \quad m = \begin{bmatrix} m_{11} & m_{12} & m_{13} \\ m_{21} & m_{22} & m_{23} \\ m_{31} & m_{32} & m_{33} \end{bmatrix} \quad (1.71)$$

The diattenuator matrix is given by [6], [18], [19]

$$M_D = T_u \begin{bmatrix} 1 & m_{01} & m_{02} & m_{03} \\ m_{01} & a + bm_{01}^2 & bm_{01}m_{02} & bm_{01}m_{03} \\ m_{02} & bm_{02}m_{01} & a + bm_{02}^2 & bm_{02}m_{03} \\ m_{03} & bm_{03}m_{01} & bm_{03}m_{02} & a + bm_{03}^2 \end{bmatrix} = T_u \begin{bmatrix} 1 & \mathbf{D}^T \\ \mathbf{D} & m_D \end{bmatrix}, \quad (1.72)$$

$$D = \sqrt{m_{01}^2 + m_{02}^2 + m_{03}^2}, \quad a = \sqrt{1 - D^2}, \quad b = \frac{1 - \sqrt{1 - D^2}}{D^2}$$

where  $T_u$  is the transmittance of diattenuator for unpolarized light. The retarder matrix  $M_R$  can be calculated by multiplying the Mueller matrix  $M$  and the inverse diattenuator matrix  $M_D^{-1}$  [6], [18], [19].

$$M_R = \frac{1}{a} \begin{bmatrix} a & 0 & 0 & 0 \\ 0 & m_{11} - b(m_{10}m_{01}) & m_{12} - b(m_{10}m_{02}) & m_{13} - b(m_{10}m_{03}) \\ 0 & m_{21} - b(m_{20}m_{01}) & m_{22} - b(m_{20}m_{02}) & m_{23} - b(m_{20}m_{03}) \\ 0 & m_{31} - b(m_{30}m_{01}) & m_{32} - b(m_{30}m_{02}) & m_{33} - b(m_{30}m_{03}) \end{bmatrix} \quad (1.73)$$

$$= \begin{bmatrix} 1 & \mathbf{0}^T \\ \mathbf{0} & m_R \end{bmatrix}, \quad D = \sqrt{m_{01}^2 + m_{02}^2 + m_{03}^2}, \quad a = \sqrt{1 - D^2}, \quad b = \frac{1 - \sqrt{1 - D^2}}{D^2}$$

The total retardance  $R$  and the retardance vector  $\mathbf{R}$  are given by

$$R = |\mathbf{R}| = \cos^{-1}\left(\frac{|\text{tr}(m_R) - 1|}{2}\right) \quad (0 \leq R \leq \pi) \quad (1.74)$$

$$R = |\mathbf{R}| = 2\pi - \cos^{-1}\left(\frac{|\text{tr}(m_R) - 1|}{2}\right) \quad (\pi \leq R \leq 2\pi) \quad (1.75)$$

$$\mathbf{R} = \begin{pmatrix} R_H \\ R_{45} \\ R_C \end{pmatrix} = \frac{R}{2\sin(R)} \begin{pmatrix} M_R(2,3) - M_R(3,2) \\ M_R(3,1) - M_R(1,3) \\ M_R(1,2) - M_R(2,1) \end{pmatrix} \quad (1.76)$$

Thus, a retarder Mueller matrix has 3 degrees of freedom given by its retardance vector. In terms of the retarder Mueller matrix elements, the scalar linear retardance  $R_L$  and optical rotation  $\psi$  can be written as [20]

$$\begin{aligned} R_L &= \sqrt{R_H^2 + R_{45}^2} = \\ &= \cos^{-1}\left(\sqrt{(M_R(2,2) + M_R(3,3))^2 + (M_R(3,2) - M_R(2,3))^2} - 1\right) \end{aligned} \quad (1.77)$$

$$\psi = \tan^{-1}\left[\frac{M_R(3,2) - M_R(2,3)}{M_R(2,2) + M_R(3,3)}\right] \quad (1.78)$$

Finally, the Mueller matrix of the pure depolarizer with the principal axes along  $s_1$ ,  $s_2$  and  $s_3$  axes ( $\mathbf{S} = (1, (\vec{s})^T)^T$ ,  $\vec{s} = (s_1, s_2, s_3)$ ) can be expressed by

$$M_\Delta = \begin{bmatrix} 1 & 0 & 0 & 0 \\ 0 & a & 0 & 0 \\ 0 & 0 & b & 0 \\ 0 & 0 & 0 & c \end{bmatrix} \quad (|a|, |b|, |c| \leq 1) \quad (1.79a)$$

In general, the principal axes of a depolarizer can be along any three orthogonal axes. Thus, a more general expression for a depolarizer is given by

$$M_\Delta = \begin{bmatrix} 1 & \mathbf{0}^T \\ \mathbf{0} & m_\Delta \end{bmatrix} \quad m_\Delta^T = m_\Delta \quad (1.79b)$$

The Mueller matrix, shown in Eq. (1.79b), has only six degrees of freedom because it does not include the polarizance that a depolarizer may display. Then, the most general expression for depolarizer with polarizance is:

$$M_\Delta = \begin{bmatrix} 1 & \mathbf{0}^T \\ \mathbf{P}_\Delta & m_\Delta \end{bmatrix}, \quad m_\Delta^T = m_\Delta \quad (1.80)$$

where  $\mathbf{P}_\Delta$  denotes the polarizance vector of a depolarizer. The general form for the depolarizing Mueller matrix (Eq. (1.80)) has nine degrees of freedom, and it has zero diattenuation or retardance. It can characterize the polarizing capability of depolarizer, as well its depolarization properties, described by the eigenvalues and eigenvectors of  $m_\Delta$ .

The depolarization coefficient  $\Delta$  is given by

$$\Delta = 1 - \frac{|\text{tr}(m_\Delta) - 1|}{3} \quad (0 \leq \Delta \leq 1) \quad (1.81)$$

### 1.4.3. Logarithmic decomposition of the Mueller matrix

Different algorithms of decomposition of Mueller matrix have been extensively studied, and several methods (e.g., Lu–Chipman, reverse, symmetrical, and differential) [2], [21]–[23] were proposed for the interpretation of Mueller matrix data. Among them, a logarithmic Mueller matrix decomposition method (LMMD) developed for transmission geometry is the one that considers all optical properties as continuously distributed within the volume of the medium. [24] It makes LMMD particularly suitable for the studies of biological tissues in a transmission configuration. The key steps of LMMD are summarized below. Within the framework of the differential matrix formalism of a fluctuating anisotropic medium [3], [4], the transmission Mueller matrix is described by the following equation:

$$\frac{dM(z)}{dz} = mM(z) \quad (1.82)$$

The Mueller matrix  $M(z)$ , which is dependent on an optical path length  $z$ , is associated with a unique differential matrix  $m$ . This matrix is constant for both non-depolarizing and depolarizing media that are homogeneous along the light beam propagation direction. For a depolarizing medium, the differential matrix  $m$  can be decomposed into G-antisymmetric  $m_m$  and G-symmetric  $m_u$  [where  $G = \text{diag}(1, -1, -1, -1)$  is the Minkowski metric and T denotes matrix transposition] [25]:

$$m_m = \frac{1}{2} (m - Gm^T G), \quad m_u = \frac{1}{2} (m + Gm^T G) \quad (1.83)$$

$$m = m_m + m_u$$

$$= \begin{pmatrix} 0 & p_1 & p_2 & p_3 \\ p_1 & 0 & p_6 & -p_5 \\ p_2 & -p_6 & 0 & p_4 \\ p_3 & p_5 & -p_4 & 0 \end{pmatrix} + \begin{pmatrix} d_0 & d_1 & d_2 & d_3 \\ -d_1 & d_0 - d_7 & d_6 & d_5 \\ -d_2 & d_6 & d_0 - d_8 & d_4 \\ -d_3 & d_5 & d_4 & d_0 - d_9 \end{pmatrix} \quad (1.84)$$

The elements of matrix  $m_m$  ( $p_1$  through  $p_6$ ) represent the elementary polarization properties; linear ( $x$ - $y$ ) dichroism, linear ( $-45^\circ$  -  $+45^\circ$ ) dichroism, and circular dichroism, linear ( $x$ - $y$ ) retardance, linear ( $-45^\circ$  -  $+45^\circ$ ) retardance, and circular retardance. The dichroic and retardance elementary properties are proportional to the imaginary and real parts of the linear and circular anisotropies, respectively [3], [25]. The elements of  $m_u$  ( $d_0$  through  $d_9$ ) describe the depolarization properties of the medium. Diagonal terms ( $d_7$ ,  $d_8$ , and  $d_9$ ) represent the anisotropic depolarization coefficients, and the off-diagonal elements ( $d_1$  through  $d_6$ ) show the uncertainties of polarization properties.

The statistical interpretation of the Mueller matrix  $M$  of a continuous depolarizing medium implies that the depolarization is a result of a spatial or temporal averaging process over  $M$  when the polarization properties of medium (contained in differential matrix  $m$ ) fluctuate and matrix  $M$  varies. In such a case, it has been shown [25] that the matrix  $m_m$  represents the mean values  $\langle m \rangle$  of the polarization properties. The matrix  $m_u$  contains mean square values of the fluctuations of the polarization properties, i.e., their variances (or uncertainties)  $\langle \Delta m^2 \rangle$  linearly depends on the slab's thickness  $z$  (brackets  $\langle \dots \rangle$  in Eq. (1.85) refer to the spatial averaging in the transverse plane to the direction of light propagation). If the medium is assumed to be homogeneous in the longitudinal direction of the propagation of light, then [25]

$$M = \langle m \rangle = \langle \Delta m^2 \rangle z; \quad m_m = \langle m \rangle; \quad m_u = \langle \Delta m^2 \rangle z \quad (1.85)$$

Substituting the statistical representation of differential matrix  $m$  from Eq. (1.85) into Eq. (1.82) and integrating the latter equation along  $z$ , we obtain

$$M(z) = \exp \left[ m_0 z + \frac{1}{2} \langle \Delta m^2 \rangle z^2 \right] \quad (1.86)$$

It follows from Eq. (1.86) that the mean values of the polarimetric properties scale up linearly with the slab thickness while the depolarization properties evolve quadratically with it. The differential matrix  $m$  of a homogeneous medium can be obtained from a simulated or experimentally measured Mueller matrix  $M$  of a sample by computing the matrix logarithm, which can be represented as a sum of two matrices  $L_m$  and  $L_u$  of opposite G-symmetry:

$$L = \ln M, \quad L = L_m + L_u, \quad (1.87)$$

$$L_m = \frac{1}{2} (L - GL^T G), \quad L_u = \frac{1}{2} (L + GL^T G) \quad (1.88)$$

Calculating the logarithm of Eq. (1.86) at  $z = 1$  (i.e., taking the thickness of the slab as unit one), we observe that the antisymmetric component  $L_m$  and the symmetric component  $L_u$ , respectively, equal the mean values and (half) the variances of the polarization properties, accumulated over the slab thickness:

$$L_m = m_m = \langle m \rangle, \quad L_u = \frac{1}{2} m_u = \frac{1}{2} \langle \Delta m^2 \rangle \quad (1.89)$$

It is worth to recall that the elements of  $L_m$  and  $L_u$  matrices have a straightforward physical interpretation in terms of polarimetric properties of a sample as follows [3], [20], [25]:

Linear dichroism	$\sqrt{(L_m(1,2))^2 + (L_m(1,3))^2}$	(1.90)
Circular dichroism	$L_m(1,4)$	(1.91)
Net dichroism	$\sqrt{(L_m(1,2))^2 + (L_m(1,3))^2 + (L_m(1,4))^2}$	(1.92)
Linear retardance	$\sqrt{(L_m(2,4))^2 + (L_m(3,4))^2}$	(1.93)
Circular retardance	$L_m(2,3)$	(1.94)
Total retardance	$\sqrt{(L_m(2,4))^2 + (L_m(3,4))^2 + (L_m(2,3))^2}$	(1.95)
Total depolarization	$\frac{1}{3}  L_u(2,2) + L_u(3,3) + L_u(4,4) $	(1.96)
Orientation angle (fast axis)	$\frac{1}{2} \tan^{-1} \left[ \frac{L_m(2,4)}{L_m(3,4)} \right]$	(1.97)

## 1.5. Conclusions

In this chapter, we introduced the basic concepts of polarization. We defined the polarization ellipse as the locus of points representing the tip of electric field vector oscillating in the  $(x, y)$  plane orthogonal to the direction of the propagation of EM wave. We demonstrated that the polarization ellipse can describe any state of completely polarized light (linear, elliptical, circular). However, the polarization ellipse cannot be observed directly at optical frequencies because of its short oscillation time ( $10^{-15}$  s), and it cannot describe neither partially polarized, nor unpolarized light. Next, we introduced the Stokes parameters, based on measured light intensity, and the associated Stokes vectors in order to characterize completely polarized light, as well as partially or fully depolarized light. The Stokes parameters are observable because they are based on the intensity (the time average of the squared electric field amplitude) and can therefore be detected experimentally. In the polarimetric experiment, the incident polarized beam interacts with the sample, and the emerging beam is detected. The polarization states of both incident and emerging beams are characterized by the corresponding Stokes vectors. The transfer matrix describing the interaction of the sample with polarized light and the transformation of the polarization state of the incident light beam is called the Mueller matrix. The latter contains the most complete information on the polarimetric properties of a sample. The Mueller matrices of the basic optical elements (polarizer, retarder, depolarizer, and rotator) are introduced and discussed.

Mueller matrix data compression algorithms of polarimetric data processing are introduced; the concepts of physically realizable Mueller matrix and experimental Mueller matrix noise filtering are discussed. The special focus is placed on two particular types of Mueller matrix decomposition algorithms, namely, the Lu-Chipman polar sequential decomposition and the logarithmic (or differential) decomposition that we used for the analysis of the optical properties (diattenuation, retardance, and depolarization) of the biological specimens in our studies.

## References

1. S. R. Cloude, “Group theory and polarisation algebra”, *Optik (Stuttgart)*, vol. 75, no. 1, pp. 26–36, 1986.
2. S.-Y. Lu and R. A. Chipman, “Interpretation of Mueller matrices based on polar decomposition”, *J. Opt. Soc. Am. A, JOSAA*, vol. 13, no. 5, pp. 1106–1113, May 1996.
3. R. Ossikovski, “Differential matrix formalism for depolarizing anisotropic media”, *Opt. Lett.*, vol. 36, no. 12, pp. 2330–2332, Jun. 2011.
4. V. Devlaminck, “Depolarizing differential Mueller matrix of homogeneous media under Gaussian fluctuation hypothesis”, *J. Opt. Soc. Am. A, JOSAA*, vol. 32, no. 10, pp. 1736–1743, Oct. 2015.
5. D. W. Ball, *Field guide to spectroscopy*, SPIE Press, 2006.
6. D. H. Goldstein, *Polarized Light*, 3rd Ed. CRC Press, 2010.
7. S. Trippe, “Polarization and Polarimetry: a Review,” *J. Korean Astron. Soc.*, vol. 47, no. 1, pp. 15–39, Feb. 2014.
8. J. J. Gil and R. Ossikovski, *Polarized Light and the Mueller Matrix Approach*, CRC Press, pp. 1–398, Apr. 2016.
9. E. Collett, *Field Guide to Polarization*, SPIE Press, 2005.
10. N. Ghosh and A. I. Vitkin, “Tissue polarimetry: concepts, challenges, applications, and outlook”, *J. Biomed. Opt.*, vol. 16, no. 11, p. 110801, Nov. 2011.
11. S. Bancelin, A. Nazac, B. H. Ibrahim, P. Dokládal, E. Decencière, B. Teig, H. Haddad, H. Fernandez, M.-C. Schanne-Klein, and A. De Martino, “Determination of collagen fiber orientation in histological slides using Mueller microscopy and validation by second harmonic generation imaging”, *Opt. Express*, vol. 22, no. 19, pp. 22561–14, 2014.
12. R. A. Chipman, *Handbook of Optics, Polarimetry*, Ch. 22. pp. 1–37, May 1996.
13. S. R. Cloude and E. Pottier, “Concept of polarization entropy in optical scattering”, *Opt. Eng.*, vol. 34, no. 6, pp. 1599–1610, Jun. 1995.
14. C. J. R. Sheppard, A. L. Gratiet, and A. Diaspro, “A table of some coherency matrices, coherency matrix factors (CMFs), and their respective Mueller matrices”, *arxiv.org*. Jun-2017.
15. R. A. Chipman, “*Polarization Aberrations*”, PhD thesis, University of Arizona, 1987.
16. M. J. Hagyard, G. A. Gary, and E. A. West, “The SAMEX Vector Magnetograph: A Design Study for a Space-Based Solar Vector Magnetograph”, NASA, Scientific and Technical Information Division, 1988.

17. S. R. Cloude, “Conditions For The Physical Realisability Of Matrix Operators In Polarimetry”, *Proc. SPIE 1166*, Polarization Considerations for Optical Systems II, 1990.
18. F. Boulvert, G. Le Brun, B. Le Jeune, J. Cariou, and L. Martin, “Decomposition algorithm of an experimental Mueller matrix”, *Opt. Commun.*, vol. 282, no. 5, pp. 692–704, Mar. 2009.
19. E. Garcia-Caurel, R. Ossikovski, M. Foldyna, A. Pierangelo, B. Drévilion, and A. De Martino, “Advanced Mueller Ellipsometry Instrumentation and Data Analysis”, in *Ellipsometry at the Nanoscale*, no. 2, Springer, 2013, pp. 31–143.
20. S. Kumar, H. Purwar, R. Ossikovski, I. A. Vitkin, and N. Ghosh, “Comparative study of differential matrix and extended polar decomposition formalisms for polarimetric characterization of complex tissue-like turbid media”, *J. Biomed. Opt.*, vol. 17, no. 10, pp. 105006–13, Oct. 2012.
21. R. Ossikovski, A. De Martino, and S. Guyot, “Forward and reverse product decompositions of depolarizing Mueller matrices,” *Opt. Lett.*, vol. 32, no. 6, pp. 689–691, Mar. 2007.
22. R. Ossikovski, “Analysis of depolarizing Mueller matrices through a symmetric decomposition”, *J. Opt. Soc. Am. A, JOSAA*, vol. 26, no. 5, pp. 1109–1118, May 2009.
23. R. Ossikovski, “Differential and product Mueller matrix decompositions: a formal comparison”, *Opt. Lett.*, vol. 37, no. 2, pp. 220–222, 2012.
24. N. Ghosh, M. F. G. Wood, and I. A. Vitkin, “Influence of the order of the constituent basis matrices on the Mueller matrix decomposition-derived polarization parameters in complex turbid media such as biological tissues”, *Opt. Commun.*, vol. 283, no. 6, pp. 1200–1208, Mar. 2010.
25. R. Ossikovski and O. Arteaga, “Statistical meaning of the differential Mueller matrix of depolarizing homogeneous media”, *Opt. Lett.*, vol. 39, no. 15, pp. 4470–4473, Aug. 2014.

# Chapter 2

## Mueller Polarimetry: instrumental aspects

2.1. General principles of Mueller polarimetry .....	36
2.1.1. Design optimization of the complete Mueller polarimeter .....	37
2.1.2. Calibration of The complete Mueller polarimeter .....	40
2.2. Imaging Mueller polarimeter based on ferroelectric liquid crystals .....	44
2.2.1. Mueller microscope in transmission configuration .....	45
2.2.2. Wide-field imaging Mueller polarimeter in reflection configuration .....	47
2.3 Conclusions .....	48
References .....	49

In the Chapter 1 we briefly reviewed the fundamentals of the Mueller polarimetry (e.g., polarization ellipse, Stokes parameters, Mueller matrices of basic optical elements, etc.) and the non-linear Mueller matrix compression algorithms used for the check of physical realizability of experimental Mueller matrices, for noise filtering, and for physical interpretation of Mueller matrix data in terms of the polarimetric properties of studied samples. Now, we provide the general description of any polarimetric setup within the framework of Stokes-Mueller, then we discuss the procedure of the optimization of a complete Mueller matrix polarimeter by choosing an appropriate arrangement of the optical components of the polarization state generator (PSG) and the polarization state analyzer (PSA) that minimizes the condition numbers of the corresponding matrices and, consequently, minimizes the error propagation. The principles of the eigenvalue calibration method (ECM) of the complete Mueller polarimeter that was first developed in LPICM (École polytechnique, France) [1] are briefly recalled. We also present two custom-built multi-spectral ferroelectric liquid crystal-based imaging Mueller polarimeters (the microscope operating in transmission and the wide-field imaging system operating in reflection) that were used in our study for imaging of both thin and thick sections of biological tissue, respectively.

## 2.1. General principles of Mueller polarimetry

Hereafter, the description of the polarimetric instruments, namely, the complete imaging Mueller polarimeters used in our studies, will be done within the framework of the Stokes-Mueller formalism. The schematic operation of a polarimetric system operating in transmission configuration is shown in Fig. 2.1, but the same description holds for the reflection configuration.



*Figure 2.1 Stokes-Mueller description of the operation of any polarimetric setup.*

The polarimetric setup comprises a light source, a polarization state generator (PSG) and a polarization state analyzer (PSA), and a detector (CCD camera for imaging polarimeter). Our custom-built polarimeters are based on a sequential modulation and analysis of light beam polarization by using the discrete polarization basis states. In general, the PSG sequentially generates  $N_1$  different polarizations, represented by  $N_1$  different Stokes vectors  $\mathbf{S}_i$  of the light beam incident on a sample.  $\mathbf{M}$  is the Mueller matrix ( $4 \times 4$  real-valued matrix) that describes the polarimetric properties of a sample, and the product  $\mathbf{M} \cdot \mathbf{S}_i$  is the Stokes vector that describes the polarization state of the emerging light beam after its interaction with a sample. The light beam passes through the PSA that is characterized by the Stokes vector  $\mathbf{S}'_j$  ( $j = 1, \dots, N_2$ ). It means that if we will send the unpolarized light beam through the PSA in the reverse direction, the polarization state of the transmitted light beam will be described by the Stokes vector  $\mathbf{S}'_j$ . Finally, the light beam intensity is registered on a detector and is described by the scalar product of two Stokes vectors  $\mathbf{S}'_j \cdot \mathbf{M} \cdot \mathbf{S}_i$ .

We construct the modulation matrix  $\mathbf{W}$  ( $4 \times N_1$ ) by using the Stokes vectors  $\mathbf{S}_i$  as its columns. Depending on the value of  $N_1$  the PSG is called incomplete ( $N_1 < 4$ ), complete ( $N_1 = 4$  and the Stokes vectors are linearly independent, hence, they form a complete basis of the polarization space and matrix  $\mathbf{W}$  is invertible), and redundant ( $N_1 > 4$  and the  $\mathbf{S}_i$  vectors form an overcomplete basis of the polarization space, and, consequently, the modulation matrix  $\mathbf{W}$  ( $4 \times N_1$ ) has a pseudo-inverse).

The PSA operates as a polarization filter for the light beam emerging from a sample. Similarly to the construction of the modulation matrix  $\mathbf{W}$  ( $4 \times N_1$ ), we can build the analysis matrix  $\mathbf{A}$  ( $N_2 \times 4$ ) of the PSA. We use the Stokes vectors  $\mathbf{S}'_j$  of the polarization filter PSA to define the rows of the analysis matrix  $\mathbf{A}$ . The PSA may also be incomplete, complete, or redundant depending on the dimension  $N_2$  of the polarization space spanned by the row vectors of the analysis matrix  $\mathbf{A}$ .

Generating  $N_1$  polarization states of the incident light by PSG and projecting them on the  $N_2$  states of the polarization filter PSA we obtain the raw intensity signals matrix that can be written as

$$\mathbf{B} = \mathbf{A}\mathbf{M}\mathbf{W} \quad (2.1)$$

To obtain the Mueller matrix  $\mathbf{M}$  of a sample from the raw intensity matrix  $\mathbf{B}$ , one needs to know the matrices  $\mathbf{A}$  and  $\mathbf{W}$ , i. e. the instrument has to be calibrated. Assuming that the instrument is a complete Mueller polarimeter (i. e. elements PSG and the PSA are complete or redundant), the Mueller matrix  $\mathbf{M}$  of a sample can be calculated by inverting (or pseudo inverting in case of redundant PSG / PSA) the matrices  $\mathbf{A}$  and  $\mathbf{W}$

$$\mathbf{M} = \mathbf{A}^{-1}\mathbf{B}\mathbf{W}^{-1} \quad (2.2)$$

The polarization modulation and analysis can be implemented by using different optical components. e.g., rotating retardation plates (e.g., wave plates [2]), photoelastic modulators (PEMs) [3], liquid-crystal variable retarders (LCVR) [4], [5], or ferroelectric liquid crystals (FLCs) [6]-[10]. All approaches have some pros and cons: 1) mechanical rotation of a wave plate requires more time comparing to electrically-driven switching of LCVR or FLC state; 2) PEM-based polarimeter is challenging to miniaturize due to the large size of piezoelectric motors; 3) LCVR-based polarimeters are well suited for the imaging applications but the operation performance of LCVRs is affected by the variations of ambient temperature, and their response time (few milliseconds) may be a limiting factor for the biomedical applications. FLCs-based polarimeters do not require any mechanical moving parts and allow the fast polarization modulation (few microseconds) that can be beneficial for the analysis of biological samples. Furthermore, the liquid crystals are suitable for polarimetric imaging because of broad angular acceptance, wide clear apertures, low aberrations, and no image wander [6], [11].

### 2.1.1. Design optimization of the complete Mueller polarimeter

The main goal of the design optimization of a complete Mueller polarimeter consists in the minimization of noise in the elements of Mueller matrix  $\mathbf{M}$  in the presence of additive noise in the elements of raw measurement matrix  $\mathbf{B}$  (see Eq. (2.1)). We address this question by exploring the degrees of freedom on the selection of the appropriate PSG and PSA polarization states basis. The Stokes vectors that represent these polarization states should form the matrices  $\mathbf{A}$  and  $\mathbf{W}$  that will not increase an error propagation from  $\mathbf{B}$  to  $\mathbf{M}$ . In other words, the optimization of the  $\mathbf{A}$  and  $\mathbf{W}$  matrices has to reduce the numerical errors produced by their inversion and minimize the errors in the  $\mathbf{M}$  matrix. We restrict ourselves to the case  $N_1 = N_2 = 4$ , but the following considerations can be easily generalized for a redundant PSA / PSG.

The condition number of any square matrix  $\mathbf{X}$  is defined as

$$\mathbf{Cond}(\mathbf{X}) = \|\mathbf{X}\|\|\mathbf{X}^{-1}\| \quad (2.3)$$

where symbol  $\|\cdot\|$  denotes the norm of a matrix (or vector). The norm of matrix  $\mathbf{X}$  is chosen as

$$\|\mathbf{X}\| = \sup[\lambda_i(\mathbf{X})] \quad (2.4)$$

where  $\lambda_i$  are the singular values of matrix  $\mathbf{X}$ . It is worth to mention that for the real-valued but non-symmetric matrix its singular values are not equal to its eigenvalues and have to be calculated using general singular value decomposition algorithm [12]. According to Eqs (2.3) and (2.4), the condition number of a matrix is defined as the ratio of the largest ( $\lambda_{max}$ ) and the smallest ( $\lambda_{min}$ ) of the singular values  $\lambda_i$ :

$$\mathbf{Cond}(\mathbf{X}) = \left| \frac{\lambda_{max}}{\lambda_{min}} \right| \quad (2.5)$$

If we define the vector  $\mathbf{Y} = \mathbf{XZ}$  and use the Euclidian norm for both vectors  $\mathbf{Y}$  and  $\mathbf{Z}$ , the following relation holds

$$\|\mathbf{Y}\| \leq \|\mathbf{X}\|\|\mathbf{Z}\| \quad (2.6)$$

Let us consider the optimization of the design of the PSA first. The Stokes vector  $\mathbf{S}$  of the light incident on the PSA and the vector  $\mathbf{I}$  that is composed of four intensities measured at the detector are related by

$$\mathbf{I} = \mathbf{AS}, \quad (2.7a)$$

$$\mathbf{S} = \mathbf{A}^{-1}\mathbf{I} \quad (2.7b)$$

The rows of the matrix  $\mathbf{A}$  represent the transposed Stokes vectors of the completely polarized light. Varying the configuration of the PSA by changing the relative orientations of its optical components, the matrix  $\mathbf{A}$  will be varied as well, but its norm  $\|\mathbf{A}\|$  (see Eq. (2.4)) will hardly change. However, if  $\mathbf{A}$  becomes close to a singular matrix (e.g. two matrix rows are almost the same, that corresponds to the same polarization state being measured twice) the norm  $\|\mathbf{A}^{-1}\|$  can take an arbitrary large value.

Assuming that any intensity measurement vector  $\mathbf{I}$  is affected by an additive noise  $\delta\mathbf{I}$  (white Gaussian noise that has a zero-mean value in a normal distribution) the corresponding error in the Stokes vector  $\mathbf{S}$  and the estimation of its norm (see Eqs (2.6) and (2.7)) are given by

$$\delta\mathbf{S} = \mathbf{A}^{-1}\delta\mathbf{I} \quad (2.8)$$

$$\|\delta\mathbf{S}\| \leq \|\mathbf{A}^{-1}\| \|\delta\mathbf{I}\| \quad (2.9)$$

Whereas the amplitude of the intensity signal  $\mathbf{I}$  may vary significantly, the amplitude  $\|\delta\mathbf{I}\|$  of the additive noise is assumed to remain constant when the PSA configuration is changed. Hence, the norm of the error  $\|\delta\mathbf{S}\|$  is limited by the norm  $\|\mathbf{A}^{-1}\|$ . The latter can be minimized by the optimal design of the PSA. The minimization of the norm  $\|\mathbf{A}^{-1}\|$  is equivalent to the minimization of the condition number  $\mathbf{Cond}(\mathbf{A})$  because the variation of the norm  $\|\mathbf{A}\|$  is small for the different configurations of the PSA.

The condition number of an arbitrary matrix ranges from one for a unitary (well-conditioned) matrix to positive infinite for a singular (ill-conditioned) matrix. The rows of the matrix  $\mathbf{A}$  for the sequential PSA represent the Stokes vectors with the degree of polarization  $\rho$  ( $0 \leq \rho \leq 1$ ). For matrix  $\mathbf{A}$  to be unitary, the row vectors should form an orthogonal basis. This condition is not satisfied for any set of four Stokes vectors, as they can never be orthogonal to each other. It was demonstrated [13] that

$$\mathbf{Cond}(\mathbf{A}) \geq \sqrt{3} \quad (2.10)$$

Minimizing the condition number of the matrix  $\mathbf{A}$ , we make it maximally close to a unitary matrix. Intuitively it is clear that to achieve this optimization the polarization basis states of the PSA have to be as different as possible from each other. It was shown that for a complete PSA such optimal design corresponds to four polarization basis states being the regular tetrahedron vertices on the Poincaré sphere [14]. This criterion of the optimization of noise propagation was generalized for a redundant PSA by choosing the polarization basis states as the vertices of simple symmetric polyhedrons (e. g.  $N_2 = 6$  - vertices of an octahedron,  $N_2 = 8$  - vertices of a cube, etc.) at the Poincaré sphere [15]. It was shown that the optimization of the matrix  $\mathbf{A}$  not only minimizes the noise on the Stokes vector  $\mathbf{S}$  but also distributes noise equally among the components of  $\mathbf{S}$  [16].

These results are easily generalized to the design optimization of the PSG and the complete Mueller polarimeter. The Eq. (2.1) can be written as follows.

$$\vec{\mathbf{M}} = ((\mathbf{W}^{-1})^T \otimes \mathbf{A}^{-1}) \vec{\mathbf{B}} \quad (2.11)$$

where  $\vec{\mathbf{M}}$  and  $\vec{\mathbf{B}}$  are  $16 \times 1$  real vectors, and  $(\mathbf{W}^{-1})^T \otimes \mathbf{A}^{-1}$  is a  $16 \times 16$  real matrix. The symbol  $\otimes$  denotes the Kronecker product,  $(\cdot)^T$  stands for the transpose matrix. Since a Kronecker product of the inverse matrices is equal to the inverse of a Kronecker product, the Eq. (2.11) can be written as:

$$\vec{\mathbf{M}} = (\mathbf{W}^T \otimes \mathbf{A})^{-1} \vec{\mathbf{B}} = \mathbf{Q}^{-1} \vec{\mathbf{B}} \quad (2.12)$$

where  $(\mathbf{W}^T \otimes \mathbf{A})^{-1}$  is also a  $16 \times 16$  real matrix.

In the presence of noise on elements of the vector  $\vec{\mathbf{B}}$  (that are the measured intensities), it follows from Eqs (2.6) and (2.12):

$$\frac{\|\Delta\vec{\mathbf{M}}\|}{\|\vec{\mathbf{M}}\|} \leq \|\mathbf{Q}^{-1}\| \|\mathbf{Q}\| \frac{\|\Delta\vec{\mathbf{B}}\|}{\|\vec{\mathbf{B}}\|} = \mathbf{Cond}(\mathbf{Q}) \frac{\|\Delta\vec{\mathbf{B}}\|}{\|\vec{\mathbf{B}}\|} \quad (2.13)$$

where  $\Delta\vec{\mathbf{B}}$  is the error matrix associated with the vector  $\vec{\mathbf{B}}$ , and  $\Delta\vec{\mathbf{M}}$  represents the error matrix associated with the vector  $\vec{\mathbf{M}}$ ,  $\mathbf{Cond}(\mathbf{Q}) = \|\mathbf{Q}^{-1}\| \|\mathbf{Q}\|$  is the condition number of the matrix  $\mathbf{Q}$ .

Eq. (2.13) shows that the value of relative error of the vector  $\vec{\mathbf{M}}$  can be as large as the value of relative error of the vector  $\vec{\mathbf{B}}$  multiplied by the condition number of matrix  $\mathbf{Q}$ . Obviously, the minimization of  $\mathbf{Cond}(\mathbf{Q})$  and  $\|\Delta\vec{\mathbf{B}}\|/\|\vec{\mathbf{B}}\|$  will minimize the relative error  $\|\Delta\vec{\mathbf{M}}\|/\|\vec{\mathbf{M}}\|$ . However, even for the small values of relative error of the vector  $\vec{\mathbf{B}}$  the value of relative error of the vector  $\vec{\mathbf{M}}$  can become non-negligible if the value of  $\mathbf{Cond}(\mathbf{Q})$  is large. Thus, as previously mentioned, it is necessary to minimize the condition number  $\mathbf{Cond}(\mathbf{Q})$  to limit noise propagation. The matrix  $\mathbf{Q}$  is the Kronecker product of the transpose of matrix  $\mathbf{W}$  and the matrix  $\mathbf{A}$ . Then,  $\mathbf{Cond}(\mathbf{Q})$  can be written as [17], [18]

$$\mathbf{Cond}(\mathbf{Q}) = \mathbf{Cond}(\mathbf{W}) \mathbf{Cond}(\mathbf{A}) \quad (2.14)$$

where  $\mathbf{Cond}(\mathbf{W})$  and  $\mathbf{Cond}(\mathbf{A})$  are the condition numbers of the matrices  $\mathbf{W}$  and  $\mathbf{A}$ , respectively.

It is worth to mention that noise in all components of the Mueller matrix  $\mathbf{M}$  is minimized and equally distributed if the condition numbers of both matrix  $\mathbf{A}$  and matrix  $\mathbf{W}$  are minimized. If one is interested in measuring the specific elements of Mueller matrix only, other design optimization criteria may be applied. Whereas the minimization of both  $\mathbf{Cond}(\mathbf{A})$  and  $\mathbf{Cond}(\mathbf{W})$  minimizes the effect of statistical noise on intensity matrix  $\mathbf{B}$ , in practice it also helps to minimize the impact of the systematic errors.

The condition number of each matrix  $\mathbf{A}$  or  $\mathbf{W}$  ranges from  $\sqrt{3}$  to positive infinite (singular matrix), hence the inverse of the condition number ranges from zero (singular matrix) to  $1/\sqrt{3}$ . The optimization of the custom-built complete imaging polarimeters used in our studies was performed using the criteria of the maximization of the inverse of the condition numbers  $\mathbf{Cond}(\mathbf{A})$  and  $\mathbf{Cond}(\mathbf{W})$  (with  $1/\sqrt{3} \approx 0.5773$  being the best theoretical maximal value) [19], [20].

### 2.1.2. Calibration of the complete Mueller polarimeter

As explained above, the experimental Mueller matrix  $\mathbf{M}$  can be extracted from the raw intensity matrix  $\mathbf{B}$  provided the matrices  $\mathbf{W}$  and  $\mathbf{A}$  are known. The determination of both

matrices (**W** and **A**) is called the calibration. In practice, it is quite difficult to make the accurate models of these two matrices because of existing inaccuracies in the characteristics of optical components of PSG / PSA (polarizer and two ferro-electric liquid crystal retarders in our case), their relative alignment, interference effects, beam divergence, or Gaussian white noise. To overcome these problems the Eigenvalue Calibration Method (ECM) developed in the LPICM by E. Compain [1] was used for the calibration of the complete Mueller polarimeter. This method does not require an accurate optical modeling of the PSG and PSA components and can be applied in both transmission and reflection configurations. The ECM determines the actual **W** and **A** matrices from a set of measurements with the reference samples, namely, the linear dichroic retarders that do not need to be perfectly characterized in advance, because their optical parameters (transmission, diattenuation, retardation) are provided by the calibration procedure itself. The Mueller matrix of a linear dichroic retarder has the following form:

$$\mathbf{M}(\tau, \Psi, \Delta, \theta) = \tau \mathbf{R}(\theta) \begin{bmatrix} 1 & -\cos 2\Psi & 0 & 0 \\ -\cos 2\Psi & 1 & 0 & 0 \\ 0 & 0 & \sin 2\Psi \cos \Delta & \sin 2\Psi \sin \Delta \\ 0 & 0 & -\sin 2\Psi \sin \Delta & \sin 2\Psi \cos \Delta \end{bmatrix} \mathbf{R}(-\theta) \quad (2.15)$$

where  $\tau$  is transmission coefficient,  $\Psi$  and  $\Delta$  are the ellipsometric angles [20], and  $\theta$  is the azimuth of the element eigenaxis with respect to the reference axis  $x$ .  $\mathbf{R}(\theta)$  is the rotator matrix describing within the framework of Stokes-Mueller formalism a rotation by an angle  $\theta$  around the normal to the plane defined by the eigenaxes of the optical element.

The eigenvalues of the matrix defined in (2.15) are independent of  $\theta$  and given by:

$$\begin{aligned} \lambda_1 &= 2\tau \sin^2 \Psi \\ \lambda_2 &= 2\tau \cos^2 \Psi \\ \lambda_3 &= \tau \sin(2\Psi) \exp(i\Delta) \\ \lambda_4 &= \tau \sin(2\Psi) \exp(-i\Delta) \end{aligned} \quad (2.16)$$

where  $\lambda_1$  and  $\lambda_2$  are the real numbers, and  $\lambda_3$  and  $\lambda_4$  are the complex numbers [20]. The elements of the matrix  $\mathbf{M}(\tau, \Psi, \Delta, \theta)$  can be calculated using Eq. (2.16).

$$\begin{aligned} \tau &= 0.5(\lambda_1 + \lambda_2) \\ \cos 2\Psi &= (\lambda_2 - \lambda_1)/(\lambda_1 + \lambda_2) \\ \sin 2\Psi \cos \Delta &= (\lambda_3 + \lambda_4)/(\lambda_1 + \lambda_2) \\ \sin 2\Psi \sin \Delta &= -i(\lambda_3 - \lambda_4)/(\lambda_1 + \lambda_2) \end{aligned} \quad (2.17)$$

It means that the matrix  $\mathbf{M}(\tau, \Psi, \Delta, \theta)$  can be reconstructed from the eigenvalues except of the azimuth angle  $\theta$  and corresponding matrix  $\mathbf{R}(\theta)$ . The calculation of this angle will be addressed later.

Hereafter we describe the consequent steps of the calibration procedure. The first measurement is made without any reference sample.

$$\mathbf{B}_0 = \mathbf{A}\mathbf{W} \quad (2.18)$$

where the experimental matrix  $\mathbf{B}_0$  ( $4 \times 4$  real matrix) is a product of the matrices  $\mathbf{A}$  and  $\mathbf{W}$ . In other words, the elements of  $\mathbf{B}_0$  are the 16 intensities values corresponding to all permutations of the polarized states of the PSG and the PSA. For simplicity, we suppose that the non-systematic errors are small enough (e.g., we can always do repetitive data acquisitions and average them).

Then, a set of reference samples is measured. If we denote by  $\mathbf{M}_i$  the Mueller matrix of the reference sample  $i$  the experimental matrix  $\mathbf{B}_i$  can be expressed as [20]

$$\mathbf{B}_i = \mathbf{A}\mathbf{M}_i\mathbf{W} \quad (2.19)$$

Substituting the expression for the matrix  $\mathbf{B}_0$  from Eq. (2.18) into Eq. (2.19), the matrix  $\mathbf{B}_i$  can be written as [11]

$$\mathbf{B}_i = \mathbf{A}(\mathbf{W}\mathbf{W}^{-1})\mathbf{M}_i\mathbf{W} = \mathbf{B}_0(\mathbf{W}^{-1}\mathbf{M}_i\mathbf{W}) \quad (2.20)$$

Then, we calculate the matrix

$$\mathbf{C}_i = (\mathbf{B}_0)^{-1}\mathbf{B}_i = \mathbf{W}^{-1}\mathbf{M}_i\mathbf{W} \quad (2.21)$$

The matrix  $\mathbf{C}_i$ , that combines the inverse of  $\mathbf{B}_0$  and  $\mathbf{B}_i$  matrices, has the same eigenvalues as the matrix  $\mathbf{M}_i$ . Hence, the latter can be reconstructed from the eigenvalues of the experimental matrix  $\mathbf{C}_i$  except of the rotation matrix  $\mathbf{R}(\theta)$ .

Eq. (2.21) can be written as

$$\mathbf{M}_i\mathbf{W} - \mathbf{W}\mathbf{C}_i = \mathbf{M}_i\mathbf{W}\mathbf{I} - \mathbf{I}\mathbf{W}\mathbf{C}_i = \mathbf{0} \quad (2.22)$$

Hence,

$$(\mathbf{I} \otimes \mathbf{M}_i)\mathbf{W} - (\mathbf{C}_i^T \otimes \mathbf{I})\mathbf{W} = \mathbf{H}_i\mathbf{W} = \mathbf{0}. \quad (2.23)$$

where  $\mathbf{H}_i = ((\mathbf{I} \otimes \mathbf{M}_i) - (\mathbf{C}_i^T \otimes \mathbf{I}))$  is a  $16 \times 16$  matrix,  $\mathbf{I}$  is a  $4 \times 4$  identity matrix, and the symbol  $\otimes$  denotes the Kronecker product. Multiplied by the transpose of the matrix  $\mathbf{H}_i^T$ , the Eq. (2.16) can be written as:

$$\mathbf{H}_i^T \mathbf{H}_i \mathbf{W} = \mathbf{K}_i \mathbf{W} = \mathbf{0}. \quad (2.24)$$

where  $\mathbf{K}_i = \mathbf{H}_i^T \mathbf{H}_i$  is a  $16 \times 16$  symmetric real matrix and positive semidefinite, which means that all its eigenvalues are always zero or positive. Then, the matrix  $\mathbf{W}$ , written as a  $16 \times 1$  vector  $\mathbf{W}^{16}$ , has to be an eigenvector corresponding to a zero eigenvalue of  $\mathbf{K}_i$  matrix.

In our study, we used three different optical elements as the reference samples for the calibration, namely, a polarizer  $P0^\circ$  ( $\Psi = 0^\circ$ ), a polarizer  $P90^\circ$  ( $\Psi = 90^\circ$ ), and a phase retarder  $L30^\circ$  with the fast axis rotated by  $30^\circ$  with the respect to the transmission axis of a polarizer  $P0$  within the plane orthogonal to the direction of light propagation. The Eq. (2.24) has to be verified for all three reference sample measurements

$$\mathbf{K} \mathbf{W} = \sum_i \mathbf{K}_i \mathbf{W} = (\mathbf{H}_{P0}^T \mathbf{H}_{P0} + \mathbf{H}_{P90}^T \mathbf{H}_{P90} + \mathbf{H}_{L30}^T \mathbf{H}_{L30}) \mathbf{W} = \mathbf{0} \quad (2.25)$$

where  $\mathbf{K}$  is also a positive semidefinite symmetric real matrix, so it can be diagonalized. In theory, matrix  $\mathbf{K}$  should have only one null eigenvalue, and the others are non-zero eigenvalue because Eq. (2.25) should have only one non-trivial solution  $\mathbf{W}^{16}$ . Then, Eq. (2.25) can be written as

$$\mathbf{K} = \mathbf{O}^t \begin{bmatrix} \lambda_1 & 0 & \cdots & 0 \\ 0 & \lambda_2 & \cdots & 0 \\ \vdots & \vdots & \ddots & \vdots \\ 0 & 0 & \cdots & \lambda_{16} \end{bmatrix} \mathbf{O} \quad (2.26)$$

where  $\lambda_i$  ( $i = 1, 2 \dots 16$ ) are 16 eigenvalues of the matrix  $\mathbf{K}$  that obey the relationship  $\lambda_1 > \lambda_2 > \cdots > \lambda_{15} \gg \lambda_{16} = 0$  and  $\mathbf{O}$  is the orthonormal matrix whose rows are the eigenvectors of  $\mathbf{K}$ . [20], [21]. Because of the limited experimental precision that affects the values of the measured matrices  $\mathbf{C}_i$ , the null space of the corresponding matrix  $\mathbf{K}$  is empty. i.e. its eigenvalues are all different from zero. However, the smallest eigenvalue  $\lambda_{16}$  (that should be null in theory) is close to zero in reality.

We can now address the problem of the determination of still unknown azimuth angles  $\theta_i$ . The matrix  $\mathbf{K}_i$  can be calculated as a function of the azimuth angle  $\theta_i$ , then the matrix  $\mathbf{K}$  and its eigenvalues can also be considered as a function of the azimuth angles  $\theta_i$ . However, if the azimuth angles  $\theta_i$  are not set to their real values, Eq. (2.24) will have no non-trivial solution because all the eigenvalues of the matrix  $\mathbf{K}$  will be non-null. Hence, the correct values of the azimuth angles can be determined by minimizing the smallest eigenvalue  $\lambda_{16}$  of  $\mathbf{K}$ . This minimization method is well suited for experimental data, which are affected by the noise, which prevents the smallest eigenvalue of the matrix  $\mathbf{K}$  from being an exact zero.

The solution  $\mathbf{W}^{16}$  is the eigenvector of the matrix  $\mathbf{K}$  associated with the smallest eigenvalue, and it is used to get the matrix  $\mathbf{W}$ . Using Eq. (2.18), we can also calculate the matrix  $\mathbf{A}$ . Finally, there are two criteria to choose a good set of reference samples [20].

1. Without noise the matrix  $\mathbf{K}$  has to have only one null eigenvalue  $\lambda_{16}$ , and in practice, the ratio  $\lambda_{16}/\lambda_{15}$ , should be as close as possible to zero.
2. The other 15 eigenvalues should be as far as possible from zero, and the ratio  $\lambda_{15}/\lambda_1$ , that is much higher than error level and always less than one, should be as large as possible.

## 2.2. Imaging Mueller polarimeter based on ferroelectric liquid crystals

The custom-built imaging Mueller polarimeters operating in both transmission and reflection configurations with ferroelectric liquid crystals for light modulation and analysis were used in our studies. The PSG is composed of a linear horizontal polarizer (HP), first ferroelectric liquid crystal (FLC1), a wave plate (WP), and second ferroelectric liquid crystal (FLC2) as shown in Fig. 2.2. [6], [22]

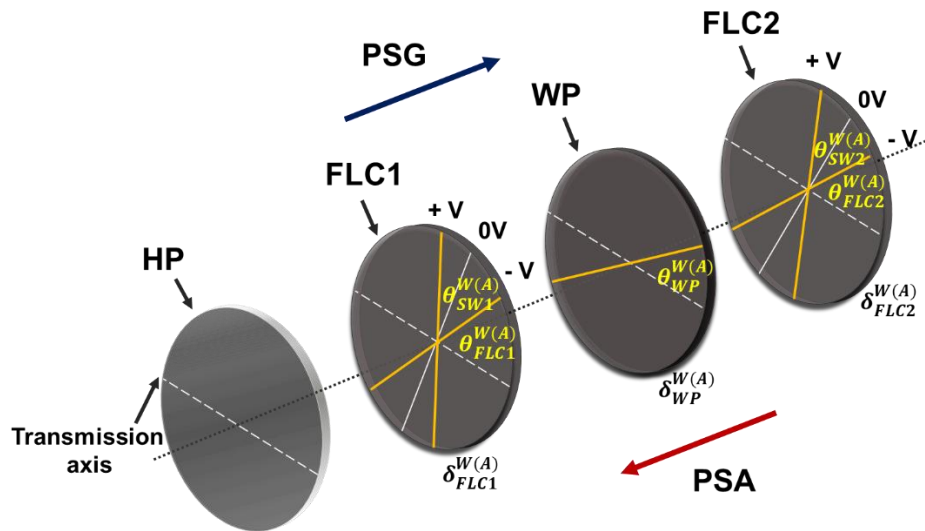


**Figure 2.2** Optical elements (a horizontal polarizer (HP), two ferroelectric liquid crystals (FLC1, FLC2), and a wave plate (WP) for the PSG and PSA. The arrows show the direction of light propagation for PSG and PSA and corresponding arrangement of the optical elements.

The orientation of the fast optical axis of the FLC<sub>*i*</sub> (*i* = 1, 2) in the plane orthogonal to the direction of light propagation is electrically switched by applying the voltage *V* (positive or negative). The angle between two extreme positions of the fast axis at  $\pm V$  applied voltage values is called the switching angle  $\theta_{SW}$  (see Fig. 2.2). The orientation (or azimuth) angle of the fast axis of FLCs with respect to the transmission axis of a polarizer is denoted as  $\theta_{FLC}$  for a negative voltage value  $-V$  and  $\theta_{SW} + \theta_{FLC}$  for a positive voltage value  $+V$ . The orientation angle of fast axis of the WP is denoted by  $\theta_{WP}$ . The phase retardance induced by the FLCs and WP is denoted as  $\delta_{FLC}$  and  $\delta_{WP}$ , respectively. Both values of retardance depend on the wavelength. Then, the Mueller matrix of the PSG can be described as [22].

$$\begin{aligned}
& \mathbf{M}_{\text{PSG}}(\delta_{\text{FLC2}}, \theta_{\text{SW2}}, \theta_{\text{FLC2}}, \delta_{\text{WP}}, \theta_{\text{WP}}, \delta_{\text{FLC1}}, \theta_{\text{SW1}}, \theta_{\text{FLC1}}) \\
& = \mathbf{M}_{\text{FLC2}} \mathbf{M}_{\text{WP}} \mathbf{M}_{\text{FLC1}} \mathbf{M}_{\text{HP}}
\end{aligned} \tag{2.27}$$

Four different polarization states that can be characterized by the corresponding Stokes vectors are generated by controlling the azimuth angles ( $\theta_{\text{FLC1}}, \theta_{\text{FLC2}}$ ) and switching the angles ( $\theta_{\text{SW1}}, \theta_{\text{SW2}}$ ) as follows [22].

$$\begin{aligned}
\mathbf{S}_{\text{W1}} &= \mathbf{M}_{\text{PSG}}(\theta_{\text{FLC1}}, \theta_{\text{FLC2}}) \mathbf{S}_{\text{in}} \\
\mathbf{S}_{\text{W1}} &= \mathbf{M}_{\text{PSG}}(\theta_{\text{FLC1}} + \theta_{\text{SW1}}, \theta_{\text{FLC2}}) \mathbf{S}_{\text{in}} \\
\mathbf{S}_{\text{W1}} &= \mathbf{M}_{\text{PSG}}(\theta_{\text{FLC1}}, \theta_{\text{FLC2}} + \theta_{\text{SW2}}) \mathbf{S}_{\text{in}} \\
\mathbf{S}_{\text{W1}} &= \mathbf{M}_{\text{PSG}}(\theta_{\text{FLC1}} + \theta_{\text{SW1}}, \theta_{\text{FLC2}} + \theta_{\text{SW2}}) \mathbf{S}_{\text{in}}
\end{aligned} \tag{2.28}$$

where  $\mathbf{S}_{\text{in}} (= [\mathbf{1} \ \mathbf{0} \ \mathbf{0} \ \mathbf{0}]^T)$  represents Stokes vector of the unpolarized incident light. The PSA is identical to the PSG, but its elements are placed in a reverse order. The Mueller matrix of the PSA is given as:

$$\begin{aligned}
& \mathbf{M}_{\text{PSA}}(\theta_{\text{FLC1}}, \theta_{\text{SW1}}, \delta_{\text{FLC1}}, \theta_{\text{WP}}, \delta_{\text{WP}}, \theta_{\text{FLC2}}, \theta_{\text{SW2}}, \delta_{\text{FLC2}}) \\
& = \mathbf{M}_{\text{HP}} \mathbf{M}_{\text{FLC1}} \mathbf{M}_{\text{WP}} \mathbf{M}_{\text{FLC2}}
\end{aligned} \tag{2.29}$$

The wave plate compensates partially for the spectral dependence of the retardance on the FLCs, and it makes the condition number constant or slightly varying within the visible wavelength spectral range [6], [22]. The orientation angles of all three retarders with respect to the laboratory reference frame (transmission axis of HP) and the corresponding calibration matrices  $\mathbf{W}$  and  $\mathbf{A}$  were determined by applying the ECM, as was previously explained.

### 2.2.1. Mueller microscope in transmission configuration

The custom-built Mueller polarimetric FLC-based microscope operating in a visible wavelength range (450 nm – 700 nm) was used to measure the Mueller matrix of thin tissue sections in a transmission configuration. The optical layout and photo of the instrument are shown in Fig. 2.3. The illumination arm of the setup consists of a white-light LED source and a set of lenses which combined with a condenser lens, illuminate the sample with uniform intensity and polarization according to the widely used Kohler configuration. Two diaphragms are used in between the lenses for independent control of beam divergence and size followed by a polarization state generator (PSG). The PSG is mounted just before the condenser lens, and it is composed of a linear polarizer, two ferroelectric liquid crystal retarders (Meadowlark FPR-200-1550), and a quarter wave retarder placed between the two ferroelectric liquid crystal retarders according to Fig. 2.2.. The light transmitted/scattered by the sample is captured by an imaging lens and directed to the PSA. The optical elements,

used in this work to illuminate and to image the sample, have been either a cemented achromatic doublet lens (Thorlabs AC254-030-A-ML), a low magnification microscope objective (Nikon CFI LU Plan Fluor, 5x, NA 0.15), or even a medium magnification microscope objective (Nikon CFI LU Plan Fluor, 20x, NA 0.45). The condenser and the imaging optics have always been kept identical to each other in order to match their respective numerical apertures. After the PSA, the light passes through an afocal relay pair (.75x) to adjust magnification, and finally it reaches a CCD camera (AV Stingray F-080B) coupled to a telephoto lens fussed to the infinite. The sample is placed on the principal object plane of the imaging optics; thus, a real space image of a sample is formed on the CCD detector. The wavelength of 533 nm was selected for our measurements by placing an interferential filter (spectral bandwidth of 20 nm) before PSG. The measurements of histological cuts of skin models were performed with a 20× objective with a field of view (FoV) of about 600  $\mu\text{m}$  [23].

During standard operation of the microscope, the fact of switching from sample-to-sample, caused important variations in the overall signal registered by CCD. The transmitted intensity for thinner samples was higher compared to thicker ones, in accordance with the Beer-Lambert law. To avoid the saturation problem, we used the measurement protocol described below. Due to the technical characteristics of the CCD detector, the polarimetric measurements were performed within a given intensity range to ensure the linearity of CCD response. Therefore, the integration time of a CCD was adjusted for every sample to get a well-balanced signal level for all 16 images needed to measure the corresponding Mueller matrix. This procedure helped us avoid both over- and under-exposure. It is worth noting that while all histological cuts were relatively thin and transmitted a significant fraction of the direct light, the scattering of light produced noticeable effects in depolarization parameters due to the incoherent summation of direct and scattered light signal on CCD.

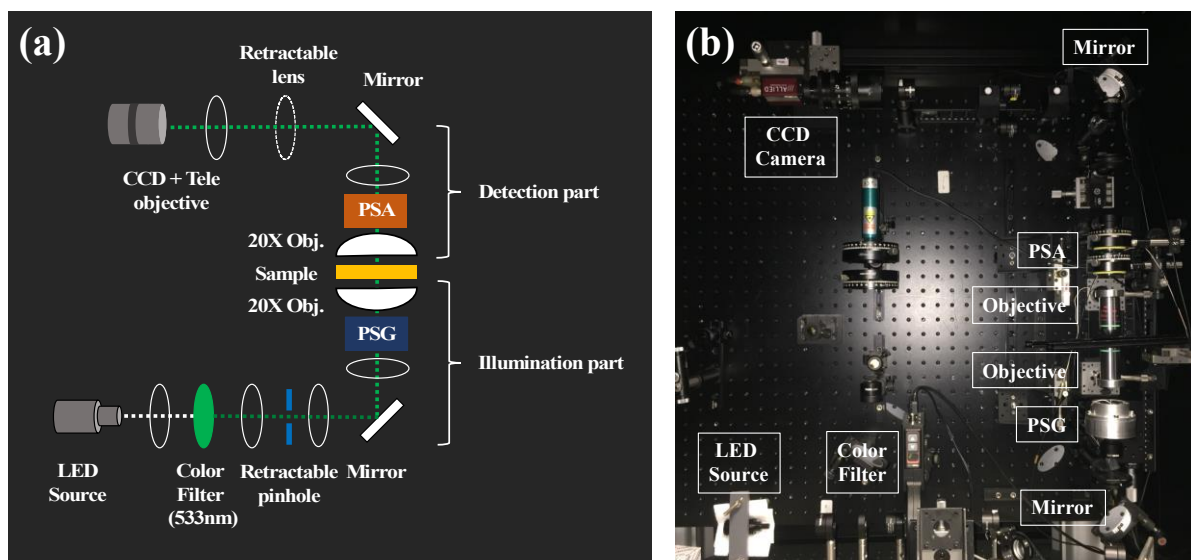


**Figure 2.3** Mueller matrix microscope in transmission configuration: (a) optical layout, (b) photo.

## 2.2.2. Wide-field imaging Mueller polarimeter in reflection configuration

We studied thick sections of the fixed and fresh biological specimens with the multi-spectral wide-field imaging Mueller polarimeter operating in backscattering configuration, which is the most relevant for clinical applications of optical techniques using visible light. The optical layout and photo of the instrument are shown in Fig. 2.4 [19], [24]-[26]. We outline the main characteristics and operational principles of the instrument.

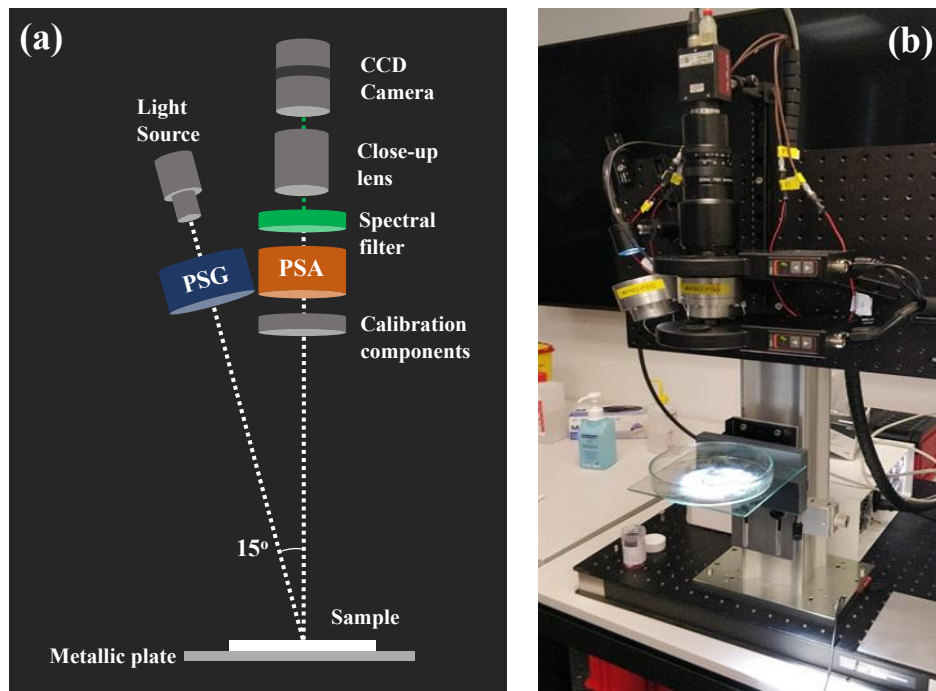


**Figure 2.4** Wide-field imaging Mueller polarimeter (a) schematic optical layout; (b) photo.

A linear polarizer, a first ferroelectric liquid crystal, a quarter wave plate and a second ferroelectric liquid crystal were assembled sequentially for the polarization state generator (PSG) according to the schema shown in Fig (2.2). Another set of the same optical elements assembled in reverse order for the polarization state analyzer (PSA). They were introduced into the illumination and detection arms of a conventional imaging system, respectively. A xenon lamp was used as the incoherent white light source for the sample illumination. Each ferroelectric liquid crystal works as a wave plate with the fixed retardation and fast optical axis orientation switching between  $0^\circ$  and  $45^\circ$ . The PSG modulates the polarization of the incident light beam illuminating the sample at an incidence angle of about  $15^\circ$  and spot size  $\sim 10$  cm along the main ellipse axis. The light backscattered by a sample passes through the PSA before being detected by a CCD camera (Stingray F080B, Allied Vision, Germany,  $512 \times 386$  pixels) with its optical axis placed normal to the sample imaging plane (see Fig. 2.4a). To measure the 16 elements of the Mueller matrix [27], four different polarization states of incident light sequentially generated by the PSG are projected on four polarization

configurations by the PSA. A rotating wheel, placed in front of the PSA, contains reference samples for calibration of the instrument, namely, two polarizers with eigenaxes oriented at  $0^\circ$  and  $90^\circ$  and a wave plate with the optical axis oriented at  $30^\circ$ . The optimal PSG and PSA polarization states are defined by the automated ECM procedure described previously [4].

A rotating wheel, placed behind the PSA, holds the 40 nm bandpass interference filters for performing multi-wavelength measurements from 450 to 700 nm in steps of 50 nm. There are two main reasons for using the broadband filter. First, the intensity of monochromatic normally backscattered light decreases significantly, because light propagation through optically thick biological tissue is dominated by multiple scattering. Using a broadband dichroic filter helps to increase the signal-to-noise ratio of the backscattered signal. Second, the intensities at different wavelengths are summed incoherently, thus erasing the speckle patterns seen when using a coherent light source.

The measurement protocol includes the sequential acquisition of 16 intensity images for four different input and four different output polarization basis states of the PSG and PSA, respectively, at each measurement wavelength. Rapid polarization modulation supported by electrically switchable ferroelectric liquid crystals results in the acquisition of 16 images in a few seconds. Mueller matrix images of a sample are then calculated from the raw intensity measurements at each measurement wavelength [20].

## 2.3 Conclusions

The instrumental principles of Mueller polarimetry were introduced. The optimal design of a complete Mueller polarimetric system was discussed in terms of the minimization of error propagation from the raw intensity data to the elements of the reconstructed Muller matrix of a sample. This can be achieved by selecting an appropriate basis of polarization states for both polarization generation and analysis that should minimize the condition number for both matrices of PSG and PSA. For a complete PSG/PSA, such optimal design corresponds to the basis of four polarization states being the regular tetrahedron vertices on the Poincaré sphere. The theoretical limit on the minimum condition number of a complete Mueller polarimeter is equal to  $\sqrt{3}$ .

The calibration of a complete Mueller polarimeter is also a crucial step for calculating the experimental Mueller matrices from the raw intensity measurements. The eigenvalue calibration method (ECM) that allows obtaining the calibration data without the exact modeling of optical components of both PSG and PSA is presented and discussed.

Two experimental setups that were used for the polarimetric measurements of biological tissue specimens, namely, custom-built multi-wavelength imaging Mueller polarimeters based on the FLCs have been described. Both PSG and PSA consist of two FLCs, one wave plate, and one polarizer. The transmission Mueller microscope was used for the measurements of the thin sections of biological tissue, whereas wide-field imaging Mueller polarimeter operating in reflection configuration was used to measure thick tissue samples.

## References

1. E. Compain and B. Dré villon, “High-frequency modulation of the four states of polarization of light with a single phase modulator” *Rev. Sci. Instrum.*, vol. 69, no. 4, pp. 1574–1580, Oct. 1998.
2. D. H. Goldstein, “Mueller matrix dual-rotating retarder polarimeter”, *Appl. Opt.*, vol. 31, no. 31, pp. 6676–6683, Nov. 1992.
3. O. Arteaga, J. Freudenthal, B. Wang, and B. Kahr, “Mueller matrix polarimetry with four photoelastic modulators: theory and calibration,” *Appl. Opt.*, vol. 51, no. 28, pp. 6805–6817, Oct. 2012.
4. A. D. Martino, Y.-K. Kim, E. Garcia-Caurel, B. Laude, and B. Dré villon, “Optimized Mueller polarimeter with liquid crystals”, *Opt. Lett.*, vol. 28, no. 8, pp. 616–618, Apr. 2003.
5. K. M. Twietmeyer, R. A. Chipman, A. E. Elsner, Y. Zhao, and D. VanNasdale, “Mueller matrix retinal imager with optimized polarization conditions” *Opt. Express*, vol. 16, no. 26, pp. 21339–21354, Dec. 2008.
6. E. Garcia-Caurel, A. De Martino, and B. Dré villon, “Spectroscopic Mueller polarimeter based on liquid crystal devices,” *Thin Solid Films*, vol. 455, pp. 120–123, May 2004.
7. A. Peinado, A. Lizana, and J. Campos, “Optimization and tolerance analysis of a polarimeter with ferroelectric liquid crystals,” *Appl. Opt.*, vol. 52, no. 23, pp. 5748–5757, Aug. 2013.
8. A. Pierangelo, S. Manhas, A. Benali, C. Fallet, J.-L. Totobenazara, M.-R. Antonelli, T. Novikova, B. Gayet, A. De Martino, and P. Validire, “Multispectral Mueller polarimetric imaging detecting residual cancer and cancer regression after neoadjuvant treatment for colorectal carcinomas,” *J. Biomed. Opt.*, vol. 18, no. 4, p. 046014, Apr. 2013.
9. J. Rehbinder, H. Haddad, S. Deby, B. Teig, A. Nazac, T. Novikova, A. Pierangelo, and F. Moreau, “Ex vivo Mueller polarimetric imaging of the uterine cervix: a first statistical evaluation,” *J. Biomed. Opt.*, vol. 21, no. 7, p. 071113, Apr. 2016.
10. J. Vizet, J. Rehbinder, S. Deby, S. Roussel, A. Nazac, R. Soufan, C. Genestie, C. Haie-Meder, H. Fernandez, F. Moreau, and A. Pierangelo, “In vivo imaging of uterine cervix with a Mueller polarimetric colposcope,” *Sci Rep*, vol. 7, no. 1, pp. 1–12, Jun. 2017.
11. A. De Martino, E. Garcia-Caurel, B. Laude, and B. Dré villon, “General methods for optimized design and calibration of Mueller polarimeters,” *Thin Solid Films*, vol. 455, pp. 112–119, May 2004.
12. G. H. Golub, C. Reinsch, “Singular value decomposition and least squares solutions,”

*Numer. Math.*, vol. 14, pp. 403–420, Apr. 1970.

13. J. S. Tyo, “Design of optimal polarimeters: maximization of signal-to-noise ratio and minimization of systematic error,” *Appl. Opt.*, vol. 41, no. 4, pp. 619–630, Feb. 2002.
14. D. S. Sabatke, M. R. Descour, E. L. Dereniak, W. C. Sweatt, S. A. Kemme, and G. S. Phipps, “Optimization of retardance for a complete Stokes polarimeter,” *Opt. Lett.*, vol. 25, no. 11, pp. 802–804, Jun. 2000.
15. D. Layden, M. F. G. Wood, and I. A. Vitkin, “Optimum selection of input polarization states in determining the sample Mueller matrix: a dual photoelastic polarimeter approach,” *Opt. Express*, vol. 20, no. 18, pp. 20466–20481, Aug. 2012.
16. J. S. Tyo, “Noise equalization in Stokes parameter images obtained by use of variable-retardance polarimeters,” *Opt. Lett.*, vol. 25, no. 16, pp. 1198–1200, Aug. 2000.
17. H. Zhang, H. Xiang, and Y. Wei, “Condition numbers for linear systems and Kronecker product linear systems with multiple right-hand sides,” *Int. J. Comput. Math.*, vol. 84, no. 12, pp. 1805–1817, Oct. 2008.
18. B. N. Datta, *Numerical linear algebra and applications*, SIAM, 2010.
19. E. Garcia-Caurel, R. Ossikovski, M. Foldyna, A. Pierangelo, B. Drévilion, and A. De Martino, “Advanced Mueller Ellipsometry Instrumentation and Data Analysis,” in *Ellipsometry at the Nanoscale*, Springer, pp. 31–143, 2013.
20. E. Compain, S. Poirier, and B. Drévilion, “General and self-consistent method for the calibration of polarization modulators, polarimeters, and Mueller-matrix ellipsometers,” *Appl. Opt.*, vol. 38, no. 16, pp. 3490–3502, Jun. 1999.
21. E. Compain and B. Drévilion, “Complete high-frequency measurement of Mueller matrices based on a new coupled-phase modulator,” *Review of Scientific Instruments*, vol. 68, no. 7, pp. 2671–2680, July 1997.
22. A. Lindberg, J. Vizet, J. Rehbinder, C. Gennet, J.-C. Vanel, and A. Pierangelo, “Innovative integrated numerical-experimental method for high-performance multispectral Mueller polarimeters based on ferroelectric liquid crystals,” *Appl. Opt.*, vol. 58, no. 19, pp. 5187–13, 2019.
23. N. Agarwal, J. Yoon, E. Garcia-Caurel, T. Novikova, J.-C. Vanel, A. Pierangelo, A. Bykov, A. Popov, I. Meglinski, and R. Ossikovski, “Spatial evolution of depolarization in homogeneous turbid media within the differential Mueller matrix formalism,” *Opt. Lett.*, vol. 40, no. 23, pp. 5634–5637, Dec. 2015.
24. P. Schucht, H. R. Lee, M. H. Mezouar, E. Hower, A. Raabe, M. Murek, I. Zubak, J. Goldberg, E. Kovari, A. Pierangelo, and T. Novikova, “Wide-Field Mueller Polarimetry of Brain Tissue Sections for Visualization of White Matter Fiber Tracts,” <http://arxiv.org/abs/2005.12440>, 2020

25. P. Schucht, H. R. Lee, M. H. Mezouar, E. Hewer, A. Raabe, M. Murek I. Zubak, J. Goldberg, E. Kövari, A. Pierangelo, T. Novikova, “Visualization of White Matter Fiber Tracts of Brain Tissue Sections with Wide-field Imaging Mueller Polarimetry,” *IEEE Trans. Med. Imaging*, 10.1109/TMI.2020.3018439, 2020
26. N. Ghosh and A. I. Vitkin, “Tissue polarimetry: concepts, challenges, applications, and outlook,” *J. Biomed. Opt.*, vol. 16, no. 11, p. 110801, Nov. 2011.
27. R. M. A. Azzam, N. M. Bashara, and S. S. Ballard, “Ellipsometry and Polarized Light,” *North-Holland: New York, Amsterdam and Oxford, 1977*

# Chapter 3

## Polarimetric Data Post-processing and Modeling

3.1. Image segmentation with statistical DBSCAN algorithm .....	53
3.2. Classification of clustering algorithms .....	54
3.3. DBSCAN clustering algorithm.....	57
3.3.1. Definitions of DBSCAN algorithm .....	57
3.3.2. Original version of DBSCAN algorithm .....	58
3.3.3. Upgraded version of DBSCAN algorithm.....	59
3.3.4. Optimization of the DBSCAN algorithm .....	60
3.3.4.1. <i>Determination of the optimal epsilon value</i> .....	60
3.3.4.2. <i>Comparison between the original and updated versions of the DBSCAN algorithm</i> .....	62
3.4. Modeling of polarized light propagation through biological tissue .....	66
3.4.1. Multiple scattering by spherical particles .....	66
3.4.1.1 <i>Parameters of scattering media</i> .....	67
3.4.1.2. <i>Vector radiative transfer equation</i> .....	71
3.4.2. Monte Carlo algorithm for solution of VRTE in scattering media .....	72
3.4.2.1. <i>Generation of random numbers with given probability distributions</i> .....	73
3.4.2.2. <i>Photon coordinates and trajectories</i> .....	75
3.4.3. Monte Carlo algorithm for anisotropic scattering media.....	80
3.4.3.1. <i>Optical anisotropy of tissue</i> .....	80
3.4.3.2. <i>Validation of the updated Monte Carlo algorithm</i> .....	82
3.5. Conclusions .....	84
References .....	85

In this chapter, we present and discuss a) the algorithm of the post-processing of experimental polarimetric data that was used for a segmentation of polarimetric images and b) the algorithm of polarized Monte Carlo modeling that was used for the interpretation of the polarimetric parameters of biological tissue.

The algorithm of statistical analysis of the large size datasets for the diagnostic segmentation of polarimetric images will be presented first. When the distribution of polarimetric properties of biological tissue in microscopic polarimetric image demonstrates a

significant standard deviation, it can be related to 1) real tissue inhomogeneity caused by the presence of different microstructures (e. g. the diseased zones of tissue or 2) fluctuations of tissue thickness and/or measurement noise. Whereas the former carries important diagnostic information, the latter may affect the accuracy of polarimetric diagnostics and needs to be filtered out. We use the statistical Density-Based Spatial Clustering of Applications with Noise (DBSCAN) method [1] for dataset noise filtering and clustering to reconstruct further the segmented image of tissue. By clustering we denote the unsupervised learning task of an assignment of the “classification labels” to unlabeled data that we will use for the automated analysis of polarimetric images for tissue diagnostics. However, the DBSCAN method is not quite suitable for a dataset of large size ( $n$ ) because its time complexity is  $\mathcal{O}(n^2)$ . To overcome this problem we develop and test a new version of DBSCAN algorithm that runs faster and requires less memory resources.

Light propagating through complex media, such as biological tissues, can be scattered by the material inhomogeneity. The random fluctuations of local refractive index in biological tissue are due to presence of variety of structures and components, like cell organelles, collagen fibers, macromolecules, etc. Tissue scatterers vary in size and shape as well. The scattering process affects both the propagation direction and the polarization of the light beam. Multiple scattering leads to the depolarization of incident polarized light that interacts with biological tissue. The depolarization can be weak for transparent tissues (e.g., cornea, crystalline lens) or strong for a highly scattering tissues (e.g., skin, brain, uterine cervix).

The presence of tissue microstructures (e.g. extracellular matrix of collagen, nerve fibers tracts, etc.) may induce the phase shift between the components of electric field of the polarized light beam (so-called form birefringence), the anisotropy of absorption may be the reason for tissue diattenuation. Thus, measuring and modeling the transformations of polarization state and/or depolarization of probing polarized light beam enables us to link these properties to the anisotropy and microstructure of biological tissue and use them for tissue diagnostics. We introduce vector radiative transfer equation (VRTE) for the description of polarized light propagation through scattering media and describe Monte Carlo (MC) algorithm used for its solution. We also implement and validate the upgraded version of the MC algorithm that accounts for both scattering and optical anisotropy of medium to mimic biological tissue

### 3.1. Image segmentation with statistical DBSCAN algorithm

The polarimetric images of biological tissue samples, obtained by applying the chosen decomposition method of the measured Mueller matrix, demonstrate image contrast between the zones of tissue with a different local microstructure that is not visible in unpolarized intensity images. From this point of view, the Mueller microscopy can assist the histology analysis of tissue by detecting and delineating the zones of interest (e. g. healthy versus pathological) in polarimetric microscopy images. To achieve this goal, a process for

discovering specific patterns in a large number of data sets (so-called data mining or knowledge discovery in databases (KDD)) should be used. It enables us to extract from a dataset the diagnostically relevant information and to transform it into a segmented image with the highlighted spatial structures.

Clustering is one of the main tasks in data mining. As a task of class identification in a multi-dimensional dataset, the clustering organizes a set of objects into groups (called the cluster). The objects in the same group are more similar (according to the chosen criteria) to each other than to those in other clusters. In our studies, we used the algorithm of the density-based spatial clustering of applications with noise (DBSCAN) [1] for the polarimetric dataset clustering and consequent segmentation of the polarimetric images. Our choice was dictated by the capability of the DBSCAN algorithm to eliminate noise from a dataset efficiently, thus, remove “pixels-outliers” from the diagnostic analysis of polarimetric images of tissue.

### 3.2. Classification of clustering algorithms

The clustering algorithms can be classified according to the approach they are using [2]. Hereafter, we briefly recall the partitional, hierarchical, and locality-based groups of clustering approaches used for data processing (see Fig. 3.1) [3].

The partitional clustering performs partitions of a dataset based on cluster centroids, which are pre-defined parameters and represent the center points of each cluster. The hierarchical clustering groups objects sequentially, and the results are presented in a dendrogram. The locality-based clustering is based on the data local relationship and scanned the entire datasets in one pass.

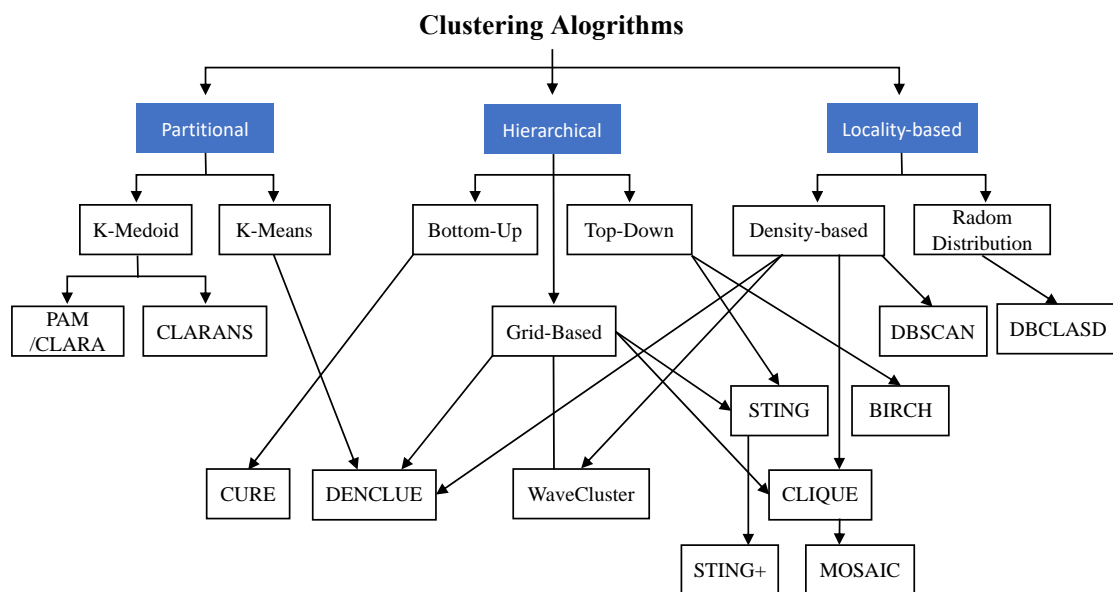


**Figure 3.1** A flowchart represents three groups of clustering approaches (partitional, hierarchical, and locality-based) and corresponding algorithms.

The main principles of clustering algorithms based on these approaches are explained below. The partitional clustering constructs clusters as a single partition of the dataset for a given parameter. The clustering starts with an initial partition of a dataset based on a cluster centroid, pre-defined randomly or manually. The cluster is created by minimizing the sum of the distances between the cluster centroid and each cluster point in a chosen parametric space. Then, clustering will be optimized toward increasing similarity and minimizing cost function (square of the distance between each centroid and objects in a corresponding cluster). The **k**-means clustering and **k**-medoid clustering are both partitional clustering algorithms. The former one uses its “gravity center” as a cluster centroid, whereas the latter uses one of the input datasets points as a cluster centroid (see Fig. 3.2).

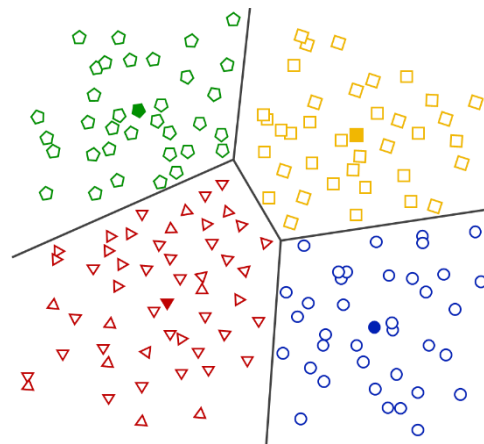


**Figure 3.2** An example of centroid-based clustering of a 2D dataset.

However, this clustering approach has several disadvantages. As the number of clusters has to be defined in advance (an input parameter of the algorithm), this clustering approach may produce an erroneous data partition if pre-defined number of clusters **k** does not match the real number of clusters in a dataset. Being an algorithm based on the variance minimization in the multi-variable space, the algorithm may reach a local optimum depending on the initial partition. To find a global optimum, the partitional clustering is usually run multiple times with different random initializations. This algorithm is very sensitive to the outliers, namely, the data points located relatively far from the majority of dataset points. Moreover, this clustering algorithm cannot correctly detect the clusters of arbitrary shapes.

The hierarchical clustering (or connectivity-based clustering) performs a sequence of partitions connecting objects based on the distance and represents the results by using a dendrogram. There are two types of hierarchical clustering algorithms - agglomerative and divisive. The agglomerative algorithm uses a bottom-up approach by repeating amalgamations of the clusters until the pre-defined threshold is reached (see Fig. 3.3). Contrary to the agglomerative algorithm, the divisive algorithm explores a top-down approach by recursively dividing the clusters at each step.

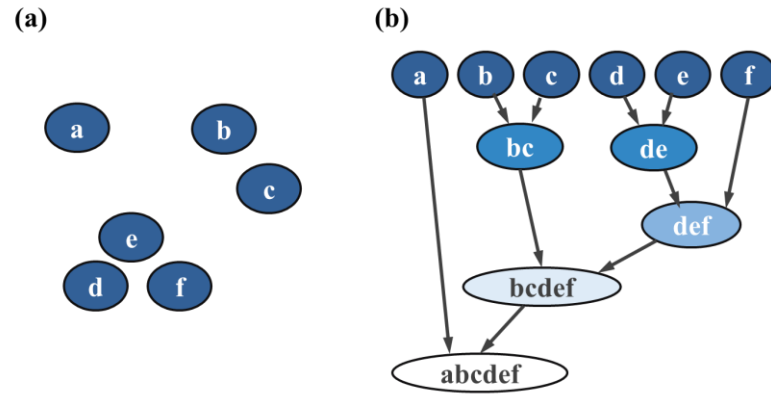


**Figure 3.3** An example of hierarchical agglomerative clustering of a 2D dataset using the Euclidian distance metric: (a) raw data; (b) hierarchical clustering dendrogram.

The hierarchical clustering algorithms are easy to understand. However, the time complexity (parameter that provides an estimation of the execution time in terms of the size of a dataset  $n$ ) of hierarchical clustering  $O(n^3)$  prevents it from using for large dataset clustering, as execution time becomes prohibitively long. The hierarchical clustering is sequential, i. e. at each step the partition of a dataset is based on clustering results of the previous step. If some dataset points were mistakenly allocated to a cluster at early steps, it is impossible to reallocate them during further clustering steps. Since the hierarchical clustering does not have a notion of noise, it is also not robust to the outliers.

Locality-based clustering constructs the clusters based on the local relationships. There are two types of locality-based clustering algorithms - distribution-based and density-based ones. The former approach assumes that dataset is composed of the distributions (e. g. Gaussian distributions). Clusters are defined as dataset points that belong to the same distribution. As distance from distribution center increases, the probability that a data point belongs to this distribution decreases (see Fig. 3.4). When the type of data distribution is not known, one should use a different clustering algorithm.

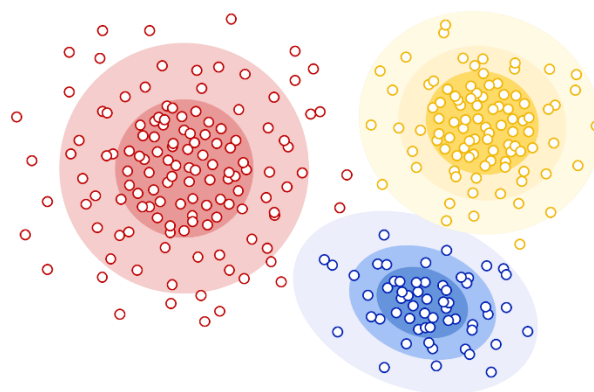


**Figure 3.4** An example of distribution-based clustering of a 2D dataset.

The density-based clustering connects areas of high density into clusters. This allows for arbitrary-shaped clusters as far as dense areas of data can be connected. Density-based clustering algorithm does not require defining the number of clusters as an input parameter. Moreover, by algorithm design the outliers are not assigned to any cluster (see Fig. 3.5) Because of the above mentioned benefits, we chose the density-based clustering algorithm for processing our polarimetric image data.

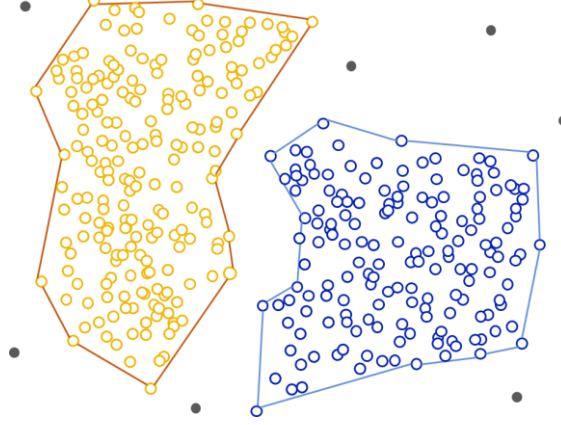


**Figure 3.5** An example of density-based clustering of a 2D dataset. There are two clusters, grey symbols represent data outliers (noise)

### 3.3. DBSCAN clustering algorithm

DBSCAN (Density-Based Spatial Clustering of Applications with Noise), proposed by Ester et al., is one of the popular density-based clustering methods [1], [2]. We will briefly introduce the basics of the DBSCAN algorithm by defining its input parameters, namely, radius  $\epsilon$  (real number) and threshold  $MinPts$  (integer number) as well as the concepts of (directly) density-reachable and density-connected points of a dataset. The procedure of cluster expansion will be explained using the notion of both core and border points.

#### 3.3.1. Definitions of DBSCAN algorithm

**Definition 1.** The  $\epsilon$ -neighborhood of an object  $\mathbf{p} \in \mathbf{D}$  is defined as a subset of objects from  $\mathbf{D}$ :

$$N_{\epsilon}(\mathbf{p}) = \{\mathbf{q} \in \mathbf{D} \mid \mathit{dist}(\mathbf{p}, \mathbf{q}) \leq \epsilon\}, \quad (3.1)$$

where  $\mathit{dist}(\mathbf{p}, \mathbf{q})$  is the distance between two objects  $\mathbf{p} \in \mathbf{D}$  and  $\mathbf{q} \in \mathbf{D}$ .

**Definition 2.** An object  $\mathbf{p} \in \mathbf{D}$  is called a *core object* if  $N_{\epsilon}(\mathbf{p}) \geq MinPts$

**Definition 3.** An object  $\mathbf{q} \in \mathbf{D}$  is *directly-density-reachable* from an object  $\mathbf{p} \in \mathbf{D}$ , if  $\mathbf{q} \in N_{\epsilon}(\mathbf{p})$  and  $\mathbf{p}$  is a core object.

**Definition 4.** An object  $q \in D$  is *density-reachable* from an object  $p \in D$  if there is a sequence of the objects  $\{p_1, p_2, \dots, p_n\}$ ,  $p_1 = p$  and  $p_n = q$ , such that  $p_{i+1}$  is directly density-reachable from  $p_i$  ( $i \in \{1, 2, \dots, n-1\}$ ).

**Definition 5.** An object  $p$  is *density-connected* to an object  $q$ , if there is an object  $t \in D$ , such that both  $p$  and  $q$  are density-reachable from an object  $t$ .

**Definition 6.** A density-based cluster  $C$  is a non-empty subset of  $D$  that obeys following conditions:

1.  $\forall p, q$ : if  $p \in C$  and  $q$  is density-reachable from  $p$ , then  $q \in C$  (maximality).
2.  $\forall p, q$ :  $p$  is density-connected to  $q$  (connectivity).

**Definition 7.** An object  $p$  is *noise* if it does not belong to any clusters.

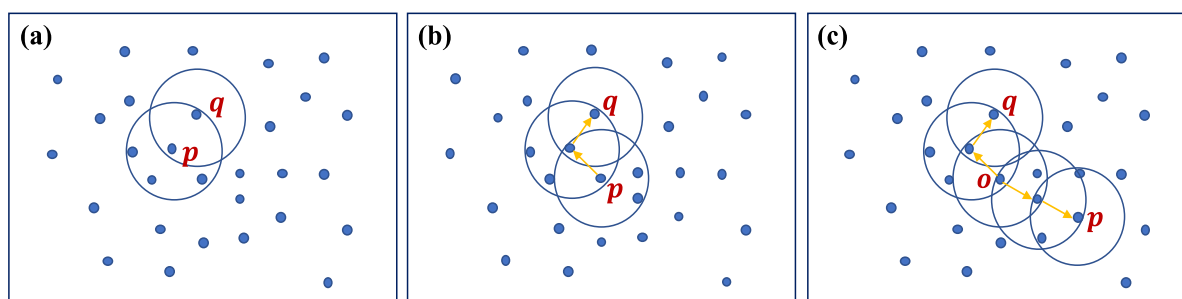


**Figure 3.6** The illustration of cluster generation and expansion in a 2D space ( $MinPts=4$ ) (a)  $p$  is a core point ( $N_\epsilon(p) > MinPts$ ),  $q$  is a border point ( $0 < N_\epsilon(q) < MinPts$ ), and they are directly density-reachable, (b)  $p$  is density-reachable to  $q$ , and (c)  $p$  is density-connected to  $q$ .

### 3.3.2. Original version of DBSCAN algorithm

The DBSCAN algorithm makes use of two input parameters (radius  $\epsilon$  and threshold  $MinPts$ ) to determine the density of a cluster. First, it is necessary to define the values of these two parameters and to create a multi-dimensional dataset that will be used for clustering. After then, the DBSCAN algorithm starts to run at an arbitrary dataset point  $p$ , and searches the points in its  $\epsilon$ -neighborhood. If the number of points in  $\epsilon$ -neighborhood of point  $p$  is larger or equal than  $MinPts$  value, a new cluster will be initiated, and the point  $p$  would be a core point. This cluster will be expanded until all the points that are density-reachable from the core point  $p$  will be assigned to this cluster. The points, located on the edge of a cluster, are called border points. When a cluster cannot be expanded anymore, a new arbitrary point that does not belong to any cluster is selected from a dataset, and the procedure of a new cluster initiation and expansion will be repeated sequentially. If some points were not classified as the core or border points, they are labelled as noise. Finally, the clustering stops when there is no new point that can be added to any cluster [1], [4].

### 3.3.3. Upgraded version of DBSCAN algorithm

Despite the obvious advantages of using the DBSCAN algorithm for data clustering (arbitrary number and shape of clusters, no dependence on data point processing order, detection of noise), this algorithm has difficulty dealing with high-dimensional data. The worst-case running time complexity of each step of the clustering process for a dataset  $D(n)$  ( $n$  is the size of a dataset) is  $\mathcal{O}(n)$  and it can be reduced to  $\mathcal{O}(\log_m n)$  when using a spatial index ( $m$  is the number of entries in  $R^*$ -tree [5]). Then, the time complexity of the DBSCAN algorithm is  $\mathcal{O}(n^2)$  or  $\mathcal{O}(n \log_m n)$ , respectively. Such time complexity and required memory budget become prohibitive for using the DBSCAN algorithm on large size datasets. For example, the segmentation of an image taken with a camera with spatial resolution of  $800 \times 600$  pixels requires clustering of a dataset of 480000 pixels and over 128Gb of RAM. In this respect, the original version of the DBSCAN algorithm is not adapted for the clustering of high-dimensional datasets. Hence, we modified the original DBSCAN algorithm to reduce its execution time and memory budget.

The main computational burden of the DBSCAN algorithm is related to the distance calculations between all dataset points. For a dataset  $D(n)$  of  $n$  objects the size of a dataset of all distances is  $n \times n$ . For the image segmentation problem that was discussed above, the size of dataset of all distances for all image pixels becomes very massive ( $480000 \times 480000$ ), and this distance dataset has to be recall in every steps of clustering (480000 times).

So, at first, we suggest reducing the size of dataset of distance from  $n \times n$  to  $n \times 1$ , which is used in each step of clustering.  $n$  is the size of the datasets. This simple modification can significantly reduce the number of distance calculations, and the impact of this reduction on the execution time increases with the increase of a dataset size. Since the usage of the memory is related to the number of calculations, this method also enables us to calculate the large size of datasets with a relatively less memory budget.

Secondly, we adopted a different strategy for assigning the  $\varepsilon$ -neighborhood points of a given core point to the corresponding cluster depending on whether the  $\varepsilon$ -neighborhood point is a border point or not. The procedure of cluster expansion terminates as one encounters the border points. It can be interpreted in a such way that finding a border point is crucial to delineate the limits of a cluster, whereas all other  $\varepsilon$ -neighborhood points will form a cluster. It is logical to expect that most of the border points are located close to the surface of the sphere of radius  $\varepsilon$  with the center at given core point, as shown in Fig. 3.7 (a). Hence, we make an assumption that all points within an inner sphere defined by a radius  $\varepsilon/r$  ( $1 \leq r \leq \infty$ ) (1) will be automatically assigned to the same cluster as a core point. i.e., when the cluster is formed, the only points where in outside of the inner sphere (red circle in Fig. 3.7 (a)) are considered to classify the cluster. It means that only these points need the computations of the distance, then this method can reduce the total number of the calculations. Furthermore, applying the second modification to the first modification, the size of distance calculation ( $n \times 1$ ) in each step also can be reduced (it depends on the number of points in inner sphere).

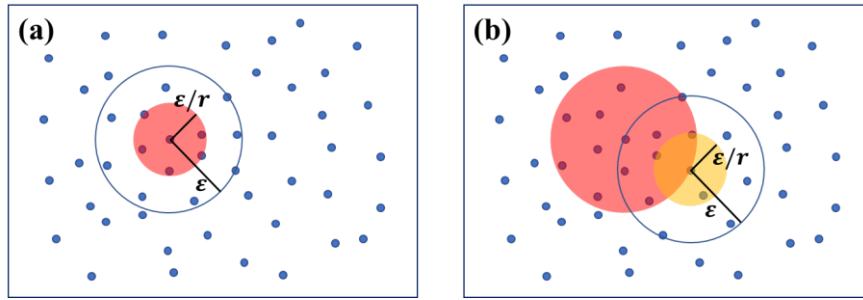


**Figure 3.7** The illustration of the updated version of the DBSCAN clustering algorithm (a) generation of a cluster; if both *MinPts* and  $\epsilon$  criteria are matched, red region (radius  $\epsilon/r$ ) is automatically attributed to the same cluster as the core point, (b) expansion of the cluster; if both *MinPts* and  $\epsilon$  criteria are matched, the points, located in the yellow region, would also be attributed to the same cluster. This expansion process will be repeated until there will be no point to assign to a cluster.

### 3.3.4. Optimization of the DBSCAN algorithm

#### 3.3.4.1. Determination of the optimal epsilon value

Before running the DBSCAN algorithm one needs to create a multi-dimensional dataset and define the values of input parameters, namely, radius  $\epsilon$  (plus scaling factor  $r$  for the updated version of the DBSCAN) and threshold value *MinPts*. Hereafter, we will focus on how to choose the optimal values of the radius  $\epsilon$  and the scaling factor  $r$ . The choice of optimal multi-dimensional space for the segmentation of experimental polarimetric images will be discussed in the Chapter 4.

In the original version of the DBSCAN algorithm, the  $k$ -dist graph was proposed to determine the optimal values of the parameters  $\epsilon$  and *MinPts* [1]. For a given value of the integer parameter  $k$ , we calculate the distance (called  $k$ -dist) from each dataset point to its  $k$ -th nearest neighbor. In other words, we define the function that maps our dataset  $D$  to a set of real values. When the value of  $\epsilon$  is set to be equal to  $k$ -dist value for a selected dataset point, the number of points within the sphere of radius  $\epsilon$  and with center at this selected dataset point will be more or equal to  $k+1$ . If we plot the values of the  $k$ -dist parameter in the descending order for all dataset points (so called sorted  $k$ -dist graph), the optimal value of  $\epsilon$  will correspond to the kink in the  $k$ -dist graph (see Fig. 3.8).

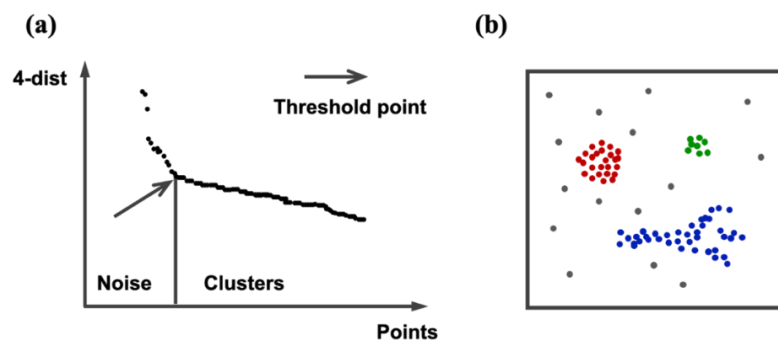


**Figure 3.8** (a) Example of sorted 4-dist plot for a 2D dataset shown in panel (b). Adapted from [1].

In the original DBSCAN algorithm, the value of  $k$  was fixed at 4 for any clustering process of a 2D dataset, because the experiments did not show significant difference in clustering results for  $k > 4$ . Hence, the value of  $\text{MinPts}$  was set to 4 for clustering of any 2D dataset. However, this method is not adapted for the datasets of large size, as the calculation for the sorted 4-th dist plot will take too much time. Moreover, the value of 4 is too small for clustering of our experimental large size datasets as there are many similar data represented by the points located at the same distance from a core point. Using a threshold value of  $\text{MinPts}=4$  all dataset points will be assigned either to noise or to one cluster only depending on the value of  $\epsilon$ . To solve these problems, we modified the original method to determine the optimal values of input parameters much faster.

To illustrate the main steps of the modified algorithm we created a dataset by selecting the values of all pixels in the experimental polarimetric images of a thin section of human skin model to generate a dataset of 480000 points (see Chapter 4 for the details). The procedure of the determination of the optimal values of DBSCAN input parameters is described below.

1. Random and uniform sampling of the original large size dataset to generate a dataset of a smaller size (e.g., 10000, 20000, 30000, and 40000 points).
2. Calculation of all distances between each pair of points for a small size dataset.
3. Finding the maximum value of distance  $d^{max}$  for a small size dataset.
4. Calculation of the total number of  $\epsilon$ -neighborhood points for all dataset points for varying values of radius  $\epsilon \in [0, d^{max}]$ . The radius increased with a step of 0.1.
5. Plotting the total number of  $\epsilon$ -neighborhood points versus radius  $\epsilon$ .
6. Determination of the optimal value of  $\epsilon$  as the value of x-intercept of the linear regression curve fit of the total number of  $\epsilon$ -neighborhood points corresponding to the fast growing part of a plot (see Fig. 3.9).

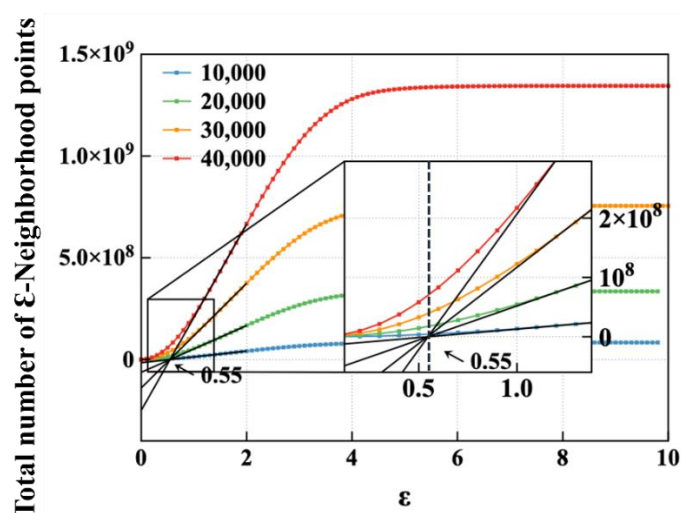


**Figure 3.9** Blue, green, orange, and red lines show the results for the datasets of different size - 10000, 20000, 30000, and 40000 points, respectively. These datasets were created by random and uniform sampling of the complete dataset of 480000 points. The linear regression curves have very close x-intercept values for all datasets (see inset).

Rapid increase in total number of  $\epsilon$ -neighborhood points with radius  $\epsilon$  reflects the increase in number of the (directly) density-reachable and density-connected points (see Fig. 3.9). For the values of radius  $\epsilon$  smaller than x-intercept value the total number of  $\epsilon$ -neighborhood points is mainly defined by the contribution of the directly density-reachable points, whereas the contribution of the density-connected points becomes dominant for the values of radius  $\epsilon$  larger than x-intercept value, i.e. the x-intercept value for radius  $\epsilon$  corresponds to the transition from the directly density-reachable clustering regime to the density-connected one. For this reason, we consider the x-intercept value as the optimal value of radius  $\epsilon$ . In practice, this value can be slightly affected by the presence of density-reachable points. However, the values of x-intercept for different plots corresponding to 4 datasets of different size (10000, 20000, 30000, and 40000 points) are very close to 0.55 (see the inset of Fig. 3.9). Therefore, with high degree of certainty an optimal value of radius  $\epsilon$  can be defined from a small size sampling dataset (e.g. 10000 or 20000). Consequently, it will significantly reduce the computational time.

### 3.3.4.2. Comparison between the original and updated versions of the DBSCAN algorithm

As was previously mentioned, the original version DBSCAN is not applicable for large size datasets because of prohibitive execution time and computer memory budget. We developed an updated version of the DBSCAN algorithm to reduce the time complexity of clustering.

To check the efficiency of the updated version of the DBSCAN algorithm we used a large size experimental dataset described in the previous section and performed a random uniform sampling to create the datasets of different smaller size (10000, 20000, 30000, 40000, 50000, 60000, 70000, 80000, 90000, 100000, 150000, and 200000 points). The values of radius  $\epsilon$  and threshold MinPts were fixed at 0.3 and 250, respectively. For an updated version of the DBSCAN algorithm, the scaling value  $r$  was equal to 2. The execution time for both original and updated versions of the DBSCAN clustering algorithm is shown in Fig 3.10 and Tab. 3.1.

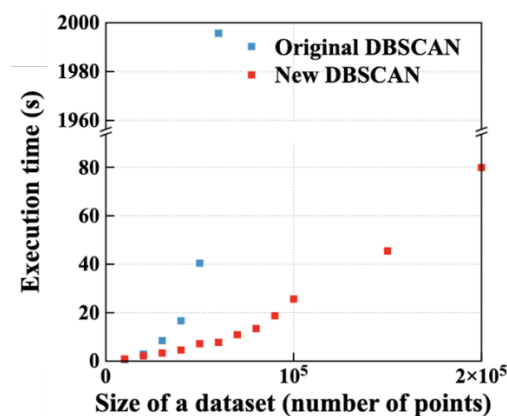


**Figure 3.10** The execution time versus the size of a dataset. Blue dots - original version of the DBSCAN algorithm, red dots - updated version of the DBSCAN algorithm. The disconnection between the values of 80 and 1960 are shown by the break of vertical axis.

**Table 3.1** The execution time (s) for different sizes of a dataset (Original vs Updated DBSCAN).

<b># of data</b>	<b>10000</b>	<b>20000</b>	<b>30000</b>	<b>40000</b>	<b>50000</b>	<b>60000</b>
<b>Original</b>	0.6	2.9	8.5	16.7	40.4	1995.7
<b>Updated</b>	0.9	2.2	3.3	4.6	7.2	7.7
<b># of data</b>	<b>70000</b>	<b>80000</b>	<b>90000</b>	<b>100000</b>	<b>150000</b>	<b>200000</b>
<b>Original</b>	X	X	X	X	X	X
<b>Updated</b>	10.9	13.4	18.7	25.6	45.5	79.9

For a relatively small size of a database (e.g., 10000 points), the original version of the DBSCAN algorithm performs clustering faster than the updated version of the DBSCAN. However, the execution time for both versions of the algorithm is less than 1 second. With the increase of a dataset size the execution time for the updated version of the DBSCAN algorithm becomes significantly shorter compared to that of the original version of the DBSCAN. For example, the execution time for the original version of the DBSCAN for a dataset containing 60000 points is about half an hour (1995.7 seconds) compared to 7.7 seconds for the updated version of DBSCAN algorithm. Moreover, the memory budget for the original version of the DBSCAN used for clustering of a dataset containing 60000 points almost reached the maximum limit of 32Gb RAM available on our computer, meaning that we cannot perform clustering of the larger size datasets with the original version of the DBSCAN. Contrary to that the updated version of the DBSCAN algorithm effectively performs clustering of all datasets. For example, the execution time for clustering of a dataset containing 150000 points takes 45 seconds only with the updated version of the DBSCAN algorithm, which is close to the execution time for the original DBSCAN algorithm used for clustering of a smaller dataset containing 50000 points.

To check the dependence of the execution time on radius  $\epsilon$ , we varied the values of  $\epsilon$  from 0.05 to 7 and performed clustering of a dataset containing 40000 points with both original and updated versions of the DBSCAN algorithms. The value of parameter MinPts was equal to 250 for both versions of the DBSCAN algorithm, the scaling parameter  $r$  was equal to 2 for the updated version of the DBSCAN. The results are shown in Fig. 3.11 and Tab. 3.2.

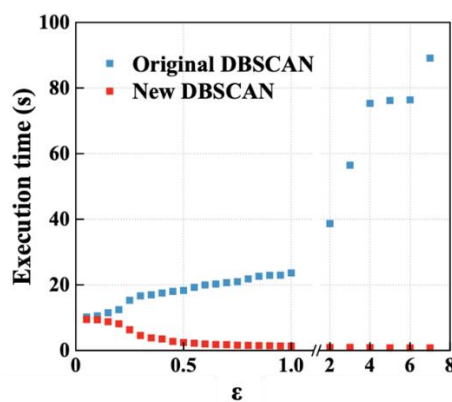


**Figure 3.11** The execution time versus radius  $\epsilon$  for a dataset containing 40000 points. Blue dots - the results for the original version of the DBSCAN algorithm, red dots - the results of the updated version of the DBSCAN algorithm. The disconnection between the values of 1 and 2 on the horizontal axis is shown with the axis-break.

**Table 3.2** The execution time (s) for different values of radius  $\epsilon$  (Original vs Updated DBSCAN).

<b>Epsilon (<math>\epsilon</math>)</b>	<b>0.05</b>	<b>0.1</b>	<b>0.15</b>	<b>0.2</b>	<b>0.25</b>	<b>0.3</b>	<b>0.35</b>
<b>Original</b>	10.2	10.5	11.5	12.5	15.3	16.7	17.0
<b>New</b>	9.4	9.4	8.8	8.1	6.3	4.6	3.8
<b>Epsilon (<math>\epsilon</math>)</b>	<b>0.4</b>	<b>0.45</b>	<b>0.5</b>	<b>0.55</b>	<b>0.6</b>	<b>0.65</b>	<b>0.7</b>
<b>Original</b>	17.5	18.0	18.3	19.3	20.0	20.3	20.7
<b>New</b>	3.5	2.7	2.4	2.2	2.0	1.8	1.8
<b>Epsilon (<math>\epsilon</math>)</b>	<b>0.75</b>	<b>0.8</b>	<b>0.85</b>	<b>0.9</b>	<b>0.95</b>	<b>1</b>	<b>2</b>
<b>Original</b>	21.0	21.8	22.6	22.9	22.9	23.6	38.7
<b>New</b>	1.6	1.5	1.5	1.4	1.4	1.3	1.0
<b>Epsilon (<math>\epsilon</math>)</b>	<b>3</b>	<b>4</b>	<b>5</b>	<b>6</b>	<b>7</b>		
<b>Original</b>	56.5	75.3	76.2	76.4	89.1		
<b>New</b>	0.9	0.9	0.8	0.8	0.8		

In the original version of the DBSCAN algorithm, the increase of radius  $\epsilon$  leads to the increase of time for  $\epsilon$ -neighborhood calculations. As expected, the execution time for the original DBSCAN algorithm increases from 10 to 90 seconds as the value of radius  $\epsilon$  changes from 0.05 to 7 (see Fig. 3.11 and Tab. 3.2). On the contrary, the execution time for the updated version of the DBSCAN algorithm decreases with the increase of radius  $\epsilon$ . The amount of automatically assigned points increases with the radius  $\epsilon/r$  increase of inner sphere. Consequently, the total number of distance calculations is reduced, and it also leads to the reduction of the execution time.

The dependence of the execution time on threshold parameter MinPts is shown in Fig. 3.12 and Tab. 3.3. The values of radius  $\epsilon$  and size of a dataset were fixed at 0.3 and 40000, respectively. For the updated version of the DBSCAN algorithm, the scaling parameter  $r$  was equal to 2.

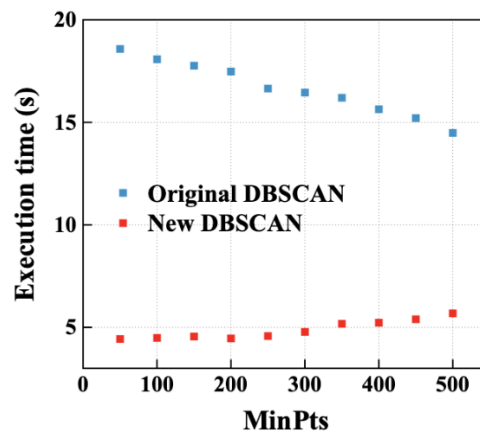


**Figure 3.12** The execution time versus threshold parameter MinPts, Blue dots – the results of the original version, red dots - the results of the updated version of the DBSCAN algorithm.

**Table 3.3** The execution time (s) for different values of the threshold parameter MinPts (Original vs Updated DBSCAN).

<b>MinPts</b>	<b>50</b>	<b>100</b>	<b>150</b>	<b>200</b>	<b>250</b>	<b>300</b>
<b>Original</b>	18.6	18.1	17.8	17.5	16.7	16.5
<b>New</b>	4.4	4.5	4.6	4.5	4.6	4.8

MinPts	350	400	450	500
Original	16.2	15.6	15.2	14.5
New	5.2	5.2	5.4	5.7

The execution time of the original version of the DBSCAN algorithm decreases with MinPts increase (see Fig. 3.12). It reflects the fact that the number of core points decreases with MinPts increase. i.e., most of the points are classified as noise, and the process of cluster expansion does not work properly despite a short execution time. The execution time of the updated version of the DBSCAN algorithm increases slightly with MinPts increase. Similar to the original version of the DBSCAN algorithm, the number of points, classified as noise, increases with MinPts increase for the updated version of the DBSCAN. However, the execution time of the latter also depends on the number of points within inner sphere. These points are automatically assigned to a cluster and it reduces the execution time.

Finally, we studied the dependence of the execution time on the scaling factor  $r$ . The parameter  $1/r$  was varied from 0 to 0.9 with a step of 0.1. The radius  $\epsilon$  and threshold MinPts values were fixed at 0.3 and 250, respectively. The size of a dataset was 40000. The results are shown in Fig. 3.13 and Tab. 3.4.

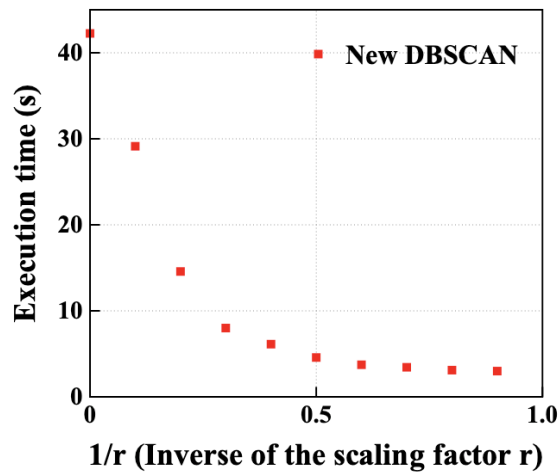


**Figure 3.13** The execution time versus the inverse of scaling factor  $r$ . The results are shown for the updated version of the DBSCAN algorithm.

**Table 3.4** The execution time (s) for the different values of  $1/r$  (Original vs Updated DBSCAN)

$1/r$	<b>0.00</b>	<b>0.10</b>	<b>0.20</b>	<b>0.30</b>	<b>0.40</b>	<b>0.50</b>
New	42.3	29.1	14.6	8.0	6.1	4.6
$1/r$	<b>0.60</b>	<b>0.70</b>	<b>0.80</b>	<b>0.90</b>		
New	3.7	3.4	3.1	3.0		

By choosing the scaling factor  $r$  we divided the volume of a sphere  $S_\epsilon(p)$  of radius  $\epsilon$  and center at a core point  $p$  into two regions: an inner sphere  $S_{\epsilon/r}(p)$  of radius  $\epsilon/r$  with the same center and the outer shell  $S_\epsilon(p) - S_{\epsilon/r}(p)$ . All dataset points that belong to an inner sphere  $S_{\epsilon/r}(p)$  are automatically assigned to the cluster formed by a core point  $p$  by the updated

version of DBSCAN algorithm. The inverse of the scaling factor  $r$  defines the border between two regions. When the value of  $r \rightarrow \infty$  the corresponding value of  $1/r \rightarrow 0$ , and the updated version of DBSCAN performs clustering the same way as the original version of the DBSCAN algorithm with no reduction of the execution time. When the value of  $1/r \approx 1$ , almost all points within a sphere  $S_\varepsilon(p)$  are located within an inner sphere  $S_{\varepsilon/r}(p)$  as well. Hence, they are automatically assigned to the cluster of a core point  $p$  thus, reducing significantly the execution time of the updated version of the DBSCAN algorithm (see Fig. 3.13).

## 3.4. Modeling of polarized light propagation through biological tissue

### 3.4.1. Multiple scattering by spherical particles

It was demonstrated that an analytical solution to the problem of scattering of plane electromagnetic (EM) wave by single dielectric spherical scatterer exists [6] and many asymptotic approximations of this solution are well studied [7]. Contrary to that EM wave scattering by a very large random group of particles occupying a volume in space is a problem of enormous complexity. The individual scattering field created by a single particle in response to the scattered field of other particles can be comparable with the field created in response to the incident field. This means that single scattering approach is no longer valid. To solve the problem of multiple scattering numerically we assume [8].

1. Each particle and a detector are located in the far field zones of all other scattering particles. Thus, a spherical wave created by a single scatterer in response to the incident plane wave can also be considered as a plane wave when it reaches the next particle. At least, the mean distance between the scatterers has to be much larger than their radius and wavelength.
2. At any space point the total electric field can be represented as sum of contributions from light-scattering paths going through all possible particles sequences. All paths going through the same particle more than once can be neglected (Twersky approximation, see Fig. 3.14(b)) [9]. This assumption is justified when the total number of scattering particles in a volume is very large.
3. Full ergodicity of the system, i.e. the time-averaging of random object can be replaced by ensemble averaging (over position and state of the object).
4. Position and state of each particle are independent of each other and of positions and states of all other particles. Spatial distribution of particles in a host medium is random.

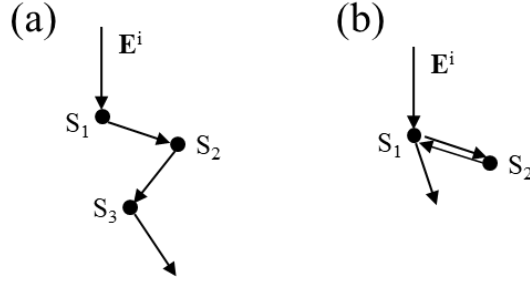


**Figure 3.14** (a) Triple scattering, self-avoiding path, (b) triple scattering, a path goes through particle  $S_1$  twice.

Any interference effects among scattered waves emerging at the same point of the sample surface but with different paths are neglected for real space imaging. Only intensities of individual emerging waves are summed and not their fields. It means that speckles, which are normally seen in the light scattered by a static sample illuminated with spatially and temporally coherent light, are not considered.

### 3.4.1.1 Parameters of scattering media

**Mean free path.** We consider a homogeneous host medium with a refractive index  $n_m$  that contains identical spherical scatterers distributed randomly and uniformly within host medium. Light beam passes through a scattering non-absorbing medium in  $z$  direction. We indicate by  $N_s$  the number of scatterers per unit volume (i.e. scatterer number density). An average number of scatterers  $N$  found in a slice of thickness  $dz$  and unit area illuminated by a light beam:

$$N = N_s dz \quad (3.2)$$

Using the definition of particle scattering cross-section  $C_s$  [6] and denoting by  $I(z)$ , the intensity of the light at the depth  $z$ , we obtain the following relations:

$$I(z + \Delta z) = I(z) - I N_s C_s dz \quad (3.3)$$

$$\frac{dI}{dz} = -\mu_s I \Rightarrow I(z) = I_0 \exp(-\mu_s z) \quad (3.4)$$

where  $\mu_s = N_s C_s$  is the scattering coefficient of medium. It is measured in inverse length ( $\text{cm}^{-1}$ ) units. Hence, we can define the scattering mean free path  $l_s$  as

$$l_s = \frac{1}{\mu_s} \quad (3.5)$$

Parameter  $l_s$  provides the mean distance between two successive scattering events. From Eq. (3.4), it follows that  $\mu_s$  characterizes the extinction of incident beam because of the scattering. For a polydisperse scattering media (populations of scatterers of different size), Eqs (3.4) and (3.5) can be generalized as

$$\mu_s = \sum_i \mu_s^i = \sum_i N_s^i C_s^i \quad (3.6)$$

When both scatterings by particles and absorption by a homogenous medium are combined, the extinction of the incident beam will still have an exponential dependence on distance  $z$ , whereas the extinction parameter is defined as

$$\mu_e = \mu_a + \mu_s \quad (3.7)$$

where  $\mu_a$  is the absorption coefficient of a host medium.

**Scattering matrix.** The perpendicular and parallel components of the incident and scattered wave obey the following relation [6]:

$$\begin{bmatrix} E_{\parallel}^s \\ E_{\perp}^s \end{bmatrix} = \frac{\exp(jkn_m(z-r))}{jkn_m r} \begin{bmatrix} S_2(\theta) & 0 \\ 0 & S_1(\theta) \end{bmatrix} \begin{bmatrix} E_{\parallel}^0 \\ E_{\perp}^0 \end{bmatrix} \quad (3.8)$$

where the complex amplitude functions  $S_1$  and  $S_2$  are defined as:

$$S_1(\theta) = \sum_n \frac{2n+1}{n(n+1)} (a_n \pi_n(\cos \theta) + b_n \tau_n(\cos \theta)) \quad (3.9a)$$

$$S_2(\theta) = \sum_n \frac{2n+1}{n(n+1)} (a_n \tau_n(\cos \theta) + b_n \pi_n(\cos \theta)) \quad (3.9b)$$

$$\pi_n(\cos \theta) = \frac{P_n^1(\cos \theta)}{\sin \theta}, \quad \tau_n(\cos \theta) = \frac{P_n^1(\cos \theta)}{d\theta}, \quad P_n^1 = -\frac{dP_n}{d\theta} \quad (3.9c)$$

$P_n^m(\cos \theta)$  are Legendre functions of the first kind of degree  $n$  and order  $m$  ( $n = m, m+1, \dots$ ). Coefficients  $a_n$  and  $b_n$ : are calculated as

$$a_n = \frac{\psi'_n(mx)\psi_n(x) - m\psi'_n(x)\psi_n(mx)}{\psi'_n(mx)\xi_n(x) - m\xi'_n(x)\psi_n(mx)} \quad (3.10a)$$

$$b_n = \frac{m\psi'_n(mx)\psi_n(x) - \psi'_n(x)\psi_n(mx)}{m\psi'_n(mx)\xi_n(x) - \xi'_n(x)\psi_n(mx)} \quad (3.10b)$$

$$\psi_n(\rho) = \rho j_n(\rho), \quad \xi_n(\rho) = \rho h_n^{(2)}(\rho) \quad (3.10c)$$

where  $j_n(\rho)$  is a spherical Bessel function,  $h_n^{(2)}(\rho)$  is a spherical Hankel function,  $x = kn_m a$  is a size parameter,  $k = \omega\sqrt{\mu_0\varepsilon_0} = \omega/c = 2\pi/\lambda$  is a wavenumber in a vacuum,  $a$  – radius of spherical particle,  $n_p$  is a refractive index of a particle,  $m$  is the relative index contrast ( $m = n_p/n_m$ ).

In general, even for linearly polarized incident light, the scattered light is elliptically polarized because both  $S_1(\theta)$  and  $S_2(\theta)$  are complex numbers with different phases. The relation between the Stokes parameters of the incident and scattered wave follows from Eq. (3.8).

$$\begin{bmatrix} I^s \\ Q^s \\ U^s \\ V^s \end{bmatrix} = \frac{1}{k^2 n_m^2 r^2} \begin{bmatrix} m_{00} & m_{01} & 0 & 0 \\ m_{01} & m_{11} & 0 & 0 \\ 0 & 0 & m_{22} & m_{23} \\ 0 & 0 & -m_{23} & m_{33} \end{bmatrix} \begin{bmatrix} I^i \\ Q^i \\ U^i \\ V^i \end{bmatrix} \quad (3.11a)$$

$$m_{00} = \frac{1}{2} (|S_2|^2 + |S_1|^2), \quad m_{01} = \frac{1}{2} (|S_2|^2 - |S_1|^2) \quad (3.11b)$$

$$m_{22} = \frac{1}{2} (S_2^* S_1 + S_2 S_1^*), \quad m_{23} = \frac{1}{2} (S_2^* S_1 - S_2 S_1^*) \quad (3.11c)$$

Not all coefficients are linearly independent:

$$m_{00}^2 = m_{11}^2 + m_{22}^2 + m_{33}^2 \quad (3.11d)$$

**Scattering anisotropy.** The parameters  $\mu_a$  and  $\mu_s$  describe the attenuation of incident beam propagating through media. However, the scattering by particle may also change the angular distribution of the light intensity. To quantify this scattering anisotropy, we first consider the scattering of unpolarized light by a single spherical particle. Let us introduce the phase function  $p(\theta)$ , which is the probability of incident wave to be scattered in the solid angle  $d\Omega = 2\pi \sin \theta d\theta$ . This solid angle contains all directions with polar angle varying within the interval  $[\theta, \theta + \Delta\theta]$ . The phase function is the probability distribution function, hence, for a non-absorbing medium:

$$\int_{4\pi} p(\theta) d\Omega = \int_0^\pi p(\theta) 2\pi \sin \theta d\theta = 1 \quad (3.12)$$

The total intensity  $I^s$  scattered in  $\theta$  direction and distance  $r$  from the light source can be expressed via the complex amplitude functions  $S_1$  and  $S_2$  of the transverse electric field components, and the intensity  $I^o$  of unpolarized incident beam can be expressed as

$$I^s(\theta) = \frac{1}{2} (I_{||}^s + I_{\perp}^s) = \frac{|S_1(\theta)|^2 + |S_2(\theta)|^2}{2k^2 n_m^2 r^2} I^o \quad (3.13)$$

The energy flux  $F(\theta)$  in solid angle  $d\Omega$  can be written as

$$F(\theta) = I_s(\theta) r^2 d\Omega = C_s I^o p(\theta) d\Omega \quad (3.14)$$

Combining Eqs (3.13) and (3.14) we obtain the expression for the phase function

$$p(\theta) = \frac{|S_1(\theta)|^2 + |S_2(\theta)|^2}{4\pi k^2 n_m^2} \quad (3.15)$$

The average cosine of the scattering angle, called asymmetry parameter  $g$ , is given by

$$g = \langle \cos \theta \rangle = \int_0^\pi \cos \theta [p(\theta) 2\pi \sin \theta] d\theta \quad (3.16)$$

The relation  $-1 \leq g \leq 1$  always holds. The values of anisotropy parameter  $g$  for some special scattering regimes are listed below:

- isotropic scattering (Rayleigh scattering),  $g = 0$ ;
- forward scattering ( $\theta = 0^\circ$ ),  $g = 1$ ;
- backward scattering ( $\theta = 180^\circ$ )  $g = -1$ .

For the majority of biological tissues the value of  $g$  varies from 0.6 to 0.99 [10]. Several analytical approximations for phase functions  $p(\theta)$  have been proposed. The most widely used is the Henyey-Greenstein function defined as:

$$p(\theta) = \frac{1}{4\pi} \frac{1 - g^2}{[1 + g^2 - 2g \cos(\theta)]^{3/2}} \quad (3.17)$$

Henyey-Greenstein function ranges from backscattering through isotropic scattering to forward scattering by the variation of anisotropy parameter ( $-1 \leq g \leq 1$ ).

**Transport mean free path**  $l'_s$  is defined for the media composed of anisotropically scattering particles with  $g > 0$ :

$$l'_s = \frac{l_s}{(1 - g)} \quad (3.18)$$

Parameter  $l'_s$  is the mean distance required for scattered light to deviate significantly from the direction of the incident beam. When  $g \approx 1$  ( $\theta \approx 0^\circ \Rightarrow$  forward scattering regime), scattered wave slightly deviated from the direction of incident wave. Many scattering events, and consequently, longer distance  $l'_s \gg l_s$ , traveled through the medium will be needed to

reach a significant deviation. When  $g \approx 0$  (scattering is close to isotropic), the transport mean free path become comparable with the mean free path  $l'_s \approx l_s$ .

**Optical albedo**  $\varpi$  of both scattering and absorbing medium is defined as a ratio of scattering and total extinction coefficients:

$$\varpi = \frac{\mu_s}{\mu_s + \mu_a}, \quad 0 \leq \varpi \leq 1 \quad (3.19)$$

In an absorbing medium the norm of the phase function (see Eq. (3.12)) is modified as

$$\int_{4\pi} p(\theta) d\Omega = \varpi \quad (3.20)$$

### 3.4.1.2. Vector radiative transfer equation

The radiative transfer theory (RTT) is a phenomenological approach describing the transport of energy in the medium composed of a variety of discrete and randomly distributed particles. In the framework of vector RTT, the interaction of a polarized light beam with a scattering medium can be described by the solution of an integro-differential vector radiative transfer equation (VRTE), that describes the energy conservation law:

$$\begin{aligned} & \frac{1}{v} \frac{\partial \mathbf{L}(\mathbf{r}, \hat{\mathbf{\Omega}}, t)}{\partial t} + \hat{\mathbf{\Omega}} \nabla \mathbf{L}(\mathbf{r}, \hat{\mathbf{\Omega}}, t) \\ & = \int_{\Omega'} \mu_s \mathbf{P}(\hat{\mathbf{\Omega}}' \rightarrow \hat{\mathbf{\Omega}}) \mathbf{L}(\mathbf{r}, \hat{\mathbf{\Omega}}', t) d\Omega' + \Sigma(\mathbf{r}, \hat{\mathbf{\Omega}}, t) - \mu_e \mathbf{L}(\mathbf{r}, \hat{\mathbf{\Omega}}, t) \end{aligned} \quad (3.21)$$

where  $\mathbf{r}$  describes the position within the scattering medium,  $t$  - time,  $\mathbf{L}$  - vectorial radiance that is composed of the components of Stokes vector,  $\hat{\mathbf{\Omega}}$  is the unit vector of direction,  $v = c/n_m$  is the speed of light propagation within the medium. The phase function  $\mathbf{P}(\hat{\mathbf{\Omega}}' \rightarrow \hat{\mathbf{\Omega}})$  is an angular dependent  $4 \times 4$  real matrix that also depends on input vectorial radiance  $\mathbf{L}$  because of normalization conditions. Both scattering and absorption coefficients are considered as constant in terms of time.

The propagation of light directed into the solid angle  $d\Omega$  leads to the variation of  $\mathbf{L}$ . The attenuation of light due to the absorption and scattering is characterized by the extinction coefficient  $\mu_e$ . The light beams can be deflected from their initial directions  $\hat{\mathbf{\Omega}}'$  and scattered into solid angle  $d\Omega$ , thus changing  $\mathbf{L}$ . The presence of the internal sources (if any) continuously distributed within the volume and characterized by their radiance  $\Sigma(\mathbf{r}, \hat{\mathbf{\Omega}}, t)$  will also change the vectorial radiance  $\mathbf{L}$ . Eq. (3.21) is a linear first order partial integro-differential equation. It can be converted into an integral equation by the method of characteristics [11]. If there is only an external source of photons, the VRTE can be reformulated as

$$\mathbf{L} = \mathbf{KL} + \mathbf{Q}' \quad (3.22a)$$

where  $\mathbf{K}$  is integral operator. We consider the solution of Eq. (3.22a) obtained by iterations:

$$\mathbf{L}_0 = \mathbf{Q}' \quad (3.22b)$$

$$\mathbf{L}_1 = \mathbf{KL}_0 \quad (3.22c)$$

$$\mathbf{L}_{n+1} = \mathbf{KL}_n \quad (3.22d)$$

It can be shown that at certain conditions on  $\mathbf{K}$  and  $\mathbf{Q}'$ , this iterative process converges to the solution of Eq. (3.21). The estimation of the integral of collision  $\mathbf{K}$  will be performed by the Monte Carlo technique, presented in the next section.

### 3.4.2. Monte Carlo algorithm for solution of VRTE in scattering media

For any application the Monte Carlo method requires a stochastic model where the mean values of certain random variables are the values of the physical properties (in our case, the Mueller matrix coefficients of the scattering medium) to be determined by means of the numerical calculation [12]. These mean values are calculated by averaging over the multiple series of independent samples.

To solve the vector RTE in turbid media with Monte Carlo technique one needs to simulate the random walk of incident “photon packages” within the scattering and absorbing media before being detected. This approach is particularly appropriate for the modeling of real optical experiments with complex geometry (optical interfaces of arbitrary shape, various configurations for signal detection), and samples combined of different optical materials (scattering, absorbing, having different optical refractive indices, etc.).

The drawback of using Monte Carlo method for the solution of radiative transport problem is its high computational cost. As the technique is not deterministic, we have to estimate the variance of the quantities of interest – Mueller matrix coefficients of the sample. When the calculated standard deviation is below the defined threshold (obviously, its value influences the accuracy of the final results) the calculations are stopped. As it follows from the central limit theorem, the Mueller matrix coefficients are within  $\pm 3\%$  of the mean values with 95% confidence when the variance threshold is set at 1.5%. The decreases of standard variance and standard deviation are proportional to  $1/n$  and  $1/\sqrt{n}$ , respectively, where  $n$  is the number of simulated photon trajectories. However, the time complexity of Monte Carlo method for the solution of radiative transport problem can be addressed by the algorithm parallelization. Each photon’s trajectory is calculated independently, so the algorithm can be accelerated significantly by using its GPU-based implementation.

The propagation of polarized wave through scattering media has been studied by many groups, particularly from atmospheric optics, astronomy, and oceanography communities.

Kattawar and Plass solved VRTE for the multiple-scattered light in haze and clouds by the Monte Carlo method [13].

In biomedical optics, Monte Carlo based software has been used for the modeling of polarized light interaction with tissue. By measuring the intensities and polarization properties of the reflected/transmitted light one can extract the unknown optical properties of the biological sample  $(\mu_s, \mu_a, g)$  by solving an inverse scattering problem. It is expected that the optical properties of pathological tissues differ from that of a healthy one. These markers could be used for the optical diagnostics and pave the way for the new non-invasive diagnostic tools.

Monte Carlo code for the solution of RTE in multilayered tissues was developed by Wang et al. [14]. Three free versions of Monte Carlo code for the calculations of backscattering Mueller matrix, including the effect of skewed illumination, were developed by Ramella-Roman et al. [15], [16]. Another free Monte Carlo code has been proposed by D. Côté and A. Vitkin [17]. The generalized Monte Carlo model for simulation of coherent effects of multiple scattering, including Coherent Back-Scattering (CBS) and temporal intensity fluctuation of polarized laser radiation scattered within the random inhomogeneous turbid medium was developed by I. Meglinski [18], [19]. The online GPU-accelerated multipurpose Monte Carlo simulation tool for the needs of biophotonics and biomedical optics was developed by I. Meglinski and A. Doronin [20].

The first version of our polarized Monte Carlo code was developed for the metrological applications [21] and later generalized for the modeling of polarized light propagation in biological tissue [22]. The photons, emitted by source, are characterized by their position, direction of propagation and given polarization (Stokes vector). They are propagating like ballistic ones till the next scattering site. The elastic scattering change the direction and polarization of photon. The absorption by the medium gradually reduces the statistical weight of a photon. The photon can be reflected or refracted crossing the interfaces according to Fresnel's law. Photons will follow a random walk trajectory within a defined computational domain comprising regions with different optical properties. This process is repeated for the "photon packages" with different initial states of polarization. The photon intensities of the photons that reach the detector are averaged incoherently. No speckle effect is taken into account, because spatially incoherent light was used in our experiments. The average values of photon intensities provide the quantities of interest, namely, Mueller matrix coefficients of a sample. The main steps of the algorithm are detailed below.

### *3.4.2.1. Generation of random numbers with given probability distributions.*

Let us define as  $P(z)$  the probability distribution function of a random variable  $z$  ( $z_0 \leq z \leq z_i$ ). It means that probability

$$dP(z \in dz) = P(z)dz \quad (3.23)$$

Then, the cumulative probability function  $f_P(z)$  is given by

$$f_P(z) = \int_{z_0}^z P(v)dv \quad (3.24)$$

It is clear that if  $z_0 \leq z \leq z_i$  with the probability distribution function  $P(z)$ , the cumulative probability function  $f_P(z)$  varies between 0 and 1 with its own probability distribution function  $Q(f_P)$ , which is related to  $P(z)$  as

$$Q(f_P)df_P = P(z)dz \quad (3.25)$$

It follows from Eq. (3.25) that the cumulative probability function  $f_P(z)$  is uniformly distributed between 0 and 1.

$$Q(f_P) = \frac{P(z)}{df_P/dz} = 1 \quad (3.26)$$

Hence, if we generate a random uniformly distributed variables  $f_P \in [0,1]$ , the solutions to Eq. (3.24) will obey a defined probability distribution function  $P(z)$  and  $z_0 \leq z \leq z_i$ . When photon propagates through homogeneous absorbing and scattering medium, characterized by its extinction coefficient  $\mu_e$ , the probability of photon not being scattered or absorbed over the distance  $z$  is given by

$$P(z)dz = \mu_e \exp(-\mu_e z)dz \quad (3.27)$$

Putting Eq. (3.27) into Eq. (3.24), we obtain

$$f_P(z) = \int_{z_0}^z \mu_e \exp(-\mu_e v)dv = (1 - \exp(-\mu_e z)) \quad (3.28)$$

or

$$z = -\frac{\ln(1 - f_P)}{\mu_e} = \frac{\ln(f'_P)}{\mu_e} \quad (3.29)$$

where  $f'_P$  is random variable that is uniformly distributed on  $[0,1]$ . When probability distribution function  $P(z)$  cannot be integrated analytically, one can implement so-called acceptance-rejection method. The random equidistributed draws of both  $z \in [z_0, z_1]$  and  $x \in [0,1]$  are performed independently by a standard numerical random number generator. Then,  $P(z)$  is calculated and compared with  $x$ . If

$$x \leq P(z) \quad (3.30)$$

the value of  $z$  is accepted, otherwise it is rejected. When the dimensionality of the problem increases the acceptance-rejection method can lead to a lot of unwanted samples being taken before the accepted sample is generated. Let us consider the case, when the probability density function depends on two variables (not necessarily independent) and can be decomposed into the sum of two positive terms,

$$P(\theta, \phi) = f_1(\theta, \phi) + f_2(\theta, \phi) \quad (3.31)$$

the functions  $f_1$  and  $f_2$  are not the probability density functions because they are not normalized. Introducing the norms  $F_1$  and  $F_2$  (the integrals of  $f_1$  and  $f_2$  over the full finite range of variations of variables  $\theta$  and  $\phi$ ), we can present the probability density function  $P(\theta, \phi)$  as a linear combination of two probability density functions  $P_1(\theta, \phi)$  and  $P_2(\theta, \phi)$ :

$$P(\theta, \phi) = F_1 P_1(\theta, \phi) + F_2 P_2(\theta, \phi) \quad (3.32)$$

We can interpret Eq. (3.32) as a splitting of all possible events generating the pair of  $(\theta, \phi)$  variables into two mutually excluding groups. The numerical procedure for generating the  $(\theta, \phi)$  pairs can be described as:

- Draw a number  $u$ , which is uniformly distributed in the interval  $[0, 1]$ ;
- If  $u < F_1/(F_1 + F_2)$ , the pair  $(\theta, \phi)$  has to be drawn following the probability density function  $P_1$ ,
- Otherwise, the probability density function  $P_2$  has to be used.

This method is of particular interest if the variables  $\theta$  and  $\phi$  can be considered as independent ones for both probability density functions  $P_1$  and  $P_2$ , as it will be shown below.

### 3.4.2.2. *Photon coordinates and trajectories.*

Since Monte Carlo algorithm simulates the random trajectory of a polarized photon within scattering and absorbing medium, one have to define the photon path. It is constructed as the recursive sequence of the following steps:

1. Creation of source photon with a chosen position, direction, and initial polarization.
2. Definition of the site and type of next event (scattering on particle, transmission or reflection on the interfaces). If the photon has reached the boundaries of the domain of simulations, go to step 5.
3. Change the direction of photon propagation and its polarization according to the type of event.
4. Scoring, check if photon stays within the domain of simulations. If so, back to step 2.
5. The photon path terminates whenever it reaches the boundaries of the domain of simulations, which means that it has no return possibility.

The sequence of  $N$  photons (package) with the same input Stokes vector  $\mathbf{S}^{\text{in}}$  (i.e. same polarization state) is emitted from the source. Due to the statistical nature of Monte Carlo technique each individual photon follows its own trajectory in the scattering and absorbing medium and, finally, contributes to the detector (if being detected) independently, carrying its unique output Stokes vector. Hence, for the fixed  $\mathbf{S}^{\text{in}}$  an output Stokes vector is found by averaging over the simulated output polarization states of the photon. This step is repeated with the same  $\mathbf{S}^{\text{in}}$  until the variance threshold is reached.

For the accurate estimation of the Mueller matrix of the sample the initial polarization state of photon package has to be varied over the surface of the Poincaré sphere widely enough. The initial polarization states can be defined as four fixed polarization states with linearly independent Stokes vectors. The optimal choice corresponds to vortices of regular tetrahedron inscribed into Poincaré sphere. When using this sampling approach the following matrix equation is obtained

$$\mathbf{F} = \mathbf{M} \cdot \mathbf{W} \quad (3.33)$$

where four different input Stokes vectors form the columns of matrix  $\mathbf{W}$  and four corresponding output Stokes vectors form the columns of matrix  $\mathbf{F}$ . When four  $\mathbf{S}^{\text{in}}$  are linearly independent,  $\mathbf{W}$  can be inverted and Mueller matrix is defined as

$$\mathbf{M} = \mathbf{F} \cdot \mathbf{W}^{-1} \quad (3.34)$$

Let us now consider in details the phenomena treated within step 2 of the Monte Carlo algorithm, namely, scattering on spherical scatterers and reflection/transmission on interfaces.

**Scattering by spheres embedded in a homogeneous medium.** It was already shown that for photon propagating in scattering and absorbing medium with extinction coefficient  $\mu_e$  the distance  $d$  between two scattering events is a random variable defined as

$$d = \frac{\ln(z)}{\mu_e} \quad (3.35)$$

where  $z$  is a random number uniformly distributed between 0 and 1 (see Eqs (3.27)-(29)). The probability  $P(\theta, \phi)$  that the photon will be scattered at angle  $\theta$  and its initial local reference frame  $(\mathbf{e}_x^o, \mathbf{e}_y^o, \mathbf{e}_z^o)$  will be rotated by angle  $\phi$  (see Fig. 3.15) is calculated as a function of the photon energy, radius of spherical scatterer and relative optical index contrast using analytical Mie solution [6].

First, we need to rotate vector  $\mathbf{S}^o$  and reference frame  $(\mathbf{e}_x^o, \mathbf{e}_y^o, \mathbf{e}_z^o)$  in Stokes parametric space and real space, respectively, by angle  $\phi$  about the direction of propagation  $\mathbf{e}_z^o$ .

$$\mathbf{S}^i = \mathbf{R}_M(\phi) \cdot \mathbf{S}^o, \quad \begin{cases} \mathbf{e}_x^i = \cos \phi \mathbf{e}_x^o + \sin \phi \mathbf{e}_y^o \\ \mathbf{e}_y^i = -\sin \phi \mathbf{e}_x^o + \cos \phi \mathbf{e}_y^o \\ \mathbf{e}_z^i = \mathbf{e}_z^o \end{cases} \quad (3.36)$$

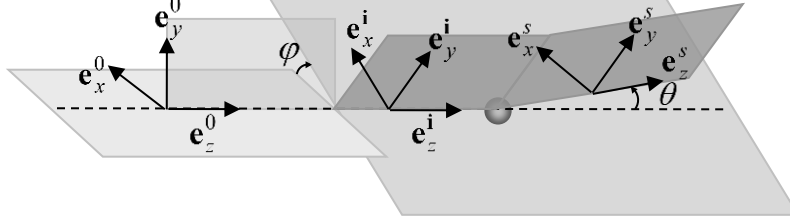


**Figure 3.15** (adapted from [23]). Scattering angles  $\theta$  and  $\phi$  are not independent parameters. The initial local reference frame  $(\mathbf{e}_x^o, \mathbf{e}_y^o, \mathbf{e}_z^o)$  is rotated by angle  $\phi$  to obtain the incident frame  $(\mathbf{e}_x^i, \mathbf{e}_y^i, \mathbf{e}_z^i)$  with unit vectors  $\mathbf{e}_x^i$  and  $\mathbf{e}_y^i$  parallel and perpendicular to the scattering plane defined by the incident direction and direction of scattering (which is defined by angle  $\theta$ ). After scattering of photon by sphere its new polarization state is given by Mie solution defined in the scattering reference frame  $(\mathbf{e}_x^s, \mathbf{e}_y^s, \mathbf{e}_z^s)$ , which becomes a new local reference frame.

The scattering of photon by the angle  $\theta$  is described by Mueller matrix  $\mathbf{M}(\theta)$  defined by Eq.(3.11a) in a scattering reference frame. This reference frame is obtained by rotating the incident reference frame by  $(\mathbf{e}_x^i, \mathbf{e}_y^i, \mathbf{e}_z^i)$  about the direction  $\mathbf{e}_y^i$  (perpendicular to the scattering reference plane) by the angle  $\theta$ .

$$\mathbf{S}^s = \mathbf{M}(\theta)\mathbf{R}_M(\phi) \cdot \mathbf{S}^o, \quad \begin{cases} \mathbf{e}_x^s = \cos \theta \mathbf{e}_x^i - \sin \theta \mathbf{e}_z^i \\ \mathbf{e}_y^s = \mathbf{e}_y^i \\ \mathbf{e}_z^s = \sin \theta \mathbf{e}_x^i + \cos \theta \mathbf{e}_z^i \end{cases} \quad (3.37)$$

The intensity  $dI^s$  of the light scattered in a solid angle  $d\Omega$  about the direction  $\hat{\Omega}$  is given by the first component of the Stokes vector of scattered light  $\mathbf{S}^s$ :

$$dI^s = S_0^s(\theta, \phi)d\Omega \quad (3.38)$$

where

$$\begin{aligned} S_0^s(\theta, \phi) &= m_{00}(\theta)I + m_{01}(\theta) \cos(2\phi) Q - m_{01}(\theta) \sin(2\phi) U = \\ &= \frac{1}{2} [ |S_1(\theta)|^2 (I - Q \cos(2\phi) + U \sin(2\phi)) + |S_2(\theta)|^2 (I + Q \cos(2\phi) - U \sin(2\phi)) ] \end{aligned} \quad (3.39)$$

where  $|S_i(\theta)|^2$  are the squared values of complex amplitude functions (see Eqs 3.9(a), (b)). The total intensity of scattered light is obtained by integrating the intensity of the scattered light over all directions of propagation included in the sphere of unit volume:

$$I^s = \int S_0^s d\Omega = \int_{\theta=0}^{\theta=\pi} \int_{\phi=0}^{\phi=2\pi} S_0^s(\theta, \phi) \sin \theta d\theta d\phi = \pi I \int_{\theta=0}^{\theta=\pi} (|S_1(\theta)|^2 + |S_2(\theta)|^2) \sin \theta d\theta =$$

$$= \pi I \int_{\theta=0}^{\theta=\pi} (|S_1(\theta)|^2) \sin \theta d\theta + \pi I \int_{\theta=0}^{\theta=\pi} (|S_2(\theta)|^2) \sin \theta d\theta = \pi I (T_1 + T_2) \quad (3.40)$$

The intensity of the scattered light in any direction of propagation, characterized by the angles  $\theta$  and  $\phi$ , is proportional to the number of the photons scattered along that direction. The combined angular probability density function  $P(\theta, \phi)$  can be written as

$$P(\theta, \phi) d\theta d\phi = \frac{S_o^s(\theta, \phi)}{I^s} \sin \theta d\theta d\phi \quad (3.41)$$

This function is a joint probability density function of the random variables  $\theta$  and  $\phi$ . Hence, we can apply the acceptance–rejection method described above to generate the values of angles  $\theta$  and  $\phi$ . Three random numbers  $\theta_o$ ,  $\phi_o$ , and  $\xi$ , uniformly distributed over the intervals  $[0, \pi]$ ,  $[0, 2\pi]$ , and  $[0, \max_{\theta, \phi} S_o^s(\theta, \phi)]$ , respectively, are generated first. If  $\xi \leq S_o^s(\theta_o, \phi_o)$ , the pair  $\theta_o$  and  $\phi_o$  is accepted, otherwise random draw of  $\theta_o$ ,  $\phi_o$ , and  $\xi$  is repeated. This probability of acceptance is always smaller than 0.5 (limit case for very small scattering particles) and decreases with the increase of size of scatterers, leading to the unproductive increase of computational time.

In order to avoid this problem, we decompose the angular probability density function  $P(\theta, \phi)$  in a sum of two positive terms (see Eq. (3.32)). First, we define  $\phi_0$  and  $W$  from the following expressions using the first three components of incident Stokes vector:

$$I^2 W^2 = Q^2 + U^2 \quad (3.42a)$$

$$\tan 2\phi_0 = U/Q \quad (3.42b)$$

$W \in [0, 1]$  because  $I^2 \geq Q^2 + U^2 + V^2$ . It follows from Eq. (3.42) that

$$Q = IW \cos(2\phi_0) \quad (3.43a)$$

$$U = IW \sin(2\phi_0) \quad (3.43b)$$

It can be easily shown that multiplying (3.43a) by  $\cos 2\phi$  and (3.43b) by  $\sin 2\phi$ , then subtracting them, we get

$$Q \cos 2\phi - U \sin 2\phi = IW \cos 2(\phi - \phi_0) \quad (3.44)$$

Consequently, substituting Eq. (3.44) in (3.39) we obtain

$$\begin{aligned} S_o^s(\theta, \phi) &= \frac{1}{2} [|S_1(\theta)|^2 (I - IW \cos 2(\phi - \phi_0)) + |S_2(\theta)|^2 (I + IW \cos 2(\phi - \phi_0))] = \\ &= \frac{I}{2} [|S_1(\theta)|^2 (1 - W + 2W \sin^2(\phi - \phi_0)) + |S_2(\theta)|^2 (1 - W + W \cos^2(\phi - \phi_0))] \end{aligned}$$

(3.45)

Using Eqs (3.40) and (3.45), the combined angular probability density function  $P(\theta, \phi)$  from Eq. (3.41) can be written as

$$\begin{aligned} P(\theta, \phi) &= \frac{1}{2\pi(T_1 + T_2)} [t_1(\theta, \phi) + t_2(\theta, \phi)] \\ &= \frac{1}{2\pi} \left[ \frac{T_1}{(T_1 + T_2)} \frac{t_1(\theta, \phi)}{T_1} + \frac{T_2}{(T_1 + T_2)} \frac{t_2(\theta, \phi)}{T_2} \right] \end{aligned} \quad (3.46)$$

where

$$t_i(\theta, \phi) = \frac{1}{2} |S_i(\theta)|^2 \sin \theta \left[ 1 - W + 2W \sin^2(\phi - \phi_0 + (i - 1) \frac{\pi}{2}) \right], i = 1, 2 \quad (3.47)$$

Functions  $P_1(\theta, \phi) = \frac{t_1(\theta, \phi)}{T_1}$  and  $P_2(\theta, \phi) = \frac{t_2(\theta, \phi)}{T_2}$  are the probability density functions. Moreover, each of the functions  $P_1$  and  $P_2$  is the product of  $P_i(\theta)$  and  $P_i(\phi)$  ( $i = 1, 2$ ), meaning that random variables  $\theta$  and  $\phi$  are statistically independent. The procedure of generating the angles  $\theta$  and  $\phi$  can be summarized as

1. The technique of decomposition in the sum of two positive terms applied first to choose either probability density function  $P_1(\theta, \phi)$  or  $P_2(\theta, \phi)$ .
2. Angle  $\theta$  is obtained by applying the acceptance-rejection method for the probability density function.

$$P_i(\theta) = \frac{|S_i(\theta)|^2 \sin \theta}{\int_0^\pi |S_i(\theta)|^2 \sin \theta d\theta} \quad (3.48)$$

3. Then, again the technique of decomposition is applied to the probability density functions

$$P_1(\phi) = \frac{1}{2\pi} (1 - W) + \frac{1}{\pi} W \sin^2(\phi - \phi_0) \quad (3.49a)$$

$$P_2(\phi) = \frac{1}{2\pi} (1 - W) + \frac{1}{\pi} W \cos^2(\phi - \phi_0) \quad (3.49b)$$

because these probability density functions are the sum of constant  $(1 - W)/2\pi$  and function  $g_i(\phi) = \frac{W}{\pi} \sin^2(\phi - \phi_0 + (i - 1) \frac{\pi}{2})$ ,  $i = 1, 2$ .

4. For the choice of constant the angle  $\phi$  is drawn uniformly over the interval  $[0, 2\pi]$ . Otherwise, the angle  $\phi$  is determined by the inversion of the probability density function  $G_i(\phi) = \frac{\pi}{W} g_i(\phi)$  obtained by normalization of  $g_i$ .

**Interaction with the interfaces.** When photon with current position  $\mathbf{r}_n$  and direction of propagation  $\mathbf{\Omega}_n$  continues his travel within the scattering medium, we first calculate the scattering distance  $d$  from Eq. (3.35) and compare it with the geometrical distance  $d_0$  to the closest interface defined as  $\mathbf{r}_{n+1} - \mathbf{r}_n = d_0 \hat{\mathbf{\Omega}}_n$ . If  $d_0 < d$ , the next location of photon will be considered at the interface, where it can be reflected or transmitted. Making choice between reflection and transmission, we use the Fresnel law for the interface between two semi-infinite media. First we rotate the frame of reference  $(\mathbf{e}_x, \mathbf{e}_y, \mathbf{e}_z)$  by the corresponding angles until the axes x and y become perpendicular and parallel, respectively, to the plane of incidence. Then the reflectivity for an incoming Stokes vector  $\mathbf{S} = [I, Q, U, V]^T$  is defined as

$$R = \frac{1}{2} [(r_{\parallel}^2 + r_{\perp}^2) + Q(r_{\parallel}^2 - r_{\perp}^2)] \quad (3.50)$$

where  $r_{\parallel}$  and  $r_{\perp}$  are the complex reflectance coefficients from the reflection Jones matrix. The random number  $p_R$ , uniformly distributed over  $[0, 1]$ , is generated and compared with  $R$ . If  $p_R < R$ , the photon is reflected at the interface, otherwise it is transmitted. The state of polarization of reflected/transmitted photon is the product of its Stokes vector and interface reflection/transmission Mueller matrix obtained from the Fresnel law. The new direction of propagation is obtained by means of the Snell law.

### 3.4.3. Monte Carlo algorithm for anisotropic scattering media

#### 3.4.3.1. *Optical anisotropy of tissue*

Many biological tissues (e.g., cornea, tendon, sclera, muscle, retina) are not only scattering, but also optically anisotropic. The latter is often due to the presence of ordered microstructures in tissue. For example, tissue extracellular matrix that contains aligned fibers of collagen produces so-called form birefringence. The arrangement of collagen fibers is directly related to the orientation of the optical axis. The density of collagen fibers affects the magnitude of the polarimetric properties (e.g., scalar linear birefringence and linear diattenuation). Some chiral aggregates can create an optical activity which is related to the circular birefringence and the circular diattenuation. The chiral molecules (e.g., glucose) also can generate both circular birefringence and circular diattenuation (see Fig. 3.16) [10].

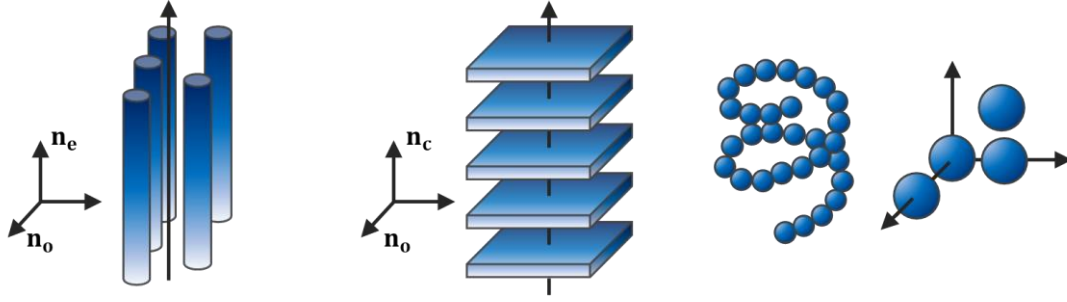


**Figure 3.16** Structurally anisotropic models of biological tissue and tissue components: (a) long dielectric cylinders, (b) dielectric plates, and (c) chiral aggregates of particles.

In case of form anisotropy (or form birefringence) the phase velocity of light propagating along the axis of the aligned fibers (fast optical axis) is not the same as for light propagating in the direction perpendicular to the axis of the aligned fibers (slow optical axis). It results in a non-zero value of the relative optical phase between two orthogonal polarization components of polarized light propagating through such media. The phase retardation  $\Delta$  is defined as

$$\Delta = \frac{2\pi\Delta n d}{\lambda} \quad (3.51)$$

where  $d$  is the path length of light propagation through the uniaxial birefringent medium, and  $\lambda$  is the wavelength of the probing light beam,  $\Delta n$  is defined as

$$\Delta n = n(\theta) - n_o \quad (3.52)$$

$n(\theta)$  is the effective refractive index seen by light propagating at angle  $\theta$  with respect to the extraordinary axis of birefringent material (see Fig. 3.17), and it is given by [24]

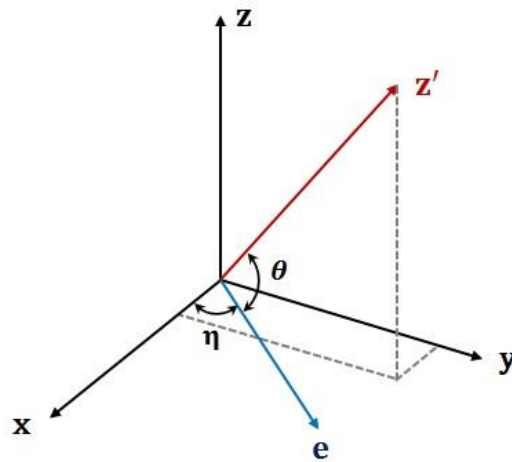


**Figure 3.17** Vector of optical axis  $e$  ( $\cos \eta, \sin \eta$ ) and direction of light propagation  $z'$  ( $u_x, u_y, u_z$ ) in the laboratory coordinate system.

$$n(\theta) = \frac{n_o n_e}{(n_e^2 \cos^2 \theta + n_o^2 \sin^2 \theta)^{0.5}} \quad (3.53)$$

$n_o$  and  $n_e$  are the ordinary and extraordinary refractive indices of the uniaxial birefringent medium, respectively. The angle  $\theta$  is defined from the scalar product of the vector of light propagation direction and the vector defining the orientation of the extraordinary axis as [24]

$$\theta = \cos^{-1} \left( \frac{u_x \cos \eta + u_y \sin \eta}{(u_x^2 + u_y^2 + u_z^2)^{0.5}} \right) \quad (3.54)$$

### 3.4.3.2. Validation of the updated Monte Carlo algorithm

When the optical axis of linear uniaxial birefringent medium is parallel to  $x$ -axis, the Mueller matrix of retarder is given by

$$M_\Delta = \begin{bmatrix} 1 & 0 & 0 & 0 \\ 0 & 1 & 0 & 0 \\ 0 & 0 & \cos \Delta & \sin \Delta \\ 0 & 0 & -\sin \Delta & \cos \Delta \end{bmatrix} \quad (1.42)$$

To account for the phase shift of light propagating at the angle  $\theta$  with respect to the direction of the optical axis, we need to calculate the matrix product  $M_\Delta(\beta) = R(\beta)M_\Delta R(-\beta)$ , where  $M(\beta)$  is the matrix of rotation in Stokes space (see Eq. (1.51), the rotation angle  $\beta$  is defined as the angle between the local fast axis  $\mathbf{f} = \mathbf{k} \times \mathbf{e}$  (cross product between the vector of photon propagation direction  $\mathbf{z}' = \mathbf{k}$  and the vector of the optical axis  $\mathbf{e}$ ) and unit vector of  $y'$ -axis of the local coordinate system (see Fig. 3.18).

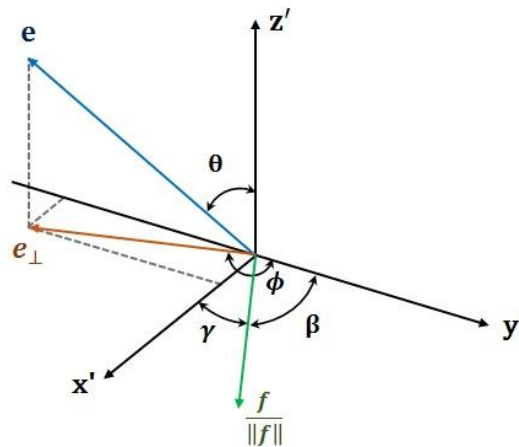


**Figure 3.18** Vector of optical axis  $\mathbf{e}$  in the local coordinate system  $(x', y', z')$

We assume that tissue linear birefringence is small enough (typical values of  $\Delta n$  for biological tissue are about  $10^{-5}$  [10]), so it does not affect the calculations of the single

scattering matrix (see Eqs. (3.11)). The updated polarized Monte Carlo algorithm for the solution of VRTE in scattering anisotropic medium has one extra step during the calculations of the trajectory of photon random walk, namely, the Stokes vector of a scattered photon is multiplied by the retarder matrix  $M_{\Delta}(\beta)$ , where the retardation  $\Delta$  is calculated from Eq. (3.51) for the distance  $d$  travelled by a photon to the next scattering event site or to the boundary of birefringent medium.

To validate the updated version of the algorithm we simulated the backscattered Mueller matrix images of two optical scattering phantoms with isotropic and linear birefringent host medium. The optical axis of the latter was aligned with  $x$ -axis of the laboratory coordinate system. Point source emits a given number ( $10^7 \sim 10^8$ ) of mono-energetic polarized photons ( $\lambda = 633\text{nm}$ ) that impinge top flat surface of each phantom at normal incidence. The thickness of each phantom is 1 cm, scattering coefficient  $\mu_s = 10 \text{ cm}^{-1}$ , there is no absorption ( $\mu_a = 0$ ). The radius of spherical scatterers  $R_s = 200 \text{ nm}$ , the refractive index of spherical particles is  $n_p = 1.59$ , the refractive index of the isotropic host medium  $n_m = 1.33$ ,  $\Delta n_{\text{max}} = 10^{-5}$  for the birefringent host medium. All those parameters can be adjusted to mimic the optical properties of a real biological sample. The results of the simulation are presented in Fig. 3.19. All elements of the Muller matrix images  $m_{ij}^*(x, y)$  are normalized by  $m_{00}(x, y)$  pixel-wise:  $m_{ij}^*(x, y) = m_{ij}(x, y)/m_{00}(x, y)$ .

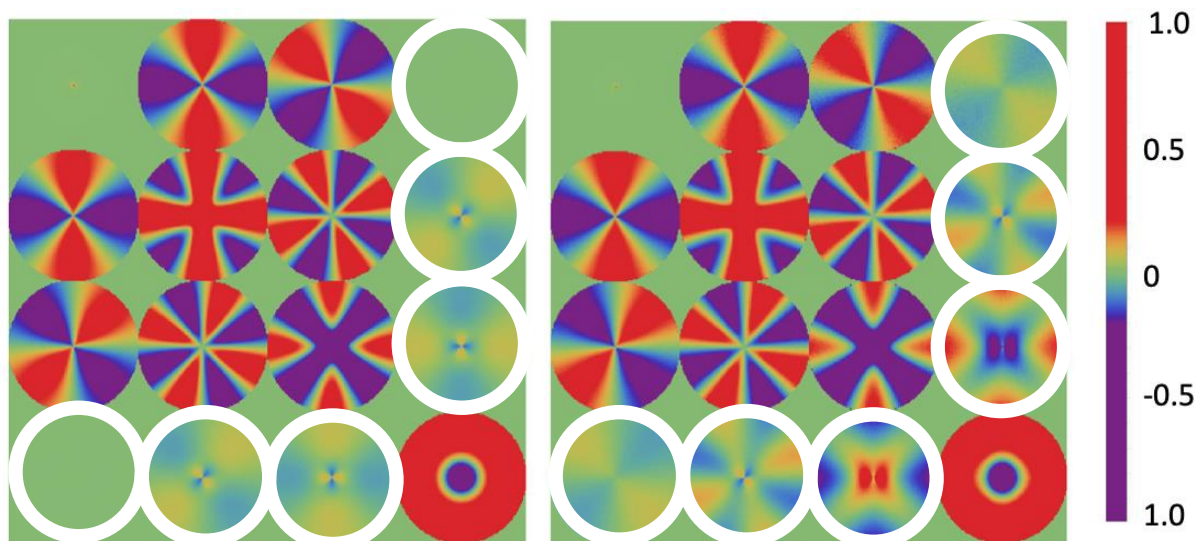


**Figure 3.19** Simulated backscattered Mueller matrix images of isotropic medium with embedded spherical scatterers (left) and linear birefringent scattering medium with randomly and uniformly distributed spherical scatterers (right). White circles highlight the difference in MM coefficients. The area of each image is  $1\text{cm}^2$ .

The top left  $3 \times 3$  blocks of the Mueller matrix images are identical for both isotropic and anisotropic phantoms. Different spatial patterns in  $m_{03}$  and  $m_{30}$  images of both phantoms demonstrate the presence of non-zero circular dichroism for the anisotropic phantom. The impact of optical anisotropy of host medium is clearly seen in  $m_{13}$ ,  $m_{31}$ ,  $m_{23}$ , and  $m_{32}$  images of birefringent scattering medium. It is worth to mention that these spatial patterns will not be observed at diffuse uniform illumination of a sample because of spatial averaging.

### 3.5. Conclusions

We reviewed a number of image processing methods with a special focus on the DBSCAN density-based clustering algorithm that has been used in our studies for the image segmentation to extract the regions of interest (ROI) effectively. This method is well adapted for finding the clusters of arbitrary shape and handling noise data effectively. However, the time complexity of the DBSCAN algorithm prevents it from using on the large size datasets. To address this problem, we developed the updated version of the DBSCAN algorithm that allows efficient clustering of the large size datasets. We explored the idea of cluster expanding by assigning all points of the  $\varepsilon/r$ -neighborhood of an arbitrary core point to the corresponding cluster. Then, the procedure of a point-by-point cluster expansion applies only to the dataset points that belong to the  $\varepsilon$ -neighborhood of a core point but do not belong to the  $\varepsilon/r$ -neighborhood of the same core point. This approach reduces considerably the execution time and memory budget for the updated version of the DBSCAN algorithm for large size datasets. We developed a heuristic method for finding the optimal value of the input parameter  $\varepsilon$ . The results of parametric studies on the performance of both original and updated versions of the DBSCAN algorithm are reported.

In this Chapter, we also discussed the Monte Carlo statistical algorithm for the solution of a vector radiative transfer equation (VRTE) that was used to calculate the Mueller matrix of optical phantoms of biological tissue.

Biological tissues are extremely complex objects containing a large number of randomly distributed multi-disperse microscopic scatterers and anisotropic microstructures. We introduced the parameters for the description of scattering media. A transfer matrix for scattering was determined by analytical Mie solution for a single spherical scatterer. This matrix describes the changes of photon's polarization state and direction of propagation after each scattering event. The angles of deflection and rotation of the polarization plane were calculated using the rejection method. The multi-layered structure of tissue was modeled by the reflection or transmission of polarized photons on the interfaces according to Fresnel laws. The host medium may also be absorbing. The random walk of a photon continued within a scattering medium until it was either absorbed within the sample or moved outside the sample volume, where it can be lost or be registered by a detector.

The polarization states of the incident light can also be changed by the interactions with microstructures of the biological tissue sample that cause tissue birefringence. We updated the Monte Carlo algorithm for a solution of the vector radiative transfer equation to account for the anisotropy of tissue refractive index. The comparative simulations of both isotropic and anisotropic scattering phantoms demonstrate the impact of host medium birefringence on certain coefficients of the Mueller matrix.

Both DBSCAN clustering algorithm and polarized Monte Carlo simulations were used for the post-processing and interpretation of the experimental polarimetric data for biological tissue. These results will be presented and discussed in the next Chapters.

## References

1. M. Ester, H. P. Kriegel, J. Sander, X. Xu, "A density-based algorithm for discovering clusters in large spatial databases with noise.," *AAAI press, KDD-96 Proc.*, pp. 1–6, Jul. 1996.
2. S. F. Galán, "Comparative evaluation of region query strategies for DBSCAN clustering," *Inf. Sci.*, vol. 502, pp. 76–90, Oct. 2019.
3. E. Kolatch, "Clustering Algorithms for Spatial Databases: A Survey," April. 2001.
4. W. Ashour and S. Sunoallah, "Multi Density DBSCAN," in *Intelligent Data Engineering and Automated Learning - IDEAL 2011, Springer*, pp. 446–453, 2011.
5. N. Beckmann, H. P. Kriegel, R. Schneider, and B. Seeger, "The R\*-tree: an efficient and robust access method for points and rectangles," *SIGMOD '90, Proc. 1990 ACM SIGMOD international conference on Management of data*, pp. 322–331, 1990.
6. C. F. Bohren, D. R. Huffman, Chapter 4. Absorption and scattering by sphere, in *Absorption and Scattering of Light by Small Particles*, Wiley-VCH, 2004.
7. H. C. van de Hulst, Chapter 4, Wave propagation in a medium containing scatterers, in *Light scattering by small particles*, Dover, New York, 1981.
8. M. I. Mishchenko, L. D. Travis, A.A. Lacis, *Multiple Scattering of Light by Particles: Radiative Transfer and Coherent Backscattering*, Cambridge University Press, 2006.
9. M. I. Mishchenko, "Vector radiative transfer equation for arbitrarily shaped and arbitrarily oriented particles: a microscopic derivation from statistical electromagnetics", *Appl. Opt.*, Vol. 41, no. 33, p.p. 7114-7134, 2002.
10. V. V. Tuchin, L. V. Wang, and D.A. Zimnyakov, *Optical Polarization in Biomedical Applications*, Springer-Verlag, Berlin Heidelberg, pp. 1–285, 2006.
11. G. I. Bell and S. Glasstone, *Nuclear reactor theory*, Litton Educational Publishing, Inc, 1970.
12. I. Lux and L. Koblinger, *Monte-Carlo particle transport methods: neutron and photon calculations*, CRC Press, Boca Raton, 1991.
13. G. W. Kattawar and G. N. Plass "Radiance and polarization of multiple scattered light from haze and clouds," *Appl. Opt.*, vol. 7, no. 8, p.p. 1519-1527, 1968.
14. L. Wang, S. L. Jacques, and L. Zheng, "MCML-Monte Carlo modeling of light transport in multi-layered tissues," *Comput. Methods Programs Biomed.*, vol. 47, no. 2, p.p. 131-146, 1995.

15. J. C. Ramella-Roman, S. A. Prahl, and S. L. Jacques, "Three Monte Carlo programs of polarized light transport into scattering media: part I," *Opt. Express*, vol. 13, no. 12, p.p. 4420- 4438, 2005.
16. J. C. Ramella-Roman, S. A. Prahl, and S. L. Jacques, "Three Monte Carlo programs of polarized light transport into scattering media: part II," *Opt. Express*, vol. 13, no. 12, p.p. 10392-10405, 2005.
17. D. Coté, I. A. Vitkin, "Robust concentration determination of optically active molecules in turbid media with validated three-dimensional polarization sensitive Monte Carlo calculations," *Opt. Express*, vol. 13, no. 1, p.p. 148-163, 2005.
18. A. Doronin, C. Macdonald, and I. Meglinski, "Propagation of coherent polarized light in highly scattering turbid media," *J. Biomed. Opt.*, Vol.19, No.2, p.p. 025005, 2014.
19. A. Doronin, A. J. Radosevich, V. Backman, and I. Meglinski, "Two electric field Monte Carlo models of coherent backscattering of polarized light", *J. OPT. SOC. AM. A*, Vol. 31, No. 11, p.p. 2394 – 2400, 2014.
20. A. Doronin, I. Meglinski, "Online object oriented Monte Carlo computational tool for the needs of biomedical optics", *Biomed. Opt. Express*, vol. 2, no. 9, p.p. 2461–2469, 2011.
21. B. Kaplan, G. Ledanois, and B. Drévilion. "Mueller matrix of dense polystyrene latex sphere suspensions: measurements and Monte Carlo simulation," *Appl. Opt.*, vol. 40, no. 16, p.p. 2769-2777, 2001.
22. M. R. Antonelli, A. Pierangelo, T. Novikova, P. Validire, A. Benali, B. Gayet, and A. De Martino, "Mueller matrix imaging of human colon tissue for cancer diagnostics: how Monte Carlo modeling can help in the interpretation of experimental data," *Opt. Express*, vol. 18, no. 10, p.p. 10200-10208, 2010.
23. Kaplan, Applications métrologiques de l'ellipsométrie de Mueller, PhD thesis, Ecole polytechnique, Paris, France, 23 April 2002.
24. P. Ghassemi, L. T. Moffatt, J. W. Shupp, J. C. Ramella-Roman, "A new approach for optical assessment of directional anisotropy in turbid media," *J. Biophotonics*, vol. 9, no. 1-2, Jan. 2016.

# Chapter 4

## Digital histology of thin sections of human skin tissue models with Mueller microscopy

4.1. Human Skin Equivalents (HSE).....	88
4.2. Dependence of polarization and depolarization parameters on sample thickness .....	90
4.2.1. Measurements of skin sample thickness.....	91
4.2.2. Thickness dependence of polarization and depolarization parameters.....	94
4.3. Image segmentation (DBSCAN) for advanced analysis of tissue polarimetric properties .....	98
4.4. Mitigating the impact of the spatial fluctuations of tissue section thickness.....	103
4.5. Monte Carlo modeling of experimental polarimetric data for dermal layer of HSE.....	106
4.5.1. Optical models of HSE dermal layer .....	107
4.5.2. Rotation invariants of logarithmic decomposition.....	108
4.5.3. Choice of an appropriate optical model of the dermis.....	111
4.5.3.1. <i>Ruled out optical models</i> .....	111
4.5.3.2. <i>SCB optical model</i> .....	113
4.6. Conclusions .....	115
References .....	116

The preliminary studies of isotropic and anisotropic scattering phantoms in our laboratory (LPICM, École Polytechnique) demonstrated the validity of the logarithmic Mueller matrix decomposition (LMMD) in transmission configuration [1], [2]. This approach was subsequently extended to the biological tissue models. In this chapter, we will report on the results of our studies of the full-thickness skin equivalents with transmission Mueller microscopy and LMMD, discussing their potential diagnostics value [3], [4].

Skin tissue models are widely employed as an alternative to animal models or human donor tissue. The skin equivalents are grown in vitro from human cells, and they accurately reproduce the anatomy of human skin. Since human skin equivalents (HSE) can be produced with less variability compared to real human skin, these tissue models were chosen for our

studies. We verified the validity of the LMMD for the HSE by measuring five skin model tissue sections of different nominal thicknesses (5  $\mu\text{m}$ , 10  $\mu\text{m}$ , 16  $\mu\text{m}$ , 20  $\mu\text{m}$ , and 30  $\mu\text{m}$ ) and applied the statistical density-based spatial clustering algorithm for the applications with noise (DBSCAN) to define the outliers in the studied dataset and remove the corresponding image pixels from the subsequent analysis. Finally, we suggested the algorithm of mitigation of the impact of tissue thickness fluctuations on the polarimetric images of both scalar retardance and depolarization obtained from LMMD for the thin tissue sections measured in transmission. We derived the thickness-invariant parameters by using Beer-Lambert law as well as the linear dependence of retardance and dichroism and the quadratic dependence of depolarization on thickness as predicted by the differential Mueller matrix formalism for depolarizing anisotropic media [5], [6].

The Monte Carlo model was used to interpret the experimental results obtained for the thin sections of skin tissue equivalents. The logarithmic decomposition of both measured and simulated Mueller matrices of the samples was used to analyze the microstructure of full-thickness human skin equivalents. A set of rotation invariants for the logarithmic Mueller matrix decomposition (LMMD) were derived to rule out the impact of sample orientation. These invariants were calculated and used for both simulated and measured Mueller matrices to analyze the optical properties of the dermal layer of skin equivalents. To fit the experimental data, several optical models, namely, spherical scatterers within birefringent host medium, and a combination of spherical and cylindrical scatterers within either isotropic or birefringent host medium, were tested. We demonstrated that only the simulations with a model combining spherical and cylindrical scatterers within the birefringent host medium could reproduce the experimental trends seen in the changes of optical properties of the dermal layer (e.g., linear retardance, linear dichroism, and anisotropic linear depolarization) with layer thickness. It proves that Mueller polarimetry may provide relevant information not only on the size of dominant scatterers (e.g., cell nuclei versus subwavelength organelles) but also on its shape (e.g., cells versus collagen fibers).

## 4.1. Human skin equivalents (HSE)

The human skin equivalents were prepared by the biologists from the Translational Center for Regenerative Therapies, Fraunhofer Institute for Silicate Research (Wurzberg, Germany). The structure of a natural skin can be roughly described by three layers: the superficial epidermis, the adjacent dermis, and the underlying subcutis (mostly fatty tissue) (see Fig. 4.1).

The skin equivalents were produced *in vitro* from human cells and reflected the anatomy of real human skin (apart from the subcutis that was not included in the skin equivalent model). The skin models were generated from primary human skin cells (keratinocytes and fibroblasts) [7], [8]. The former cells differentiate *in vitro* and form an epidermis with the same anatomical layers as *in vivo*: stratum basale, stratum spinosum, stratum granulosum, and stratum corneum. The dermal part of the skin model consists of a collagen type 1

hydrogel with human primary fibroblasts. The real dermis can be divided into an upper part (stratum papillare) and a lower part (stratum reticulare). The stratum papillare of the dermis was not recreated in the skin model because it serves only as the mechanical interlocking of the epidermis and dermis. However, the sizes and shapes of the typical cell in the skin equivalent model are the same as the ones in real human skin *in vivo*.

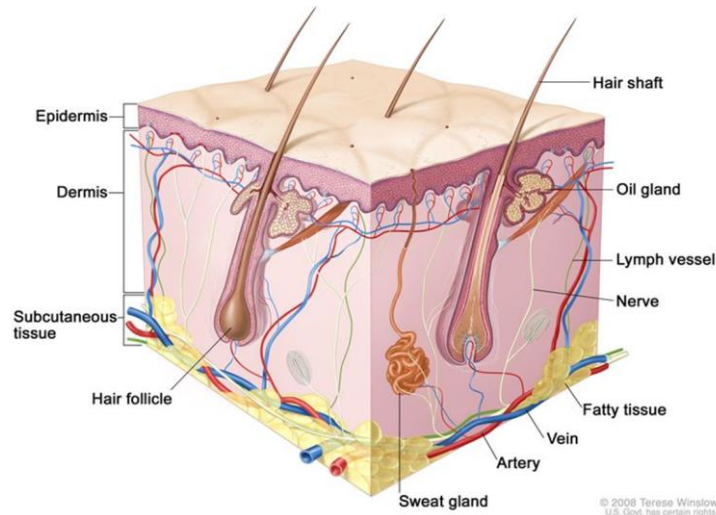


**Figure 4.1** Three layers of human skin tissue: epidermis, dermis, and subcutaneous. © Skin Cancer Screening (PDQ®), <https://www.cancer.gov/types/skin/patient/skin-screening-pdq>

These similarities and other functional properties, such as transporter expression and barrier function, led to the use of such skin models as alternatives to animal models or human donor tissue. This is one of the reasons why these models achieved regulatory acceptance by validation and adoption in the Organization for Economic Cooperation and Development guidelines for regulatory toxicological tests, e.g., skin irritation/corrosion (OECD TG 439 [9]). It means that these models are employed in Europe and other OECD countries to categorize substances for their potential to cause skin irritation and corrosion.

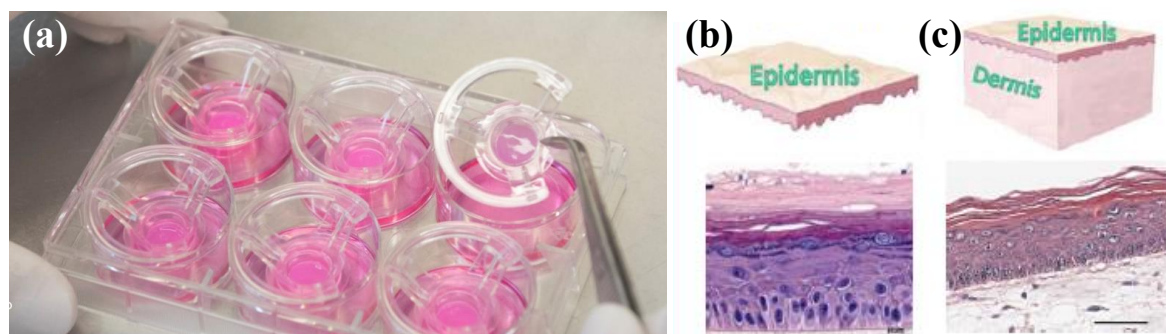


**Figure 4.2** (a) Photo of the Snapwell cell culture inserts used for the growth of the 3D *in-vitro* skin tissue models © K. Dobberke, Fraunhofer ISC, Germany. (b) schematic representation (top) and the microscopy image of the hematoxylin-eosin stained thin section of the reconstructed human epidermis; (c) schematic representation (top) and the microscopy image of the hematoxylin-eosin stained thin section of the full-thickness skin model, scale bar 100  $\mu\text{m}$  © Florian Groeber-Becker, Fraunhofer ISC, Germany.

The detailed procedure of the preparation of thin unstained sections of skin tissue models is described below.

1. The skin tissue models were grown in the cell culture inserts (Snapwell™ from Corning Inc.) with a diameter of 12 mm. The obtained disks of skin tissue equivalents were about 12 mm in diameter and about 600 μm thick. The thicknesses of the epidermal and dermal layers were about 100 μm and 500 μm, respectively.
2. The grown tissue models were rinsed with the phosphate-buffered salt solution and fixed with Roti®-Histofix 4% for 4 hours at room temperature.
3. Fixed samples were embedded in paraffin in an embedding machine.

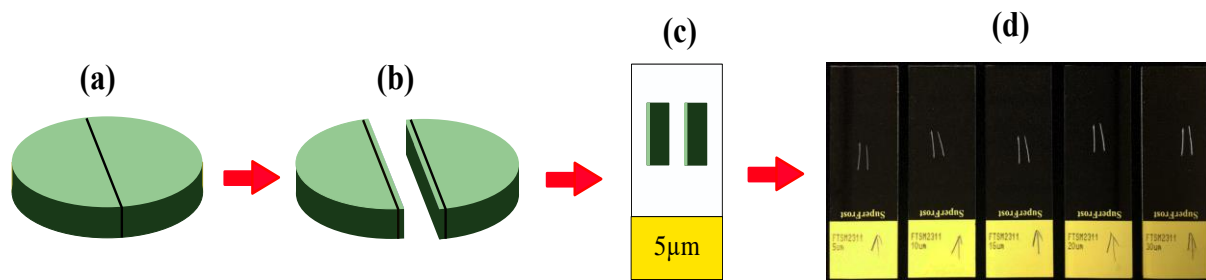


**Figure 4.3** Schematic of the preparation of the skin model tissue thin sections; (a) block of paraffin-embedded skin tissue equivalent; (b) cutting the block of the paraffin-embedded skin tissue sample in two pieces and slicing 5 μm thick stripes from both pieces with a microtome blade; (c) removing paraffin and placing two thin stripes of unstained skin equivalent on the microscope glass without a coverslip; repeating the same procedure for four adjacent sections of the different nominal thicknesses (10 μm, 16 μm, 20 μm, and 30 μm); (d) photo of five samples of different thicknesses.

During the next step a disk of the paraffin-embedded skin tissue model was cut along the diameter (see Fig. 4.3 (a)). Then, a set of the adjacent histological sections of different thickness (5 μm, 10 μm, 16 μm, 20 μm, and 30 μm) was cut from both parts of a disk using a microtome (see Figs. 4.3 (b)). Thereafter, the thin sections of tissue were deparaffinized for 20 minutes in the Roticlear® solvent. Then the stripes of unstained skin model tissue were placed on a microscope glass slide (Figs. 4.3 (c) and (d), tissue stripe lateral dimensions were about 10 mm x 0.5 mm). There was no glass coverslip used in our studies.

## 4.2. Dependence of polarization and depolarization parameters on sample thickness

In homogeneous anisotropic scattering media, the differential Mueller matrix formalism predicts linear and quadratic thickness dependence for the polarization (retardance and dichroism) and the depolarization properties, respectively, as shown by Eq. 1.86. We measured the prepared samples of thin sections of skin tissue model with a custom-built Mueller microscope, described in Chapter II. Then, we applied pixel-wise the LMMD of the experimental Mueller matrix images of the samples. We have delineated the zone of dermal layer on the images of scalar retardance, linear and circular depolarization for all measured

samples. Then, we calculated the mean values and the standard deviations of the optical properties (polarization and depolarization parameters) of the dermal layer for all samples, to verify the predicted dependence of the above mentioned parameters on sample thickness in case of biological tissue. In transmission measurement configuration, the length of the path of the detected light beam through a thin tissue section is equivalent to the thickness of a sample, which, in turn, has an impact on the polarization state of the detected light. Therefore, the exact thickness of a tissue section should be known for a correct assessment of the dependence of polarimetric properties (retardance, dichroism, and depolarization) on tissue thickness.

#### 4.2.1. Measurements of skin sample thickness

We have used a stylus profilometer (Bruker's DektakXT®, USA) to measure the thickness of thin tissue sections and checked whether it matches the nominal thickness (NT) values (5 - 30  $\mu\text{m}$ ).

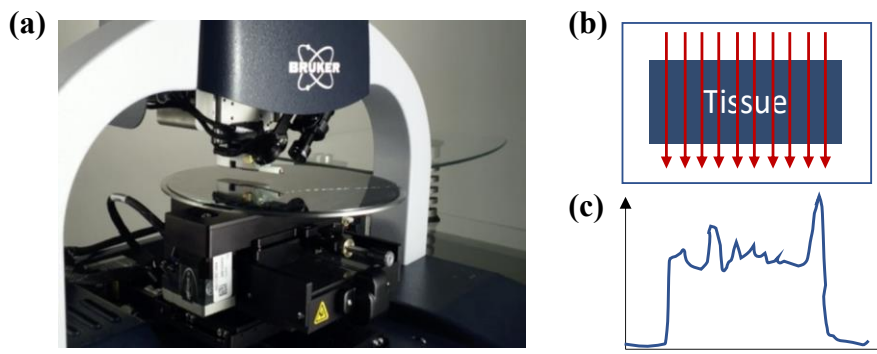


**Figure 4.4** (a) Photo of stylus profilometer; (b) scanning patterns (10 times), red arrows show the direction of the stylus passes and (c) 2D depth profile of the sample.

The number of depth scans for a generation of a 3D image was set to 10, and the width of the scanning area was fixed at 500  $\mu\text{m}$  (see Fig. 4.4), close to the field-of-view (FoV) of the transmission Mueller microscope. We scanned the same regions of tissue sections that were measured with the Mueller microscope in transmission. The resulting 3D depth profiles provided information on homogeneity and uniformity of sample thickness. It is worth noting that the thickness uniformity of thin tissue sections depends strongly on a positioning of a paraffin block with embedded tissue with respect to the microtome blade during the preparation of the sample.

The first batch of the thin sections of artificial skin tissue was prepared (Fraunhofer ISC, Germany) by placing the paraffin-embedded tissue disk for cut with microtome as shown in Fig. 4.5 (a). Then, the obtained thin sections of skin tissue model of different NT (5  $\mu\text{m}$  – 30  $\mu\text{m}$ ) were measured with the stylus profilometer as described above. The values of tissue thickness were averaged over ten profilometer scans for each measured thin tissue section. The mean values of sample thickness and corresponding values of standard deviation are given in Tab. 4.1.

**Table 4.1** Thickness of thin sections of HSE tissue (batch I), measured and nominal values.

Nominal thickness ( $\mu\text{m}$ )	Mean measured thickness ( $\mu\text{m}$ )	Standard deviation ( $\mu\text{m}$ )
5	2.38	0.97
10	5.40	2.26
16	X	X
20	X	X
30	13.61	6.29

As shown in Fig. 4.5 (b), the samples were already deformed before measuring depth profile by profilometer. For example, the 3D depth profile of a sample (NT 5  $\mu\text{m}$ ) (see Fig. 4.5 (c)) shows an inhomogeneous morphology.

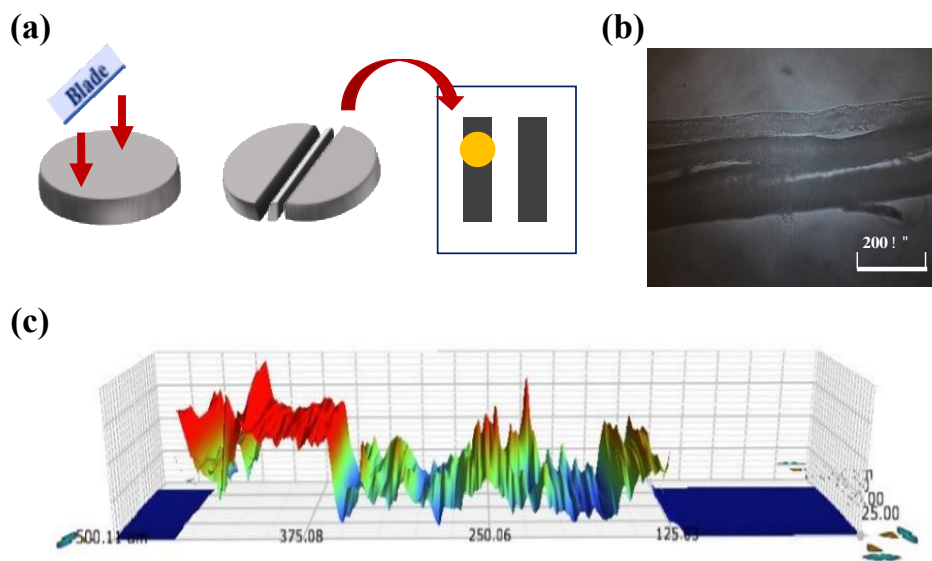


**Figure 4.5** (a) Explanation of tissue sectioning along with the vertical to the orientation of collagens; red arrow shows section direction, yellow circle represents the zone where is scanned with profilometer, (b) 20X microscopic image of the thin tissue section (NT - 5  $\mu\text{m}$ ), yellow circle indicates the location of a spot measured with Mueller microscope; (c) corresponding 3D thickness profile measured with profilometer.

The central part of a sample is significantly thinner compared to the edge parts. These variations of sample thickness make the mean values of measured thickness differ significantly from the nominal ones. The difference becomes larger for thicker samples. Furthermore, two tissue sections (NTs 16  $\mu\text{m}$  and 20  $\mu\text{m}$ ) were not measured with profilometer because the tissue stripes were detached from the glass during the scanning with profilometer. To sum up the results, we figured out that the tissue sections from the first batch are non-homogenous in thickness and cannot be used in our studies.

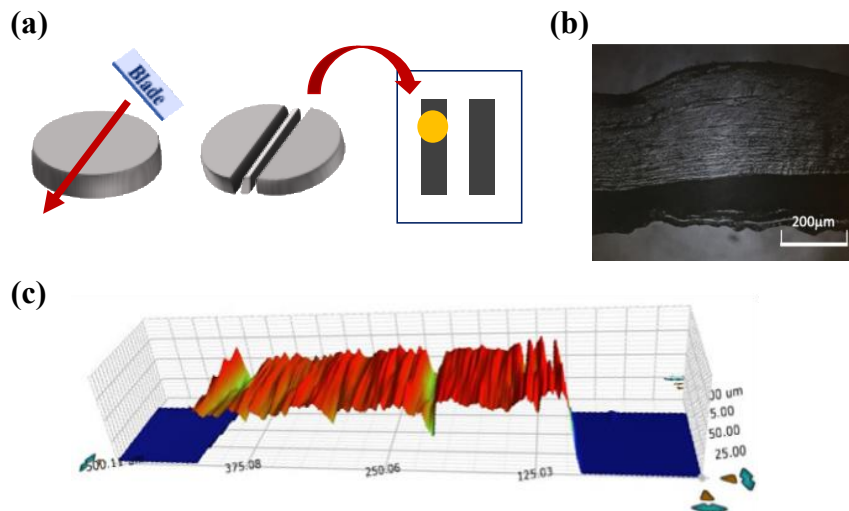


**Figure 4.6** (a) Explanation of tissue sectioning along with the parallel to the orientation of collagens; red arrow shows section direction, yellow circle represents the zone where is scanned with profilometer, (b) 20X microscopic image of the thin tissue section (NT - 10  $\mu\text{m}$ ) yellow circle indicates the location of a spot measured with Mueller microscope; (c) corresponding 3D thickness profile measured with profilometer.

The sectioning of a paraffin block with embedded tissue with a microtome can generate intractable problems for a correct evaluation of tissue section thickness. To address these problems (e.g., high non-uniformity of tissue section thickness, non-reproducible scans, torn tissue), the second batch of thin skin tissue model sections was prepared (Fraunhofer ISC, Germany) by changing the positioning of a paraffin block with embedded tissue with respect to the microtome blade as shown in Fig. 4.6 (a).

The second batch of the thin sections of HSE was also measured with the stylus profilometer, and mean values of thickness and corresponding values of standard deviation were calculated for each thin tissue section. Changing the cutting direction of the paraffin-embedded tissue, we reduced tissue damage and scraping by the microtome blade and improved significantly the uniformity of the thickness of thin tissue sections (Fig. 4.6(b), (c)).

However, the mean values of thickness, presented in Tab. 4.2, still differ from the nominal ones, and this difference becomes larger for thicker samples. The thin sections of tissue-containing paraffin blocks were cut by the microtome with a micrometer-controlled precision. The analysis of data from Tab. 4.2 suggests that the deparaffinization step of sample preparation procedure induces significant variations in the thickness of tissue sections, most probably because of the different local intake of paraffin by tissue.

**Table 4.2** Thickness of thin sections of HSE tissue (batch II), measured and nominal values

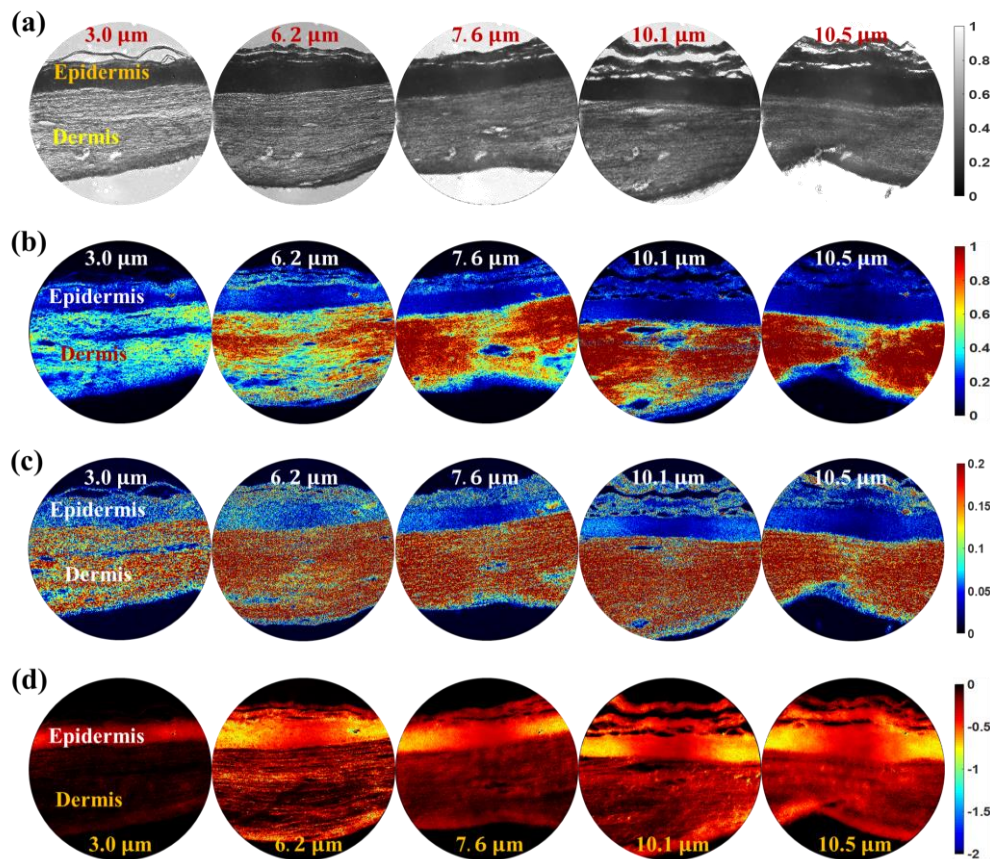
Nominal thickness ( $\mu\text{m}$ )	Mean measured thickness ( $\mu\text{m}$ )	Standard deviation ( $\mu\text{m}$ )
5	3.0	0.8
10	6.2	1.1
16	7.6	2.3
20	10.1	4.2
30	10.5	2.9

## 4.2.2. Thickness dependence of polarization and depolarization parameters

A set of five HSE thin histological sections (batch II) with the varying nominal thickness (5, 10, 16, 20, and 30  $\mu\text{m}$ ) was measured with the Mueller microscope in transmission configuration. All experimental Mueller matrix images of histological sections were processed by applying the LMMD pixel-wise.

Then, we calculated the parameters that are invariant under rotation of a sample in the imaging plane, namely, total linear retardance  $R_T = \sqrt{p_4^2 + p_5^2}$  ( $p_4$  and  $p_5$  are sample linear retardance in the  $0-90^\circ$  and the  $\pm 45^\circ$  frames, respectively, see Eq. (1.84)) and total linear dichroism  $D_T = \sqrt{p_1^2 + p_2^2}$  ( $p_1$  and  $p_2$  are sample linear dichroism in the  $0-90^\circ$  and the  $\pm 45^\circ$  frames, respectively, see Eq. (1.79)). The dimensionless diagonal coefficients  $L_u(2,2)$  and  $L_u(3,3)$  that are also labeled as  $\alpha_{22}$  and  $\alpha_{33}$  (see Eq. (1.88)) represent the linear depolarization properties in the  $0-90^\circ$  and the  $\pm 45^\circ$  frames, respectively. The coefficient  $L_u(4,4)$ , labeled as  $\alpha_{44}$ , stands for the circular depolarization property.

The corresponding maps of the total linear retardance, total linear dichroism, and depolarization parameters (coefficients  $\alpha_{22}$ ,  $\alpha_{33}$ , and  $\alpha_{44}$ ) of five HSE tissue sections are shown in Fig. 4.7. Three different zones are clearly distinguishable in the maps of the total linear retardance  $R_T$ , total linear dichroism  $D_T$ , and depolarization coefficients  $\alpha_{22}$ ,  $\alpha_{33}$ , and  $\alpha_{44}$ : 1) bare glass with no tissue, 2) dermis, and 3) epidermis of the HSE.



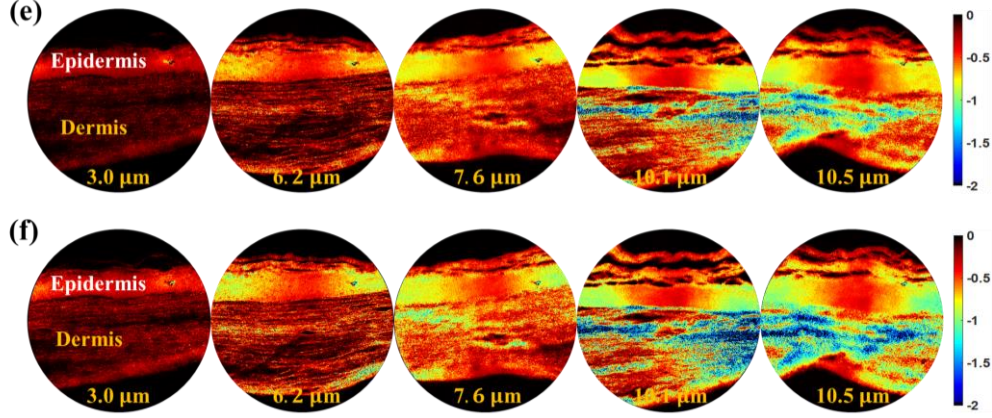


**Figure 4.7** Maps of (a) total intensity, (b) total linear retardance  $R_T$  (in radians), (c) dimensionless total linear dichroism  $D_T$ , and dimensionless diagonal coefficients (d)  $\alpha_{22}$ , (e)  $\alpha_{33}$ , (f)  $\alpha_{44}$  of the matrix  $L_u$ , calculated from the experimental Mueller matrix data by applying pixel-wise LMMD. Labels represent the mean thickness of thin histological sections measured with a stylus profilometer. FoV is about  $600 \mu\text{m}$ .

The zone of bare microscope glass in polarimetric images does not possess any measurable total linear retardance ( $R_T = 0$ ), total linear dichroism ( $D_T = 0$ ), as well as does not depolarize transmitted light ( $\alpha_{22}$ ,  $\alpha_{33}$ , and  $\alpha_{44} = 0$ ). The dermal part of a skin model histological section demonstrates strong retardance. This effect is related to the anisotropy of the refractive index of HSE tissue due to the presence of the aligned collagen fibers in dermal zone. In all images (see Fig. 4.7), there is a thin layer of epidermis on top of dermis. The former layer does not show any significant retardance for any tissue section thickness. This is an expected result because the epidermal layer does not contain any aligned collagen fibers.

To quantify the optical parameters of the HSE tissue sections, at first, we manually selected the region of interest (ROI), namely, dermis layer and analyzed the pixels within this region. We calculated the average values of the optical parameters  $R_T$ ,  $D_T$ ,  $\alpha_{22}$ ,  $\alpha_{33}$ , and  $\alpha_{44}$  for dermal layer (see Tab. 4.3). The absolute values of the ROI-averaged circular depolarization parameter  $|\alpha_{44}|$  are larger compared to the absolute values of linear depolarization parameters  $|\alpha_{22}|$  and  $|\alpha_{33}|$ . It shows that the linear polarization of incident light is preserved better compared to the circular polarization, thus, underlining the dominance of the Rayleigh scattering regime over the Mie scattering regime in our samples [10]. The total ROI-averaged linear dichroism for dermis zone has non-zero values for all HSE tissue thicknesses. The origin of this phenomenon will be discussed later in this Chapter.

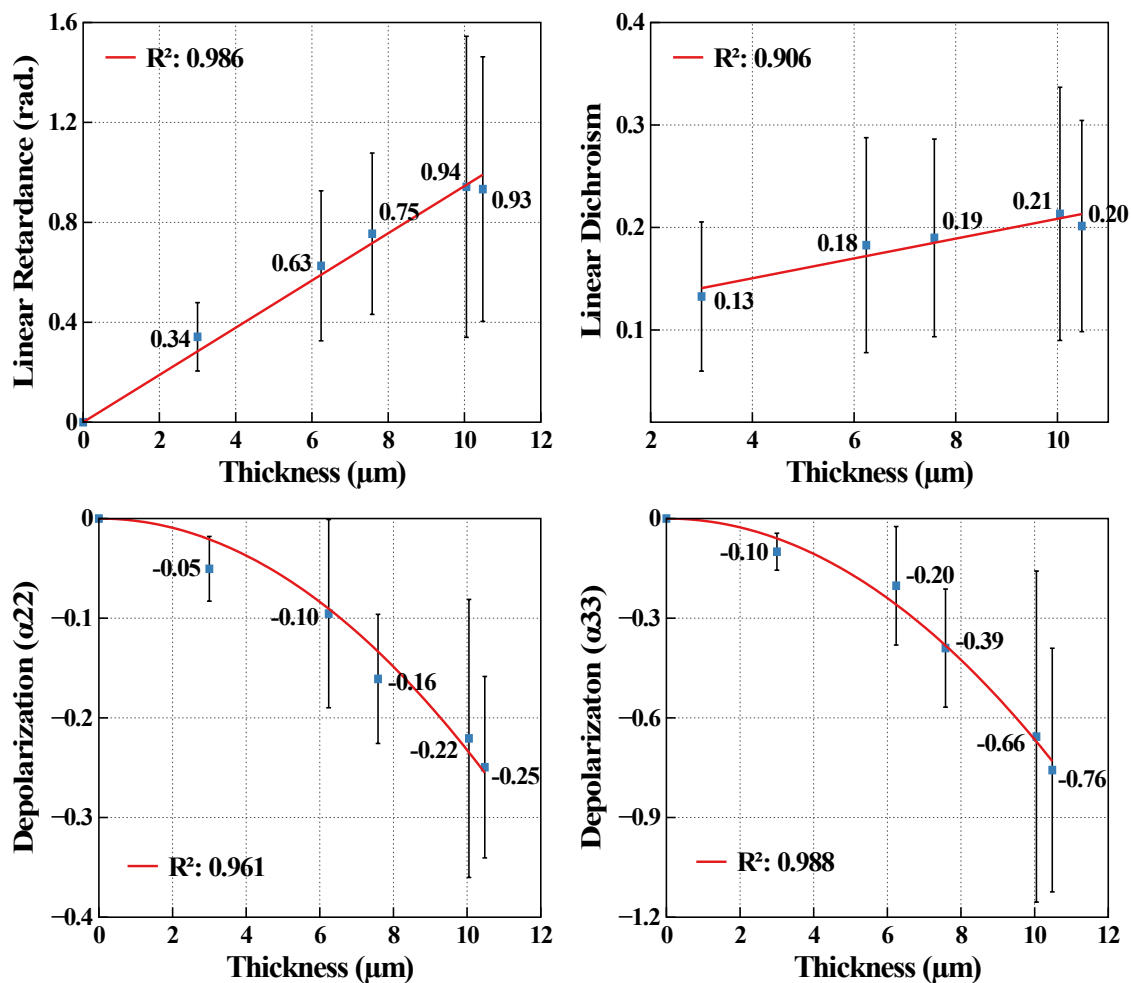
**Table 4.3** The values of optical parameters  $R_T$ ,  $D_T$ ,  $\alpha_{22}$ ,  $\alpha_{33}$ , and  $\alpha_{44}$  averaged over manually delineated zone of dermis in the images of the five HSE tissue sections of different thicknesses

Real thickness ( $\mu\text{m}$ )	$R_T$	$D_T$	$\alpha_{22}$	$\alpha_{33}$	$\alpha_{44}$
3.0	0.34	0.13	-0.05	-0.10	-0.14
6.2	0.63	0.18	-0.10	-0.20	-0.28
7.6	0.75	0.19	-0.16	-0.39	-0.53
10.1	0.94	0.21	-0.22	-0.66	-0.91
10.5	0.93	0.20	-0.25	-0.76	-1.03

The absolute values of the depolarization parameters spatially averaged over the dermal zone continuously increase with the thickness. As expected, there was no circular retardance and no circular dichroism observed for all tissue sections (coefficients  $p_3 = p_6 = 0$ , Eq. (1.84)). It can be explained by the fact that the optical activity in biological tissues is related to the presence of chiral molecules (e.g., glucose), which were absent in the studied fixed HSE tissue sections.

We have focused on the analysis of the dermal zone of skin model sections because this part of tissue possesses both polarization and depolarization properties contrary to the epidermis layer, which only depolarizes light. Thus, to verify the predictions of the differential Mueller matrix formalism regarding thickness dependence of the polarization and depolarization parameters of fluctuating anisotropic media, first we need to estimate the mean values of polarization and depolarization parameters in the dermal zone of HSE tissue.

As was previously mentioned, the real thickness of tissue section should be identified for a correct assessment of the dependence of polarimetric parameters on thickness. The mean values and the standard deviations of the polarization and depolarization parameters calculated from the pixel-wise LMMD for the dermal layer zone in the polarimetric images of each tissue section were plotted versus the corresponding values of the sample thickness measured with a stylus profilometer (see Fig. 4.8).



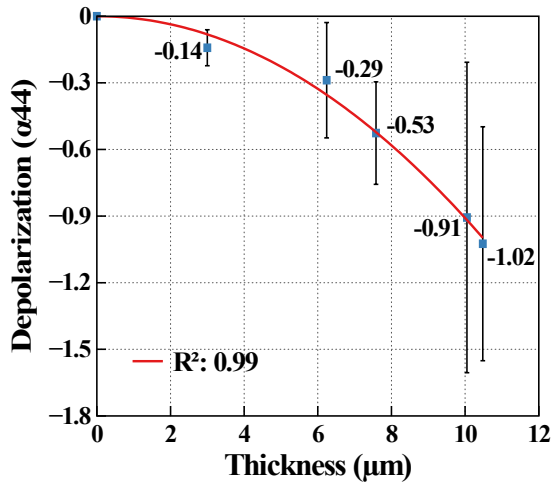


**Figure 4.8** Thickness dependence plots of (a) total linear retardance (radians), (b) dimensionless total linear dichroism, (c-e) dimensionless depolarization parameters  $\alpha_{22}$ ,  $\alpha_{33}$ , and  $\alpha_{44}$  averaged over a zone of dermal layer of HSE tissue sections. Experimental data are shown by blue symbols, solid red lines represent the results of (a) linear and (b-d) quadratic fit.

As mentioned above, the presence of non-zero linear dichroism can be explained by scattering on the non-spherical scatterers, like elongated collagen fibers [11]. While the intercept of the linear regression curve with the Y-axis for the total linear retardance  $R_T$  is equal to zero, it is not the case for the linear regression curve for the linear dichroism  $D_T$ . We attribute this effect to the scattering of transmitted light on a rough surface of the tissue. (see Fig. 4.9). Surface scattering of an anisotropic medium does not affect the retardance values but contributes to the increase of values of linear dichroism [12]. As shown in the Figs. 4.8, the value of total linear retardance  $R_T$  and total linear dichroism  $D_T$  depends on the thickness linearly. The values of linear depolarization coefficients  $\alpha_{22}$ ,  $\alpha_{33}$  are not equal, thus indicating the dependence of linear depolarization on the orientation of a sample in the imaging plane (or anisotropy of linear depolarization). All depolarization coefficients  $\alpha_{22}$ ,  $\alpha_{33}$ , and  $\alpha_{44}$  vary quadratically with thickness.

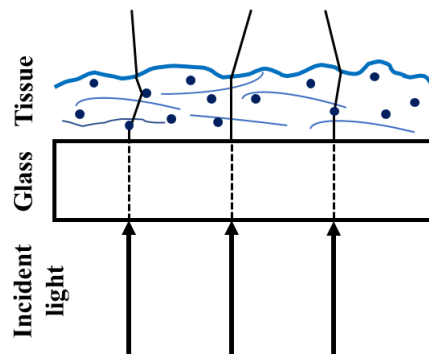


**Figure 4.9** Bulk and surface scattering of light transmitted through a thin section of HSE tissue.

### 4.3. Image segmentation (DBSCAN) for advanced analysis of tissue polarimetric properties

First, we selected the region of interest (ROI) manually, extracted information (e.g., scalar retardance, dichroism, and depolarization) for the pixels within the region, and then calculated the mean values of the optical parameters and its standard deviation over the ROI. This approach was adopted to analyze the polarization and depolarization parameters of the dermal layer of the HSE tissue sections. However, manual selection of the pixels does not account for the inhomogeneous thickness or uneven surface of the sample that, in turn, leads to quite wide distributions of the values of tissue's optical parameters and high values of the standard deviation (see Tab. 4.4).

**Table 4.4** The values of standard deviation of the optical parameters  $R_T$ ,  $D_T$ ,  $\alpha_{22}$ ,  $\alpha_{33}$ , and  $\alpha_{44}$  of dermis zone for the five thin tissue sections of different thicknesses

Real thickness ( $\mu\text{m}$ )	$R_T$	$D_T$	$\alpha_{22}$	$\alpha_{33}$	$\alpha_{44}$
3.0	0.14	0.07	0.03	0.06	0.08
6.2	0.30	0.11	0.09	0.18	0.26
7.6	0.32	0.10	0.07	0.18	0.23
10.1	0.60	0.12	0.14	0.50	0.70
10.5	0.53	0.10	0.09	0.37	0.53

Therefore, to delineate more precisely both epidermal and dermal zones of HSE tissue sections in microscopic images, we have applied the statistical algorithm of density-based spatial clustering for the applications with noise (MATLAB subroutine DBSCAN) [13] for the image segmentation.

An appropriate choice of the parametric space for the implementation of the DBSCAN algorithm is one of the critical factors to obtain meaningful clustering results. To illustrate our methodology on choosing the optimal input dataset of optical parameters for the statistical analysis and image segmentation, we plotted the 2D histograms of different combinations of the measured optical parameters (transmitted intensity, total linear retardance, total linear dichroism, linear depolarization  $\alpha_{22}$ ,  $\alpha_{33}$ , and circular depolarization  $\alpha_{44}$ ) for the 10  $\mu\text{m}$  thick histological section of HSE tissue (see Fig. 4.10).

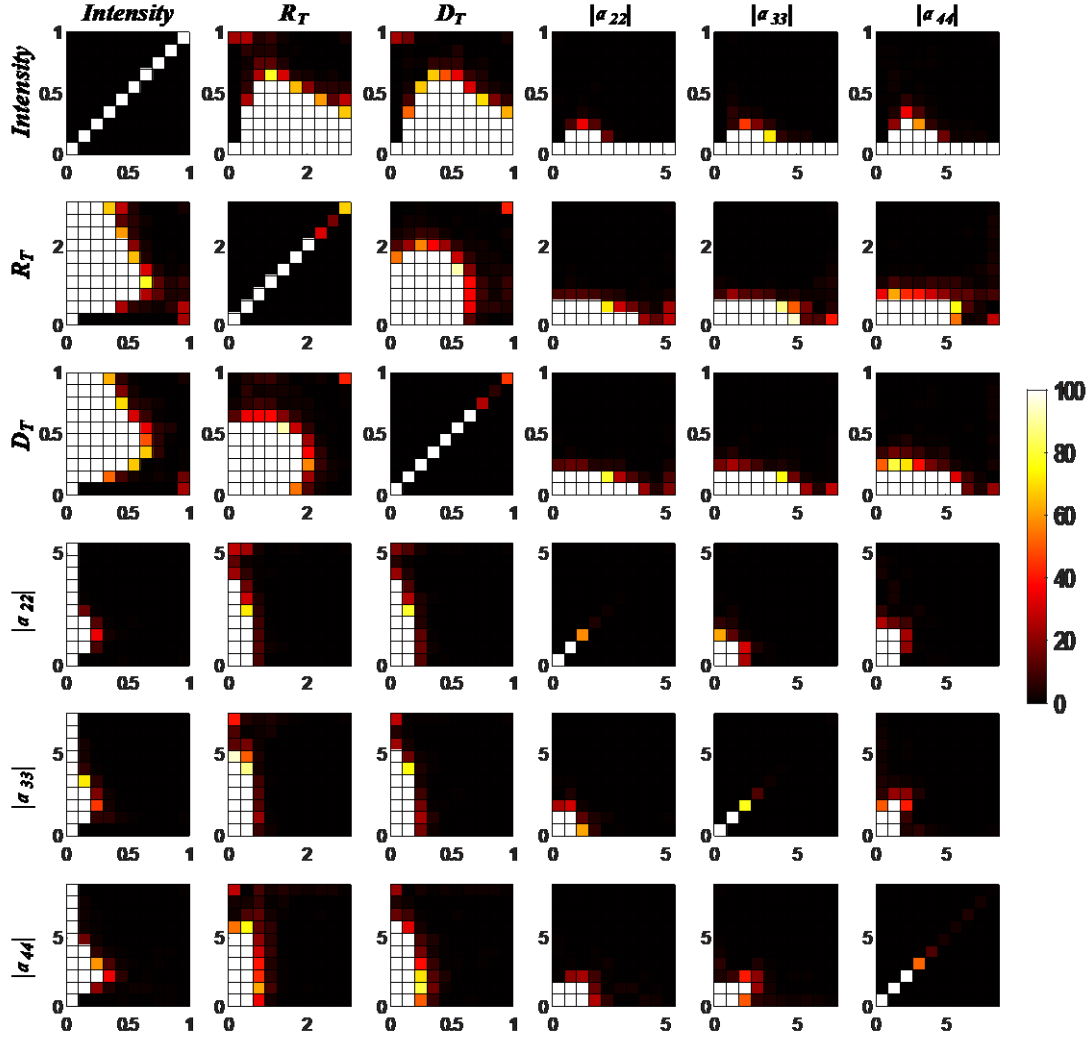


**Figure 4.10** The  $6 \times 6$  matrix of 2D histograms of the total transmitted intensity, linear retardance, linear dichroism, and the absolute values of the linear and circular depolarization ( $|\alpha_{22}|$ ,  $|\alpha_{33}|$ , and  $|\alpha_{44}|$ ) for dermal layer of HSE section of  $10 \mu\text{m}$  NT.

The 2D histogram shows the probability distribution within [0-100] range. Both  $x$ - and  $y$ -axes represent the values of each optical parameter in its [min max] range. The  $x$ - and  $y$ -axes of 2D histograms, located on the diagonal of  $6 \times 6$  matrix shown in Fig. 4.10, represent the values of the same optical parameter. Obviously, these values are perfectly correlated (i.e., correlation coefficient is equal to 1) and all non-zero values of the probability distribution function are located along the  $45^\circ$  diagonal line of the 2D histogram.

Since the DBSCAN algorithm is based on the estimation of data density in a chosen parametric space, a well-spread distribution of a dataset is beneficial for data clustering. In this regard, the selection of the optical parameters that are less correlated (i.e., the probability distribution cannot be fitted by a linear function in 2D histogram), is necessary to form an optimal parametric space. The  $6 \times 6$  matrix of the 2D histograms in Fig. 4.10 demonstrates that the correlation between the total linear retardance and other optical parameters (second column) is similar to that of the total linear dichroism and other optical parameters (third column). All depolarization parameters  $\alpha_{22}$ ,  $\alpha_{33}$ , and  $\alpha_{44}$  also show similar correlation with

other properties. Therefore, the values of  $M_{00}$  (sample total transmittance),  $R_T$  (total linear retardance), and  $\alpha_{44}$  (circular depolarization) at each pixel of an image were used as input information for the DBSCAN algorithm. The latter parameter was chosen because it has higher values compared to the depolarization parameters  $\alpha_{22}$ ,  $\alpha_{33}$ . Furthermore, each parameter value range was standardized using z-score in order to prevent any parameter from being dominant in data clustering:

$$\begin{aligned} X &= (R_T - \langle R_T \rangle) / \sigma_{R_T}, \\ Y &= (\alpha_{44} - \langle \alpha_{44} \rangle) / \sigma_{\alpha_{44}}, \\ Z &= (M_{00} - \langle M_{00} \rangle) / \sigma_{M_{11}} \end{aligned} \quad (4.1)$$

where the angle brackets  $\langle \dots \rangle$  denote the mean value, whereas  $\sigma$  stands for the parameter standard deviation.

In our work, the maximal size of the dataset is defined by the resolution of the CCD camera (600 pixels  $\times$  800 pixels, i.e. 480000 pixels) that was used for the image registration in the transmission Mueller microscope. As was already explained in Chapter 3, the DBSCAN algorithm requires the calculation of distances between each pair of points from the dataset representing the image pixels in a multi-parametric space. Direct implementation of the DBSCAN algorithm for the microscopic image segmentation takes very long time and requires a prohibitive Random Access Memory (RAM) budget to calculate all distances. For example,  $2.304 \times 10^8$  distance calculations between each pair of dataset points are necessary for the dataset of 480000 points representing the image of 600 pixels  $\times$  800 pixels, and our current computational resources (RAM 32GB) do not allow us to calculate each distance. Elimination of the empty (i.e., out of FoV) pixels considerably reduces the total number of pixels that we need to analyze. The size of the dataset is reduced by almost factor of 2 (from 480000 to 250491). However, even the reduced dataset is still too large to calculate all distances for each pair of dataset points using a 32GB RAM.

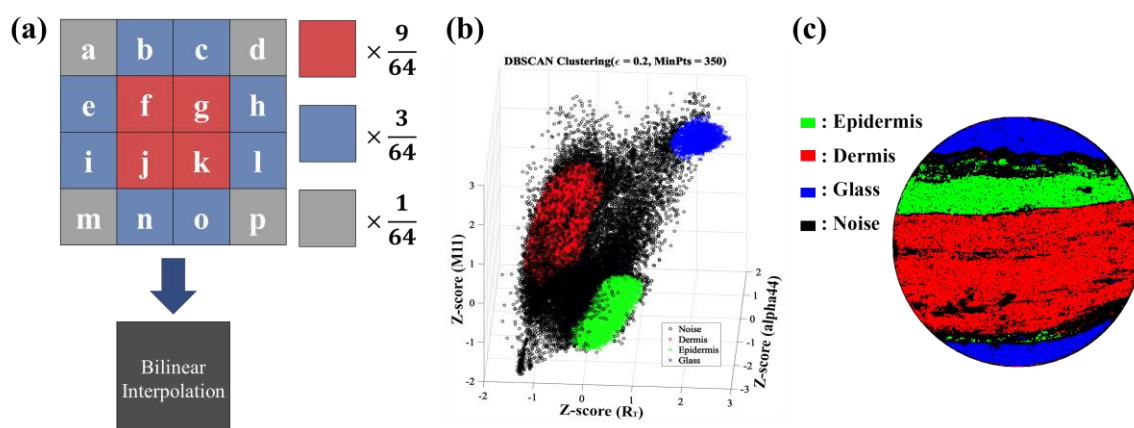


**Figure 4.11** (a) Illustration of the calculation of weighted average of pixel values in the nearest 2 by 2 neighborhood; (b) clustering results in a z-score space (see text),  $R_T$  – linear retardance,  $\alpha_{44}$  – circular depolarization parameter,  $M_{11}$  – total transmitted intensity. Black markers show noise, blue ones – bare glass, red ones – dermis, green ones - epidermis; (c) corresponding image segmentation: noise, bare glass, dermis, and epidermis zones are rendered in black, blue, red, and green, respectively.

Next, for the dataset size reduction we re-arranged the neighboring pixels into  $2 \times 2$  blocks (we called it "superpixel") and defined its value by a bilinear interpolation: an output pixel value is a weighted average of pixel values in the nearest 2 by 2 neighborhood (see Fig. 4.11 (a)). Thus, the reduced number (one quarter, or 63479) of pixels was used for the image segmentation with the DBSCAN algorithm. We ran the DBSCAN subroutine with the input parameters  $MinPts = 300$ , radius  $\varepsilon = 0.2$ , and obtained three well-defined clusters corresponding to the zones of 1) bare glass, 2) dermal layer, 3) epidermal layer, and random outliers (or noise). The results of the segmentation for a histological HSE section of  $10 \mu\text{m}$  NT are presented in Figs 4.11 (b), (c). The reconstructed images of HSE sections of five different nominal thicknesses are shown in Fig. 4.12.

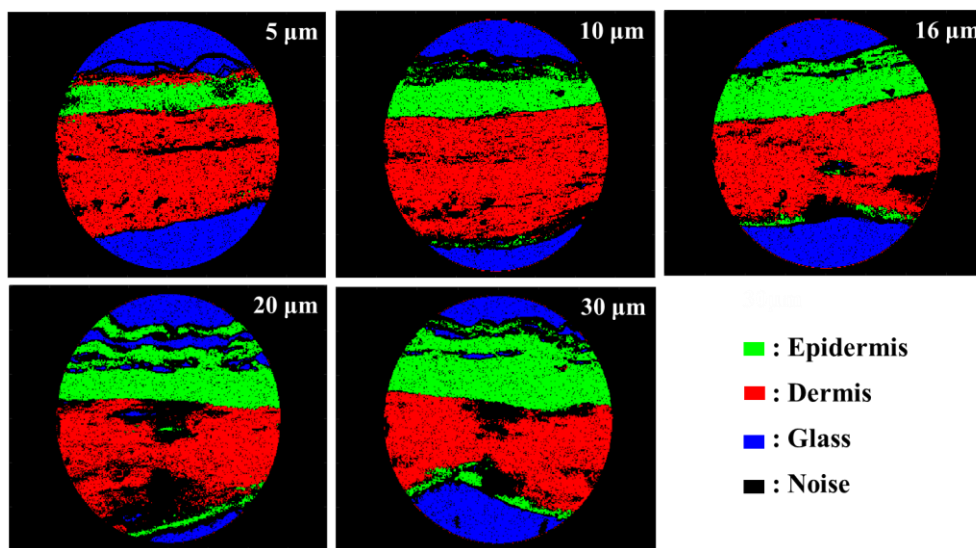


**Figure 4.12** Reconstructed images of the HSE sections of different NT: 5, 10, 16, 20, 30  $\mu\text{m}$ .

The segmented images make it easy to distinguish between the different sample zones (epidermis, dermis) and bare glass. As was mentioned above, all depolarization parameters  $\alpha_{22}$ ,  $\alpha_{33}$ , and  $\alpha_{44}$  demonstrate similar correlation with other optical parameters (see Fig. 4.10). Consequently, the clustering results are almost the same, if we chose the values of parameter  $\alpha_{22}$  or  $\alpha_{33}$  instead of parameter  $\alpha_{44}$  as input information.

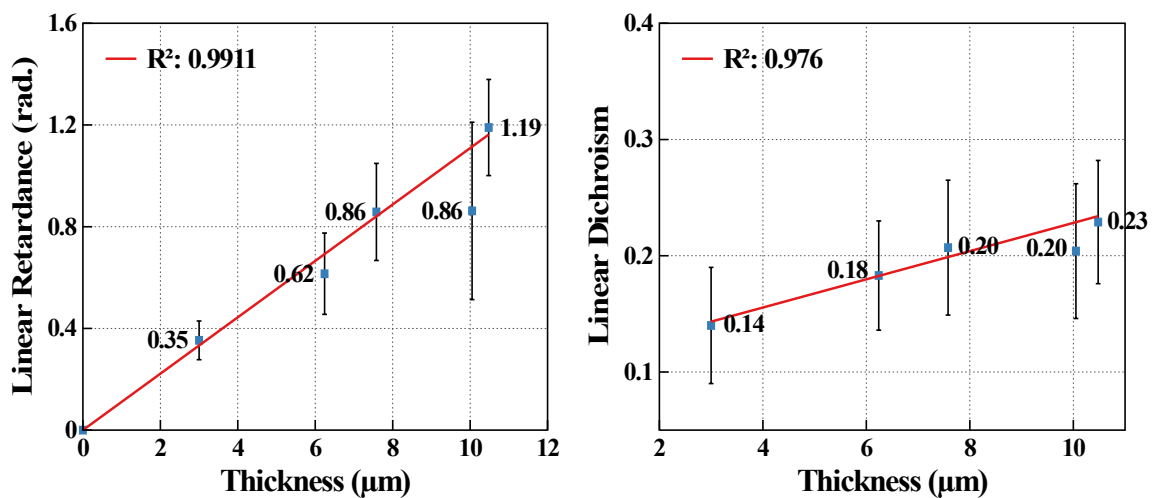
The thin green layer located above the dermis region is also present in the segmented images of the skin tissue section of the nominal thickness of  $16 \mu\text{m}$ ,  $20 \mu\text{m}$ , and  $30 \mu\text{m}$ . Despite being classified as the epidermis, this layer makes part of the dermis. Most probably, the edge part of the dermal layer has a different thickness because of cutting artifacts that, in turn, alters all optical parameters used for image segmentation. After noise filtering and selecting the group of pixels rendered in red color that corresponds to the dermal layer of HSE thin section, the mean values and standard deviation of polarization and depolarization parameters were calculated for the dermal layer in the images of all tissue sections (see Tab. 4.5).

**Table 4.5** The values of the optical parameters  $R_T$ ,  $D_T$ ,  $\alpha_{22}$ ,  $\alpha_{33}$ , and  $\alpha_{44}$  averaged over the dermis zone selected with the DBSCAN algorithm in the images of the five HSE sections of different thickness

Real thickness ( $\mu\text{m}$ )	$R_T$	$D_T$	$\alpha_{22}$	$\alpha_{33}$	$\alpha_{44}$
3.0	$0.35 \pm 0.08$	$0.14 \pm 0.05$	$-0.05 \pm 0.02$	$-0.10 \pm 0.03$	$-0.14 \pm 0.04$
6.2	$0.62 \pm 0.16$	$0.18 \pm 0.05$	$-0.08 \pm 0.03$	$-0.15 \pm 0.07$	$-0.21 \pm 0.09$
7.6	$0.86 \pm 0.19$	$0.21 \pm 0.06$	$-0.16 \pm 0.04$	$-0.37 \pm 0.07$	$-0.51 \pm 0.09$
10.1	$0.86 \pm 0.35$	$0.20 \pm 0.06$	$-0.18 \pm 0.09$	$-0.47 \pm 0.19$	$-0.63 \pm 0.25$
10.5	$1.19 \pm 0.19$	$0.23 \pm 0.05$	$-0.21 \pm 0.05$	$-0.67 \pm 0.14$	$-0.91 \pm 0.16$

We also plotted the averaged values of polarization and depolarization parameters of the dermis regions (red color in Fig. 4.12) versus the thickness of HSE sections measured with stylus profilometer (see Fig. 4.13).

Compared to the previous results obtained by manual selection of the zone of dermal layer (see Tab. 4.4), there is a significant reduction of the standard deviation values. It proves that we have effectively removed the outliers from our dataset by applying the DBSCAN algorithm. The larger reduction of the standard deviation values was observed for thicker tissue sections (6.2  $\mu\text{m}$  and 10.1  $\mu\text{m}$ ), thus, indicating the increase in tissue thickness non-uniformity with tissue thickness. We demonstrated that the DBSCAN algorithm is an efficient method to eliminate the noise from the dataset before the analysis of optical parameters in a selected ROI. Fig. 4.13 shows that the polarization parameters (total linear retardance  $R_T$  and total linear dichroism  $D_T$ ) depend linearly on thickness, whereas anisotropic depolarization coefficients, which means that  $\alpha_{22}$ ,  $\alpha_{33}$  and  $\alpha_{44}$  show different values, vary quadratically with the thickness. We attribute the non-zero values of standard deviation for the optical parameters within the dermal zone delineated with the DBSCAN algorithm (see Tab. 4.5) to the spatial fluctuations of the skin section optical properties (e.g., local variation in the density of fibroblast cells, spread in the collagen fiber orientation) within the imaging plane.



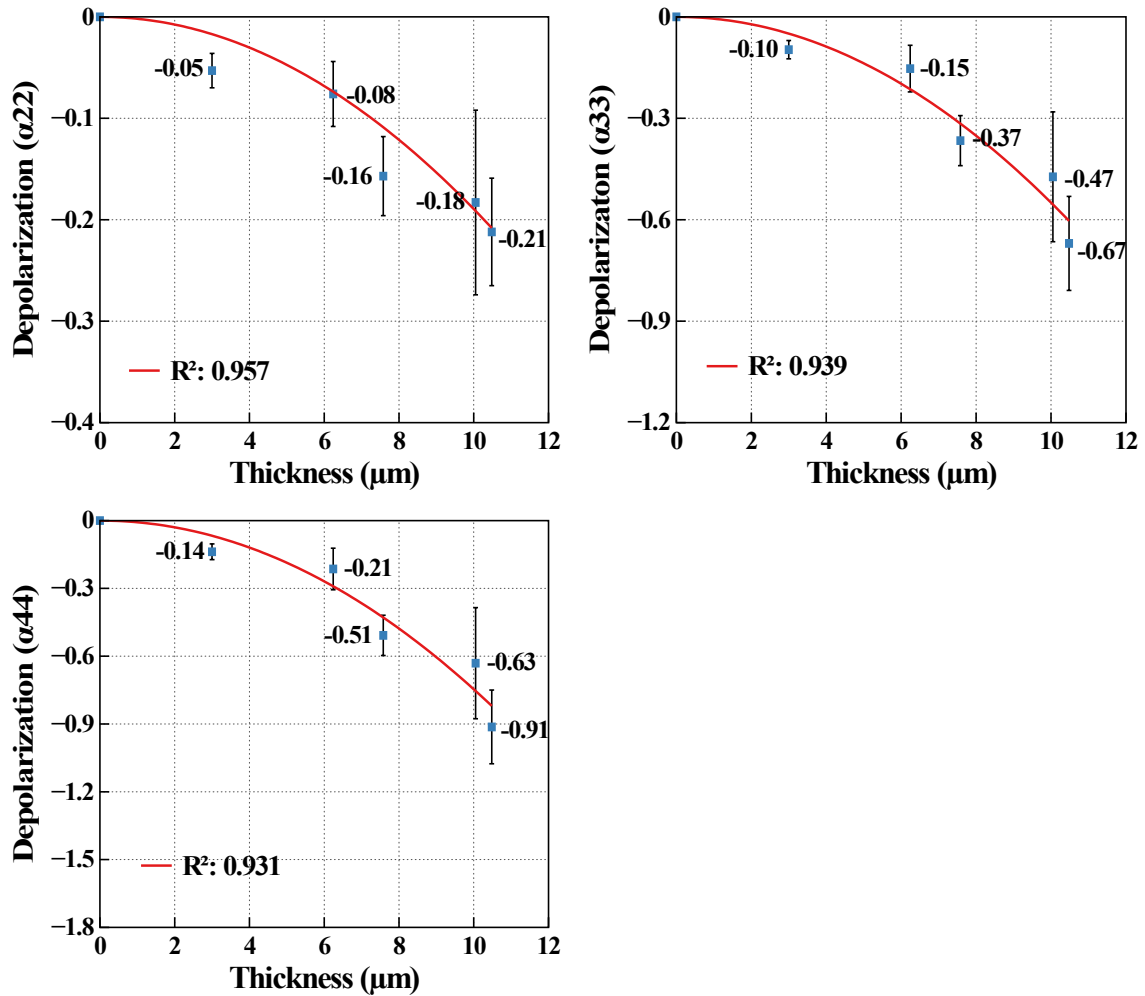


**Figure 4.13** Thickness dependence plots of (a) total linear retardance (radians), (b) dimensionless total linear dichroism, (c-e) dimensionless depolarization coefficients  $\alpha_{22}$ ,  $\alpha_{33}$  and  $\alpha_{44}$  averaged over a dermal layer of the histological sections. Experimental data are shown by blue symbols, solid red lines represent the results of (a) linear and (b-d) quadratic fit.

#### 4.4. Mitigating the impact of the spatial fluctuations of tissue section thickness.

The pathological changes in tissue (cancer, fibrosis, inflammation) will affect both its polarization and depolarization properties. The ultimate goal of digital histology analysis consists of delimiting the abnormal zones in a microscope image of thin histological section using the maps of optimal optical markers that provide the highest image contrast.

In the transmission measurement configuration, the thickness of a thin tissue section would be equivalent to the optical path length that, together with the tissue's optical properties (e. g. the anisotropy of the refractive index, scattering coefficient, absorption coefficient) will have impact on the polarization and depolarization parameters calculated from the experimental matrices measured with Mueller microscope. As we have shown in the previous section, both polarization and depolarization parameters of anisotropic scattering

media may also vary with the thickness of tissue because of the different path length of the probing light beam. Therefore, controlling the thickness of histological sections is one of the crucial issues for a precise tissue diagnostics with polarized Mueller microscopy. However, in clinical practice, it is impossible to measure a real depth profile of histological sections with a profilometer as we did in these studies because the standard tissue sections are mounted on a microscope glass slide and protected by a coverslip (i.e., the tissue is "sandwiched" between two glasses).

We explore several approaches to eliminate the impact of variation of tissue's thickness on its measured polarization and depolarization parameters. During the calibration of the transmission Mueller microscope, a bare glass was used as the reference sample. Since the Mueller matrix of a bare glass was included in the calibration data,  $M_{00}$  element of the Mueller matrix represents a transmittance  $I/I_0$  of the tissue sample (without the glass), where  $I_0$  is the intensity of incident light beam,  $I$  is the intensity of transmitted light beam. Transmittance verifies the Beer-Lambert law:

$$\ln(I/I_0) = -\mu_T d = \ln(M_{00}) \quad (4.2)$$

where  $I_0$  and  $I$  represent the intensities of input and output light beam, respectively,  $\mu_T = \mu_a + \mu_s$  is a sum of the absorption coefficient  $\mu_a$  and scattering coefficient  $\mu_s$  of the medium,  $d$  is the physical thickness of a sample. The intensity  $I_0$  of the input light beam was controlled by the exposure time. However, during the measurements of tissue sections of different thicknesses, the exposure time was varied in order to prevent the saturation of the detected signal. That is why measured  $M_{00}$  values for different tissue sections were re-scaled to match an exposure time of 250 ms used in the calibration process. Finally, applying Eq. (4.2) pixel-wise to  $M_{00}$  image, one can produce a microscopic image of the optical density of the studied tissue section.

We assume that all skin model tissue sections are homogeneous along the incident light beam path (few microns scale), but tissue properties may vary in the imaged plane (FoV few hundreds of microns). Because of the linear dependence of retardance and quadratic dependence of depolarization on thickness, the following relations hold for each pixel  $(k, l)$  of the microscopic image of histological sections:

$$R_T^{k,l} = A^{k,l} d^{k,l}, \quad \alpha_{ii}^{k,l} = B^{k,l} (d^{k,l})^2, \quad (i = 2, 3, 4) \quad (4.3)$$

where  $d^{k,l}$  is tissue local thickness,  $A^{k,l}$  and  $B^{k,l}$  are linear and quadratic fit coefficients for a pixel  $(k, l)$ . Consequently, the following quantities should not directly depend on the local thickness of the tissue section:

$$R_T^{k,l} / \ln(M_{11}^{k,l}) = -A^{k,l} / \mu_T^{k,l} \quad (4.4)$$

$$\alpha_{ii}^{k,l} / \ln^2(M_{11}^{k,l}) = -B^{k,l} / (\mu_T^{k,l})^2 \quad (4.5)$$

$$(R_T^{k,l})^2 / \alpha_{ii}^{k,l} = (A^{k,l})^2 / B^{k,l} \quad (4.6)$$

$$\alpha_{ii}^{k,l} / (R_T^{k,l})^2 = (B^{k,l})^2 / A^{k,l} \quad (4.7)$$

The left- and right-hand sides of the Eqs (4.4) - (4.7) are invariant under tissue thickness fluctuations. Using these equations, we have calculated the microscopic maps of all HSE histological sections of different thicknesses (see Fig. 4.14). While the values of  $\mu_T^{k,l}$ ,  $A^{k,l}$ , and  $B^{k,l}$  may still vary across the microscopic image, these variations are related to the variations in tissue's optical properties, not in tissue's physical thickness.

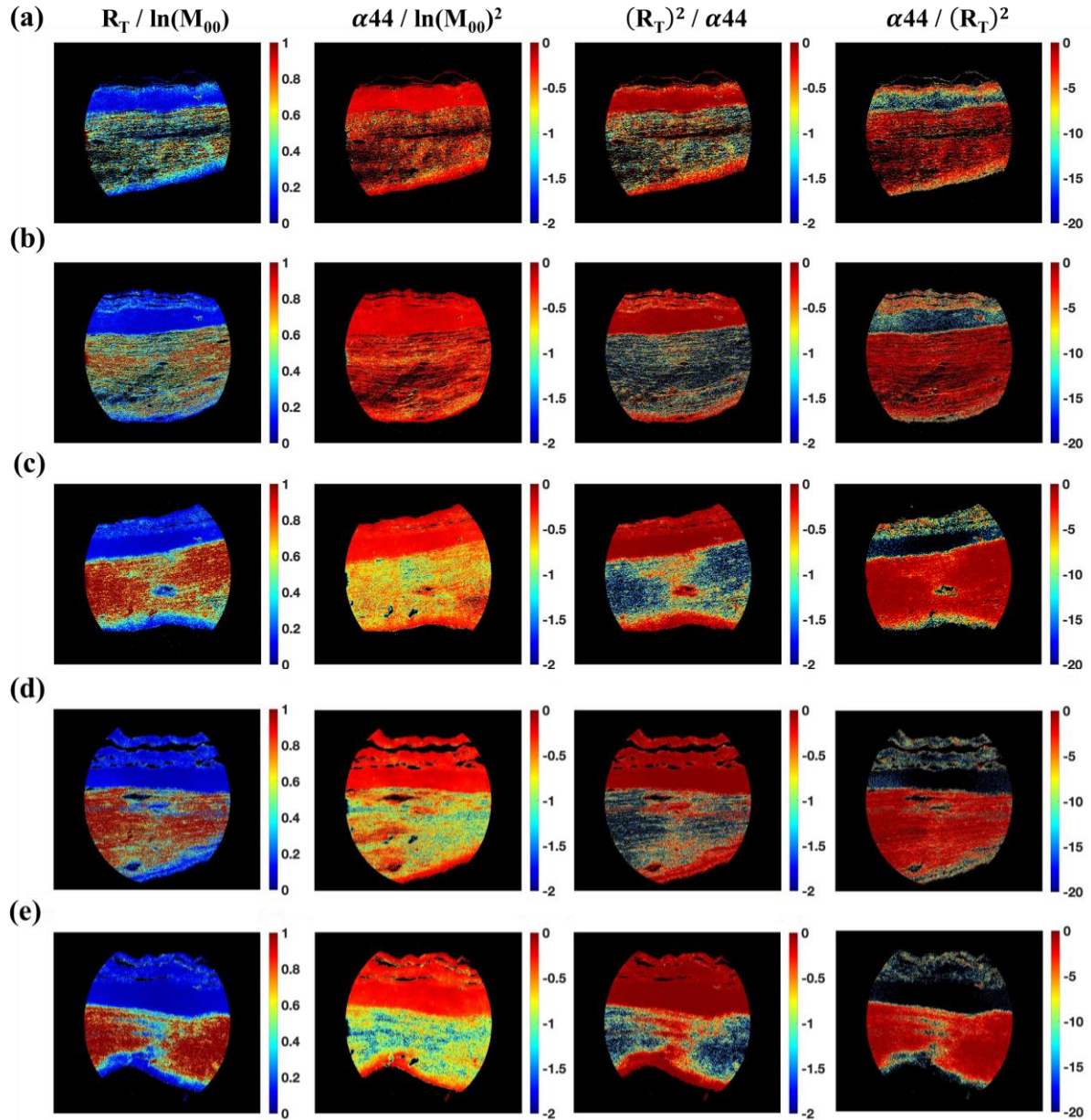


**Figure 4.14** Maps of  $R_T / |\ln(M_{00})|$ ,  $\alpha_{44} / \ln(M_{00})^2$ ,  $(R_T)^2 / \alpha_{44}$ , and  $\alpha_{44} / (R_T)^2$  parameters for HSE histological sections of (a) 5  $\mu\text{m}$ , (b) 10  $\mu\text{m}$ , (c) 16  $\mu\text{m}$ , (d) 20  $\mu\text{m}$ , and (e) 30  $\mu\text{m}$  of nominal thickness. Field of view is about 600  $\mu\text{m}$ . All these ratios are invariant under tissue thickness fluctuations.

We assume that the distributions of the ratios  $R_T / \alpha_{44}$ ,  $R_T / |\ln(M_{00})|$ ,  $\alpha_{44} / \ln(M_{00})^2$ ,  $(R_T)^2 / \alpha_{44}$  and  $\alpha_{44} / (R_T)^2$  values that are thickness invariant, should become more peaked

compared to the distributions of both  $R_T$  and  $\alpha_{44}$  values, which depend on the fluctuations of both thickness and optical tissue properties within the dermal layer of HSE sections. To check this assumption, we performed a statistical analysis of these distributions. We used the value of entropy  $H(p) = -\sum_{i=1}^N p_i \log(p_i)$  of a discrete probability distribution  $p$  as an inverse metric of distribution peakedness [14]. Indeed, more peaked distributions are less undetermined. Hence, their entropy should be lower compared to broader distributions. The calculated values of entropy (in nats) are presented in Tab. 4.6.

For the dermal layer of HSE sections, the entropy values of the distributions of the thickness-invariant parameters ( $R_T/\alpha_{44}$ ,  $R_T/|\ln(M_{00})|$ ,  $\alpha_{44}/\ln(M_{00})^2$ ,  $(R_T)^2/\alpha_{44}$  and  $\alpha_{44}/(R_T)^2$ ) are smaller than analogous values for the thickness-dependent parameters. Hence, the thickness-invariant parameters have more narrow distributions compared to those of the thickness-dependent parameters ( $R_T$ ,  $\alpha_{44}$ ). Among thickness-invariant parameters,  $\alpha_{44}/\ln(M_{00})^2$  presents the smallest value of entropy of the distribution compared to other thickness-invariant parameters (see Tab. 4.6).

**Table 4.6** Entropy of the distributions of parameters defined by Eq (4.3)-(4.6) within the dermal layer.

Real thickness ( $\mu\text{m}$ )	$H(R_T)$	$H(\alpha_{44})$	$H\left(\frac{R_T}{ \ln(M_{00}) }\right)$	$H\left(\frac{\alpha_{44}}{\ln(M_{00})^2}\right)$	$H\left(\frac{R_T^2}{\alpha_{44}}\right)$	$H\left(\frac{\alpha_{44}}{R_T^2}\right)$
3.0	3.99	3.99	3.96	3.12	3.94	3.76
6.2	4.10	4.07	4.07	2.36	4.03	3.82
7.6	3.98	3.98	3.97	3.84	3.96	3.91
10.1	4.08	4.08	4.06	2.2.	4.01	3.19
10.5	3.67	3.66	3.66	3.67	3.65	3.61

Hence, for purely depolarizing samples, the maps of the parameter  $\alpha_{44}/\ln(M_{00})^2$  may provide the highest image contrast relevant for the histological diagnostic of thin tissue sections. The distributions of the ratio  $\alpha_{44}/(R_T)^2$  have also the small values of entropy, indicating that the maps of this ratio may be used for the histological analysis of both birefringent and depolarizing samples. We demonstrated that using the dependence of polarization and depolarization parameters on thickness, predicted by the differential MM formalism, one can produce the microscopic images with less fluctuations and higher contrast.

## 4.5. Monte Carlo modeling of experimental polarimetric data for dermal layer of HSE

To interpret the experimentally observed anisotropy of linear depolarization and presence of linear dichroism measured with transmission Mueller microscope within dermal zone of HSE thin sections, we performed a numerical modeling of polarimetric response of dermal layer using the polarized Monte Carlo algorithm [15]. The simulated geometry and the parameters of dermal layer optical phantoms are described below.

A virtual light source illuminates uniformly the flat top surface of an optical phantom of a dermal layer at normal incidence. The light source emits a given number ( $10^7$  to  $10^8$ ) of monoenergetic photons with the preset states of polarization. Every photon travels a certain distance within the sample before being scattered on a sphere or cylinder. For each collision event, this distance is determined statistically using a mean free path parameter calculated from the scattering cross-sections of scatterers and their number density. The sizes, refractive indices, and number densities of both sphere and cylinder scatterers as well as refractive index of isotropic host medium or ordinary and extraordinary refractive indices and spatial orientation of the optical axis of linear birefringent host medium are the input parameters of our optical model and can be adjusted to mimic the conditions of real biological tissue.

The photon changes its polarization state and direction of propagation after each scattering event. The angles of deflection and rotation of polarization plane are calculated using the rejection method [16]. A transfer matrix for scattering is determined by Mie theory for spherical scatterers or scattering matrix theory for infinite-long cylinder [11]. The host medium is not absorbing. The random walk of a photon continues within a scattering medium until it is moved outside the sample volume, where it can be lost or hit a detector. The simulated transmitted Muller matrices of the optical phantoms of HSE dermal layer were spatially averaged to reproduce the diffused uniform illumination of the thin sections of HSE in Mueller microscopy experiments. The simulated Mueller matrices of the optical phantoms of varying thickness were decomposed using LMMD algorithm, and obtained values of polarization and depolarization parameters were compared with the corresponding experimental data.

#### 4.5.1. Optical models of HSE dermal layer

To create an appropriate optical phantom (or optical model) of a skin dermis zone, one needs to account for both fibroblasts and well-aligned collagen fibers that form the dermal layer of HSE [7], [8]. Whereas light scattering on cells and fibers produces the depolarization, the optical anisotropy of a dermal layer results in retardance due to the form birefringence [17]. Thus, the monodisperse spherical scatterers in an optical model of the dermal layer were used to reproduce isotropic scatterings on cells. Infinitely long cylindrical scatterers were added to the optical model to simulate the effect of form birefringence due to the presence of aligned collagen fibers in the dermis. The refractive indices of spherical and cylindrical scatterers ( $n_s$ ,  $n_c$ ) and isotropic medium ( $n_m$ ) were set to be equal to 1.45 and 1.33, respectively.

The validity of replacing a form birefringence by an intrinsic birefringence of uniaxial linear anisotropic host medium with an in-plane optical axis was also explored with the following set of parameters: ordinary index  $n_m^o = 1.33$ , and extraordinary index  $n_m^e = 1.33 + \Delta n$ , ( $\Delta n = 10^{-5}$ ). The values of refractive indices are taken as for bulk fresh tissue, while noting that those values may be somewhat different for the studied fixed unstained tissue sections. Most probably, it is not so important for our consideration because the refractive index of a scatterer and its size are highly correlated parameters in Mie electromagnetic scattering problem. With our choice of refractive index values for both

scatterers and host medium, the optical contrast  $n_s/n_m$  (or  $n_c/n_m$ ) is more than one. Keeping constant the value of optical contrast, the size of scatterers was varied to reproduce the general trends in polarization and depolarization parameters in our simulations. This might be a reasonable assumption for performing the parametric numerical studies to reproduce the experimental trends.

In our experiments a dermal layer of all HSE sections demonstrated higher circular depolarization compared to the linear one ( $|\alpha_{44}| > |\alpha_{22}|$ ,  $|\alpha_{44}| > |\alpha_{33}|$ ), thus, indicating the dominance of Rayleigh scattering regime over Mie scattering regime. Hence, it justifies the use of the sub-wavelength spherical and cylindrical scatterers in the optical model of dermal layer. The wavelength of probing light was fixed at 533 nm, so the spherical and cylindrical scatterers whose diameter ranged from 0.01  $\mu\text{m}$  to 0.5  $\mu\text{m}$  were tested. Their concentrations, described by the scattering coefficients  $\mu_s$  and  $\mu_c$ , respectively, were varied from 5  $\text{cm}^{-1}$  to 5000  $\text{cm}^{-1}$ . The parameter  $\Delta n$  for the uniaxial birefringent host medium was adjusted to fit the experimental results [3] for the total linear retardance parameter  $R_T$ . The optical axis of a linear uniaxial birefringent host medium was always oriented parallel to the sample surface, reflecting the arrangement of collagen fibers in the dermal layer of histological sections in the imaging plane of the Mueller microscope. The GPU acceleration allowed us to carry out the simulations in a wide range of parameters to find the best fit values.

Histological sections of HSE of varying thickness (nominal values 3  $\mu\text{m}$  ~ 30  $\mu\text{m}$ ) were mounted on 1 mm thick microscopy glass slides in our experiments [3]. During the Mueller polarimetric microscope calibration with Eigenvalue Calibration Method [18], the measurements of air (one of the reference samples) were performed through a bare microscopy glass slide. Hence, the contribution of glass was excluded from the Mueller matrices of all measured histological cuts. To model our experimental setup, the Monte Carlo simulations in transmission configuration were performed for the range of histological cut thicknesses defined from profilometer measurements [19] without adding a 1 mm thick glass layer to our optical model. A spatially uniform light beam was normally incident onto the flat front surface of a sample. No back-surface roughness of thin tissue section was taken into account in our optical model. The simulated images of forward scattering Mueller matrix elements were spatially averaged over a centered circle of 600  $\mu\text{m}$  in diameter to reproduce the experimental conditions, and the resulting Mueller matrices were decomposed using LMMD algorithm [5].

#### 4.5.2. Rotation invariants of logarithmic decomposition

The set of polarization and depolarization parameters obtained from the LMMD include the values of retardance (linear ( $p_4 = LB$ ,  $p_5 = LB'$ ) and circular ( $p_6 = CB$ )), dichroism (linear ( $p_1 = LD$ ,  $p_2 = LD'$ ) and circular ( $p_3 = CD$ )), and depolarization coefficients (linear ( $\alpha_{22}$ ,  $\alpha_{33}$ ) and circular ( $\alpha_{44}$ )) [5]. The parameters  $LB$ ,  $CD$  and  $\alpha_{22}$  are defined with respect to the framework of  $0^\circ$ - $90^\circ$ , the parameters  $LB'$ ,  $LD'$  and  $\alpha_{33}$  are defined with respect to the framework of  $\pm 45^\circ$ .

Neither optical activity nor circular dichroism was detected in the polarimetric measurement data for skin model histological cuts ( $CB = 0$ ,  $CD = 0$ ). The well-aligned collagen fibers in a dermal layer of HSE sections define the direction of the optical axis of a uniaxial linear birefringent medium. In our experiments the orientation of histological cuts in the imaging plane was performed manually, thus, producing a small variation in the azimuth of the optical axis from sample to sample. That is why the measured values of polarization parameters  $LB, LB'$  for different HSE sections depend not only on sample thickness, but also on the position of thin tissue sections in the imaging plane. To exclude the latter, we have introduced the parameter of a total linear retardance  $R_T = \sqrt{LB^2 + LB'^2}$ , which does not depend on the azimuth of the optical axis.

The polarimetric measurements of the histological sections of HSE have also demonstrated the effect of anisotropy of linear depolarization ( $\alpha_{22} \neq \alpha_{33}$ ) [3], [19]. Both parameter  $\alpha_{22}$  and parameter  $\alpha_{33}$  are not invariant under the in-plane rotation of a sample. Therefore, we also derived rotation invariants for linear depolarization to eliminate the effect of sample orientation with respect to the laboratory coordinate system. The logarithm of Mueller matrix  $\mathbf{M}$  is calculated as

$$\mathbf{L} = \ln \mathbf{M} = \ln(\mathbf{U}\mathbf{\Lambda}\mathbf{U}^{-1}) = \mathbf{U} \ln(\mathbf{\Lambda}) \mathbf{U}^{-1} \quad (4.8)$$

where  $\mathbf{\Lambda}$  is a diagonal matrix of eigenvalues of  $\mathbf{M}$  and  $\mathbf{U}$  is a matrix with the columns-eigenvectors of matrix  $\mathbf{M}$ . The rotational transformation of a Mueller matrix in transmission configuration is described by  $\mathbf{M}' = \mathbf{R}(\alpha)\mathbf{M}\mathbf{R}(-\alpha)$ , where

$$\mathbf{R}(\alpha) = \begin{bmatrix} 1 & 0 & 0 & 0 \\ 0 & \cos(2\alpha) & -\sin(2\alpha) & 0 \\ 0 & \sin(2\alpha) & \cos(2\alpha) & 0 \\ 0 & 0 & 0 & 1 \end{bmatrix} \quad (4.9)$$

Rotational transformation does not affect the eigenvalues of the matrix. Therefore, we have

$$\begin{aligned} \mathbf{L}' &= \ln \mathbf{M}' = \ln(\mathbf{R}(\alpha)\mathbf{U}\mathbf{\Lambda}\mathbf{U}^{-1}\mathbf{R}(-\alpha)) \\ &= \mathbf{R}(\alpha)\mathbf{U} \ln(\mathbf{\Lambda}) \mathbf{U}^{-1}\mathbf{R}(-\alpha) = \mathbf{R}(\alpha)\mathbf{L}\mathbf{R}(-\alpha) \end{aligned} \quad (4.10)$$

which means that the rotation transformation of matrix  $\mathbf{L}$  is the same as for the Mueller matrix  $\mathbf{M}$ . As a result, the rotation invariants of matrix  $\mathbf{L}$  should take the same form as the invariants for the Mueller matrix  $\mathbf{M}$  [20]. If we denote  $s_n = \sin(n\alpha)$  and  $c_n = \cos(n\alpha)$  and decompose the matrix  $\mathbf{R}(\alpha)\mathbf{L}\mathbf{R}(-\alpha)$  into the sum of the matrices  $\mathbf{L}_m$  and  $\mathbf{L}_u$  ( $\mathbf{G}$ -antisymmetric and  $\mathbf{G}$ -symmetric components [5], we get the following expressions:

$$\mathbf{L}'_m = \frac{1}{2} \begin{bmatrix} m_1 & m_2 & m_3 & m_4 \\ m_5 & m_6 & m_7 & m_8 \\ m_9 & m_{10} & m_{11} & m_{12} \\ m_{13} & m_{14} & m_{15} & m_{16} \end{bmatrix} \quad (4.11)$$

$$\begin{aligned} m_1 = m_6 = m_{11} = m_{16} = 0, m_2 = m_5 = (L_{12} + L_{21})c_2 - (L_{13} + L_{31})s_2, \\ m_3 = m_9 = (L_{13} + L_{31})c_2 + (L_{12} + L_{21})s_2, m_4 = m_{13} = L_{14} + L_{41}, \\ m_7 = -m_{10} = L_{23} - L_{32}, m_8 = -m_{14} = (L_{24} - L_{42})c_2 + (L_{43} - L_{34})s_2, \\ m_{12} = -m_{15} = (L_{34} - L_{43})c_2 + (L_{24} - L_{42})s_2. \end{aligned}$$

$$\mathbf{L}'_u = \frac{1}{2} \begin{bmatrix} u_1 & u_2 & u_3 & u_4 \\ u_5 & u_6 & u_7 & u_8 \\ u_9 & u_{10} & u_{11} & u_{12} \\ u_{13} & u_{14} & u_{15} & u_{16} \end{bmatrix} \quad (4.12)$$

$$\begin{aligned} u_1 = 2L_{11}, u_6 = L_{22} + L_{33} + (L_{22} - L_{33})c_4 - (L_{23} + L_{32})s_4, \\ u_{11} = L_{22} + L_{33} + (L_{33} - L_{22})c_4 + (L_{23} + L_{32})s_4, u_{16} = 2L_{44}, \\ u_2 = -u_5 = (L_{12} - L_{21})c_2 + (L_{31} - L_{13})s_2, u_3 = -u_9 = (L_{13} - L_{31})c_2 + (L_{12} - L_{21})s_2, \\ u_4 = -u_{13} = L_{14} - L_{41}, u_7 = u_{10} = (L_{23} + L_{32})c_4 + (L_{22} - L_{33})s_4, \\ u_8 = u_{14} = (L_{24} + L_{42})c_2 - (L_{43} + L_{34})s_2, u_{12} = u_{15} = (L_{34} + L_{43})c_2 + (L_{24} + L_{42})s_2. \end{aligned}$$

The rotation invariants of the matrix  $\mathbf{L}_m$  are total linear birefringence

$$\begin{aligned} R_T &= \sqrt{L_{m42}^2 + L_{m43}^2} = \sqrt{L_{m24}^2 + L_{m34}^2} \\ &= [(L_{24} - L_{42})^2 + (L_{34} - L_{43})^2]/4 \end{aligned} \quad (4.13)$$

total linear dichroism

$$\begin{aligned} D_T &= \sqrt{L_{m12}^2 + L_{m13}^2} = \sqrt{L_{m21}^2 + L_{m31}^2} \\ &= [(L_{12} + L_{21})^2 + (L_{13} + L_{31})^2]/4 \end{aligned} \quad (4.14)$$

circular birefringence

$$R_C = L_{m23} = -L_{m32} = (L_{23} - L_{32})/2 \quad (4.15)$$

and circular dichroism.

$$D_C = L_{m14} = L_{m41} = (L_{14} + L_{41})/2 \quad (4.16)$$

Using the notation  $\alpha_{ii} = L_{u_{ii}}$ , ( $i = 2, 3, 4$ ) for the diagonal elements of matrix  $\mathbf{L}_u$ , the rotation invariants of the matrix  $\mathbf{L}_u$  can be written in terms of linear (isotropic) depolarization

$$\alpha_L = (\alpha_{22} + \alpha_{33})/2 = (L_{u22} + L_{u33})/2 \quad (4.17)$$

and circular depolarization.

$$\alpha_{44} = L_{u44} \quad (4.18)$$

The four elements at the corners of the matrix  $\mathbf{L}$  are also invariant under rotation, as well as the squared sum of the matrix elements from the first and last columns and the first and last rows. To find the rotational invariant for linear anisotropic depolarization, we applied the Mueller matrix transformation [20] of  $\mathbf{L}$  and obtained:

$$\alpha_{LA} = \frac{1}{2} \sqrt{(\alpha_{22} - \alpha_{33})^2 + (L_{u23} + L_{u32})^2} \quad (4.19)$$

In the optical model of dermal layer of HSE the orientation of the optical axis of linear birefringent medium and the orientation of the axis of cylindrical scatterers was always set along x-axis. In the experiments, the orientation of the aligned collagen fibers with respect to the edge of a microscope glass slide (i.e., laboratory x-axis) depends on the sample preparation and may slightly vary from one histological slide to another. Therefore, we used the derived set of rotation invariants with non-zero values, namely,  $R_T$ ,  $D_T$ ,  $\alpha_L$ ,  $\alpha_{44}$ , and  $\alpha_{LA}$  for the comparison of the results of measurements and simulations.

### 4.5.3. Choice of an appropriate optical model of the dermis

Several optical models were tested to reproduce the optical effects observed in a dermal zone of samples. Some of them were ruled out for the reasons discussed in the next section. Finally, the optical model that includes both spherical and cylindrical scatterers randomly distributed in the linear birefringent host medium was selected for the polarized Monte Carlo simulations of HSE dermal layer.

#### 4.5.3.1. Ruled out optical models

The goal of our modeling was to 1) reproduce the linear dependence of the polarization parameters and quadratic dependence of the depolarization parameters of HSE dermal layer on its thickness 2) understand the origin of anisotropy of the linear depolarization and non-zero dichroism measured HSE dermal layer with Mueller microscope in transmission configuration.

It was already demonstrated that an isotropic medium with spherical scatterers does not possess any retardance [21], [22]. A phase shift in the detected signal can be induced by scattering of polarized light by cylindrical scatterers as well as by polarized light passing through a birefringent medium. First, we tested the optical model of HSE dermal layer that consists of spherical and cylindrical scatterers that are randomly and uniformly distributed in the isotropic host medium (SC model). Our modeling results demonstrated that the SC model felt short of reproducing the experimental values of retardance for low values of the  $\mu_c$  parameter. The volume density of cylindrical scatterers had to increase significantly to fit the experimental trends in retardance values, but with an increase of the parameter  $\mu_c$  SC model

produced very high values of dichroism and depolarization, which by far exceed the corresponding experimental values. Therefore, we have discarded the SC model from further consideration. We concluded that the uniaxial linear birefringent host medium has to be a necessary component of our optical model to reproduce the experimental trends. Linear birefringent host medium will increase the simulated retardance values without pushing up the dichroism and depolarization parameters of a simulated optical phantom.

We also tested the optical model of HSE dermal layer that consists of spherical scatterers that are randomly and uniformly distributed in a uniaxial linear birefringent host medium (SB model). The values of parameter  $\Delta n$ , the radius of spherical scatterers  $R_s$ , and the scattering coefficient  $\mu_s$  were varied to find the best fit to the experimental data. The SB optical model fits well the experimental values of retardance [19] with optimal values of  $\Delta n = 0.0057$  and  $R_s = 0.05 \mu\text{m}$  (see Fig. 4.15 (a)).

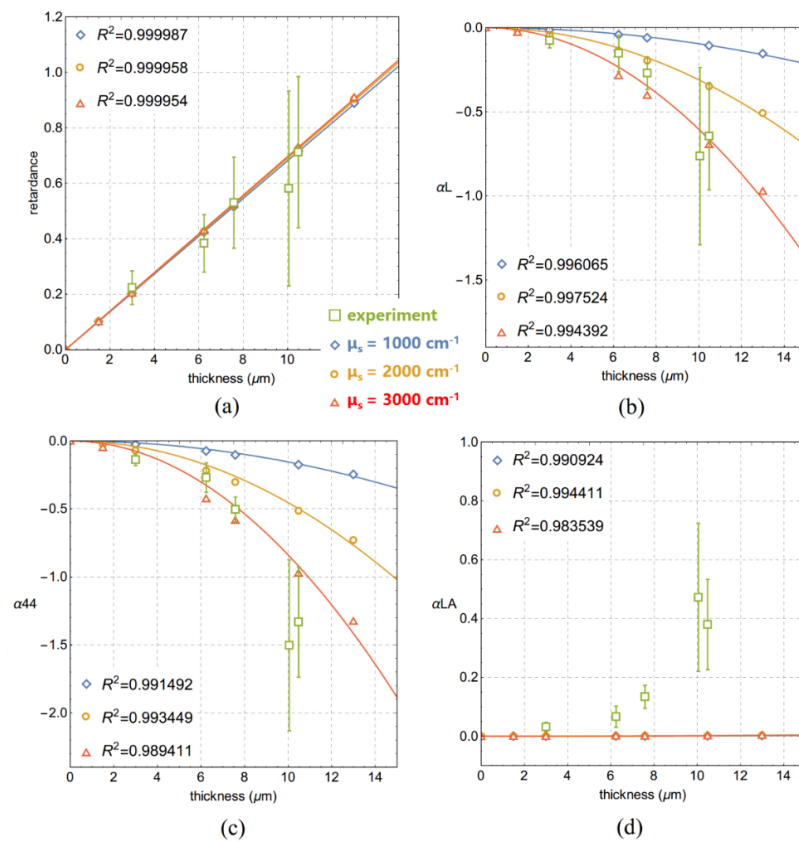


**Figure 4.15** Results of Monte Carlo simulations with the SB optical model for different dermal layer thickness: (a) total linear retardance  $R_T$  (radians) and dimensionless depolarization parameters (b)  $\alpha_L$ , (c)  $\alpha_{44}$ , and (d)  $\alpha_{LA}$ . Simulated data are shown by open symbols corresponding to different concentrations of spherical scatterers. Open boxes with standard deviation represent the experimental data. Solid lines show the results of (a, d) linear and (b, c) parabolic fit of the simulated data.

It is worth to mention that the optimal value of  $\Delta n$  for the fixed tissue cuts was found about two orders of magnitude larger compared to the values reported for the fresh biological tissue [17]. The simulation results with the SB optical model confirmed the linear dependence of total linear retardance  $R_T$  calculated from LMMD on layer thickness. The simulated values of

depolarization parameters  $\alpha_L, \alpha_{44}$  have demonstrated a quadratic dependence on thickness (see Fig. 4.15 (b), (c)). No anisotropy of linear depolarization was observed with the SB model, as simulated values of  $\alpha_{LA} = 0$  for all layer thickness (Fig. 4.16 (d)).

The experimental values of depolarization coefficients  $\alpha_{22}, \alpha_{33}$ , and  $\alpha_{44}$  for a dermal layer of skin model histological cuts obey the relation:  $|\alpha_{22}| < |\alpha_{33}| < |\alpha_{44}|$  [3]. However, the simulations with the SB model could not reproduce the effect of anisotropy of linear depolarization ( $|\alpha_{LA}| \neq 0$ ) observed experimentally (see Fig. 4.16 (d)). Moreover, no linear dichroism can be simulated with the SB model, while the non-zero values of the linear dichroism were measured in our experiments [3]. Therefore, we concluded that the optical SB model of the dermal layer of skin model histological cuts has to be modified in order to reproduce experimental trends.

#### 4.5.3.2. SCB optical model

We then added to the SB optical model of HSE dermal layer the cylindrical scatterers that are also distributed randomly and uniformly in the linear birefringent host medium (SCB model) to reproduce the effects of anisotropy of linear depolarization and non-zero linear dichroism. We used the same set of parameter values as for the SB optical model but added a group of cylindrical scatterers of radius  $R_c = 0.05 \mu m = R_s$ , with cylinders' axes aligned along the X-axis. The scattering coefficient for the spherical scatterers  $\mu_s$  was fixed at  $1500 \text{ cm}^{-1}$  and the scattering coefficient for the cylindrical scatterers  $\mu_c$  was varied from  $500$  to  $1500 \text{ cm}^{-1}$ .

The results obtained with the SCB optical model after applying LMMD to the simulated Mueller matrices for the layers of varying thickness are shown in Fig. 4.16. The presence of the cylindrical scatterers has minimal influence on the values of linear retardance, but it has a significant impact on the values of linear dichroism and anisotropic depolarization effect. The SCB optical model yields the values of total linear retardance that also match well the experimental data (see Fig. 4.16(a)). The linear increase of total linear retardance  $R_T$  and linear dichroism values on thickness are shown in Figs 4.16 (a) and (b), respectively. The non-zero intercept of the linear regression curve for the experimental linear dichroism values with the y-axis (Fig. 4.16 (b)) was explained by the scattering of transmitted light on the rough back surface of tissue [3]. It was shown that for the anisotropic media, a surface scattering does not affect the retardance values but has an impact on linear dichroism values [23]. The quadratic dependence of  $\alpha_L, \alpha_{44}$ , and  $\alpha_{LA}$  on thickness is also confirmed. Moreover, an anisotropic depolarization effect ( $|\alpha_{LA}| \neq 0$ ) is well reproduced with the SCB optical model (see Fig. 4.16 (c-e)).

The impact of a radius of cylindrical scatterers  $R_c$  on anisotropic linear depolarization  $\alpha_{LA}$  was also studied (see Fig. 4.17). Our simulations show that the cylinders with a smaller radius produce stronger anisotropy in linear depolarization. Hence, the presence of anisotropic linear depolarization is an indication of the scattering on small-size fibroid scatterers in the studied medium (so-called from birefringence). The values of the parameter  $\alpha_{LA}$  can be used for the estimation of the characteristic size of the non-spherical scatterers.

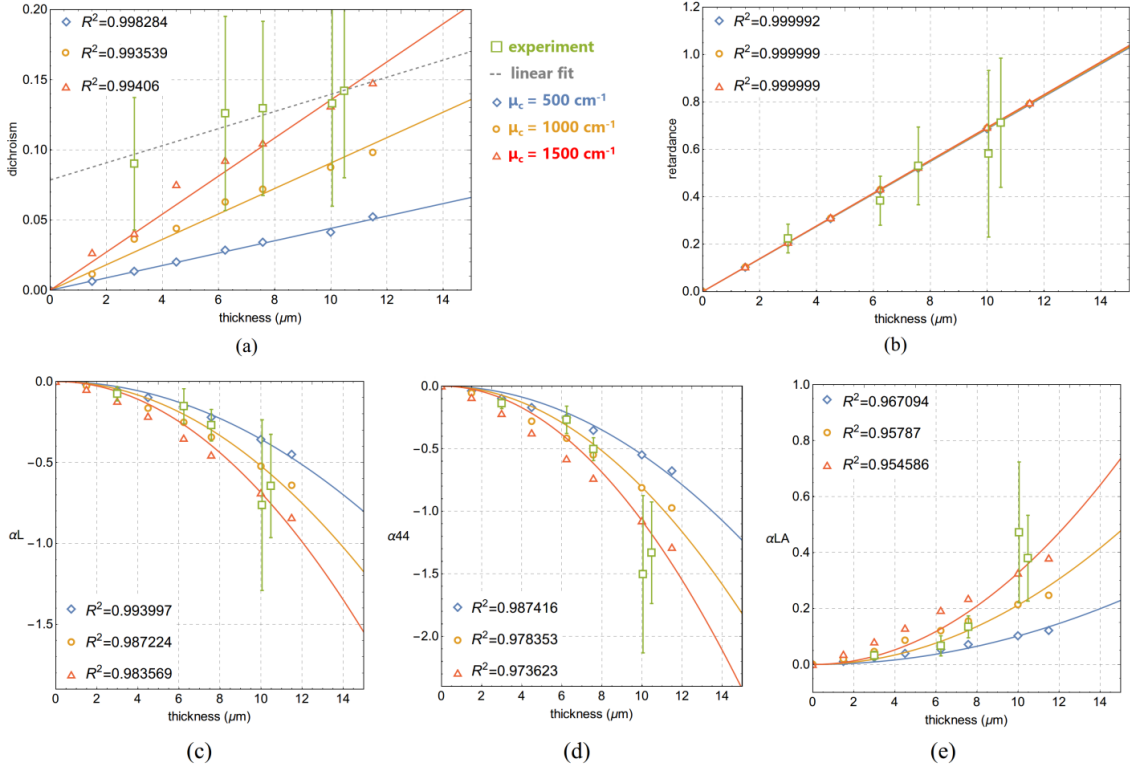


**Figure 4.16** Results of Monte Carlo simulations using the SCB optical model of HSE dermal layer. Dependence on the layer thickness of (a) total linear dichroism  $D_T$  (dashed line is a linear regression curve for the experimental data), (b) total linear retardance  $R_T$ , (c-e) depolarization parameters  $\alpha_L$ ,  $\alpha_{44}$ , and  $\alpha_{LA}$ , respectively. Simulated data are shown by open symbols corresponding to different scattering coefficients  $\mu_c$  (i.e., different concentrations of cylindrical scatterers),  $\mu_s = 1500 \text{ cm}^{-1}$ ,  $R_s = R_c = 0.05 \mu\text{m}$ . Open boxes with error bars represent the experimental data. Solid lines show the results of (a), (b) linear, and (c)-(e) quadratic fit of the simulated data.

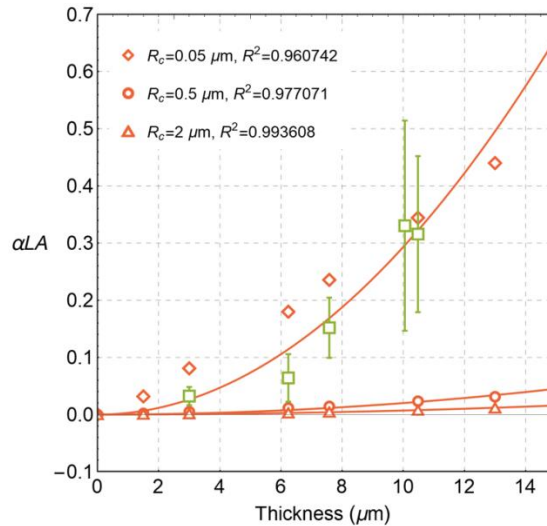


**Figure 4.17** Dependence of parameter  $\alpha_{LA}$  on layer's thickness for the different radius of cylindrical scatterers. The parameters of the SBC optical model are:  $\mu_s = \mu_c = 1500 \text{ cm}^{-1}$ ,  $R_s = 0.05 \mu\text{m}$ . Open symbols correspond to the different radii of cylindrical scatterers:  $R_c = 0.05, 0.5, \text{ and } 2 \mu\text{m}$ , respectively. The concentration of cylindrical scatterers  $c_c$  was adjusted to keep a constant value of the scattering coefficient  $\mu_c$ . Open boxes with error bars represent the experimental data. Solid lines show the results of a parabolic fit of the simulated data.

To summarize, an appropriate optical model for a dermal layer of unstained fixed histological cuts of skin model tissue should include the sub-wavelength spherical scatterers, and well-aligned cylindrical scatterers both distributed in a uniaxial linear birefringent medium. This model can qualitatively reproduce the thickness dependence of polarization and depolarization properties obtained from LMMD of the experimental Mueller matrices of a dermal layer of skin model histological cuts [3].

## 4.6. Conclusions

The experimental studies of histological sections of HSE with the transmission Mueller microscope have confirmed the predictions of the phenomenological differential formalism of fluctuating anisotropic media for biological tissues. The logarithmic decomposition of Mueller matrix (LMMD) was applied to study a dependence of total linear retardance, total dichroism, and depolarization parameters on thickness. We have demonstrated that the total linear retardance and the total linear dichroism of HSE dermal layer depend linearly on the thickness, whereas the depolarization parameters demonstrate quadratic dependence on thickness. The set of optical parameters, including the circular depolarization and total linear birefringence (both derived from the logarithmic decomposition of MM of HSE sections) and the intensity of transmitted light (element  $M_{00}$ ), was effectively used for the automated segmentation of microscopy images and delineation of the zones of bare glass, dermis, and epidermis using the upgraded version of the statistical algorithm of density-based spatial clustering of the applications with noise.

A significant problem, overlooked by many researchers working in the field of polarized light histology, appears to be the control and characterization of the real thickness of studied tissue sections. The important point is that the nominal thickness of tissue sections used for histopathology analysis may vary significantly from the real one due to technical specifics of the preparation of tissue sections. The pathological changes of tissue (cancer, fibrosis, inflammation) will affect the measured polarization and depolarization parameters of tissue. However, changing the thickness of tissue section and, consequently, the path length of the probing light beam will also affect these parameters. Thus, for separating the contribution of both factors and reliable diagnostics of tissue with polarized light, the impact of the varying path length of light on polarization and optical depolarization markers of the specific disease has to be taken into account. In order to mitigate the impact of tissue thickness fluctuations and to increase the contrast of polarimetric images relevant for diagnostic purposes, we have proposed several approaches based on using the linear and quadratic dependence of retardance and depolarization on thickness, respectively, combined with the estimation of the intensity decay with thickness from the Beer-Lambert law.

The polarization state of light incident on biological tissue is changed by its interaction with tissue microstructures. These modifications depend on both size (nm to  $\mu\text{m}$ ) and shape of the scatterers. Polarized Monte Carlo algorithm was used for the solution of vector radiative transfer equation to model the propagation of polarized light within the birefringent

scattering media and understand the physical origins of the anisotropy of linear depolarization and the presence of linear dichroism that were experimentally observed for dermal layer of HSE with transmission Mueller microscope.

The rotation invariant parameters of the logarithmic decomposition of Mueller matrix were derived, and the parameter  $\alpha_{LA}$  was proposed as a maker for anisotropy of linear depolarization. Three different optical models modes were tested to explain the results of transmission Mueller microscopy measurements of the skin equivalents. We demonstrated that 1) linear birefringence of the host medium is a necessary parameter of the optical model of HSE dermal layer for reproducing the experimental trends in total linear retardance values, and 2) anisotropic scatterers are the essential component of the optical model of HSE dermal layer for reproducing both linear dichroism and anisotropic depolarization effects.

Although the depolarization of transmitted light was reproduced with two optical models of HSE dermal layer (SB and SCB), the experimentally observed effect of anisotropy of linear depolarization ( $\alpha_{LA} \neq 0$ ) was found in simulations with the SCB optical model only. Both HSE section measurements and simulations with the SCB optical model confirmed the presence of the non-zero linear dichroism calculated with LMMD for both measured and simulated Mueller matrices. With polarized Monte Carlo simulations, we have shown that applying the logarithmic decomposition of the transmission Mueller matrix of tissue may provide the relevant information not only on the average size of dominant scatterers but also on their shape.

## References

1. N. Agarwal, J. Yoon, E. Garcia-Caurel, T. Novikova, J.-C. Vanel, A. Pierangelo, A. Bykov, A. Popov, I. Meglinski, and R. Ossikovski, "Spatial evolution of depolarization in homogeneous turbid media within the differential Mueller matrix formalism," *Opt. Lett.*, vol. 40, no. 23, pp. 5634–4, 2015.
2. S. H. Yoo, R. Ossikovski, and E. Garcia-Caurel, "Experimental study of thickness dependence of polarization and depolarization properties of anisotropic turbid media using Mueller matrix polarimetry and differential decomposition," *Appl. Surf. Sci.*, vol. 421, pp. 870–877, Nov. 2017.
3. H. R. Lee, P. Li, T. S. H. Yoo, C. Lotz, F. K. Groeber-Becker, S. Dembski, E. Garcia-Caurel, R. Ossikovski, H. Ma, and T. Novikova, "Digital histology with Mueller microscopy: how to mitigate an impact of tissue cut thickness fluctuations," *J. Biomed. Opt.*, vol. 24, no. 7, pp. 1–10, Aug. 2019.
4. H. R. Lee, C. Lotz, F. K. Groeber-Becker, S. Dembski, E. Garcia-Caurel, R. Ossikovski, and T. Novikova, "Mueller microscopy of full thickness skin models combined with image segmentation," *Proc SPIE 11076*, Advances in Microscopic Imaging II, 2019
5. R. Ossikovski, "Differential matrix formalism for depolarizing anisotropic media," *Opt. Lett.*, vol. 36, no. 12, pp. 2330–2332, Jun. 2011.

6. R. Ossikovski and O. Arteaga, "Statistical meaning of the differential Mueller matrix of depolarizing homogeneous media," *Opt. Lett.*, vol. 39, no. 15, pp. 4470–4, 2014.
7. A. Rossi, A. Appelt-Menzel, S. Kurdyn, H. Walles, and F. Groeber, "Generation of a Three-dimensional Full Thickness Skin Equivalent and Automated Wounding," *J. Vis. Exp.*, no. 96, p.p. 52576, Feb. 2015.
8. C. Reuter, H. Walles, and F. Groeber, "Preparation of a Three-Dimensional Full Thickness Skin Equivalent," *Methods Mol. Biol.*, vol. 1612, pp. 191–198, 2017.
9. OECD, *Test No. 439: In Vitro Skin Irritation-Reconstructed Human Epidermis Test Method*. OECD Guidelines for the Testing of Chemicals, Section 4, *OECD Publishing*, Paris, 2019.
10. H. C. van de Hulst, *Light Scattering by Small Particles*. Courier Corporation, 1981.
11. C. F. Bohren and D. R. Huffman, *Absorption and Scattering of Light by Small Particles*. John Wiley & Sons, 1998.
12. G. J. Simpson and K. L. Rowlen, "Molecular Orientation at Surfaces: Surface Roughness Contributions to Measurements Based on Linear Dichroism," *J. Phys. Chem. B*, vol. 103, no. 19, pp. 3800–3811, 1999.
13. M. Ester, H. -P. Kriegel, J. Sander, X. Xu, "A Density-Based Algorithm for Discovering Clusters in Large Spatial Databases with Noise," *AAAI press*, KDD-96 Proceedings, pp. 1–6, Jul. 1996.
14. C. E. Shannon, "A mathematical theory of communication," *Bell Syst. Tech. J.*, vol. 27, no. 3, pp. 379-423, 1948.
15. N. Ortega-Quijano and J. L. Arce-Diego, "Depolarizing differential Mueller matrices," *Opt. Lett.*, vol. 36, no. 13, pp. 2429–2431, Jul. 2011.
16. I. Lux, L. Koblinger *Monte Carlo Particle Transport Methods: Neutron and Photon Calculations*, CRC press, pp. 1–529, Jul. 2010.
17. V. V. Tuchin, L. V. Wang, and D. A. Zimnyakov *Optical Polarization in Biomedical Applications*, Springer, pp. 1–285, Aug. 2019.
18. B. Dré villon, E. Compain, and S. Poirier, "General and self-consistent method for the calibration of polarization modulators, polarimeters, and Mueller-matrix ellipsometers," *Appl. Opt.*, vol. 38, no. 16, pp. 3490–3502, Jun. 1999.
19. H. R. Lee, T. S. H. Yoo, P. Li, C. Lotz, F. K. Groeber-Becker, S. Dembski, E. Garcia-Caurel, R. Ossikovski, and T. Novikova, "Mueller microscopy of anisotropic scattering media: theory and experiments," *Proc. SPIE 10677*, Unconventional Optical Imaging, 1067718, 2018.

20. P. Li, D. Lv, H. He, and H. Ma, "Separating azimuthal orientation dependence in polarization measurements of anisotropic media," *Opt. Express*, vol. 26, no. 4, pp. 3791–3800, Feb. 2018.
21. S. Bartel and A. H. Hielscher, "Monte Carlo simulations of the diffuse backscattering Mueller matrix for highly scattering media," *Appl. Opt.*, vol. 39, no. 10, pp. 1580–10, 2000.
22. M.-R. Antonelli, A. Pierangelo, T. Novikova, P. Validire, A. Benali, B. Gayet, and A. D. Martino A. Benali, A. Pierangelo, A. De Martino, B. Gayet, M.-R. Antonelli, P. Validire, and T. Novikova, "Impact of model parameters on Monte Carlo simulations of backscattering Mueller matrix images of colon tissue," vol. 2, no. 7, pp. 1836–1851, Jul. 2011.
23. G. J. Simpson and K. L. Rowlen, "Molecular Orientation at Surfaces: Surface Roughness Contributions to Measurements Based on Linear Dichroism," *J. Phys. Chem. B*, vol. 103, no. 19, pp. 3800–3811, 1999.

# Chapter 5

## Wide-field imaging Mueller polarimetry for the visualization of brain white matter fiber tracts

5.1. Introduction .....	119
5.2. Materials and Methods .....	122
5.2.1. Sample preparation .....	122
5.2.2. Measurement Protocol .....	123
5.3. Results and discussion .....	123
5.3.1. Fixed human brain tissue .....	123
5.3.2. Fresh animal brain tissue .....	129
5.4. Conclusions .....	132
References .....	133

### 5.1. Introduction

Surgery is the crucial treatment step for most patients with brain tumors, especially gliomas [1]-[4]. While some well-delineated brain tumors such as metastases can be removed en-bloc, most gliomas, which tend to grow infiltrative in the white matter within the brain, are removed piece by piece. During surgery, as the surgeon follows the tumor into the depth of the brain and removes it in a piecemeal fashion, it is essential that surgeon identifies and respects the border between the tumor and the surrounding brain tissue in order to perform a radical tumor resection, whereas preserving neurological function. However, although it is easy to identify the tumor in preoperative magnetic resonance imaging (MRI), solid tumor tissue is often difficult to differentiate from infiltrated white matter during surgery, even when using a state-of-the-art intra-operative microscope.

Patients in whom a piece of the tumor is left behind due to poor visualization of the tumor border have a worse prognosis than those in whom the entire tumor was removed, as the tumor invariably grows back from the remnants [5]-[7]. Furthermore, information on the neurological function of a given area of exposed white matter seen during surgery is very limited. The white matter of the healthy brain is made up of fiber tracts that comprise bundles of axons. Each axon is surrounded by a myelin sheath, which acts as an electrical insulator to accelerate the propagation of action potential (see Fig. 5.1). Myelin is a lipid-rich substance with a refractive index higher than that of the surrounding glia, in the visible wavelength range [8].

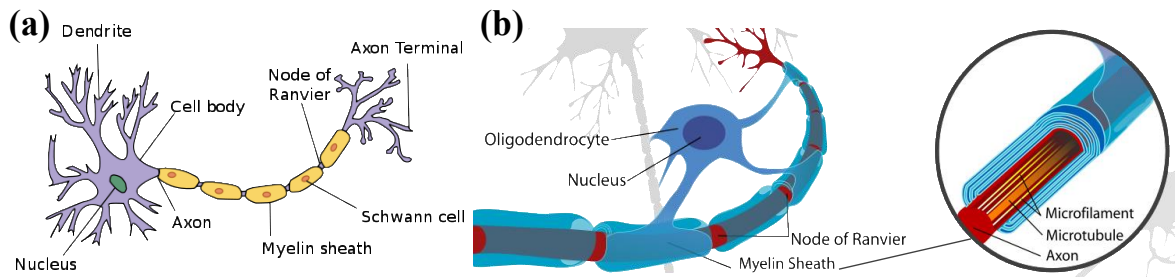


**Figure 5.1** Scheme of the a) structure of simplified neuron and b) neuron's axon and its myelin sheath. Adapted from [<https://en.wikipedia.org/wiki/Myelin>]

To some degree, the differences in texture, roughness, color, and vascularization can help to identify tumor tissue, especially when using a neurosurgical microscope. In addition, several experimental methods have been investigated for their ability to discern brain tumor tissue. For instance, orally administered 5-aminolevulinic acid (5-ALA) is taken up by cells and metabolized to protoporphyrin IX, which accumulates in tumor cells of higher-grade gliomas and exhibits fluorescent properties [9]-[11]. By illuminating the exposed brain tissue with blue light through the surgical microscope, tumor cells fluoresce red, making tumor cell clusters visible. 5-ALA has entered clinical routine [9], [12], however, its benefit is limited to high-grade gliomas, as it is not suitable for visualizing low-grade gliomas or metastases due to insufficient protoporphyrin IX accumulation in tumor tissue.

The installation of an MRI device in the operating room helps to identify tumor remnants during surgery and has been shown to increase the rate of gross total resection in patients with high-grade glioma [13], [14]. However, the significant financial costs and extra time needed for scanning prevent intra-operative MRI from becoming the gold standard of care. Other approaches, such as intra-operative ultrasound, have not proven reliable in estimating the extent of resection and the residual tumor volume [15]. In summary, the attempts to visualize tumor cells have so far failed to reliably identify the tumor-brain interface during surgery for many intrinsic brain tumors.

The schematic of a brain section in a coronal plane is shown in Fig. 5.2. The cell bodies of neurons lie within the superficial layer of the brain, which is called the gray matter or cortex (Fig. 5.2, top left inset). The axons, constituting the white matter of the brain, conduct electrical impulses (action potential) between nerve cell bodies located in the gray matter of

the brain or the spinal cord. Large numbers of axons are joined together in fiber tracts. For example, the corticospinal tract connects the neurons to the spinal cord and is responsible for voluntary movement of the limbs, whereas the anterior-posterior-running arcuate fasciculus fiber tract is responsible for speech (Fig. 5.2, top right inset). A brain tumor displaces these fiber tracts.

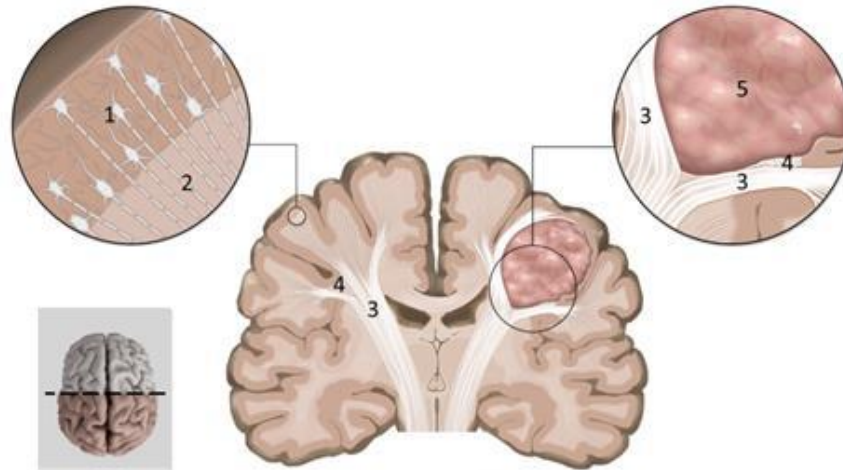


**Figure 5.2** Schematic of brain cross-section in a coronal plane. Left bottom inset – view of a brain from above, the dashed line shows the location of a coronal plane; left top inset: 1 - cell bodies of neurons lie within the brain gray matter; 2 - axons; the neurons connect to other areas of the brain or the spinal cord via their axons. Top right inset: 3 - corticospinal tract; 4 - anterior-posterior-running arcuate fasciculus fiber tract; 5 - tumor. See explanations in the text.

The white matter of the healthy brain is made up of fiber tracts that comprise bundles of axons. Its white color is caused by the strong scattering of light, which results in depolarization of incident polarized light. In addition to light scattering, the densely packed and aligned rods of myelin produce strong optical anisotropy (so-called “form birefringence”) of brain white matter. Consequently, the brain fiber tracts must exhibit uniaxial linear birefringence with the optical axis oriented along the direction of the fiber bundle. The structure of healthy white matter is highly ordered, but the brain tumor tissue shows that the cells grow in a mostly chaotic way. This difference in structural complexity is currently not detectable during surgery with a white-light surgical microscope. These difficulties in identifying tumor, function, and fiber tracts are key contributors to the risk of both incomplete resection (too little resection) and neurological deficits (too much resection).

We performed the proof-of-principle studies to explore the potential of wide-field imaging Mueller polarimetry for the visualization of fiber tracts of brain white matter that may help to detect the exact border between tumor and white matter of healthy surrounding brain tissue.

## 5.2. Materials and Methods

### 5.2.1. Sample preparation

Human brain tissue was obtained from the autopsy of an anonymous donor. The brain was formalin-fixed, and one half of a thick section of the fixed human brain in a coronal plane was used for polarimetric measurements (see Figs. 5.3 (a, b)). The dimensions of the brain section were approximately 9 cm × 6 cm × 1 cm. The remaining fixed brain tissue was paraffin-embedded according to standard procedure. Thin whole-mount sections were prepared from the part of the brain adjacent to the part that had been imaged. Whole-mount sections were stained with Bielschowsky silver impregnation (see Fig. 5.3 (c)), and subsequently digitized on an M8 robotic microscope (Precipoint, Fresing, Germany). A waiver for ethical approval was obtained from the Ethics Committee of the Canton of Bern (KEK 2017-1189).

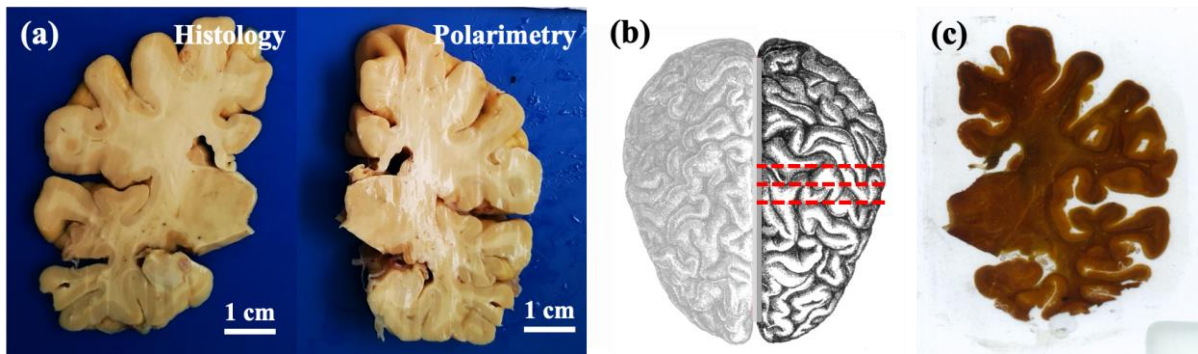


**Figure 5.3** Photos of (a) two adjacent 1 cm thick sections of the fixed human brain (one half) in a coronal plane (Department of Pathology, University Hospital of Bern, Switzerland); (b) schematic of brain (top view), red lines show the location of coronal plane cuts of one half of a brain. (c) thin whole-mount section stained with Bielschowsky silver impregnation (Department of Pathology, University Hospital of Geneva, Switzerland).

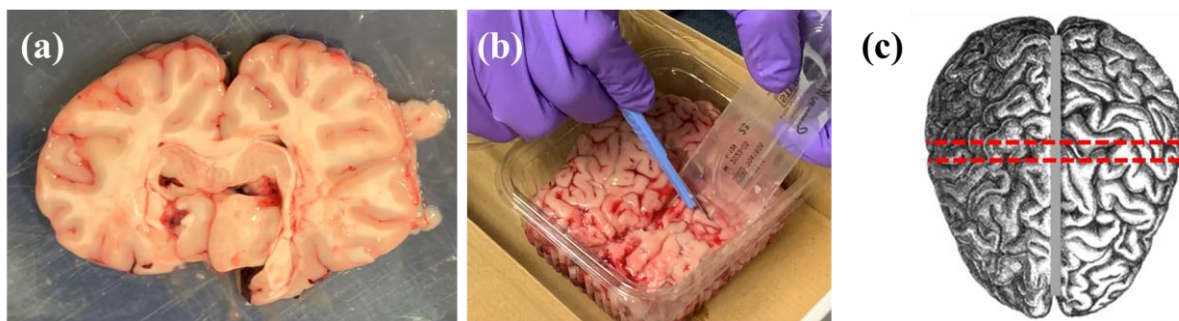


**Figure 5.4** Photo of (a) 1 cm thick fresh calf brain section in a coronal plane; (a) fixed human brain (one half), (b) sectioning of fresh calf brain; (c) schematic of brain (top view), red lines show the location of coronal plane cuts.

The whole fresh (not fixed with formalin) calf brain was bought from a local French butcher. The brain tissue was cut in a coronal plane without formalin-fixation to prepare a thick section (see Fig. 5.4). The dimensions of the calf brain tissue section were approximately 9 cm × 7 cm × 1 cm. This section was rinsed with cold water to remove visible blood clots that may affect polarimetric measurements.

### 5.2.2. Measurement Protocol

The unstained thick sections of both fixed human brain and fresh calf brain were measured with the wide-field imaging Mueller polarimeter [16], [17] in reflection configuration that is the most relevant configuration for clinical applications of optical techniques using visible light. The illuminated spot was about 10 cm in diameter.

A thick section of human brain tissue was removed from the formalin and placed flat in a glass Petri dish 14.5 cm in diameter. The measurements of the Mueller matrix were performed first on the tissue in air, then a sufficient amount of distilled water was poured into the Petri dish to cover the surface of the tissue and optical measurements were repeated. Covering the tissue with water leads to significant partial index matching and flattening of the interface, which, in turn, mitigates most of the artifacts related to sample surface topography.

In order to exclude potential artifacts of the fixation technique we repeated the polarimetric measurements on a non-formalin-fixed calf brain. A thick section of fresh cadaveric calf brain was put into the empty glass Petri dish and imaged with the Mueller polarimeter immediately after preparation. The measurements were also repeated after pouring the distilled water into the Petri dish for removing the impact of the surface scattering, as it was done for the measurements of the formalin-fixed thick section of human brain.

To interpret Mueller matrices of brain tissue measured in backscattering configuration in terms of its basic polarimetric properties (depolarization, retardance, and dichroism) we applied the polar Lu-Chipman decomposition algorithm that allows decomposition of any physically realizable Mueller matrix into the product of three Mueller matrices of the basic optical elements, namely, diattenuator, retarder, and depolarizer. As was explained in the Chapter 1, polar Lu-Chipman decomposition provides the data on the sample depolarization, and both vectors of retardation and diattenuation.

## 5.3. Results and discussion

### 5.3.1. Fixed human brain tissue

We explored the sensitivity of polarized light to the optical anisotropy of brain white matter. The measurements of the formalin-fixed non-tumorous human brain thick section were performed at the wavelength of 550 nm first. The wide-field imaging Mueller polarimeter provided 16 polarimetric images of the Mueller matrix. The maps of basic optical parameters

of the brain specimen (retardance, diattenuation, and depolarization) were obtained by applying pixel-wise Lu-Chipman polar decomposition of Mueller matrix.

The grayscale total intensity image and the corresponding maps of the total depolarization, the linear retardance, and the azimuth of the fast optical axis of a thick section of the formalin-fixed human brain specimen are shown in Fig. 5.5. Neither circular birefringence nor linear or circular dichroism was detected experimentally in these samples. These results are quite typical polarimetric responses of thick specimens measured in reflection [18]-[20]. The polarimetric images were calculated from the Mueller matrix of the sample, measured in “air conditions” at the wavelength of 550 nm. Since the wavelength of the light is 550 nm, the light penetration depth in the tissue is only a few hundred microns.

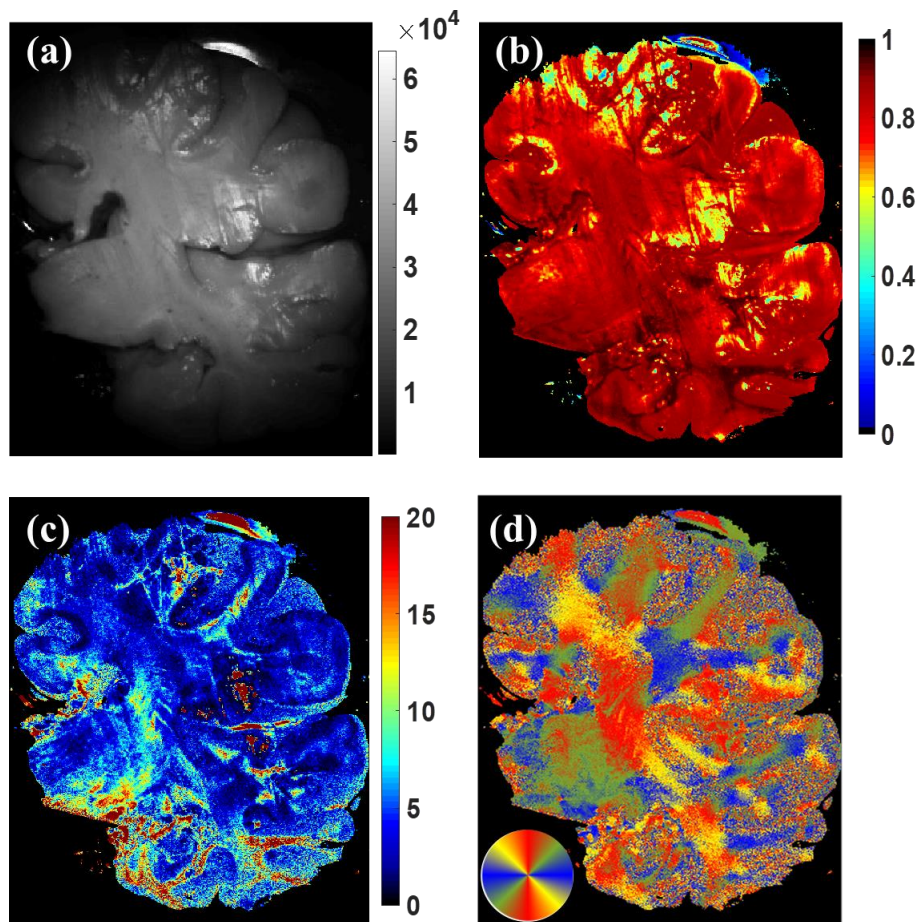


**Figure 5.5** Images of a thick coronal section of the fixed human brain measured in air at 550 nm: (a) total intensity, (b) total depolarization, (c) linear retardance (degrees), and (d) azimuth of the fast optical axis. Note, that the polarimetric maps are not affected by a non-uniform illumination from the slightly divergent incident light beam.

The bright zones of specular reflection in the gray-scale intensity image (see Fig. 5.5 (a)) demonstrate low depolarization values (yellow regions in the map of total depolarization (Fig. 5.5 (b))). The traces of the cutting blade on the surface of the brain specimen show more contrast in depolarization map compared to the total intensity image. The depth of light penetration in the tissue is only a few hundred microns at the measurement wavelength of

550 nm. When measuring this specimen in air, the depolarization response of the bulk tissue is strongly affected by the surface contribution.

The cortex of the formalin-fixed human brain specimen is less depolarizing than the white matter of the specimen. This contrast in depolarization is clearly seen in the bottom part of the depolarization map that is not contaminated by the contribution of specular reflection.

The maps of the scalar linear retardance and the azimuth of the fast optical axis are shown in Figs. 5.5 (c) and (d). As expected, the white matter of healthy brain tissue demonstrates measurable linear retardance of about 5 degrees all the way up to 20 degrees. The zone of brain white matter shows both higher depolarization and higher retardance values compared to the zone of the brain cortex. The map of the azimuth of the fast optical axis shows the orientation of fiber bundles of brain white matter.

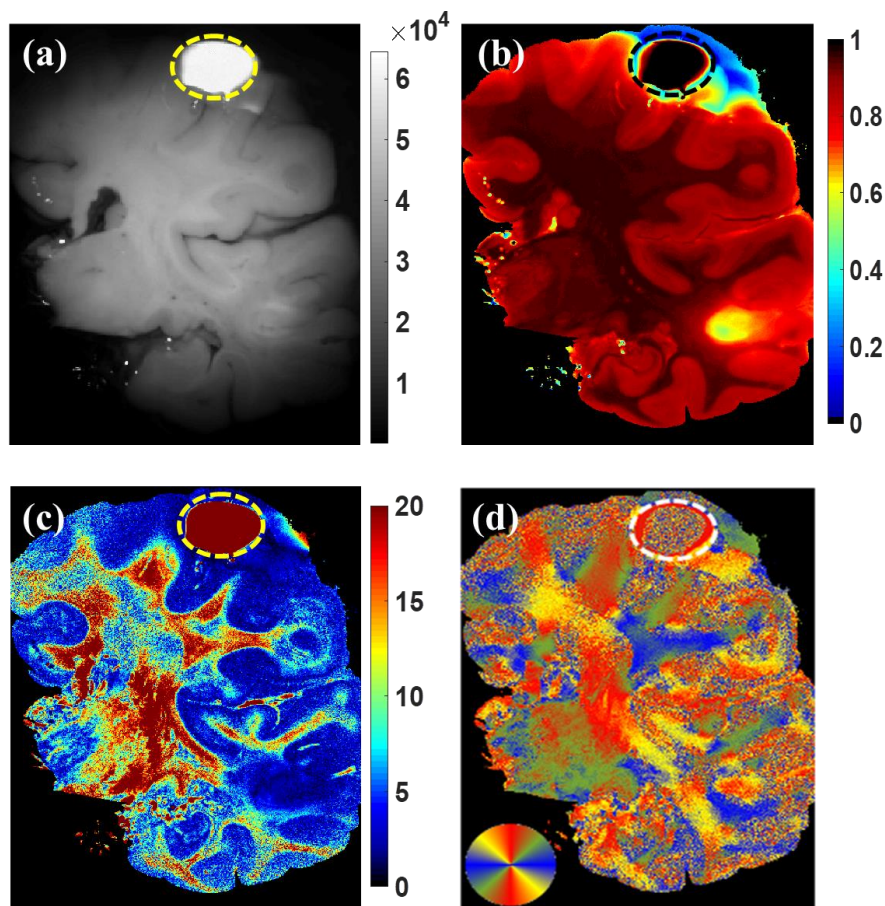


**Figure 5.6** Images of a 1 cm thick coronal section of a fixed human brain immersed in water and measured at 550 nm: (a) total intensity, (b) total depolarization, (c) linear retardance (degrees), and (d) azimuth of the fast optical axis. The dashed line delineates the area of specular reflection on the air-water interface.

Fig. 5.6 shows the gray-scale intensity image, the maps of the total depolarization, the scalar linear retardance, and the azimuth of the fast optical axis of the same formalin-fixed human brain specimen immersed entirely in water. The polarimetric measurements were also performed at a wavelength of 550 nm.

The regions delineated with the dashed line in Fig. 5.6 represent the zone of specular reflection of the slightly divergent incident light beam (AOI  $\sim 15^\circ$ ) from the air-water interface as detected by a CCD camera. We excluded this zone from further analysis. The surface topography was flattened by the index matching (although incomplete). The traces of the cutting blade on the surface of the specimen are eliminated in the depolarization and scalar retardance maps. Hence the impact of surface scattering on depolarization and scalar retardance was largely mitigated. The contrast between the cortex and white matter of brain was enhanced in the maps of total depolarization and scalar linear retardance compared to the measurements in air (see Figs. 5.5 (b), (c) and Figs. 5.6 (b), (c)).

The values of the depolarization and the scalar linear retardance within the zone of white matter of formalin-fixed human brain specimen measured in water were higher compared to the corresponding values for the same brain section measured in air. The maps of the azimuth of the optical axis (Fig. 5.5 (d) and Fig. 5.6 (d)) are very similar for both measurement conditions. It can be explained by the suppression of the surface scattering effect in the measurements of a specimen immersed in water. Consequently, it leads to a reduction of the contribution of photons with a short path length. As a consequence, we collect the photons that travel longer distances within brain tissue. Bulk scattering randomizes and erases the polarization for the majority of detected photons, but a tiny portion of the detected signal, which remains polarized, accumulates a larger phase shift (i.e. a larger value of the scalar retardance). For the brain sample measured in air, a fraction of the photons with a short path length had introduced only a small phase shift and, hence, did not affect the calculations of the azimuth of the fast optical axis.

A fusion of polarimetric images is performed to highlight a 2D spatial structure of brain white matter in the imaging plane. The polarimetric maps of the scalar linear retardance, the total depolarization, and the azimuth of the fast optical axis of formalin-fixed human brain specimen were used for the data fusion. The process of fusion is illustrated in Fig. 5.7.

The maps of the scalar linear retardance, the depolarization, and the ratio of total depolarization to the square of scalar total linear retardance are shown in Figs. 5.7 (a), (b), (d), respectively. Since this ratio combines both scalar retardance and depolarization, its map demonstrates a clear border between the white and grey matter of a brain. The map of the azimuth of the optical axis (Fig. 5.7 (c)) helps to trace the orientation of brain fiber tracts. However, the azimuth within the cortex zone looks random, indicating the absence of ordered tissue structures at the scale of spatial resolution of our Mueller polarimeter. Then, the map of the azimuth of the optical axis is cropped (see Fig. 5.7 (e)) using the borders of the dark red region (the depolarization values of 0.9 - 1) in the map of total depolarization for a delineation of the zone of brain white matter. Finally, a merged map (see Fig. 5.7. (f)) is obtained by adding two images from Figs. 5.5 (d), (e). It shows a well-delineated border between the gray and white matter zones in the image of thick section of brain tissue as well as identifies the directions of brain white matter fiber tracts (myelinated axons).

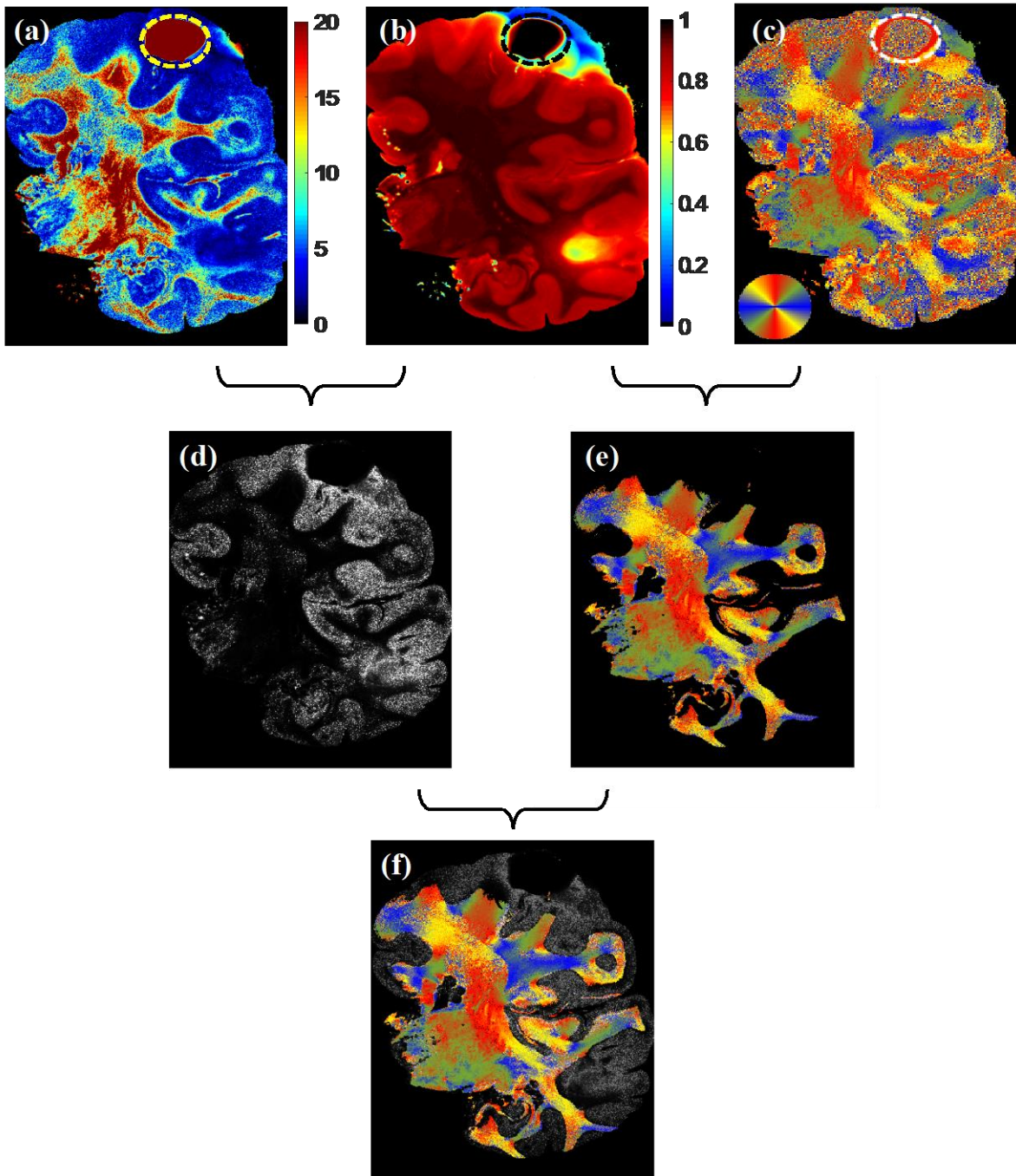


**Figure 5.7** Illustration of the polarimetric image fusion, cropping and merging process: the maps of the polarimetric input parameters - (a) scalar linear retardance, (b) total depolarization, (c) azimuth of the fast optical axis; (d) data fusion map shows the ratio (total depolarization / (scalar linear retardance)<sup>2</sup>); (e) cropped map of the azimuth of the fast optical axis in the zone of brain white matter; (f) map of the merged data.

The map of the azimuth of the fast optical axis of the white matter of fixed human brain tissue measured in reflection and the photo of a corresponding whole mount thin, silver-stained histological section, are shown in Figs. 5.8 (a), (c). It is worth to note that silver-staining of a thin histological section is a gold standard technique used for the ex-vivo visualization of brain fiber tracts.

To check the correlation of the azimuth values with the orientation of fiber tracts, we selected in the polarimetric map of the azimuth five zones: A1-A4 corresponding to the U-fibers tract in the white matter region and one zone A5 in the cortex region. Each pixel in the azimuth map (see Fig. 5.8 (a)) is described by the unit vector with the angle corresponding to the azimuth of the optical axis. All selected zones A1-A5 in the azimuth map (see Fig. 5.8 (b)), represent squares of  $9 \times 9$  pixels. The corresponding zones B1-B5 of the same U-fibers tract and cortex were also selected in the image of the silver-stained thin histological section (Fig. 5.8 (d)). The azimuth angle of the optical axis changes from  $90^\circ$  (A1 zone) to  $+45^\circ$  (A4 zone), thus, reproducing the shape of the U-fibers tract in the histology image.

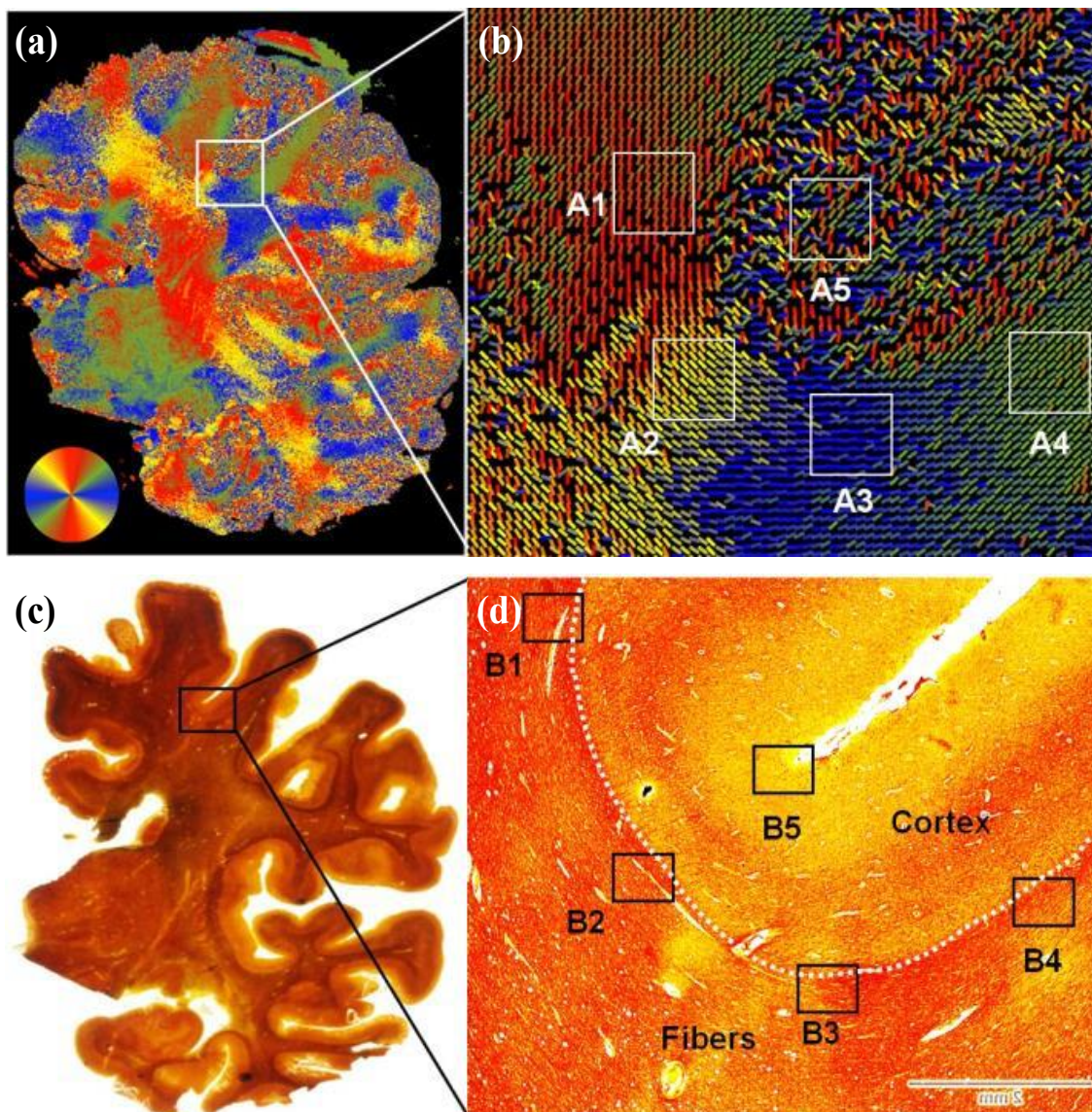


**Figure 5.8** Images of coronal section of a fixed human brain specimen: (a) azimuth of optical axis; (c) photo of the whole mount silver-stained thin section; the enlarged insets (b)  $71 \times 66$  pixels, and (d) scale bar 2 mm show U-fibers that curve around the superior frontal sulcus, connecting the superior and medial frontal gyrus. A1-A5 consist of  $9 \times 9$  pixels.

Then, we calculated the circular histograms for the selected zones A1-A5 (see Fig. 5.9 (a)). The enlarged histological images of the corresponding zones B1-B5 are presented in Fig. 5.9 (b). The circular histograms for the A1-A4 zones show high directionality and low spread. The circular histogram for the cortex zone A5 demonstrates the isotropic distribution of the azimuth, thus, confirming the absence of optical anisotropy in gray matter of a brain at the mesoscale of several hundred microns defined by the spatial resolution of our instrument.

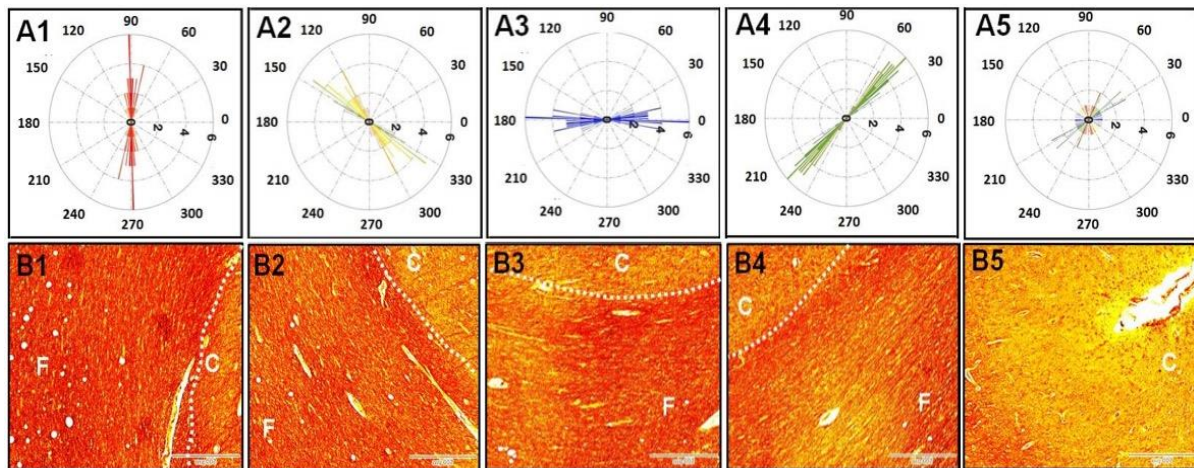


**Figure 5.9** (a) Circular histograms of the azimuth of the optical axis for the zones A1-A5 in Fig. 5.8 (b); (b) the corresponding enlarged zones B1-B5 of U-fibers tract in Fig. 5.5 (d), scale bar - 500 microns. C - cortex zone, F - white matter fiber tract zone, white dashed line represents the border between the cortex and brain white matter.

The circular histograms for the zones A1-A4 demonstrate a compelling correlation with the direction of the fibers in the enlarged images of the corresponding zones B1-B4 of the thin silver-stained tissue section. The random distribution of the azimuth of the optical axis in the cortex zone A5 is supported by the enlarged histological image of the corresponding zone B5 that contains many cells and sparse, randomly distributed fibers. The mean values and standard deviations of the distributions of the azimuth angle for the zones A1-A5 are given in Tab. 5.1.

**Table 5.1** Mean value and standard deviation (StD) of the azimuth angle: zones A1 – A5

Zone	A1	A2	A3	A4	A5
Mean (°)	91.1	136.3	179.5	49.1	13.2
StD	10.4	5.9	11.1	11.8	50.5

### 5.3.2. Fresh animal brain tissue

To exclude the impact of tissue fixation with formalin on the polarimetric parameters, we also performed the wide-field polarimetric measurements on unfixed specimen of fresh cadaveric calf brain tissue in air with the same imaging Mueller polarimeter in backscattering

configuration. The results of measurements at 550 nm are shown in Fig. 5.10. The bright zones in the gray scale intensity image (Fig. 5.10(a)) are due to specular reflections because the surface of the sample is not flat. The values of the depolarization of fresh brain white matter measured in air vary between 0.75 and 1 and are comparable with the corresponding values of the depolarization measured for the formalin-fixed human brain tissue (Fig. 5.5 (b)). The contrast between gray matter and white matter of brain on the depolarization map of fresh brain tissue is less marked than that seen in fixed tissue. It is known that tissue fixation with formalin links soluble and structural proteins together and affects the optical properties of tissue, like the depolarization power and the scalar retardation [21].

The values of the scalar linear retardance of the fresh brain tissue measured in air (Fig. 5.10(c)) are comparable with the corresponding values measured for the formalin-fixed brain tissue immersed in water (Fig. 5.5(c)). The map of the azimuth of the optical axis (Fig. 5.10 (d)) also clearly highlights the directions of fiber tracts similar to the azimuth maps of fixed brain tissue in the white matter zone (Fig. 5.5 (d), Fig. 5.6 (d)). We also observe the U-fibers tracts at the periphery of the fresh calf brain specimen and thick vertical and horizontal fiber tracts in the central part of the map of the azimuth map of the optical axis.

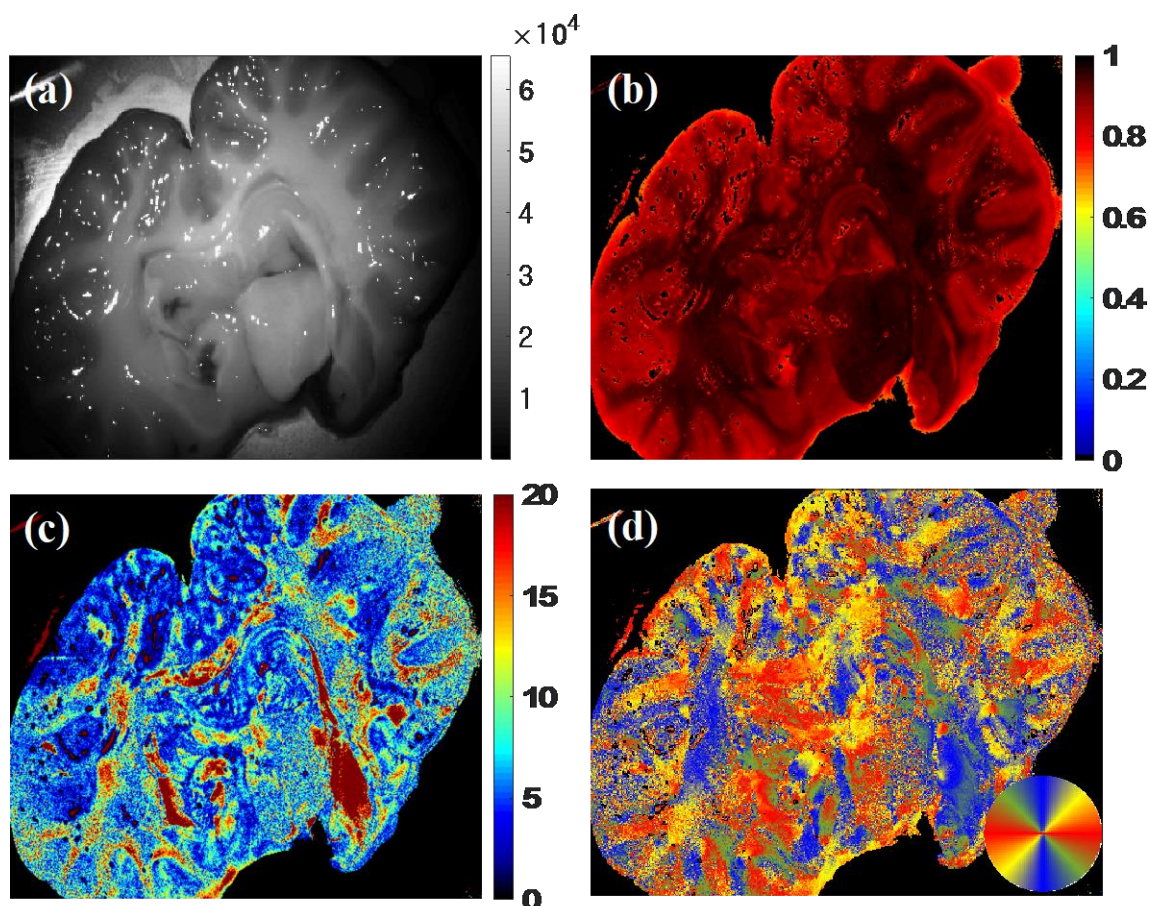


**Figure 5.10** Images of a thick section of fresh cadaveric calf brain measured in air in reflection with the wide-field imaging Muller polarimeter: (a) grayscale total intensity image, (b) depolarization, (c) scalar retardance (degrees), and (d) azimuth of the fast optical axis.

We repeated the measurements of fresh calf brain sample entirely immersed in distilled water in order to flatten the surface of the sample by index matching. The gray-scale intensity image, the total depolarization, the scalar linear retardance, and the azimuth of the fast optical axis are shown in Fig. 5.11.

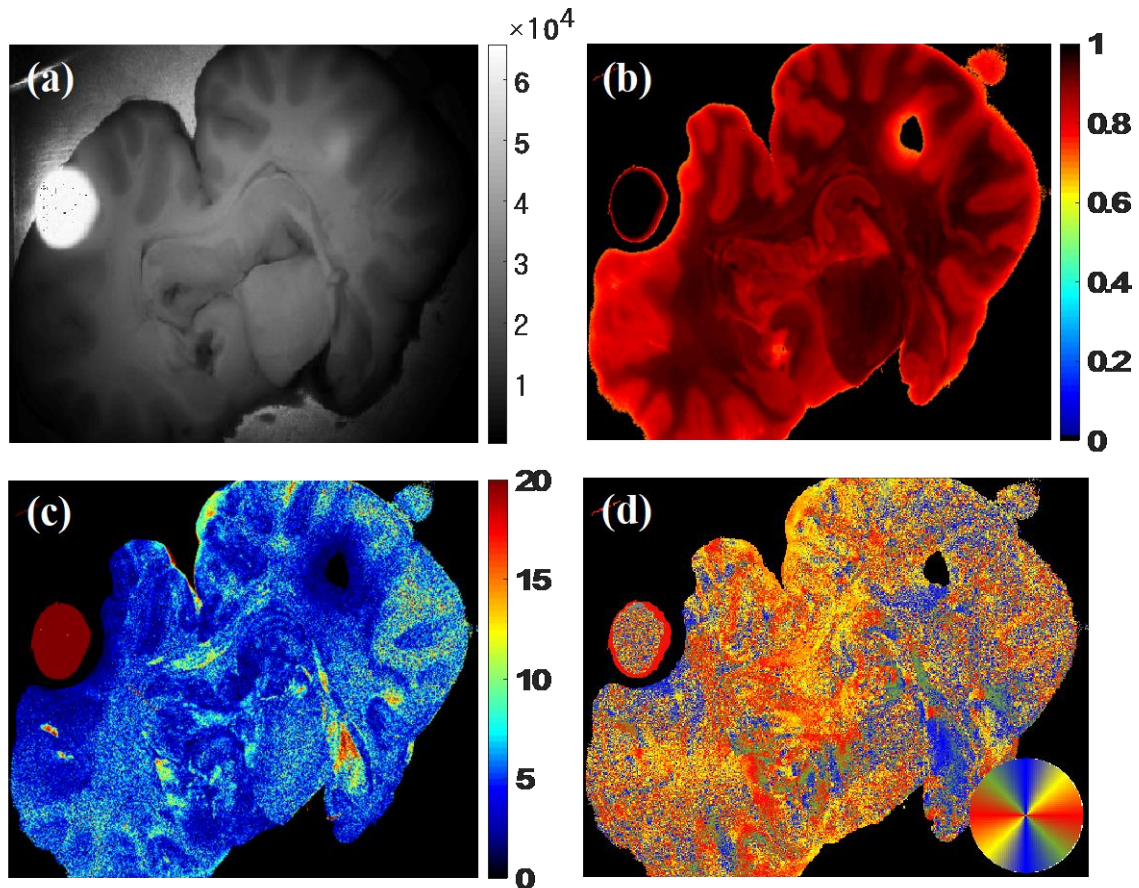


**Figure 5.11** Images of a thick section of fresh cadaveric calf brain totally immersed in water and measured in reflection with the wide-field imaging Muller polarimeter: (a) grayscale total intensity image, (b) depolarization, (c) scalar retardance (degrees), and (d) azimuth of the fast optical axis.

The bright spot in the intensity image (Fig. 5.11 (a)) is also due to specular reflection of the slightly divergent incident light beam at the air-water interface. The contrast between cortex and white matter of the fresh calf brain in the depolarization map (see Fig. 5.11 (b)) is similar to that seen in Fig. 5.10 (b). It means that the surface scattering does not affect significantly the depolarization of light backscattered from fresh calf brain tissue, i.e. the depolarization is caused by bulk backscattering mainly. Contrary to formalin-fixed brain tissue, the white matter of water immersed fresh brain tissue does not demonstrate high retardance value and the contrast between the grey and white matter zones is decreased (Fig. 5.11 (c)). The map of the azimuth of the optical axis shows random orientation of the optical axis pixel-wise that means that water immersion erases the anisotropy of the refractive index of white matter of healthy brain. Most probably, this effect is due to the water intake by fresh brain tissue.

The measurements of both fixed human and fresh cadaveric animal brain tissue were also performed with the wavelengths of 600 nm and 650 nm. The absolute values for the

depolarization and the scalar linear retardance, as well as the image contrast for the depolarization, the scalar linear retardance, and the azimuth of the optical axis, were very similar to those found at 550 nm. The lack of spectral sensitivity in our studies can be explained by the fact that all polarimetric measurements were made in brain tissue obtained post-mortem. There is almost no blood in a fixed tissue specimen ( $< 1\%$  according to the analysis done by the pathologist for the fixed brain specimen). The amount of blood in fresh cadaveric animal tissue is also significantly less than in live brain tissue, and blood hemoglobin is known to be the main cause of the visible light absorption in tissue, with the peaks of absorption at 500 nm and 550 nm [22]. It is highly likely that the spectral dependence of polarimetric parameters in the visible wavelength range will also reveal contrast enhancement when imaging live brain tissue. The depth of light penetration in fresh tissue depends strongly on the wavelength used [23], [24]. Taking polarimetric images at different wavelengths in real-time during neurosurgery may help surgeons to estimate the remaining tumor thickness and guide tumor resection.

## 5.4. Conclusions

We demonstrated the feasibility of visualizing white matter fiber tracts with a wide-field imaging Mueller polarimeter operating in the visible wavelength range in backscattering configuration. The main finding of our study is the sensitivity of backscattered polarized light to optical anisotropy, induced by the densely packed neuron bundles constituting the fiber tracts of healthy brain white matter, which are not visible to the naked human eye. This result was confirmed by histological analysis of a silver-stained thin section of a brain specimen. The directions of fibers in the brain white matter, which are visible on the enlarged optical *transmission* microscopy images of a silver-stained *thin section*, are well represented by the azimuth of the optical axis calculated from the Mueller matrix images of a *thick specimen* measured in *reflection*.

We showed that the wide-field Mueller polarimetry of thick sections of brain tissue in backscattering configuration clearly demonstrates the presence of fiber tracts on the images of total depolarization and linear retardance. Moreover, the orientation of the fiber tracts in the brain white matter is visualized on the map of the azimuth of the optical axis. This is the most robust indicator of fiber tract directions, and it works well for both fixed and fresh brain tissue. The azimuth of the optical axis is almost insensitive to surface roughness, which is essential for the envisaged clinical applications, where the surface morphology of the surgical site will differ significantly from the conditions of our proof-of-principle studies.

Our findings open the field for the clinical implementation of Mueller polarimetry, an optical imaging technique with several key advantages. First, being a wide field polarimetric imaging modality, it does not require sample scanning or image stitching. This makes it faster and easier to use than polarization-sensitive optical coherence tomography [25] or polarization-sensitive optical coherence microscopy [26], two-photon excited fluorescence,

and second harmonic generation microscopy [27]. Second, our imaging Mueller polarimeter operates in the visible wavelength range, which precludes any potential harm to patients, and is based on reflection geometry, which is a significant step toward in vivo applications. Despite the shallow penetration depth of light within biological tissue in the visible wavelength range (e.g., compared to the ultrasound imaging modality), the wide-field Mueller imaging polarimetry is capable of providing additional information on the type of tissue and relative spatial orientation of brain tissue fiber tracts at sight at any given moment during neurosurgery. Further studies are envisaged to confirm the potential of the wide-field Mueller imaging polarimetry to visualize the border between the tumor and healthy brain tissue, first ex vivo, then in vivo.

## References

1. R. Soffietti, B. G. Baumert, L. Bello, A. Von Deimling, H. Duffau, M. Frénay, W. Grisold, R. Grant, F. Graus, K. Hoang-Xuan, M. Klein, B. Melin, J. Rees, T. Siegal, A. Smits, R. Stupp, and W. Wick, “Guidelines on management of low-grade gliomas: Report of an EFNS–EANO Task Force,” *Eur. J. Neurol.*, vol. 17, no. 9, pp. 1124–1133, Sep. 2010.
2. C. L. Pedersen and B. Romner, “Current treatment of low grade astrocytoma: A review,” *Clin. Neurol. Neurosurg.*, vol. 115, no. 1, pp. 1–8, Jan. 2013.
3. E. B. Claus and P. M. Black, “Survival rates and patterns of care for patients diagnosed with supratentorial low-grade gliomas: Data from the SEER program, 1973-2001,” *Cancer*, vol. 106, no. 6, pp. 1358–1363, Mar. 2006.
4. P. Y. Wen and S. Kesari, “Malignant Gliomas in Adults,” *N. Engl. J. Med.*, vol. 359, no. 5, pp. 492–507, Jul. 2008.
5. N. Sanai, M.-Y. Polley, M. W. McDermott, A. T. Parsa, and M. S. Berger, “An extent of resection threshold for newly diagnosed glioblastomas: Clinical article,” *J. Neurosurg.*, vol. 115, no. 1, pp. 3–8, Jul. 2011.
6. M. Lacroix, D. Abi-Said, D. R. Fourney, Z. L. Gokaslan, W. Shi, F. DeMonte, F. F. Lang, I. E. McCutcheon, S. J. Hassenbusch, E. Holland, K. Hess, C. Michael, D. Miller, and R. Sawaya, “A multivariate analysis of 416 patients with glioblastoma multiforme: prognosis, extent of resection, and survival,” *J. Neurosurg.*, vol. 95, no. 2, pp. 190–198, Aug. 2001.
7. N. Sanai, M. B. Berger, “Glioma extent of resection and its impact on patient outcome,” *Neurosurgery*, vol. 62, no. 4, pp. 753-764, 2008.
8. J. M. Pusterla, A. A. Malfatti-Gasperini, X. E. Puentes-Martinez, L. P. Cavalcanti, and R. G. Oliveira, “Refractive index and thickness determination in Langmuir monolayers of myelin lipids,” *Biochim. Biophys. Acta – Biomemb.*, vol. 1859, no. 5,

pp. 924–930, May 2017.

9. W. Stummer, U. Pichlmeier, T. Meinel, O. D. Wiestler, F. Zanella, and H.-J. Reulen, “Fluorescence-guided surgery with 5-aminolevulinic acid for resection of malignant glioma: a randomised controlled multicentre phase III trial,” *Lancet Oncol.*, vol. 7, no. 5, pp. 392–401, May 2006.
10. W. Stummer, S. Stocker, S. Wagner, H. Stepp, C. Fritsch, C. Goetz, R. Kiefmann, H. J. Reulen, “Intraoperative detection of malignant gliomas by 5-aminolevulinic acid-induced porphyrin fluorescence,” *Neurosurgery*, vol. 42, no. 3, pp. 516-518, 1998
11. K. M. Hebeda, A. E. Saarnak, M. Olivo, H. J. Sterenborg, J. G. Wolbers, “5-Aminolevulinic acid induced endogenous porphyrin fluorescence in 9L and C6 brain tumours and in the normal rat brain,” *Acta Neurochir (Wien)*, vol. 140, no. 5, pp. 512-513, 1998.
12. P. Schucht, S. Knittel, J. Slotboom, K. Seidel, M. Murek, A. Jilch, A. Raabe, and J. Beck, “5-ALA complete resections go beyond MR contrast enhancement: shift corrected volumetric analysis of the extent of resection in surgery for glioblastoma,” *Acta Neurochir (Wien)*, vol. 156, no. 2, pp. 305–312, Feb. 2014.
13. C. Nimsy, O. Ganslandt, B. von Keller, J. Romstöck, and R. Fahlbusch, “Intraoperative High-Field-Strength MR Imaging: Implementation and Experience in 200 Patients1,” *Radiology*, vol. 233, no. 1, pp. 67–78, Oct. 2004.
14. C. Senft, A. Bink, K. Franz, H. Vatter, T. Gasser, and V. Seifert, “Intraoperative MRI guidance and extent of resection in glioma surgery: a randomised, controlled trial,” *Lancet Oncol.*, vol. 12, no. 11, pp. 997–1003, Oct. 2011.
15. A. K. Petridis, M. Anokhin, J. Vavruska, M. Mahvash, and M. Scholz, “The value of intraoperative sonography in low grade glioma surgery,” *Clin. Neurol. Neurosurg.*, vol. 131, pp. 64–68, Apr. 2015.
16. P. Schucht, H. R. Lee, M. H. Mezouar, E. Hewer, A. Raabe, M. Murek I. Zubak, J. Goldberg, E. Kövari, A. Pierangelo, T. Novikova, “Visualization of White Matter Fiber Tracts of Brain Tissue Sections with Wide-field Imaging Mueller Polarimetry,” *IEEE Trans. Med. Imaging*, 10.1109/TMI.2020.3018439, 2020.
17. P. Schucht, H. R. Lee, M. H. Mezouar, E. Hewer, A. Raabe, M. Murek, I. Zubak, J. Goldberg, E. Kovari, A. Pierangelo, and T. Novikova, “Wide-Field Mueller Polarimetry of Brain Tissue Sections for Visualization of White Matter Fiber Tracts,” <http://arxiv.org/abs/2005.12440>, 2020.
18. A. Pierangelo, S. Manhas, A. Benali, M.-R. Antonelli, T. Novikova, P. Validire, B. Gayet, and A. De Martino, “Use of Mueller polarimetric imaging for the staging of human colon cancer,” *Proc. SPIE 7895*, Optical Biopsy IX, 78950E, 2011.
19. T. Novikova, A. Pierangelo, S. Manhas, A. Benali, P. Validire, B. Gayet, and A. De Martino, “The origins of polarimetric image contrast between healthy and cancerous human colon tissue,” *Appl. Phys. Lett.*, vol. 102, p. 241103-241106, Jun. 2013.

20. A. Pierangelo, A. Nazac, A. Benali, P. Validire, H. Cohen, T. Novikova, B. H. Ibrahim, S. Manhas, C. Fallet, , M.-R. Antonelli, and T. Novikova, A.-D. Martino “Polarimetric imaging of uterine cervix: a case study,” *Opt. Express*, vol. 21, no. 12, pp. 14120–14130, Jun. 2013.
21. M. F. G. Wood, N. Vurgun, M. A. Wallenburg, and I. A. Vitkin, “Effects of formalin fixation on tissue optical polarization properties,” *Phys. Med. Biol.*, vol. 56, no. 8, pp. N115–N122, Apr. 2011.
22. S. Prahl, “Optical absorption of hemoglobin,” (Portland, OR: Oregon Medical Laser Center), available at <http://omlc.ogi.edu/spectra/hemoglobin/>, 1999.
23. A. Pierangelo, S. Manhas, A. Benali, C. Fallet, M.-R. Antonelli, T. Novikova, B. Gayet, P. Validire, and A. De Martino, “Ex vivo photometric and polarimetric multilayer characterization of human healthy colon by multispectral Mueller imaging,” *J. Biomed. Opt.*, vol. 17, no. 6, p. 066009, Jun. 2012.
24. T. Novikova, A. Pierangelo, A. De Martino, A. Benali, and P. Validire, “Polarimetric imaging for cancer diagnosis and staging,” *OSA Optics and photonics News Magazine*, vol.23, no.10, pp. 26-33, 2012.
25. K. S. Yashin, E. B. Kiseleva, E. V. Gubarkova, A. A. Moiseev, S. S. Kuznetsov, P. A. Shilyagin, G. V. Gelikonov, I. A. Medyanik, L. Y. Kravets, A. A. Potapov, E. V. Zagaynova, and N. D. Gladkova, “Cross-Polarization Optical Coherence Tomography for Brain Tumor Imaging,” *Front. Oncol.*, Apr. 2019, available at <https://doi.org/10.3389/fonc.2019.00201>.
26. H. Wang, T. Akkin, C. Magnain, R. Wang, J. Dubb, W. J. Kostis, M. A. Yaseen, A. Cramer, S. Sakadžić, and D. Boas, “Polarization sensitive optical coherence microscopy for brain imaging,” *Opt. Lett.*, vol. 41, no. 10, pp. 2213–2216, May 2016.
27. L. Jiang, X. Wang, Z. Wu, H. Du, S. Wang, L. Li; N. Fang, P. Lin, J. Chen, D. Kang, S. Zhuo, “Label-free imaging of brain and brain tumor specimens with combined two-photon excited fluorescence and second harmonic generation microscopy,” *Laser Phys. Lett.*, vol. 14, no. 10, pp. 105401, Sep. 2017.

# General conclusions and Perspectives

The main goal of the thesis was the demonstration of the feasibility of digital histology and optical biopsy of biological tissue with imaging Mueller polarimetry. Our comprehensive proof-of-principle studies of both thin and thick sections of biological tissue include the fundamental theory of Mueller polarimetry, experiments with the custom-built imaging Mueller polarimeters, Monte Carlo modeling, and image processing (DBSCAN) using the experimental polarimetric images of tissue.

The interaction of incident polarized light with biological tissue can be used to probe the optical anisotropy and depolarization properties of tissue. We explored the potential of imaging Mueller polarimetry combined with the appropriate data post-processing algorithms as fast and non-contact imaging technique for digital histology and optical biopsy of tissue, because Mueller polarimetry is capable to detect the above mentioned optical parameters. We measured two different types of biological tissues (thin sections of human skin models and thick sections of brain tissue) using ferroelectric liquid crystal-based Mueller polarimeters in transmission (microscope) and in reflection (wide-field imaging polarimeter) configuration, respectively.

To check the feasibility of the reduction in a number of steps in the conventional histological section preparation procedure (e.g., formalin-fixation, embedding in paraffin wax, sectioning, deparaffinization, and staining with dyes), the unstained skin model sections were measured with Mueller microscope. We have demonstrated that the polarimetric parameters, extracted from the measured Mueller matrix of unstained tissue section, can provide reliable tissue characterization and classification depending on tissue regions (e.g., dermis and epidermis in human skin equivalents). It might be helpful for rapid sample preparation, as well as for accurate analysis of biological tissue.

The image segmentation was used for improved visualization of different zones in the polarimetric image of a sample. Two different approaches were tested – data fusion and data clustering. Imaging Mueller polarimetry provides us a full set of polarimetric images that can be used for data post-processing and image segmentation. For example, we showed that fusion of polarimetric images sharpens the border between white matter and gray matter of healthy brain tissue. Using the unsupervised DBSCAN algorithm for data clustering we demonstrated that it can automatically label the zones of interest in polarimetric images according to tissue optical properties.

The validity of the differential Mueller matrix formalism for biological tissue was proven experimentally. The thickness invariant optical parameters were suggested for more accurate analysis of polarimetric images. The rotation invariants of the logarithmic decomposition of

Mueller matrix were derived for the numerical simulation and interpretation of the experimental polarimetric results for the dermal layer of skin equivalents.

The extension of polarized Monte Carlo algorithm to model the birefringent host medium was performed and validated by simulating backscattered Mueller matrix images of two scattering optical phantoms with isotropic and anisotropic host media, respectively. The polarized Monte Carlo modeling was used to understand the microstructure and optical properties of the biological tissue specimens.

Summarizing the results of the thesis, we have shown that imaging Mueller polarimetry combined with the appropriate data post-processing algorithms can be an attractive option for digital histology as well as for optical biopsy of tissue. To do so we have used experiments with both tissue equivalents and real biological tissue specimens and supported our conclusions with polarimetric data clustering, fusion and Monte Carlo modeling

The perspectives for future studies are listed below.

1. Wide-field imaging brain polarimetry is ready for extensive experimental campaign in the clinical settings (near-in-situ). The goal is to test the capability of this imaging modality to visualize the border between brain tumor and surrounding tissue on freshly excised human brain tumoral specimens. This step in the development of the technique shall bring invaluable data for the design of polarimetric add-on for a commercial surgical microscope.
2. Polarized Monte Carlo simulations of the backscattered Mueller matrices of optical anisotropic scattering phantoms with the uneven air-tissue interface will provide the insights on the impact of tissue surface morphology on the coefficients of Mueller matrix and extracted polarimetric parameters of tissue. Modeling of the backscattered Mueller matrices of multi-layered optical phantoms with the optical axes of each layer oriented at the different azimuth and varying top layer thickness will give information on the effective probing depth of light beam. It can be useful for the estimation of depth sensitivity of Mueller polarimetry in the visible wavelength range.
3. Important remaining step towards automated digital histology implementation shall include the number of studies of different tissue types at various medical conditions (e. g. healthy, inflammation, pre-cancer).
4. Further improvement of DBSCAN clustering algorithm for the automated selection of the optimal values of the input parameters will help to perform accurate diagnostic clustering of polarimetric data in a real time. Collaboration with group of Dr. Alex Doronin from University of Victoria on neural-network research in this direction looks logical and promising.

# List of figures

<b>Figure 1.1</b>	<i>Description of a polarization ellipse in x-y laboratory coordinate system. <math>\psi</math> is the orientation angle, <math>\chi</math> is the ellipticity angle, <math>\alpha</math> is the auxiliary angle. ....</i>	8
<b>Figure 1.2</b>	<i>The Poincaré sphere. <math>L_0</math>, <math>L_{90}</math>, <math>L_{+45}</math>, <math>L_{-45}</math>, <math>RC</math>, and <math>LC</math> represents the linear horizontal, linear vertical, linear <math>+45^\circ</math>, linear <math>-45^\circ</math>, right circular, left circular polarized light, respectively. ....</i>	15
<b>Figure 1.3</b>	<i>The incident beam interacts with a sample, and the emerging beam comes out. ....</i>	16
<b>Figure 1.4</b>	<i>The propagation of a polarized light through a polarizer. <math>p_x</math> and <math>p_y</math> are the attenuation coefficients. ....</i>	17
<b>Figure 1.5</b>	<i>The propagation of polarized light through a retarder. The two-phase shifts (<math>+\phi/2</math> and <math>-\phi/2</math>) are along the x- and y-axis, respectively. ....</i>	19
<b>Figure 1.6</b>	<i>The rotation of the optical field components by a rotator. ....</i>	20
<b>Figure 1.7</b>	<i>The derivation of the Mueller matrix for rotated polarizing components. ....</i>	21
<b>Figure 1.8</b>	<i>The propagation of polarized light through a depolarizer. ....</i>	24
<b>Figure 2.1</b>	<i>Stokes-Mueller description of the operation of any polarimetric setup. ....</i>	36
<b>Figure 2.2</b>	<i>Optical elements (a horizontal polarizer (HP), two ferroelectric liquid crystals (FLC1, FLC2), and a wave plate (WP) for the PSG and PSA. The arrows show the direction of light propagation for PSG and PSA and corresponding arrangement of the optical elements. ....</i>	44
<b>Figure 2.3</b>	<i>Mueller matrix microscope in transmission configuration: (a) optical layout, (b) photo. ....</i>	46
<b>Figure 2.4</b>	<i>Wide-field imaging Mueller polarimeter (a) schematic optical layout; (b) photo. ....</i>	47
<b>Figure 3.1</b>	<i>A flowchart represents three groups of clustering approaches (partitional, hierarchical, and locality-based) and corresponding algorithms. ....</i>	54
<b>Figure 3.2</b>	<i>An example of centroid-based clustering of a 2D dataset. ....</i>	55
<b>Figure 3.3</b>	<i>An example of hierarchical agglomerative clustering of a 2D dataset using the Euclidian distance metric: (a) raw data; (b) hierarchical clustering dendrogram. ....</i>	56
<b>Figure 3.4</b>	<i>An example of distribution-based clustering of a 2D dataset. ....</i>	56
<b>Figure 3.5</b>	<i>An example of density-based clustering of a 2D dataset. There are two clusters, grey symbols represent data outliers (noise) ....</i>	57
<b>Figure 3.6</b>	<i>The illustration of cluster generation and expansion in a 2D space (MinPts=4) (a) <math>p</math> is a core point (<math>N\epsilon(p) &gt; \text{MinPts}</math>), <math>q</math> is a border point (<math>0 &lt; N\epsilon(q) &lt; \text{MinPts}</math>), and they are directly density-reachable, (b) <math>p</math> is density-reachable to <math>q</math>, and (c) <math>p</math> is density-connected to <math>q</math>. ....</i>	58
<b>Figure 3.7</b>	<i>The illustration of the updated version of the DBSCAN clustering algorithm (a) generation of a cluster; if both MinPts and <math>\epsilon</math> criteria are matched, red region</i>	

(radius  $\epsilon/r$ ) is automatically attributed to the same cluster as the core point, (b) expansion of the cluster; if both MinPts and criteria are matched, the points, located in the yellow region, would also be attributed to the same cluster. This expansion process will be repeated until there will be no point to assign to a cluster. ....60

**Figure 3.8** (a) Example of sorted 4-dist plot for a 2D dataset shown in panel (b). Adapted from [1].....60

**Figure 3.9** Blue, green, orange, and red lines show the results for the datasets of different size - 10000, 20000, 30000, and 40000 points, respectively. These datasets were created by random and uniform sampling of the complete dataset of 480000 points. The linear regression curves have very close x-intercept values for all datasets (see inset).....61

**Figure 3.10** The execution time versus the size of a dataset. Blue dots - original version of the DBSCAN algorithm, red dots - updated version of the DBSCAN algorithm. The disconnection between the values of 80 and 1960 are shown by the break of vertical axis.....62

**Figure 3.11** The execution time versus radius  $\epsilon$  for a dataset containing 40000 points. Blue dots - the results for the original version of the DBSCAN algorithm, red dots - the results of the updated version of the DBSCAN algorithm. The disconnection between the values of 1 and 2 on the horizontal axis is shown with the axis-break. ....63

**Figure 3.12** The execution time versus threshold parameter MinPts, Blue dots – the results of the original version, red dots - the results of the updated version of the DBSCAN algorithm. ....64

**Figure 3.13** The execution time versus the inverse of scaling factor  $r$ . The results are shown for the updated version of the DBSCAN algorithm. ....65

**Figure 3.14** (a) Triple scattering, self-avoiding path, (b) triple scattering, a path goes through particle  $S_1$  twice. ....67

**Figure 3.15** (adapted from [23]). Scattering angles  $\theta$  and  $\varphi$  are not independent parameters. The initial local reference frame ( $e_x, e_y, e_z$ ) is rotated by angle  $\varphi$  to obtain the incident frame ( $e_{xi}, e_{yi}, e_{zi}$ ) with unit vectors  $e_{xi}$  and  $e_{yi}$  parallel and perpendicular to the scattering plane defined by the incident direction and direction of scattering (which is defined by angle  $\theta$ ). After scattering of photon by sphere its new polarization state is given by Mie solution defined in the scattering reference frame ( $e_{xs}, e_{ys}, e_{zs}$ ), which becomes a new local reference frame.....77

**Figure 3.16** Structurally anisotropic models of biological tissue and tissue components: (a) long dielectric cylinders, (b) dielectric plates, and (c) chiral aggregates of particles. ....81

**Figure 3.17** Vector of optical axis  $\mathbf{e}$  ( $\cos \eta, \sin \eta$ ) and direction of light propagation  $\mathbf{z}'$  ( $u_x, u_y, u_z$ ) in the laboratory coordinate system.....81

**Figure 3.18** Vector of optical axis  $\mathbf{e}$  in the local coordinate system ( $\mathbf{x}', \mathbf{y}', \mathbf{z}'$ ) .....82

**Figure 3.19** Simulated backscattered Mueller matrix images of isotropic medium with embedded spherical scatterers (left) and linear birefringent scattering medium with randomly and uniformly distributed spherical scatterers (right). White circles highlight the difference in MM coefficients. The area of each image is  $1\text{cm}^2$ . ....83

<b>Figure 4.1</b>	<i>Three layers of human skin tissue: epidermis, dermis, and subcutaneous. © Skin Cancer Screening (PDQ®), <a href="https://www.cancer.gov/types/skin/patient/skin-screening-pdq">https://www.cancer.gov/types/skin/patient/skin-screening-pdq</a> .....</i>	<i>89</i>
<b>Figure 4.2</b>	<i>(a) Photo of the Snapwell cell culture inserts used for the growth of the 3D in-vitro skin tissue models © K. Dobberke, Fraunhofer ISC, Germany. (b) schematic representation (top) and the microscopy image of the hematoxylin-eosin stained thin section of the reconstructed human epidermis; (c) schematic representation (top) and the microscopy image of the hematoxylin-eosin stained thin section of the full-thickness skin model, scale bar 100 <math>\mu\text{m}</math> © Florian Groeber-Becker, Fraunhofer ISC, Germany.....</i>	<i>89</i>
<b>Figure 4.3</b>	<i>Schematic of the preparation of the skin model tissue thin sections; (a) block of paraffin-embedded skin tissue equivalent; (b) cutting the block of the paraffin-embedded skin tissue sample in two pieces and slicing 5 <math>\mu\text{m}</math> thick stripes from both pieces with a microtome blade; (c) removing paraffin and placing two thin stripes of unstained skin equivalent on the microscope glass without a coverslip; repeating the same procedure for four adjacent sections of the different nominal thicknesses (10 <math>\mu\text{m}</math>, 16 <math>\mu\text{m}</math>, 20 <math>\mu\text{m}</math>, and 30 <math>\mu\text{m}</math>): (d) photo of five samples of different thicknesses.....</i>	<i>90</i>
<b>Figure 4.4</b>	<i>(a) Photo of stylus profilometer; (b) scanning patterns (10 times), red arrows show the direction of the stylus passes and (c) 2D depth profile of the sample. 91</i>	<i>91</i>
<b>Figure 4.5</b>	<i>(a) Explanation of tissue sectioning along with the vertical to the orientation of collagens; red arrow shows section direction, yellow circle represents the zone where is scanned with profilometer, (b) 20X microscopic image of the thin tissue section (NT - 5 <math>\mu\text{m}</math>), yellow circle indicates the location of a spot measured with Mueller microscope; (c) corresponding 3D thickness profile measured with profilometer.....</i>	<i>92</i>
<b>Figure 4.6</b>	<i>(a) Explanation of tissue sectioning along with the parallel to the orientation of collagens; red arrow shows section direction, yellow circle represents the zone where is scanned with profilometer, (b) 20X microscopic image of the thin tissue section (NT - 10 <math>\mu\text{m}</math>) yellow circle indicates the location of a spot measured with Mueller microscope; (c) corresponding 3D thickness profile measured with profilometer.....</i>	<i>93</i>
<b>Figure 4.7</b>	<i>Maps of (a) total intensity, (b) total linear retardance RT (in radians), (c) dimensionless total linear dichroism DT , and dimensionless diagonal coefficients (d) <math>\alpha_{22}</math>, (e) <math>\alpha_{33}</math>, (f) <math>\alpha_{44}</math> of the matrix Lu, calculated from the experimental Mueller matrix data by applying pixel-wise LMMD. Labels represent the mean thickness of thin histological sections measured with a stylus profilometer. FoV is about 600 <math>\mu\text{m}</math>. .....</i>	<i>95</i>
<b>Figure 4.8</b>	<i>Thickness dependence plots of (a) total linear retardance (radians), (b) dimensionless total linear dichroism, (c-e) dimensionless depolarization parameters <math>\alpha_{22}</math>, <math>\alpha_{33}</math>, and <math>\alpha_{44}</math> averaged over a zone of dermal layer of HSE tissue sections. Experimental data are shown by blue symbols, solid red lines represent the results of (a) linear and (b-d) quadratic fit. ....</i>	<i>97</i>
<b>Figure 4.9</b>	<i>Bulk and surface scattering of light transmitted through a thin section of HSE tissue. ....</i>	<i>97</i>
<b>Figure 4.10</b>	<i>The 6x6 matrix of 2D histograms of the total transmitted intensity, linear retardance, linear dichroism, and the absolute values of the linear and circular depolarization (<math> \alpha_{22} </math>, <math> \alpha_{33} </math>, and <math> \alpha_{44} </math>) for dermal layer of HSE section of 10 <math>\mu\text{m}</math> NT. ....</i>	<i>99</i>

- Figure 4.11** (a) Illustration of the calculation of weighted average of pixel values in the nearest 2 by 2 neighborhood; (b) clustering results in a z-score space (see text),  $RT$  – linear retardance,  $\alpha_{44}$ – circular depolarization parameter,  $M_{11}$  – total transmitted intensity. Black markers show noise, blue ones – bare glass, red ones – dermis, green ones - epidermis; (c) corresponding image segmentation: noise, bare glass, dermis, and epidermis zones are rendered in black, blue, red, and green, respectively. ....100
- Figure 4.12** Reconstructed images of the HSE sections of different NT: 5, 10, 16, 20, 30  $\mu\text{m}$ . ....101
- Figure 4.13** Thickness dependence plots of (a) total linear retardance (radians), (b) dimensionless total linear dichroism, (c-e) dimensionless depolarization coefficients  $\alpha_{22}$ ,  $\alpha_{33}$ , and  $\alpha_{44}$  averaged over a dermal layer of the histological sections. Experimental data are shown by blue symbols, solid red lines represent the results of (a) linear and (b-d) quadratic fit. ....103
- Figure 4.14** Maps of  $RT|\ln(M_{00})|$ ,  $\alpha_{44}\ln(M_{00})^2$ ,  $(RT)^2/\alpha_{44}$ , and  $\alpha_{44}/(RT)^2$  parameters for HSE histological sections of (a) 5  $\mu\text{m}$ , (b) 10  $\mu\text{m}$ , (c) 16 $\mu\text{m}$ , (d) 20  $\mu\text{m}$ , and (e) 30  $\mu\text{m}$  of nominal thickness. Field of view is about 600  $\mu\text{m}$ . All these ratios are invariant under tissue thickness fluctuations.....105
- Figure 4.15** Results of Monte Carlo simulations with the SB optical model for different dermal layer thickness: (a) total linear retardance  $RT$  (radians) and dimensionless depolarization parameters (b)  $\alpha_L$ , (c)  $\alpha_{44}$ , and (d)  $\alpha_{LA}$ . Simulated data are shown by open symbols corresponding to different concentrations of spherical scatterers. Open boxes with standard deviation represent the experimental data. Solid lines show the results of (a, d) linear and (b, c) parabolic fit of the simulated data. ....112
- Figure 4.16** Results of Monte Carlo simulations using the SCB optical model of HSE dermal layer. Dependence on the layer thickness of (a) total linear dichroism  $DT$  (dashed line is a linear regression curve for the experimental data), (b) total linear retardance  $RT$ , (c-e) depolarization parameters  $\alpha_L$ ,  $\alpha_{44}$ , and  $\alpha_{LA}$ , respectively. Simulated data are shown by open symbols corresponding to different scattering coefficients  $\mu_c$  (i.e., different concentrations of cylindrical scatterers),  $\mu_s = 1500 \text{ cm}^{-1}$ ,  $R_s = R_c = 0.05\mu\text{m}$ . Open boxes with error bars represent the experimental data. Solid lines show the results of (a), (b) linear, and (c)-(e) quadratic fit of the simulated data. ....114
- Figure 4.17** Dependence of parameter  $\alpha_{LA}$  on layer's thickness for the different radius of cylindrical scatterers. The parameters of the SBC optical model are:  $\mu_s = \mu_c = 1500 \text{ cm}^{-1}$ ,  $R_s = 0.05 \mu\text{m}$ . Open symbols correspond to the different radii of cylindrical scatterers:  $R_c = 0.05, 0.5, \text{ and } 2 \mu\text{m}$ , respectively. The concentration of cylindrical scatterers  $cc$  was adjusted to keep a constant value of the scattering coefficient  $\mu_c$ . Open boxes with error bars represent the experimental data. Solid lines show the results of a parabolic fit of the simulated data. ....114
- Figure 5.1** Scheme of the a) structure of simplified neuron and b) neuron's axon and its myelin sheath. Adapted from [<https://en.wikipedia.org/wiki/Myelin>]..... 120
- Figure 5.2** Schematic of brain cross-section in a coronal plane. Left bottom inset – view of a brain from above, the dashed line shows the location of a coronal plane; left top inset: 1 - cell bodies of neurons lie within the brain gray matter; 2 - axons; the neurons connect to other areas of the brain or the spinal cord via their

- axons. Top right inset: 3 - corticospinal tract; 4 - anterior-posterior-running arcuate fasciculus fiber tract; 5 - tumor. See explanations in the text. ....121
- Figure 5.3** Photos of (a) two adjacent 1 cm thick sections of the fixed human brain (one half) in a coronal plane (Department of Pathology, University Hospital of Bern, Switzerland); (b) schematic of brain (top view), red lines show the location of coronal plane cuts of one half of a brain. (c) thin whole-mount section stained with Bielschowsky silver impregnation (Department of Pathology, University Hospital of Geneva, Switzerland). ....122
- Figure 5.4** Photo of (a) 1 cm thick fresh calf brain section in a coronal plane; (a) fixed human brain (one half), (b) sectioning of fresh calf brain; (c) schematic of brain (top view), red lines show the location of coronal plane cuts. ....122
- Figure 5.5** Images of a thick coronal section of the fixed human brain measured in air at 550 nm: (a) total intensity, (b) total depolarization, (b) linear retardance (degrees), and (d) azimuth of the fast optical axis. Note, that the polarimetric maps are not affected by a non-uniform illumination from the slightly divergent incident light beam. ....124
- Figure 5.6** Images of a 1 cm thick coronal section of a fixed human brain immersed in water and measured at 550 nm: (a) total intensity, (b) total depolarization, (b) linear retardance (degrees), and (d) azimuth of the fast optical axis. The dashed line delineates the area of specular reflection on the air-water interface. ....125
- Figure 5.7** Illustration of the polarimetric image fusion, cropping and merging process: the maps of the polarimetric input parameters - (a) scalar linear retardance, (b) total depolarization, (c) azimuth of the fast optical axis; (d) data fusion map shows the ratio (total depolarization / (scalar linear retardance)<sup>2</sup>); (e) cropped map of the azimuth of the fast optical axis in the zone of brain white matter: (f) map of the merged data. ....127
- Figure 5.8** Images of coronal section of a fixed human brain specimen: (a) azimuth of optical axis; (c) photo of the whole mount silver-stained thin section; the enlarged insets (b) 71 x 66 pixels, and (d) scale bar 2 mm show U-fibers that curve around the superior frontal sulcus, connecting the superior and medial frontal gyrus. A1-A5 consist of 9 x 9 pixels. ....128
- Figure 5.9** (a) Circular histograms of the azimuth of the optical axis for the zones A1-A5 in Fig. 5.8 (b); (b) the corresponding enlarged zones B1-B5 of U-fibers tract in Fig. 5.5 (d), scale bar - 500 microns. C - cortex zone, F - white matter fiber tract zone, white dashed line represents the border between the cortex and brain white matter. ....129
- Figure 5.10** Images of a thick section of fresh cadaveric calf brain measured in air in reflection with the wide-field imaging Muller polarimeter: (a) grayscale total intensity image, (b) depolarization, (c) scalar retardance (degrees), and (d) azimuth of the fast optical axis. ....130
- Figure 5.11** Images of a thick section of fresh cadaveric calf brain totally immersed in water and measured in reflection with the wide-field imaging Muller polarimeter: (a) grayscale total intensity image, (b) depolarization, (c) scalar retardance (degrees), and (d) azimuth of the fast optical axis. ....131

# List of tables

<b>Table 1.1</b>	<i>Stokes vectors for linear horizontally, linear vertically, linear +45°, linear -45°, right circularly, and left circularly polarized light.....</i>	<i>14</i>
<b>Table 3.1</b>	<i>The execution time (s) for different sizes of a dataset (Original vs Updated DBSCAN).....</i>	<i>63</i>
<b>Table 3.2</b>	<i>The execution time (s) for different values of radius <math>\epsilon</math> (Original vs Updated DBSCAN).....</i>	<i>64</i>
<b>Table 3.3</b>	<i>The execution time (s) for different values of the threshold parameter MinPts (Original vs Updated DBSCAN).....</i>	<i>64</i>
<b>Table 3.4</b>	<i>The execution time (s) for the different values of <math>1/r</math> (Original vs Updated DBSCAN).....</i>	<i>65</i>
<b>Table 4.1</b>	<i>Thickness of thin sections of HSE tissue (batch I), measured and nominal values.....</i>	<i>92</i>
<b>Table 4.2</b>	<i>Thickness of thin sections of HSE tissue (batch II), measured and nominal values.....</i>	<i>93</i>
<b>Table 4.3</b>	<i>The values of optical parameters RT, DT, <math>\alpha_{22}</math>, <math>\alpha_{33}</math>, and <math>\alpha_{44}</math> averaged over manually delineated zone of dermis in the images of the five HSE tissue sections of different thicknesses.....</i>	<i>95</i>
<b>Table 4.4</b>	<i>The values of standard deviation of the optical parameters RT, DT, <math>\alpha_{22}</math>, <math>\alpha_{33}</math>, and <math>\alpha_{44}</math> of dermis zone for the five thin tissue sections of different thicknesses.....</i>	<i>98</i>
<b>Table 4.5</b>	<i>The values of the optical parameters RT, DT, <math>\alpha_{22}</math>, <math>\alpha_{33}</math>, and <math>\alpha_{44}</math> averaged over the dermis zone selected with the DBSCAN algorithm in the images of the five HSE sections of different thickness.....</i>	<i>102</i>
<b>Table 4.6</b>	<i>Entropy of the distributions of parameters defined by Eq (4.3)-(4.6) within the dermal layer.....</i>	<i>106</i>
<b>Table 5.1</b>	<i>Mean value and standard deviation (StD) of the azimuth angle: zones A1 – A5.....</i>	<i>129</i>

# Appendix A – List of Publications

## Journal papers

1. P. Schucht, **H. R. Lee**, M. H. Mezouar, E. Hewer, A. Raabe, M. Murek I. Zubak, J. Goldberg, E. Kövari, A. Pierangelo, T. Novikova, “Visualization of White Matter Fiber Tracts of Brain Tissue Sections with Wide-field Imaging Mueller Polarimetry,” *IEEE Trans. Med. Imaging*, 10.1109/TMI.2020.3018439, 2020.
2. P. Schucht, **H. R. Lee**, M. H. Mezouar, E. Hewer, A. Raabe, M. Murek, I. Zubak, J. Goldberg, E. Kovari, A. Pierangelo, and T. Novikova, “Wide-Field Mueller Polarimetry of Brain Tissue Sections for Visualization of White Matter Fiber Tracts,” <http://arxiv.org/abs/2005.12440>, 2020.
3. **H. R. Lee**, C. Lotz, F. K. Groeber-Becker, S. Dembski, E. Garcia-Caurel, R. Ossikovski and T. Novikova, “Tissue Phantom analysis through transmission Mueller polarimetry and differential Mueller matrix formalism: a concise review,” *Asian J. Phys.*, 2020, vol.29, nos 1 &2, pp. 01-11, Jan. 2020.
4. P. Li, **H. R. Lee**, S. Chandel, C. Lotz, F. K. Groeber-Becker, S. Dembski, R. Ossikovski, H. Ma, and T. Novikova, “Analysis of tissue microstructure with Mueller microscopy: logarithmic decomposition and Monte Carlo modeling,” *J. Biomed. Opt.*, vol. 25, no. 1, pp. 015002, Jan. 2020.
5. **H. R. Lee**, P. Li, T. S. H. Yoo, C. Lotz, F. K. Groeber-Becker, S. Dembski, E. Garcia-Caurel, R. Ossikovski, H. Ma, and T. Novikova, “Digital histology with Mueller microscopy: how to mitigate an impact of tissue cut thickness fluctuations,” *J. Biomed. Opt.*, vol. 24, no. 7, pp. 076004, Jul. 2019.
6. A. Marronnier, **H. R. Lee**, H. Lee, M. Kim, C. Eypert, J.-P. Gaston, G. Roma, D. Tondelier, B. Geffroy, and Y. Bonnassieux, “Electrical and optical degradation study of methylammonium-based perovskite materials under ambient conditions,” *Sol. Energy Mater. Sol.*, vol. 178, pp. 179–185, May 2018.
7. H. J. Lee, S. Gaiaschi, P. Chapon, A. Marronnier, **H. R. Lee**, J.-C. Vanel, D. Tondelier, J.-E. Bourée, Y. Bonnassieux, and B. Geffroy, “Direct Experimental Evidence of Halide Ionic Migration under Bias in  $\text{CH}_3\text{NH}_3\text{PbI}_{3-x}\text{Cl}_x$ -Based Perovskite Solar Cells Using GD-OES Analysis,” *ACS Energy Lett.*, vol. 2, no. 4, pp. 943–949, Apr. 2017.
8. J. Kim, **H. R. Lee**, H. P. Kim, T. Lin, A. Kanwat, A. R. bin Mohd Yusoff, and J. Jang, “Effects of UV-ozone irradiation on copper doped nickel acetate and its applicability to perovskite solar cells,” *Nanoscale*, vol. 8, no. 17, pp. 9284–9292, Apr. 2016.
9. J. Kim, **H. R. Lee**, S. J. Lee, W. J. da Silva, A. R. bin Mohd Yusoff, and J. Jang, “Graphene oxide grafted polyethylenimine electron transport materials for highly efficient organic devices,” *J. Mater. Chem. A*, vol. 3, no. 44, pp. 22035–22042, Nov. 2015.

## Proceeding papers

1. **H. R. Lee**, C. Lotz, F. K. Groeber-Becker, S. Dembski, E. Garcia-Caurel, R. Ossikovski, and T. Novikova, “Mueller microscopy of full thickness skin models combined with image segmentation,” Proc. SPIE 11076, Advances in Microscopic Imaging II, 1107615, July. 2019.
2. **H. R. Lee**, T. S. H. Yoo, P. Li, C. Lotz, F. K. Groeber-Becker, S. Dembski, E. Garcia-Caurel, R. Ossikovski, and T. Novikova, “Mueller microscopy of anisotropic scattering media: theory and experiments,” Proc. SPIE 10677, Unconventional Optical Imaging, 1067718, May. 2018.
3. T. S. Yoo, T. Genova-Hristova, **H. R. Lee**, E. Borisova, I. Terziev, E. Garcia-Caurel, R. Ossikovski, and T. Novikova, “Polarized light histology of tissue and differential Mueller matrix formalism,” Proc. SPIE 10484, Advanced Biomedical and Clinical Diagnostic and Surgical Guidance Systems XVI, 1048412, Apr. 2018.

# Appendix B – Conferences, Workshops, Exchange research visits, and Scholarships

## Conferences

### Oral presentations

1. **H. R. Lee**, P. Li, H. Ma, C. Lotz, F. K. Groeber-Becker, S. Dembski, R. Ossikovski, and T. Novikova, “Digital histology of tissue with Mueller polarimetry microscopy,” SPIE Photonics West BIOS, San Francisco, CA, USA, Mar. 2020.
2. **H. R. Lee**, C. Lotz, F. K. Groeber-Becker, S. Dembski, E. Garcia-Caurel, R. Ossikovski, and T. Novikova, “Mueller microscopy of full thickness skin models combined with image segmentation,” SPIE European Conferences on Biomedical Optics, Munich, Germany, Jun. 2019.
3. **H. R. Lee**, T. S. H. Yoo, P. Li, C. Lotz, F. K. Groeber-Becker, S. Dembski, E. Garcia-Caurel, R. Ossikovski, and T. Novikova, “Mueller microscopy of anisotropic scattering media: theory and experiments,” SPIE Photonics Europe 2018, Strasbourg, France, 22-26 Apr. 2018.

### Poster presentations

1. **H. R. Lee**, A. Doronine, and T. Novikova, “A cross-validation study of sever Monte Carlo (MC) models for simulation of polarized light propagation in turbid tissue-like scattering media,” SPIE Photonics West BIOS, San Francisco, CA, USA, Mar. 2020.
2. **H. R. Lee**, J. Park, A. Lindberg, J.-F. Arruabarrena, J. -C. Vanel, E. Garcia-Caurel, T. Novikova, R. Ossikovski, “Mueller polarimetry de théorie vers l’application,” Les Rencontres de la Cancérologie Française, Paris, France, Nov. 2018.
3. **H. R. Lee**, T. S. H. Yoo, P. Li, C. Lotz, F. K. Groeber-Becker, S. Dembski, E. Garcia-Caurel, R. Ossikovski, and T. Novikova, “Digital Histology with Mueller Polarimetry,” 2nd International Workshop on Biophotonics and Optical Angular Momentum (BIOAM-2018), Palaiseau, France, Oct. 2018.

### Other contributions

1. P. Schucht, **H. R. Lee**, M. H. Mezouar, E. Hewer, A. Raabe, M. Murek, I. Zubak, J. Goldberg, E. Kövari, A. Pierangelo, T. Novikova, “Wide-field imaging of brain white matter fiber tracts with Mueller polarimetry in backscattering configuration,” SPIE Photonics West, BiOS, Tissue Optics, Laser-Tissue Interaction and Tissue Engineering: Polarized light and Optical Angular Momentum for biomedical diagnostics, San Francisco, CA, USA, Mar. 2021. (upcoming)

2. **H. R. Lee**, M. Kupinski, A. Pierangelo, R. Ossikovski, C. Lotz, F. Kai Groeber-Becker, S. Dembski, T. Novikova, "Imaging Mueller Polarimetry for Biomedical Applications", SPIE Defense and Commercial Sensing, Symposium "Advanced imaging, simulation and visualization methods in optical sensing", Anaheim, CA, USA, Apr. 2020. (invited, rescheduled for 2021)
3. T. Novikova, **H. R. Lee**, M. Kupinski, P. Schucht, R. Ossikovski, A. Pierangelo, "Biomedical diagnostics with multi-wavelength wide-field imaging Mueller polarimetry," SPIE Optics + Photonics, Online, Aug. 2020.
4. A. Doronin, **H. R. Lee**, A. Bykov, I. Meglinski, T. Novikova, "Cloud-based online application for imitation of polarized light propagation in turbid scattering media," SPIE Optical Engineering + Applications, Online, Aug. 2020.
5. T. Novikova, **H. R. Lee**, I. Saytashev, C. Lotz, F. K. Groeber-Becker, S. Dembski, R. Ossikovski, J. C. Ramella-Roman, "Post-processing of multimodal microscopic images of tissue histological cuts for biomedical diagnostic," SPIE Photonics Europe, Online, Apr. 2020.
6. A. Doronin, **H. R. Lee**, T. Novikova, N. Vera, J. P. Staforelli, A. Bykov, I. Meglinski, "GPU-accelerated online Monte Carlo (MC) application for imitation of twisted light propagation in turbid tissue-like scattering media," SPIE Photonics West BIOS, San Francisco, CA, USA, Mar. 2020.
7. T. S. H. Yoo, T. Genova-Hristova, **H. R. Lee**, E. Borisova, I. Terziev, E. Garcia-Caurel, R. Ossikovski, T. Novikova, "Polarized light histology of tissue and differential Mueller matrix formalism," SPIE Photonics West 2018, San Francisco, CA, USA, Jan.- Feb. 2018.
8. T. S. H. Yoo, T. Genova, **H. R. Lee**, E. Borisova, I. Terziev, E. Garcia-Caurel, R. Ossikovski, T. Novikova, "Polarization image contrast between tumor and healthy tissues - ex vivo investigations," 21st International School for Junior Scientists and Students on Optics, Laser Physics & Biophotonics (SFM'17), Saratov, Russia, Sept. 2017.
9. **H. R. Lee**, S. H. Yoo, T. Genova-Hristova, E. Garcia-Caurel, E. Borisova, R. Ossikovski, T. Novikova, "Biomedical applications of Mueller polarimetry," 4th International Conference on Optical Angular Momentum (ICOAM 17), Anacapri, Italy, Sept. 2017.

## Workshops

1. GdR ISIS "Traitement des signaux polarimétriques optiques et radar", 2018
2. Université Paris-Saclay "Individual Fellowships Theoretical session", 2018
3. GdR ISIS "Journées Imagerie Optique Non Conventionnelle -13ème edition", 2018

## Exchange research visits

1. **Victoria University of Wellington**, Wellington, New Zealand, Dec. 2019  
Subject: Non-invasive polarimetric diagnostic of biological tissue aided by artificial neural networks
2. **Florida International University (FIU)**, Florida, USA, Feb. - Apr. 2019  
Subject: Studies of polarimetric and non-linear optical properties (SHG / TPEF) of mice's cervix.

# Scholarships & Funding

1. **SPIE - The international society for optics and photonics**  
: Optics and Photonics Education Scholarship, 2020
2. **French National Research Agency**  
: Labex NanoSaclay, reference: ANR-10-LABX-0035 / 2018, 2019, 2020
3. **SPIE Student Travel Grant**  
: ECBO 2019, Munich, Germany, 23-27 Jun. 2019
4. **Ecole Doctoral « Interface »**  
: Paris-Saclay University, Oct. 2017 - Sept. 2020

# Appendix C – Résumé de la thèse en français

L'imagerie polarimétrique de Mueller est une technique optique émergente pour le diagnostic non invasif des tissus. Cette technique optique explore la très haute sensibilité de la lumière polarisée sur la microstructure d'un échantillon et fournit des informations les plus complètes sur les propriétés polarimétriques de cet échantillon.

Premièrement, le potentiel du microscope Mueller à transmission fonctionnant dans la gamme du spectre visible pour l'analyse histologique automatisé a été étudié sur des coupes non colorées d'équivalents de peaux humaines. La décomposition logarithmique des matrices de Mueller expérimentales a été combinée à l'algorithme statistique du clustering basé sur la densité des points dans l'espace paramétrique pour les applications avec bruit (DBSCAN) pour la segmentation diagnostique des images microscopiques des modèles de peau humaine. La validité du formalisme de Mueller différentiel pour les milieux dépolarisants homogènes fluctuants a été confirmée expérimentalement pour les tissus biologiques. Une nouvelle méthode est suggérée pour modérer l'impact de la variation d'épaisseur qui pourrait affecter la précision des diagnostics polarimétriques des coupes histologiques. Une nouvelle version de l'algorithme DBSCAN a été développée pour réduire les temps de calculs et ainsi permettre d'analyser les ensembles de données de grande taille. Dans ces ensembles de données, les valeurs aberrantes (ou bruit) ont été filtrées efficacement, le contraste entre les zones dermiques et épidermiques de peau humaine a été considérablement augmenté. En utilisant la méthode Monte Carlo *polarisée* pour modéliser les matrices de Mueller expérimentales pour les coupes minces de modèles de peaux humaine, nous avons confirmé que le dichroïsme linéaire et l'anisotropie de la dépolarisation détectés dans la zone dermique sont dus à la présence de fibres de collagène bien alignées.

Les études ex-vivo de la preuve de principe de la sensibilité de la lumière polarisée rétrodiffusée à une structure hautement ordonnée de substance blanche cérébrale saine sont présentées dans la deuxième partie. Des coupes épaisses de cerveau humain fixées au formol, et de la cervelle de veau fraîche ont été imagées en mode réflexion avec un polarimètre de Mueller à grand champ, opérant dans la gamme de longueurs d'onde visibles.

Il est connu que les tumeurs cérébrales rompent la structure hautement ordonnée de la substance blanche du cerveau, car les cellules tumorales se développent de manière chaotique. Cependant, cette différence de complexité structurelle est difficilement détectable, même avec un microscope opératoire, pendant la neurochirurgie en raison du faible contraste visuel entre la tumeur et le tissu cérébral sain. Nous avons étudié la capacité de l'imagerie polarimétrique de Mueller à grand champ à visualiser les faisceaux de fibres de la substance blanche cérébrale saine en détectant l'anisotropie de son indice de réfraction (c'est-à-dire la biréfringence de la substance blanche du cerveau qui sera effacée par la tumeur). Les matrices de Mueller expérimentales d'échantillons de cerveau ont été traitées à l'aide de l'algorithme de décomposition Lu-Chipman. Les cartes des azimuts de l'axe optique du milieu biréfringent uniaxial corrélient incontestablement avec les images microscopiques

des coupes histologiques des tissus cérébraux colorées à l'argent, qu'est la technique de référence pour la visualisation ex-vivo des faisceaux de fibres de substance blanche du cerveau.

Ces résultats montrent le potentiel de l'imagerie polarimétrique de Mueller à grand champ pour fournir des informations sur l'orientation spatiale relative des faisceaux de fibres cérébrales, ce qui aiderait à détecter la frontière exacte entre la tumeur et le tissu cérébral saine, et guiderait le neurochirurgien lors de la résection de la tumeur et améliorerait les résultats pour des patients.

**Titre :** Etudes des milieux diffusants et anisotropes par la polarimétrie de Mueller: vers l'histologie numérique et la biopsie optique des tissus

**Mots clés :** polarimétrie de Mueller, algèbre des matrices de Mueller, traitement d'image, modélisation Monte Carlo, et diagnostique biomédical

**Résumé :** L'imagerie polarimétrique de Mueller est une technique optique émergente pour la diagnostique non invasive des tissus. Elle explore la sensibilité de la lumière polarisée aux microstructures de tissus.

Les études de coupes de peau humaine ont été effectuées par un microscope de Mueller à transmission. La compression des données polarimétriques, combinée à un algorithme de clustering approprié ont démontré l'amélioration du contraste entre différentes couches de peau, prouvant la faisabilité de l'histologie automatisé.

Des coupes épaisses de cerveau humain ont été étudiées par l'imagerie polarimétrique de Mueller à grand champ en réflexion. L'azimut de l'axe optique du milieu biréfringent uniaxial mesuré corrèle bien avec les directions des faisceaux de fibres de substance blanche du cerveau. La croissance chaotique des tumeurs cérébrales devrait effacer cette biréfringence. Donc, la polarimétrie de Mueller est prometteuse pour aider aux neurochirurgiens lors de l'ablation des tumeurs.

**Title:** Studies of scattering and anisotropic media with Mueller polarimetry: towards digital histology and optical biopsy of tissue

**Keywords:** Mueller polarimetry, algebra of Mueller matrices, image processing, Monte Carlo modeling, and biomedical diagnostics

**Abstract:** Imaging Mueller polarimetry represents an emerging optical technique for a non-invasive diagnostics of tissue. It explores the extreme sensitivity of polarized light to tissue microstructure.

The studies of unstained thin sections of human skin models were done using transmission Mueller microscope. Non-linear compression of polarimetric data combined with appropriate clustering algorithm demonstrated the contrast enhancement between different layers of skin, proving the feasibility of digital histology.

Thick sections of formalin-fixed human brain were studied using wide-field imaging Mueller polarimeter in reflection. The measured azimuth of the optical axis of uniaxial birefringent medium correlates well with the directions of brain white matter fiber tracts. Chaotic growth of brain tumors should erase this birefringence. Thus, Mueller polarimetry holds promise to detect the exact border between the tumor and healthy brain tissue, and to guide neurosurgeon during tumor resection.